MIXING OF DUST IN PROTOPLANETARY DISKS AND THE SOLAR NEBULA

by

ANNA LOUISE HAUGSJAA HUGHES
B.A., University of Montana, 2004
M.S., University of Colorado, 2006

A thesis submitted to the
Faculty of the Graduate School of the
University of Colorado in partial fulfillment
of the requirement for the degree of
Doctor of Philosophy
Department of Astrophysical and Planetary Sciences
2011

This thesis entitled:
Mixing of Dust in Protoplanetary Disks and the Solar Nebula
written by Anna Louise Haugsjaa Hughes
has been approved for the Department of Astrophysical and Planetary Sciences

Dr. Philip J. Armitage

Dr. John Bally

Dr. Stephen J. Mojzsis

Dr. Glen Stewart

Dr. Jeffrey B. Weiss

Date

The final copy of this thesis has been examined by the signatories, and we
find that both the content and the form meet acceptable presentation standards
of scholarly work in the above mentioned discipline.

Hughes, Anna Louise Haugsjaa (Ph.D., Astrophysical and Planetary Sciences)

Mixing of Dust in Protoplanetary Disks and the Solar Nebula

Thesis directed by Associate Professor Dr. Philip J. Armitage

Understanding the small-dust component of protoplanetary disks is key to understanding the conditions for planet formation. Small dust grains, particularly at large distances, provide our primary observational window into the physics of protoplanetary disks, being much more easily observed than the gas component. Furthermore, the distribution of these grains must ultimately control the timing and locations for planetesimal formation, the first major step toward planet formation. For my thesis work, I have used numerical simulations to model the radial distribution of dust grains as they are acted upon by the gas disk, including the evolution of the disk (outward expansion and inward accretion), radial and azimuthal drag of the gas flow on the particle orbits, and turbulent mixing of the particle ensemble radially within the disk. I have run simulations using a range of particle sizes and disk-model parameters and consider primarily two phenomena: the radial diffusion of hot, inner disk particles outward to large AU, relevant to the compositional makeup of bodies within our own solar system, and the time evolution of the global dust-to-gas ratio, which dictates the supply of solid material to the planetesimal- and planet-forming regions. I find that, while the degree out outward mixing depends sensitively on a number of disk-model parameters, the behavior of the global dust-to-gas distribution is relatively uniform between different disk-model simulations, suggesting that, while still mysterious, the conditions for planetesimal formation are commonly met across a range of disk configurations. Observed disk compositions correlate poorly with most observable disk parameters. However, my simulations suggest compositional properties are most-strongly controlled by the initial conditions of young disk systems.

DEDICATION

Dedicated to all of my teachers, past, present, and future.

ACKNOWLEDGEMENTS

Learning has long been a central element of my life and so I feel particularly the strong influence that my teachers have had on my life and on the person I am today. My teachers come in many forms, and I would like to here directly thank a few who have also been a part of my community and my sense of self:

Phil Armitage, Elinita Brown, Josh Colwell, David Friend, Diane Friend, Anson Haugsjaa, Cindy Haugsjaa, Steve Hughes, Jim Jacobs, Jonas Pologe, Hanna Sizemore, Eijiro Uchimoto, Andrew Ware, Alycia Weinberger.

Many people shape who we are and the things we are able to accomplish, and so I have neglected a great many people from the above list. I appoligize. Know that I have long found myself surrounded by good people, and that you are all greatly appreciated.

Contents

List of Tables

List of Figures

Chapter 1

Introduction and the Early Solar Nebula

Understanding the small-dust component of protoplanetary disks is vital if we are to understand planet formation. It is the small-dust component that links two of the biggest mysteries of the field: How should we model the disk turbulence and viscosity that drive both a disk's evolution and its structure? And how do planetesimals, the precursors of planets, form, from what, and in what environments? While fluid-dynamic theory is able to broadly sketch the shape and evolution of gas disks around young stars, observations of such disks, as well as the physical and chemical evidence of our own solar system primarily trace the solid material, comprising only about 1% of these systems. These observations are filled with seeming contradictions: hot-melt minerals embedded in comets along-side pristine ices; large grains orbiting their stars within the tenuous outer reaches of their disks. In this thesis, I use numerical simulations to trace and explore the aerodynamic radial transport of dust particles within evolving protoplanetary disks. The questions I have focused on are these: How is protoplanetary dust distributed? And how is it mixed? Ultimately, the question is: What is it, really, that builds planetary systems?

Protoplanetary disks are an integral component of the star-formation process. As prestellar material from a parent molecular cloud begins to collapse, the intrinsic angular momentum of the cloud dictates that a substantial portion of that material falls into a flattened disk structure, rather than directly onto a central point mass. Mass infalling at later times will tend to fall across wider radial extents of the disk while viscosity within the disk simultaneously allows for the rapid inward accretion of most of the disk material as well as the outward spread of some at the outer disk edge. This disk of material is termed the protoplanetary disk (called the Solar Nebula for that of our own

Solar system). It persists for some millions of years as gas continues to accrete onto the central star and provides the environment in which dust solids may be processed to larger sizes and perhaps eventually into planets. Eventually, all the gas of the disk will be stripped away, either through accretion or loss mechanisms such as photoevapration, leaving only the large bodies, rocky and icy material, behind. Such later disks of solid material are often collisional and are termed debris disks. However, observationally, all disks of material surrounding stars may be called circumstellar disks, including gas-rich protoplanetary disks and debris disks both.

Circumstellar disks of all types are often first detected as excess in the infrared emission coming from a star, resulting from the heating and re-radiation of stellar light by the disk material. Some large, nearby debris disks can be resolved in optical images that show starlight reflecting off of the tenuous debris-disk surface, much as we view the rings of Saturn. Young protoplanetary disks, however, are often optically thick and dense, observed as dark dust lanes obscuring the light of their central star (if viewed nearly edge on) or as silhouettes against the background illumination of their parent star-forming cloud.

Despite this dense, robust presence within their star-forming environment, the gas densities and pressures at the midplane of a protoplanetary disk are so low as to be classified as medium to high vacuum by absolute Earth standards, with pressures at the midplane ranging from $\sim 10^{-4}$–10^{-13} bars between the innermost and outermost regions of the disk. Furthermore, the dust particles that I consider in my simulations are mostly microscopic; millimeter-sized particles are considered quite large in the context of my results, though other studies have called grains up to centimeter scales "well-coupled" to the gas flow. The disk-evolution timescale is broadly set by the lifetimes of the gas disks, which range from around 3–6 Myr. Therefore, transport processes or loss of material that occur on much shorter timescales, ∼50,000 years or less, are often termed 'rapid' and are of particular interest.

The chronology of a planet-forming system falls into three broad stages:

1. The initial collapse of the parent cloud to form a solar-mass star proceeds on roughly 10^5 yr timescales (*Lin & Pringle*, 1990; *Enoch et al.*, 2009), and in this time the bulk of the central mass and disk system is assembled.

2. The lifetime of the gas disk is on the order of 3–6 Myr before it dissipates due to accretion onto

the star as well as via photoevaporation to free space. Recent theory suggests that the earliest disk accretion proceeds in episodic, high-intensity bursts, as most commonly measured rates are too low to build solar masses on the above timescales (*Kenyon et al.*, 1990; *Evans et al.*, 2009), but by about 10^6 years, accretion through the disk drops down to around $10^{-8} M_\odot$ per year (*Hartmann et al.*, 1998). In general, gas disks are no longer observed by around 5–10 Myr years (*Haisch, Lada, & Lada*, 2001) and therefore gas-giant planets, if they form, must do so within that time period.

3. Terrestrial-planet formation is a longer process, typically requiring around 100 Myr in current simulations of solar-system formation (*Raymond et al.*, 2009). The Kuiper belt and Oort cloud are also created during this time as the giant planets scatter planetesimals near their orbits outward. The Nice model for solar-system history (*Morbidelli et al.*, 2009a) predicts that large scale instability in the planet orbits lasted through around 700 Myr at least.

These timescales are in contrast with the 10 Gyr expected lifetime of our sun, the ∼4.5 Gyr age of our Earth, and the hundreds of millions of years for which complex life has existed on its surface.

For the above planet-formation chronology, the first, collapse stage is dominated by fluids theory and gas dynamics and is probed primarily by astronomical observations of star-forming clouds. Within this stage, the dust component exists either as an uncondensed vapor (at high temperatures near the forming star) or as fine, sub-micron-sized grains like those observed within the interstellar medium (ISM). As such, the dust is therefore treated as a well-coupled component, dynamically inseparable from the gas. In the last, terrestrial-planet–building stage, the physics is dominated by large-body orbital dynamics, the gas presumed to either be gone or to have largely negligible final impact on the outcome of events. In this stage, scientific nuances are drawn largely from the orbital architecture of both our own and extra-solar planetary systems, and the important particle components are believed to be at minimum tens of kilometers in size.

The middle, protoplanetary-disk stage, then, is an interface for both gas dominated and solid-body, celestial-mechanics–dominated disk dynamics, as well as simultaneously the transition from very small to very large solid particle sizes, including the process of planetesimal formation, which addresses the transition from cm-sized pebbles up to hundreds-of-kilometer sized bodies suitable for planet building. For this interface stage, observations of dust distributions in extra-solar protoplan-

etary disks offer some insight. But, the physics of dust-gas interactions in low-pressure, orbiting systems is difficult to probe with laboratory experiments. However, physical clues to the processes and chronologies of our own Solar Nebula do exist in the form of the mineralogies and compositions of meteorites, asteroids, and comets. Some important clues include:

* **Calcium-Aluminum-rich Inclusions (CAIs)**. These (sub)mm-sized grains are formed by condensation at some of the highest temperatures found within the early Solar-Nebula gases. They are the oldest dated solids in the solar system, with ages of ∼4,568 Myr (*Morris & Desch*, 2010), but are found within many meteorites with bulk ages 1–3 Myr younger (*Cuzzi, Davis, & Dobrovolskis*, 2003).

* **Chondrules**. These are submm–cm sized spheres of apparently shock-melted rock that make up 30–80% of primitive meteorites and appear to have formed at least 1 Myr after CAIs (*Cuzzi, Davis, & Dobrovolskis*, 2003). They are one of the primary building-blocks of the earliest large solar-system bodies and age-dating techniques indicate their formation persisted for at least 2.5 Myr (*Amelin et al.*, 2002).

* **Iron-core meteorites**. These are meteorites formed from fragments of the core of one or several differentiated-asteroid(planetesimal) parent bodies. Recent evidence suggests some may have ages almost as old as CAIs (*Kleine et al.*, 2005; *Bottke et al.*, 2006), implying the formation of massive solid bodies at the earliest times of Solar-Nebula history.

* ***Stardust* samples**. In 2006, the *Stardust* mission returned to Earth with samples of material captured from the comet 81P/Wild 2 (*Brownlee et al.*, 2006). This comet is believed to have formed beyond the orbit of Neptune and was originally thought to be composed of pristine Solar-Nebula material. However, many of the dust grains recovered are distinctly larger than those observed in the ISM. Furthermore, a large fraction of the silicate grains are crystalline, implying processing at high temperatures almost certainly at disk radii much less than where the comet formed. One of the grains recovered by *Stardust* is CAI-like in nature, and other particles appear to contain chondrule fragments (*Brownlee, Joswiak, & Matrajt*, 2011).

The results of the *Stardust* mission provided the primary motivation for the first part of my thesis research: to study the viability of outward mixing of *Stardust*-sized dust grains within a turbulent,

protoplanetary gas-disk environment. While some studies had already explored turbulent mixing as a means to explain crystalline silicates in comets, most were performed within static disk models and neglected the specific dependence on grain size of aerodynamic-transport properties. For my initial approach, I considered force-balance trajectories of individual grains orbiting and experiencing gas drag within a laminar disk flow. I then added a random walk to these trajectories to simulate the turbulent diffusion of a large ensemble of simulation particles. Tracking an ensemble of particles rather than modeling the dust as a fluid, as is most-commonly done, allows me to examine mixing of dust grains from multiple source regions within a single simulation. While I model one-dimensional (radial) transport only, this simple approach is fairly computationally inexpensive and has allowed me to explore transport of dust-grains over a wide range of parameter space, while still including disk evolution within the computation.

Many studies of grain motion and planetesimal and planet formation employ steady-disk models for simplicity. However, the constraints imposed by observations tell us that disks are not steady systems. Furthermore, characteristics of evolving-disk models (particularly those important to grain transport, such as mass-density profiles and gas-flow velocities) can differ substantially from those with a steady-disk configuration. That the elements of planetary systems form over a range of time (as demonstrated by the age-distributions of chondrules within meteorites), rather than instantaneously, means that forming systems sample a wide range of protoplanetary-disk conditions and must survive within these changing environments. These factors have been especially emphasized by the simulations pertaining to the second focus of my thesis research: using aerodynamic drag and diffusion calculations to consider the global distribution of dust solids within an evolving disk.

Observations of dust populations in disks around other stars, the chondrule-dense nature of most meteorites, and current theories of planetesimal formation all point to large (mm–cm sized) particles being an important, resilient component of protoplanetary disks and the Solar Nebula. However, the fairly straight-foward theories of headwind drag predict that these particles will fall in onto the central star on rapid timescales so-far incompatible with the evidence from CAI and chondrule chronology discussed above. This rapid-infall behavior is a robust outcome of virtually all aerodynamic grain-transport calculations, including those presented in this thesis, and I explore the universality and ramifications of this effect using my transport simulations.

This thesis is roughly divided between the physics and methodology used for my particle-transport simulations and the investigations performed using those simulations. In **Chapter 2**, I describe the model I use to define the evolving disk environment in which my simulation particles experience transport and include a discussion of the relevant observational parameters used to define and constrain my disk models. Next, in **Chapter 3**, I discuss my model for radial transport of dust grains within the disk model. I describe both the relevant physics involved, and include test cases showing that drag-advection and particle-diffusion within my model conform well to high-precision numerical calculations and analytic solutions, respectively.

In **Chapter 4**, I present the first results of my particle-transport simulations and include an overview discussion of how the different pieces of my model setup affect the simulation results. In this chapter, I focus on the outward mixing of inner-disk particles pertinent to the *Stardust* results and observations of extra-solar disk crystallinity. I find that the transport of 20 μm-sized grains (like those of *Stardust*) to the comet-forming region is compatible with turbulent mixing within a Solar-Nebula model disk, though there is a sharp decline in outward mixing for mm-sized grains. While observations of disks around other stars show few correlations between crystallinity and other physical observables of the system, I show that the observations are compatible with a spread in mixing resulting from scatter in the initial compactnesses of disks just after formation of the star-disk systems. In **Chapter 5**, I explore outward mixing for a number of other disk-model parameters. Qualitatively, these results also agree disk observations. The degree of outward mixing is found to be dependent on a few poorly-constrained model parameters, such as the disk radial-temperature profile, and on disk conditions at times too early to be readily observable within other disk systems. However, outward mixing is found to be independent of the global baseline disk temperature, as well as largely independent of the α-scaling of the disk viscosity and the initial mass of the disk, in agreement with non-correlations between disk mass and crystallinity observed for disks around other stars.

Finally, in **Chapter 6**, I focus on the global distribution of dust grains relative to the evolving gas profile. Several recent theories of planetesimal formation suggest that this process may be greatly aided by local increases in the dust-to-gas surface-density ratio (disk metallicity) above solar values. Radial drift of grains due to headwind drag has been proposed as a mechanism to produce such enhancements at small disk radii, and early calculations gave promising enhancement results.

In this chapter, I test this radial-drift hypothesis including disk evolution and radial diffusion of the dust population. I find this mechanism non-viable to produce the required enhancement values, which can be substantial in an evolving-disk scenario. These simulations also highlight the long-standing problem of the rapid loss of mm-sized grains from a smoothly defined disk model, incompatible with observations. I therefore suggest that axisymmetric disk models are insufficient to represent dust transport on a fully global scale and that non-axisymmetric structure and local enhancements likely play an important role in the evolving solids distribution.

A **glossary** is included at the end of the manuscript in Appendix C as a reference for the various symbolic variables used throughout the text. In Appendix A, I derive analytic solutions for the diffusion of a contaminant within a gas disk, while in Appendix B, I specify some of the particular numerical methods used within my code.

Chapter 2

Building a 1D Disk-Evolution Model

There are two primary models used in this work. The particle-transport model described in Chapter 3 tracks the motions of an ensemble of particles radially within a protoplanetary gas disk. The model I describe in this chapter defines that gas disk. It is a 1D, vertically isothermal, α-disk model that evolves in time due to viscous spreading and accretion, where it's primary outputs are the disk surface-density distribution as a function of radius, $\Sigma_g(R)$, and the disk temperature distribution, $T(R)$, which, for the earlier runs, is held fixed to a static $R^{-1/2}$ profile. From $\Sigma_g(R)$ and $T(R)$, the model also calculates bulk properties like the local gas density, ρ_g, as well as the radial and azimuthal (orbital) gas velocities, $v_{r,g}$ and $v_{\phi,g}$, important for computing gas-drag effects on dust particles within the disk. A parameterization of EUV photoevaporation is also included, but is important only near the end of the disk lifetime when accretion rates fall to a few$\times 10^{-10}$ $M_\odot$ yr^{-1}. The primary parameters I use to distinguish between different disk models are: $M_{D,0}$, the initial disk mass, R_d, which defines the initial compactness or spatial size of the disk, and α, which scales the magnitude of the disk viscosity. All three of these parameters have a strong impact on the lifetime and evolution of the disk structure (§2.5). My fiducial disk model uses $M_{D,0} = 0.03 M_\odot$, $R_d = 20$AU, and $\alpha = 10^{-2}$.

In this chapter and generally, when I refer to the disk and disk evolution, I am speaking primarily about the gas component of the disk which, while harder to access observationally than the dusty component, is easier to model and describe using basic physics and fluid dynamics and forms the bulk ($\sim$99%) of the disk material. The mechanics of protoplanetary-(gas)disk physics are still not well understood and I use the α model (described in §2.2 and first described by *Shakura & Sunyaev* (1973)) to parameterize disk turbulence, viscosity and evolution. Nevertheless, many observations

exist to constrain the evolutionary timeline of a disk, and I discuss these constraints and observed properties in §2.1. In §2.2, I outline the properties of the model disks used in this thesis and discuss the disk structure that results from the vertically-isothermal assumption. In §2.3, I discuss the theory used to calculate the model-disk evolution. While some of my work uses a disk model with a static disk-temperature profile, other simulations include the evolution of disk temperature due to energy-balance of stellar flux and heating by accretion. I describe the model for calculating evolving disk temperatures in §2.4. In §2.5, I present some diagnostics for comparing the model disks to observed disks and therefore selecting appropriate values for some of the intrinsic model parameters. Finally, in §2.6, I describe the method for calculating various disk-gas velocities that provide aerodynamic drag in my particle-transport simulations. I summarize the main points of my disk-evolution model in §2.7.

2.1 Observational Understanding and Constraints

While some of our understanding of the Solar Nebula and protoplanetary disks comes from studying solar-system bodies and debris, most of the constraints on disk physics come from observations of disks around other stars. It is from observations that we derive statistics on the sizes of disks, the rate at which disk matter is accreted onto host stars, and the average disk lifetimes. I will sketch the observational constraints on disk characteristics here, and also briefly discuss what is termed the minimum-mass Solar Nebula, which can be used as a tool for placing our own past disk in context with those we observe today.

Probably the disk properties that are the most straight-forward to measure are disk lifetimes and the rates of mass accretion onto disk-host stars. Disk properties are highly variable, even among same-age samples born into the same cluster, but an understanding of disk lifetimes can be gathered via statistics and large surveys of star-forming regions. These surveys tell us that, in general, most solar-type stars less than 1 Myr old have disks, and that most lose them by the time they are 3–6 Myr old (*Haisch, Lada, & Lada*, 2001; *Luhman et al.*, 2010; *Manoj*, 2010). Furthermore, disk dispersal appears to be quite rapid, on the order of a few $\times 10^5$ years, though near-IR signatures of disk material persist somewhat longer than do accretion signatures (*Fedele et al.*, 2010). There are several well-known disk examples (e.g., TW Hydra, $\sim$ 8 Myr old) that are longer-lived than the mean (*Manoj*, 2010), but little to no evidence for active disks persisting beyond 10 Myr (*Fedele*

et al., 2010). From the fall-off rate of the statistics, some stars must lose their disks on 1 Myr timescales, and both disks born into either low metallicity environments or into the denser star clusters appear to be shorter lived (*Yasui et al.*, 2009; *Luhman et al.*, 2010). However, my disk models are aimed at solar-type systems not including external, cluster-environment-type effects. Therefore, model disks with very short lifetimes are probably not good fits to the observations for my purposes.

Accretion signatures of disk material falling onto host stars can be measured via excess luminosity seen in the stellar spectra, and these measurements fall into a fairly well-established range of values, most commonly 10^{-9}–$10^{-7} M_{\odot}$ yr^{-1} (*Gullbring et al.*, 1998; *Isella, Carpenter, & Sargent*, 2009). While any given age bin may see as much as an order-of-magnitude scatter in mass-accretion rates, statistically, these rates fall off over time, being commonly $\sim 10^{-8} M_{\odot}$ yr^{-1} in 1–2 Myr old systems (*Hartmann et al.*, 1998), a few$\times 10^{-9} M_{\odot}$ yr^{-1} in some 4 Myr old systems (*Sicilia-Aguilar, Henning, & Hartmann*, 2010), and as low as a few$\times 10^{-10} M_{\odot}$ yr^{-1} in some 5 Myr old systems (*Dahm*, 2010). These accretion rates do not, however, account for the formation of the host star on the timescales that the star-disk systems typically become well-established ($<$ 1Myr), and recent evidence points to accretion rates being time-variable with episodic bursts of high-accretion (up to $10^{-4} M_{\odot}$ yr^{-1}), at least at early times when the star-forming envelope is still loading mass onto the outer disk (*Dunham et al.*, 2010; *Manoj*, 2010).

Combining the simple alpha-disk model of disk evolution (discussed in §2.2) with observed disk lifetimes and accretion-rates has allowed for estimates of the model-viscosity-scaling parameter, α, with typical values found on the order of $\alpha = 10^{-2}$ (*Hartmann et al.*, 1998). The alpha-model presumes that disk turbulence is the primary driver of disk viscosity, and while belief has long held that turbulence is fundamental to protoplanetary-disk physics, recent measurements are only just reaching the sensitivety necessary to describe the levels of turbulence present in accreting disks around other stars. Tentative measurements of turbulent linewidths measured are a few to a few tenths the local sound speed, consistent with $\alpha \sim 10^{-2}$ estimates (*M. Hughes et al.*, 2011).

The masses and spatial extents of disks are also important parameters for defining these systems, but are more difficult to pin down observationally. Most disk observations are in the form of spectral-energy-distributions (SEDs) and disk dust (only about 1% of the disk mass) emits more clearly than the gas, both for SED and spatially resolved observations. Power-law fits to dust

emission tend to show disks extending out to a few hundred AU, while observations of CO emission in the same systems more than double those disk radii, detecting gas as far out as 1000 AU (*M. Hughes et al.*, 2008) (though small disks may show gas detection only out to a couple hundred AU (*Öberg et al.*, 2010)). Because CO may be seen to emit at quite low gas densities (*Beckwith & Sargent*, 1993), this apparent discrepancy in disk-radius measurements has been largely explained by applying a similarity-solution to the disk-structure model that accounts for the viscous expansion of the disk and an exponential drop-off in surface density at the outer disk edge (*M. Hughes et al.*, 2008). Models of disk structure using similarity solutions report a characteristic radius for the disk, rather than an outer radius. This characteristic radius is typically about half the power-law dust emission measure of the radius and so on the order of a quarter or less the gas-emission radius. Characteristic radii of this type reported in the literature show quite a range in disk sizes, with characteristic radii of < 20 to $\sim$200 AU (*M. Hughes et al.*, 2008; *Isella, Carpenter, & Sargent*, 2009; *Andrews et al.*, 2010). Furthermore, some observations support the idea of disk expansion over time, noting increases in these radii over the range of disk ages (*Isella, Carpenter, & Sargent*, 2009).

Observational estimates of disk masses typically require some assumptions about the disk dust-gas composition as well as some model for the dust-particle size distribution. Nevertheless, many estimates of disk masses have been made, and these also point to distinct variation between disks born into similar environments. Typically, the numbers range from $\sim$ 0.1–40% $M_\odot$ (*Jørgensen et al.*, 2009; *Watson et al.*, 2009; *Öberg et al.*, 2010; *Andrews et al.*, 2010), and again, there is clear evidence that disk mass falls off with the age of the system. *Jørgensen et al.* (2009) measured disk masses of 1.7–46% $M_\odot$ for Class 0 sources where the disks are still being fed by the infalling envelope, but of only 0.81–5.3% $M_\odot$ for Class I sources about 1 Myr old, while *Dahm* (2010) measured disk masses of 3.7×10^{-6}–$6.5 \times 10^{-3} M_\odot$ for a set of 5 Myr old sources. The range of typical, young disk masses seems to be somewhere around 1–10% $M_\odot$. Interestingly, this is also the range given by *Weidenschilling* (1977b) for his estimate of the minimum-mass Solar Nebula. This is an estimate of the minimum mass needed in our solar-system-forming disk to be able to form our planets. It is based on taking the masses of the planets (and the asteroid belt) and then adding extra volatile mass to reach solar composition. The estimate has such a wide range due mostly to uncertainties in the compositions of the giant planets. Another commonly cited minimum-mass

model is the Hayashi-1981 model (see *Armitage* (2010) pp 4–5), which contains a mass interior to 30 AU of 0.01 $M_{\odot}$.

2.2 Basic Setup and Properties

While some studies use static, steady disk models, where the disk surface-density profile is in a steady-state balance with the viscosity and the inward flow of accretion (defined in §2.3.1), one of the primary uses of the disk model that I use is to explore the effects of the evolution of the disk surface-density. I do use a steady disk as a comparison case in Chapter 4, but otherwise, the model disks that I use begin with a $t = 0$ surface-density profile

$$\Sigma_{\rm g}\left(R, t=0\right) = \frac{\dot{M}_0}{3\pi\nu}\left(1-\sqrt{\frac{R_{\rm in}}{R}}\right)\exp\left(-\frac{R}{R_{\rm d}}\right), \tag{2.1}$$

where $\Sigma_{\rm g}$ is the surface density, R is radial distance from the central star, t is time, $\dot{M}_0$ is the $t = 0$ accretion rate onto the central star, ν is the local disk viscosity, $R_{\rm in}$ is the inner-disk boundary (set equal to the inner-grid boundary, $R_{1/2} = 0.099$ AU), and $R_{\rm d}$ is a variable controlling the compactness of the $t = 0$ profile. The $\nu^{-1}\left(1-\sqrt{R_{\rm in}/R}\right)$ terms do reference the steady-disk solution to the primary disk-evolution equation (with irrevocable mass loss, and therefore $\Sigma_{\rm g} \rightarrow 0$, past $R_{\rm in}$). However, the $\exp\left(-R/R_{\rm d}\right)$ term references the similarity solution for a viscously expanding disk and allows for a finite disk-mass distribution. The calculation for the initial disk mass for this distribution is given in §2.5, and I primarily define the disk models that I use with the initial total disk mass, $M_{D,0}$, and the initial compactness, $R_{\rm d}$ (as well as α).

This surface-density profile is evolved numerically due to viscous spreading and photoevaporation, as described in §2.3. This evolution is shown in Figure 2.1 for the fiducial disk models of Chapters 4, 5, & 6 where $M_{D,0} = 0.03 M_{\odot}$, and $R_{\rm d} = 20$ AU (and $\alpha = 10^{-2}$). Chapters 4 & 5 disks use a static temperature profile with $T \propto R^{-1/2}$, appropriate for slowly accreting, passive, flared disks, while the Chapter 6 disks evolve from initially steeper, hotter profiles. However, both sets scale to a passive-disk temperature at 1 AU of 278.9 K. As each disk evolves, the surface density drops (due to accretion onto the central star), and the disk spreads outward before dissipation via photoevaporation occurs after ∼5.5 Myr. I define $\Sigma_g\left(R\right)$ and $T\left(R\right)$ on a radial grid of 600 cells spaced logarithmically in R. Innermost and outermost grid points are placed at 0.1 and 15,000 AU,

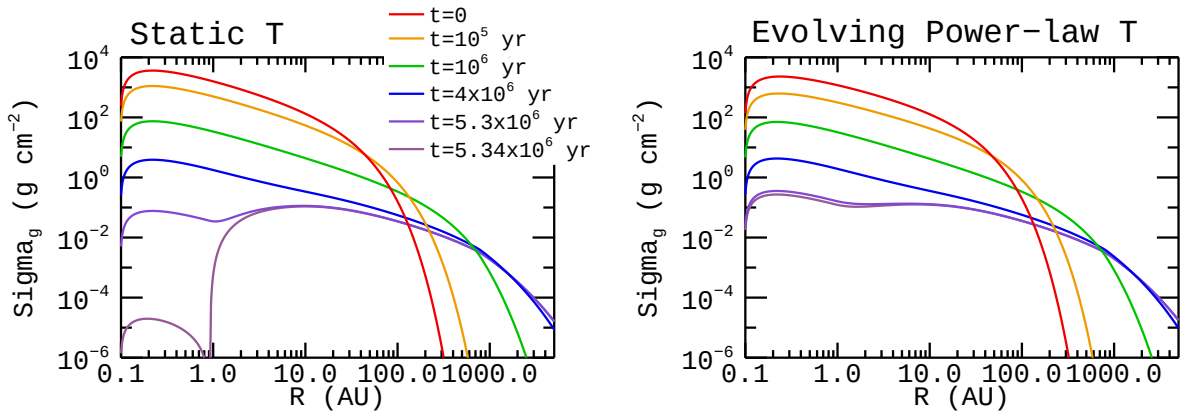

Figure 2.1: Surface-density profiles at different times for the two fiducial disk models of Chapters 4, 5, & 6. Both use $\alpha = 10^{-2}$, and $t = 0$ values of $R_d = 20$ AU and $M_{D,0} = 0.03$ $M_\odot$. However, the Chapters 4 & 5 fiducial models use a static power-law disk-temperature profile, whereas the Chapter 6 fiducial model uses an evolving power-law temperature profile that is initially hotter and steeper. Nevertheless, the evolution of the two models is very similar except that the evolving-temperature model evolves slightly more quickly near $t = 0$ and has a slightly longer lifetime before inside-out clearing via EUV photoevaporation, with gap-opening at $t = 5.47 \times 10^6$ yr.

respectively.

The vertical structure of the disk comes from basic hydrostatic force-balance:

$$-\frac{GM_\star z}{\left(R^2+z^2\right)^{3/2}} - \frac{1}{\rho_g}\frac{\partial P}{\partial z} = 0\,, \tag{2.2}$$

where G is the gravitational constant, $M_\star$ is the mass of the central star, z is the height above the disk midplane, and ρ_g and P are the local gas-density and pressure, respectively. The first term on the left-hand side corresponds to the vertical force of gravity from the central star (for simplicity and because my disks are usually not massive enough for it to matter, my models do not include the self-gravity of the disk), and the second term corresponds to the gaseous pressure support. For an ideal gas, $P = nk_BT = \rho_g k_B T/\mu m_H$, where k_B is Boltzmann's constant, T is temperature, and μ is the average mass of a gas particle in proton masses (m_H). For a vertically isothermal disk in the thin-disk limit, $(z/R)^2 \ll 1$, the local gas density is given by

$$\rho_g = \rho_{g,0}\,\exp\left(\frac{R^2}{H_g^2}\left[1-\frac{1}{2}\frac{z^2}{R^2}+...\right]\right) \approx \rho_{g,mid}\,\exp\left(-\frac{z^2}{2H_g^2}\right) \tag{2.3}$$

where $\rho_{g,mid}$ is the gas density at the mid-plane, and the local disk-gas scale height is now defined

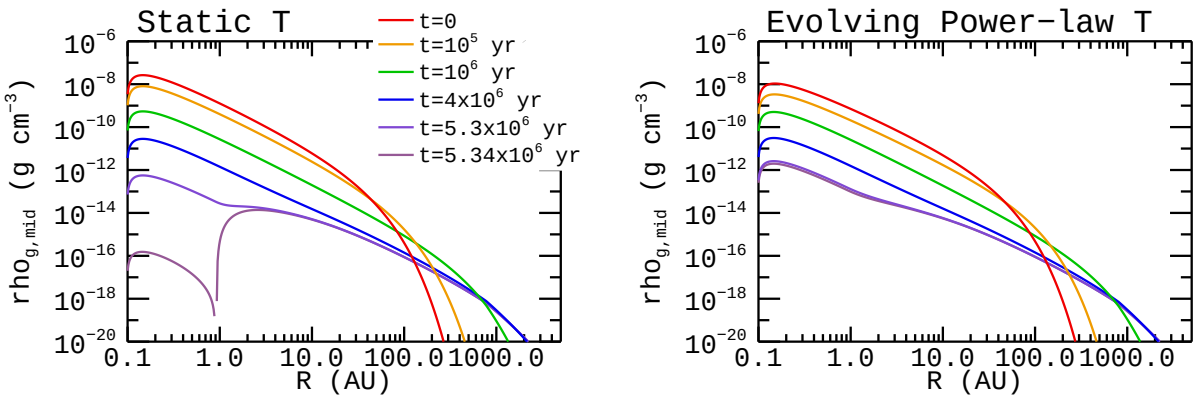

Figure 2.2: Midplane gas-density profiles for the two fiducial disk models of Chapters 4, 5, & 6. Companion plot to Figure 2.1.

here as

$$H_g = \sqrt{\frac{k_B T}{\mu m_H} \frac{R^3}{G M_\star}} = \frac{c_s}{\Omega_{\rm K,mid}}\,, \tag{2.4}$$

where c_s is the sound speed of the gas, and $\Omega_{\rm K,mid}$ is the Keplerian angular velocity at the disk midplane.

Next, in order to derive the midplane density from the surface density, I use the definition of the surface density:

$$\Sigma_g = \int_{-\infty}^{\infty} \rho_g \, dz \approx \int_{-\infty}^{\infty} \rho_{\rm g,mid} \, \exp\left(-\frac{z^2}{2H_g^2}\right) dz\,. \tag{2.5}$$

As H_g does not depend on z, and $\int_{-\infty}^{\infty} e^{-ax^2} dx = \sqrt{\frac{\pi}{a}}$, we have

$$\rho_{\rm g,mid} = \frac{\Sigma_g}{\sqrt{2\pi} H_g}\,; \tag{2.6}$$

$$\rho_{\rm g}\,(z) = \frac{\Sigma_g}{\sqrt{2\pi} H_g} \exp\left(-\frac{z^2}{2H_g^2}\right)\,. \tag{2.7}$$

Unless the disk temperature falls off very steeply in R ($T \propto R^{-3}$ or steeper), the disk scale-height will increase with distance from the star and $\rho_{\rm g,mid}$ will fall off more steeply than Σ_g. Figure 2.2 plots the evolving midplane-density profiles for the fiducial disk models shown in Figure 2.1.

Equation (2.4) shows a clear relationship between temperature and scale-height for a vertically isothermal disk. Next is to relate these quantities to the disk viscosity.

The concept of α-viscosity, put forth by *Shakura & Sunyaev* (1973), assumes that the viscosity in the disk is driven by turbulence and is approximately governed by the size and turnover velocity of the largest eddies. It assumes that "the scale of the eddies is less than the disc thickness (certainly true) and that the turbulence is subsonic (probably true)" (*Pringle* (1981); parenthetical comments original). This then leads to

$$\nu = \alpha c_s H_g \tag{2.8}$$

where ν is the viscosity, and $\alpha \leq 1$ is a dimensionless scaling parameter. Using Equation (2.4), this is often re-written

$$\nu = \alpha \Omega_{\rm K,mid} H_g^2 \,. \tag{2.9}$$

For a passive, flared disk temperature of $T \propto R^{-1/2}$, Equation (2.8) leads to $\nu \propto R$ and therefore steady-disk models with $\Sigma_g \propto 1/R$. For my fiducial models, I adopt $\alpha = 10^{-2}$. This value falls within the range of values estimated observationally (*Hartmann et al.*, 1998; *Hueso & Guillot*, 2005; *King, Pringle, & Livio*, 2007) and allows dissipation of my model disks in less than 10 Myr, as discussed in §2.5.

Other models of disk viscosity used in the literature include, e.g., the beta-prescription for viscosity, which assumes that viscosity is dependent only on local orbital parameters within the disk; viscosity based on gravitational-instability criterion within the disk; and dead-zone disk models, based on phenomena predicted for magnetorotational models of disk turbulence. Like the alpha-prescription, a beta-prescription is most-often used as a simple power-law-in-radius prescription for disk viscosity. Viscositity models based on gravitational instability are often used in conjunction with an alpha-prescription, evaluating local disk conditions for Q-parameter gravitational instability and assigning generally a higher viscosity parameter to those regions based on gravitational overturn properties. Finally, a dead-zone disk model is often described in terms of an alpha-prescription, but with a radial jump in the assumed alpha-value. A deadzone model assumes that ionization rates in the densest inner regions of a disk are incompatible with MRI-driven viscosity, creating an inner-disk dead-zone region where the total-disk viscosity is lower and mass is subsequently piled up relative to the higher-visocisity disk beyond the dead-zone. In a 2D model, the dead-zone is confined to near the midplane of the disk, with active-viscosity zones in the disk surface-layers where ionization remains efficient.

Returning to the alpha-prescription and disk model used in this work, for my vertically-isothermal disk-evolution model, the disk temperature is the fundamental parameter, so that the primary parameters of interest may be summed up with

$$\begin{aligned} H_g &= \frac{1}{\Omega_{\rm K,mid}}\sqrt{\frac{k_B T}{\mu m_H}}\,; \\ \nu &= \alpha \Omega_{\rm K,mid} H_g^2\,; \\ \text{and } \rho_{\rm g} &\approx \frac{\Sigma_g}{\sqrt{2\pi} H_g} \exp\left(-\frac{z^2}{2H_g^2}\right)\,. \end{aligned}$$

If the temperature is defined by a power law, then T, H_g, and ν can be written interchangeably as

$$\begin{aligned} T\left(r\right) &= T_\circ\, r^{q_T}\,; \\ H_g\left(r\right) &= H_\circ\, r^{q_H}\,; \\ \nu\left(r\right) &= \nu_\circ\, r^{q_\nu}\,, \end{aligned} \tag{2.10}$$

where

$$q_T = 2q_H - 3 = q_\nu - \frac{3}{2}\,. \tag{2.11}$$

For the temperature-static disk models that I run, $q_T = -1/2$, $q_H = 5/4$, and $q_\nu = 1$, appropriate for a passively heated, flared disk.

2.3 Modeling Disk Evolution

In this section, I discuss the mechanics of modeling 1D gas-disk evolution, including the basic theory and numerical approach for viscous spreading of mass and angular momentum in a cylindrical, gravitationally bound system, as well as the parameterization used to include loss of disk mass due to photoevaporation. This model for disk evolution assumes that the star and disk are already formed at $t = 0$, with a fixed, central, gravitational mass (and a fixed stellar luminosity), as initial infall and system formation are beyond the scope of the studies of this thesis. The model also assumes that disk evolution occurs in isolation, neglecting radiative or gravitational interactions that might take place with members of the system's birth cluster.

2.3.1 Theory

The derivation for the most basic form of the 1D (radial) disk evolution equation can be found in *Pringle* (1981) and results in an equation for the evolution of the disk surface density, which is:

$$\frac{\partial \Sigma_g}{\partial t} = \frac{3}{R}\frac{\partial}{\partial R}\left[R^{\frac{1}{2}}\frac{\partial}{\partial R}\left(\nu \Sigma_g R^{\frac{1}{2}}\right)\right] \tag{2.12}$$

Equation (2.12) is derived by invoking conservation of mass and conservation of angular momentum within the disk and assuming azimuthal symmetry. Conservation of mass gives:

$$R\frac{\partial \Sigma_g}{\partial t} + \frac{\partial}{\partial R}\left(R v_R \Sigma_g\right) = 0\,, \tag{2.13}$$

where v_R is the radial velocity of the disk material. Conservation of angular momentum gives:

$$R\frac{\partial}{\partial t}\left(\Sigma_g R^2 \Omega_g\right) + \frac{\partial}{\partial R}\left(R v_R \Sigma_g\, R^2 \Omega_g\right) = \frac{1}{2\pi}\frac{\partial G_\nu}{\partial R}\,, \tag{2.14}$$

where Ω_g is the orbital angular velocity of the disk gas, and G_ν is the local torque of an outer annulus of material acting on the annulus of material immediately interior. It is given by

$$G_\nu\left(R,t\right) = 2\pi R^2 dF_\nu = 2\pi R^2 \nu \Sigma_g A = 2\pi R^2 \nu \Sigma_g\, R\frac{d\Omega_g}{dR}\,, \tag{2.15}$$

where dF_ν is the viscous force per unit length, and A is the rate of the shearing.

Assuming that the disk is slowly varying and $\partial\Omega_g/\partial t = 0$ for simplicity, expanding the second term in Equation (2.14), and substituting in Equation (2.13), eliminates the $\partial\Sigma_g/\partial t$ term and provides an equation for $Rv_R\Sigma_g$. Plugging this equation back into Equation (2.13) eliminates the unknown v_R and yields the disk-evolution equation (*Pringle*, 1981) (2.9):

$$\frac{\partial \Sigma_g}{\partial t} = -\frac{1}{R}\frac{\partial}{\partial R}\left[\left(\frac{\partial}{\partial R}\left(R^2\Omega_g\right)\right)^{-1}\frac{\partial}{\partial R}\left(\nu \Sigma_g R^3 \frac{\partial \Omega_g}{\partial R}\right)\right]. \tag{2.16}$$

Equation (2.16) is a more general form of the 1D disk evolution equation, and yields the more tractable, standard-case form of the equation given in Equation (2.12) for the assumption that $\Omega_g = \Omega_{K,mid} = \sqrt{\frac{GM_\star}{R^3}}$. Therefore, the standard disk-evolution equation (which is used to evolve

the model-disk surface-density profile in my disk evolution model) assumes **a)** Keplerian velocities for the disk gas, **b)** zero gravitational contribution from the disk gas, and **c)** a constant stellar-mass value.

Equation (2.12) can be made more compact by using a change of variables: $X = \sqrt{R}$ (*Pringle, Verbunt & Wade*, 1986). This compact form is useful for numerical applications (§2.3.2 & Appendix B.1) and has:

$$\frac{\partial \Sigma_g}{\partial t} = \frac{3}{4}\frac{1}{X^3}\frac{\partial^2}{\partial X^2}\left(\nu \Sigma_g X\right) . \tag{2.17}$$

The disk-evolution equation (2.12) is best physically represented by instead expanding the second derivative in R, to produce

$$\frac{\partial \Sigma_g}{\partial t} = 3\frac{\partial^2}{\partial R^2}\left(\nu \Sigma_g\right) + \frac{9}{2}\frac{1}{R}\frac{\partial}{\partial R}\left(\nu \Sigma_g\right) . \tag{2.18}$$

Here, the change in disk surface density is broken into a diffusive and an advective component, showing that the disk as a whole will tend to spread out, but with a preferred direction of flux for the mass and angular momentum (mass inward and angular momentum outward). Importantly, it is clear that for the special case when the product $\nu\Sigma_g$ equals a constant in R, that the surface-density will remain unchanged. $\Sigma_g \propto 1/\nu$ is then the steady-state solution that (for a fixed viscosity profile) an evolving disk profile will approach over time.

One modifier to the simple $\nu\Sigma_g = C$ steady-disk profile comes from the inner edge of the disk, where a zero-torque boundary condition at $R_{\rm in}$ provides a pinch-off of the disk surface density. The steady-disk profile derived by *Pringle* (1981) (Eq. 3.9) is:

$$\nu \Sigma_g = \frac{\dot{M}}{3\pi}\left(1 - \sqrt{\frac{R_{\rm in}}{R}}\right) \tag{2.19}$$

where $\dot{M}$ is the uniform rate of mass accretion through the disk at all R.

Pringle (1981) derives an analytic solution for disk evolution from the standard equation (2.12) for the case of a constant, uniform viscosity. However, the derivation is easily expanded for any radial power-law relation for the viscosity, $\nu = \nu_0 R^b$. The derivation is performed for the simplest-

case initial condition of a delta function in Σ_g:

$$\Sigma_g\left(R,t\right)=\Sigma_{g,0}\delta\left(R-R_0\right)\ . \tag{2.20}$$

Because this derivation follows much of the same form as the derivation for the diffusion of a contaminant within a steady accretion disk that is outlined in Appendix A, I will not detail it here. A summary of the derivation is as follows

1. Changing variables with $X=\sqrt{R}$ produces the compact form of the equation (2.17).
2. Because the viscosity has been defined as independent of time and a power-law in R, the equation is now separable in R and t.
3. The time component yields exponential decay in time scaled by λ^2, the square of the constant of separation.
4. The spatial component requires another change of variables to produce a Bessel equation with Bessel-function solutions, $J_n\left(x\right)$, dependent on λ.
5. Using the δ-function initial condition, integrating over all λ, and using a Hankel transform finally switches things over to a modified Bessel function, $I_\beta\left(x\right)$.

The final, general solution, assuming initial-condition (2.20) and power-law viscosity ($b\neq 2$, as $b=2$ will not produce a Bessel equation), is given by

$$\begin{aligned}\Sigma_g\left(R,t\right)_{\delta(R-R_\circ)} &= \frac{\dot{M}}{4\pi\sqrt{3\nu_\circ}}\left[\frac{4\beta}{\sqrt{3\nu_\circ}}\right]^{4\beta}\frac{R^{-b/2}}{t}\left(\frac{R_\circ}{R}\right)^{\frac{1}{4}+\frac{1}{2}b} \\ &\quad * \ \exp\left[-4\beta^2\frac{R_\circ^{\alpha_c}+R^{\alpha_c}}{3\nu_\circ t}\right]I_\beta\left[8\beta^2\frac{\left(R_\circ R\right)^{\alpha_c/2}}{3\nu_\circ t}\right] \\ \alpha_c &= 2-b \\ \beta &= \frac{1}{2\left(2-b\right)}\end{aligned} \tag{2.21}$$

where I_β is the modified Bessel function of the first kind of order β. In the case where the viscosity is uniform everywhere in the disk ($b=0$) the final solution reduces to:

$$\Sigma_g\left(R,t\right)=\frac{\dot{M}}{12\pi\nu_\circ t}\left(\frac{R_\circ}{R}\right)^{1/4}\exp\left(-\frac{R_\circ^2+R^2}{12\nu_\circ t}\right)I_{1/4}\left(\frac{R_\circ R}{6\nu_\circ t}\right)\ , \tag{2.22}$$

which is precisely equivalent to Pringle's expression (*Pringle*, 1981) (2.13) if one perfoms the coordinate transforms into his notation:

$$\chi = \frac{R}{R_\circ} \; ; \qquad \tau = \frac{12\nu t}{R_\circ^2}$$

In Appendix B.1, I detail my numerical method for disk evolution and include test comparisons between the output of my code and this simple-case analytic solution.

2.3.2 Numerical Approach

In this subsection, I give an overview of the numeric setup for disk evolution in my code. The detailed discussion of numerical disk evolution is presented in Appendix B.1, along with tests for convergence, fidelity to the analytic test-case solution, and conservation of mass and angular momentum. This is a fairly standard setup for 1D disk evolution and grid-spacing (see, e.g., *Lin & Pringle* (1990); *Hueso & Guillot* (2005)).

The disk-evolution model uses the most compact form of the basic disk-evolution equation,

$$\frac{\partial \Sigma_g}{\partial t} = \frac{3}{4}\frac{1}{X^3}\frac{\partial^2}{\partial X^2}\left(\nu \Sigma_g X\right) \, ,$$

where $X = \sqrt{R}$. This form is both the most tractable numerically and leads to the best convergence, since the addition of multiple terms is a large source of error in numerics. Because of taking this form of the equation, some studies (e.g., *Pringle, Verbunt & Wade* (1986); *Hueso & Guillot* (2005)) have therefore used constant ΔX grid spacing. However, a logarithmic grid spacing provides the best conservation of mass and angular momentum and that is what I use in my disk evolution model (this also provides the grid spacing for the total disk-evolution + particle-transport model as a whole).

$$\begin{aligned} R_i &= R_{\rm min}\left(\frac{R_{\rm max}}{R_{\rm min}}\right)^{(i-1)/\left(n_{\rm grid}-1\right)} \\ X_i &= \sqrt{R_i} \, , \end{aligned} \tag{2.23}$$

where $n_{\rm grid}$ is the total number of points on the grid, $R_{\rm min} = R_1$ is the innermost grid point, and $R_{\rm max} = R_{n_{\rm grid}}$ is the outermost grid point. In my fiducial disk models I use $n_{\rm grid} = 600$, $R_{\rm min} = 0.1$

AU, and $R_{\max} = 15000$ AU (a large radial extent is best for preventing loss of disk mass past the outer grid boundary).

Disk evolution is evaluated using a standard time-explicit finite-difference scheme, which, for the basic disk-evolution equation (with uneven grid spacing), looks like this (*Press et al.* (1992) §19.2):

$$\frac{\Sigma_{g,i}^{j+1} - \Sigma_{g,i}^{j}}{\Delta t} = \frac{3}{4}\frac{1}{X_i^3}\frac{1}{\Delta X_i}\left[\frac{(\nu\Sigma_g X)_{i+1}^{j} - (\nu\Sigma_g X)_i^j}{\Delta X_{i+1/2}} + \frac{(\nu\Sigma_g X)_i^j - (\nu\Sigma_g X)_{i-1}^j}{\Delta X_{i-1/2}}\right], \tag{2.24}$$

where i and j are the spatial and temporal indices, repsectively, $\Delta X_i = X_{i+1/2} - X_{i-1/2}$ is the width of grid cell i and $\Delta X_{i+1/2} = X_{i+1} - X_i$ is the distance from grid point i to $i+1$. Numerical stability for this first-order scheme is given by the condition,

$$\Delta t \leq \frac{2}{3}\min\left(\frac{\Delta X_i \Delta X_{i-1/2} X_i^2}{\nu_i}\right), \tag{2.25}$$

and for my disk-evolution model I use

$$\Delta t = \zeta_{\Delta t} \times \frac{2}{3}\min\left(\frac{\Delta X_i \Delta X_{i-1/2} X_i^2}{\nu_i}\right), \tag{2.26}$$

where $\zeta_{\Delta t} = 1/2$. This time-stepping constraint is the primary draw-back to using logarithmic grid spacing; the very small grid cells in the inner-disk regions require the evolution be calculated with a very small global time-step ($\Delta t \sim 0.05$ years in my fiducial models). The effect is counter-acted a bit by the fact that the viscosity values tend to be lowest in the inner disk (the turbulence is smaller-scale). However, since the time-stepping does go as $1/\nu$, simulations using larger values of α for the disk-viscosity parameterization are proportionally more expensive to run.

2.3.3 Parameterized EUV Photoevaporation

To include EUV photoevaporation in my disk-evolution model, I use the parameterization presented in *Alexander & Armitage* (2007) of the work of *Font et al.* (2004). Because I am interested in only the surface-density profile as the disk evolves, photoevaporation is treated as simply a mass-loss

term, so that the basic equation is

$$\frac{\partial \Sigma_g}{\partial t} = \frac{3}{R}\frac{\partial}{\partial R}\left[R^{1/2}\frac{\partial}{\partial R}\left(\nu \Sigma_g R^{1/2}\right)\right] - \dot{\Sigma}_{\rm wind}\left(R,t\right) \ , \tag{2.27}$$

where $\dot{\Sigma}_{\rm wind}$ is the rate of surface-density loss due to photoevaporation. Numerically, the viscous and photoevaporative disk evolution are performed separately, so that the surface-density profile is first viscously evolved as outlined in §2.3.2 to produce a $\Sigma_{\rm visc}\left(R\right)^{j+1}$ profile. Then the photoevaporation component is subtracted following

$$\Sigma_i^{j+1} = \left(\Sigma_{visc}\right)_i^{j+1} - \Delta t \left(\dot{\Sigma}_{wind}\right)_i^j \ . \tag{2.28}$$

If the calculated mass loss is greater than the available mass remaining in a grid cell, the surface-density in that cell is set equal to zero.

Following *Alexander & Armitage* (2007), $\dot{\Sigma}_{\rm wind}\left(R,t\right)$ is broken into two components, which essentially define a first and second stage of EUV photoevaporation. The two components are called the diffuse wind, $\dot{\Sigma}_{\rm diffuse}$, and the direct wind, $\dot{\Sigma}_{\rm direct}$, referring to the respective sources of ionizing radiation.

The **diffuse wind** dominates in the beginning and is caused by radiation that scatters off the disk atmosphere and ionizes the surface layers of the disk. It is easy to see how a wind will be launched at and beyond a disk radius where the high temperature of the ionized layer allows it to be gravitationally unbound. This radius is given by

$$R_g = \frac{GM_\star}{c_{s,\rm ionz}^2} \, , \tag{2.29}$$

where $c_{s,\rm ionz} = 10$ km s^{-1} is the sound speed of the ionized gas. However, interior to this point, there is also a subsonic flow of material that, for this parameterization, may cause loss of disk gas as far inward as $\dfrac{R}{R_g} = \chi_R = 0.1$. Therefore, the diffuse wind is set equal to zero interior to $\chi_R = 0.1$. Exterior to this boundary, the equation used for the diffuse wind is given by

$$\dot{\Sigma}_{\rm diffuse}\left(R,t\right) \quad = \quad K_{\rm diff}\sqrt{\Phi_{\rm diff}\left(t\right)}\left(\frac{2}{\chi_R^{15/2}+\chi_R^{25/2}}\right)^{1/5}$$

$$* \left(\chi_R - 0.1\right)^{D_{ph}} \exp\left[B_{ph}\left(\chi_R - 0.1\right)\right] , \tag{2.30}$$

where $K_{\rm diff}$ is a constant containing numerical fit parameters for the diffuse wind density and wind launch velosity, $\Phi_{\rm diff}$ is the ionization flux, and $D_{ph} = 0.2457$ and $B_{ph} = -0.3612$ are fitting constants for the the launch velocity of the diffuse wind. K_{diff} is given by

$$K_{\rm diff} = \frac{\sqrt{3} C_{1,ph} A_{ph}\, \mu_{\rm ionz}\, m_H\, c_{s,\rm ionz}}{\sqrt{\pi\, \alpha_B\, R_g^3}} , \tag{2.31}$$

where $\mu_{\rm ionz} = 1.35$ is the average mass of an ionized wind particle in proton masses, m_H, $\alpha_B = 2.6 \times 10^{-13}$ cm^3 s^{-1} is a recombination coefficient for atomic Hydrogen, and $C_{1,ph} \simeq 0.14$ and $A_{ph} = 0.3423$ are, once again, numerical fitting factors. A_{ph} scales the wind launch velocity relative to $c_{s,\rm ionz}$, and $C_{1,ph}$ scales the base density profile.

In the first stage of EUV photoevaporation, when the wind is diffuse-wind dominated, $\Phi_{\rm diff} = \Phi = 10^{42}$ photons s^{-1} (*Alexander, Clarke, & Pringle*, 2005; *Alexander & Armitage*, 2007). However, once the viscous accretion rate drops low enough that photoevaporated material is no longer replaced by inward-flowing gas, a gap opens in the disk at $R = R_{\rm gap}$[1], and photoevaporation transitions from the diffuse-wind regime, to the direct-wind regime. During the transition from diffuse to direct wind,

$$\Phi_{\rm diff}\left(t\right) = \Phi \left(\frac{R_{\rm thin}\left(t\right)}{R_{\rm edge}\left(t\right)}\right)^2 , \tag{2.32}$$

where $R_{\rm thin}\left(t\right) < R_{\rm gap} < R_{\rm edge}\left(t\right)$, $R_{\rm thin}$ is the transition radius from the inner-disk material to the optically thin gap, and $R_{\rm edge}$ is the inner edge of the outer disk outside the gap. EUV photoevaporation is driven by ionization of hydrogen, and the optically-thin limit used to define the edges of the gap, $R_{\rm thin}$ and $R_{\rm edge}$ is given by $\Sigma_g < m_H/\sigma_{13.6\rm eV}$, where $\sigma_{13.6\rm eV} = 6.3 \times 10^{-18}$ cm^2 is the absorption cross-section for ionizing photons. Once the inner disk has viscously drained onto the central star, $R_{\rm thin} = 0$ and the diffuse wind is completely shut off.

The **direct wind** is due to ionizing radiation that directly strikes the flared inner edge of the

[1]Note that in *Alexander & Armitage* (2007), $R_{\rm gap}$ is defined as $R_{\rm crit} \approx 1.4\left(M_\star/M_\odot\right)$ AU, technically independent of where the gap actually opens (usually somewhat interior to 1.4 AU). While there seem to be other photoevaporative physics involved in defining $R_{\rm crit}$, because of this discrepancy, my disk-evolution code simply waits to define $R_{\rm gap}$ until a gap is opened and sets it equal to that initial gap location.

disk, just beyond the gap. Interior to the gap there is zero direct-wind photoevaporation. For $R > R_{\rm gap}$, the direct wind is given by

$$\dot{\Sigma}_{direct}\left(R,t\right) = f_{ph}\left(R,t\right)\, K_{\rm dir}\, R_{\rm edge}^{a_{ph}-3/2}\left(t\right)\, \sqrt{\Phi_{\rm dir}\left(t\right)}\sqrt{\frac{R^{1-2a_{ph}}}{H_g\left(R\right)}}\,, \tag{2.33}$$

where $f_{ph}\left(R,t\right)$ is a smoothing function, used to prevent the direct-wind component from diverging (unphysically) at small R, $K_{\rm dir}$ is made up of constants from the $\dot{\Sigma}_{\rm direct}$-fit relation, $\Phi_{\rm dir}$ is the direct-wind ionization flux, and $a_{ph} = 2.42$ is a direct-wind power-law scaling in R with-respect-to $R_{\rm edge}$. The fit for the direct wind presented in *Alexander & Armitage* (2007) is based on the results of *Alexander, Clarke, & Pringle* (2006). The smoothing function is given by

$$f\left(R,t\right) = \left[1 + \exp\left(-\frac{R - R_{\rm edge}\left(t\right)}{H_g\left(R = R_{\rm edge}\right)}\right)\right]^{-1}\,. \tag{2.34}$$

And,

$$K_{\rm dir} = \frac{C_{2,ph}\,\mu_{\rm ionz} m_H\, c_{s,{\rm ionz}}}{\sqrt{\pi\,\alpha_B}}\,, \tag{2.35}$$

where $C_2 = 0.235$ is a scaling constant (suitable for $H_g/R \simeq 0.05$).

Once the inner disk drains and the direct wind dominates, $\Phi_{\rm dir} = \Phi$. However, during the transition from diffuse to direct wind, the direct-wind ionizing flux is filtered by the optical depth of the inner disk, and

$$\Phi_{\rm dir}\left(t\right) = \Phi\, \exp\left[-\frac{\sigma_{\rm 13.6eV}}{m_H}\exp\left(-\frac{\chi_{ph}^2}{2}\right)\int_0^{R_{\rm edge}(t)}\frac{\Sigma_g}{\sqrt{2\pi}H_g}\,dR\right]\,, \tag{2.36}$$

where $\chi_{ph} = 2.5$ accounts for the inclusion of gas-density effects χ_{ph} scaleheights above the disk midplane. The initial gap-opening is somewhat sensitive to the evaluation of the integral in Equation (2.36), as well as to the grid-space resolution of the model in the inner disk, so logarithmic grid-spacing is a plus for this.

Figure 2.3 shows a replica the gas-disk evolution in Figures 2 & 3 in *Alexander & Armitage* (2007) using my disk-evolution code. Compared to their figures, the inner disk drains faster than it should. However my simulations are not concerned with the dynamics of particles orbiting within a rapidly clearing inner disk, and so I consider this to be a sufficiently accurate match for my

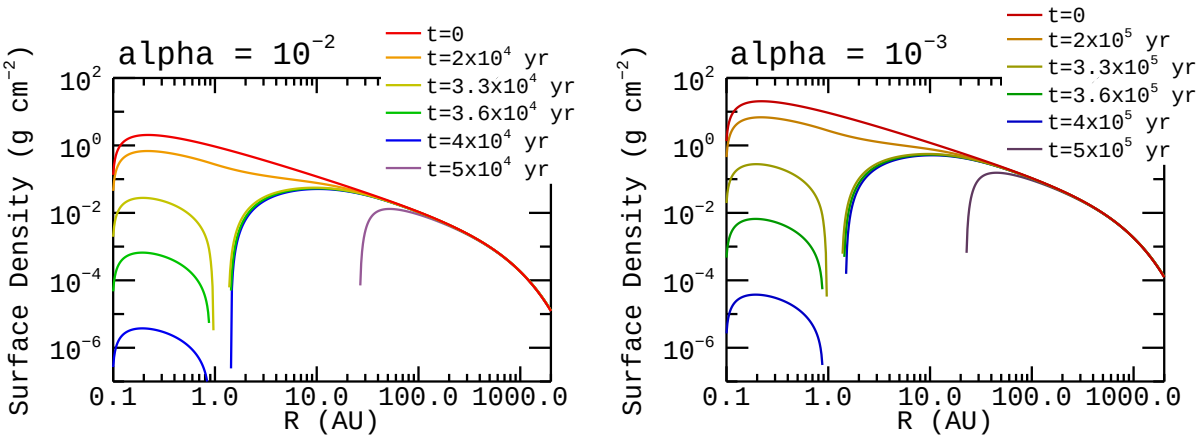

Figure 2.3: Disk evolution and EUV-photoevaporation gap opening for disk models mimicking those presented in *Alexander & Armitage* (2007): $\dot{M}_0 = 10^{-10}$ $M_\odot$ yr^{-1}, $R_d = 500$ AU. The inner disk drains slightly too fast with my disk model compared with the *Alexander & Armitage* (2007) results, but they are otherwise a good match.

purposes.

2.4 Evolving the Disk Temperature

The simulations that I run to examine the outward mixing of inner-disk grains for Chapters 4 & 5 use a static disk-temperature profile for the model-disk structure and evolution. However, at early times, during disk formation via infall and the initial period of energetic accretion, disks are believed to be much hotter (*Cassen*, 2001), particularly in the inner, planet-forming regions. Therefore, before running simulations of the global dust distribution for Chapter 6, I upgraded the disk-evolution model to include evolution of the disk-temperature profile. Interestingly, although in the α model for disk viscosity $\nu \propto T$, the end result is *not* a strong effect on the disk evolution or lifetime. While hot inner disks do drain more quickly, most of the disk mass is held at large distances from the star where the change in computed disk temperature is small and slightly more-rapid expansion at early times actually results in a slightly longer disk lifetime.

My disk-evolution code currently allows for two methods of modeling disk-temperature evolution, the second method being a parameterization of the first and therefore less computationally expensive. For the first method, I solve for the temperature at the disk midplane according to energy-balance between radiative cooling and the incident starlight at the disk surface, and heat generated at the midplane by the dissipation of energy via accretion. For the second method, I fit

a power-law distribution, $T = T_0 R^{q_T}$, (truncated at $T = 10$ K in the outer disk) to the modeled distribution and allow T_0 and q_T to change with time, following a prescribed decay toward a passive-disk profile. Because my simulations do not closely examine the chemical or mineralogical effects associated with the range of possible disk temperatures, this second, faster method for calculating disk-temperature evolution is sufficient for most of my applications. However, one initial run of disk evolution accounting for the full energy-balanced temperature is first required for a given set of disk parameters in order to choose an appropriate evolving–power-law approximation.

2.4.1 Calculating an Energy-balanced Temperature at the Disk Midplane

For the energy-balanced model, I solve for the gas temperature at the disk midplane for each radial grid point at each disk-evolution time step. I assume that the disk is everywhere in a steady-state so that the energy-flux from radiative cooling is balanced exactly by the heating fluxes from absorption of external radiation and from viscous dissipation within the disk. I assume that the disk is optically thick in the radial direction so that all energy transport is vertical relative to the disk midplane and can then solve for the temperature at each radial grid point in isolation. For simplicity, I assume that all energy loss is radiative and so do not account for some portion that may be converted into mechanical energy, e.g., in a disk wind. Therefore, the equation for energy-balance is

$$F_{\rm cool} = F_{\rm visc} + F_{\rm star} + F_{\rm cloud}\,, \tag{2.37}$$

where $F_{\rm cool}$ is the rate of energy loss per unit area due to radiative cooling, $F_{\rm visc}$ is the rate of heating by viscous dissipation, $F_{\rm star}$ is the energy flux of radiation from the central star, and $F_{\rm cloud}$ is the energy flux from the background radiation of the cloud in which the disk has formed.

Radiative heating and cooling are straight-forward. Remembering that the disk has two sides,

$$F_{\rm cool} = 2\sigma_{\rm B}\epsilon T_e^4\,, \tag{2.38}$$

where $\sigma_{\rm B} = 5.6704 \times 10^{-5}$ ergs s^{-1} cm^{-2} K^{-4} is the Stefan-Boltzman constant, $\epsilon = 1$ in the optically-thick regime is the radiative efficiency of the gas, and T_e is the effective temperature at

the disk surface. Following the approximation used in *Ciesla* (2009),

$$F_{\rm star} = 2\sigma_{\rm B}\epsilon T_{\rm irr}^4 = \frac{L_\star \phi}{2\pi R^2}\,, \tag{2.39}$$

where $T_{\rm irr}$ is the effective local temperature of irradiation from the central star, $L_\star$ is the luminosity of the central star, and ϕ is the local angle of incidence between the disk and the starlight. For most of the science simulations of this thesis, I set $L_\star = 5.0175 L_\odot$, in order to match $T\,(1{\rm AU}) = 278.9{\rm K}$ in the fiducial, passive-disk temperature models of Chapters 4 & 5. I follow *Ciesla* (2009) in setting $\phi = 0.05$ everywhere. For the background radiation

$$F_{\rm cloud} = 2\sigma_{\rm B}\epsilon T_{\rm cloud}^4\,, \tag{2.40}$$

where $T_{\rm cloud} = 10{\rm K}$ is the background temperature of the cloud environment.

For heating due to the viscous dissipation of energy, one returns to the equations for viscous torque and disk evolution discussed in *Pringle* (1981) and in §2.3.1 above. On an annulus of gas of area $2\pi R\Delta R$, work is done by the viscous torque, G_ν, at a rate of:

$$\Omega_g \frac{\partial G_\nu}{\partial R}\Delta R \equiv \left[\frac{\partial}{\partial R}\left(\Omega_g G_\nu\right) - G_\nu \frac{\partial \Omega_g}{\partial R}\right]\Delta R\,. \tag{2.41}$$

The first term of the equivalence represents the energy-transport rate, while the second term represents the rate of energy dissipation as heat within the disk. Using the relation for G_ν given in Equation (2.15), per unit area

$$F_{\rm visc} = \frac{G_\nu \Omega_g' \Delta R}{2\pi R \Delta R} = R^2 \nu \Sigma_g \left(\frac{\partial \Omega_g}{\partial R}\right)^2\,. \tag{2.42}$$

Inserting these energy-flux definitions into the energy-balance Equation (2.37) gives

$$2\sigma_{\rm B} T_e^4 = R^2 \nu \Sigma \left(\frac{\partial \Omega_g}{\partial R}\right)^2 + 2\sigma_{\rm B}\left(T_{\rm irr}^4 + T_{\rm cloud}^4\right)\,. \tag{2.43}$$

However, that Equation (2.43) is correct only in the optically thick regime, while the outer, optically thin regions of the disks are also important for my studies of long-distance particle transport. To

include optically thin solutions and to solve for the temperature at the disk midplane rather than the effective, radiative temperature at the surface, I use the approximation derived by *Nakamoto & Nakagawa* (1994):

$$\sigma_{\rm B} T_{\rm mid}^4 = \frac{1}{2} R^2 \nu \Sigma_g \left(\frac{\partial \Omega_g}{\partial R} \right)^2 \left(\frac{3}{8} \tau_R + \frac{1}{2\tau_P} \right) + \sigma_{\rm B} \left(T_{\rm irr}^4 + T_{\rm cloud}^4 \right) , \tag{2.44}$$

where $T_{\rm mid}$ is the temperature at the disk midplane, τ_R is the Rosseland mean optical depth, and τ_P is the Planck mean optical depth. Some notes on this deriviation/approximation:

* *Nakamoto & Nakagawa* (1994) note that in the optically thick regime, the radiative-diffusion approximation, in terms of the viscous heating, gives $T_{\rm mid}^4 = T_e^4 + \frac{3\tau_R}{16\sigma_{\rm B}} F_{\rm visc}$.
* In terms of heating by external radiation, re-radiation of that energy is assumed to be inefficient so that a vertically isothermal approximation can be made for those contributions.

The Rosseland mean optical depth is defined in terms of the disk surface density and the Rosseland mean opacity, κ_R.

$$\tau_R = \kappa_R \Sigma_g \, . \tag{2.45}$$

Note that untangling optical depth and opacity in the literature is a bit tricky due to different methods used to set up the problem. Some papers use Equation (2.45) as I have shown it (*Nakamoto & Nakagawa*, 1994; *Stepinski*, 1998), whereas others use $\tau_R = \kappa_R \Sigma_g / 2$ (*Ruden & Pollack*, 1991; *Hueso & Guillot*, 2005; *Ciesla*, 2009; *Rice & Armitage*, 2009). However, true contradictions in theory likely appear in few, if any of these derivations. Finally, *Nakamoto & Nakagawa* (1994) use $\tau_P / \tau_R = 2.39$, citing it as more traditional but with some observational results maybe pointing to $\tau_P / \tau_R \sim 1$ being more accurate — though it is probably also temperature dependent. For simplicity, in this temperature-evolution model, I use

$$\frac{\tau_P}{\tau_R} = 1 \, . \tag{2.46}$$

The choice of τ_P / τ_R appears to have a negligible impact on temperatures calculated for my model disks, as shown in Figure 2.6.

Next, solving Equation (2.44) for the midplane disk temperature requires solving two other

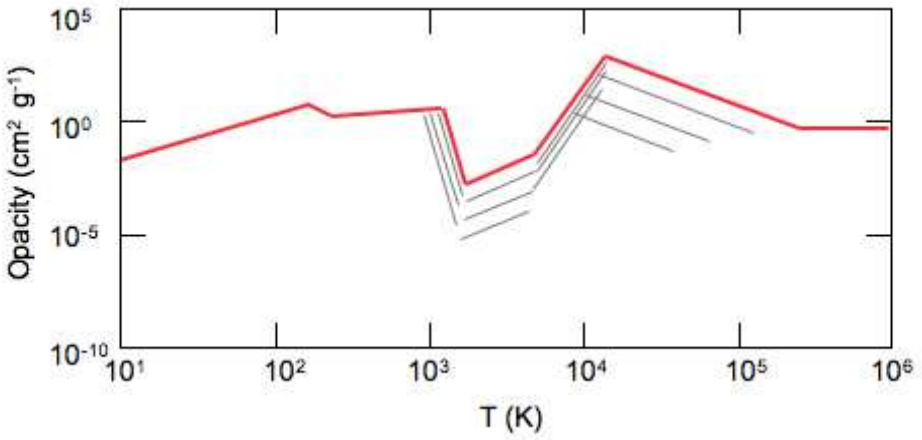

Figure 2.4: Schematic of *Bell & Lin* (1994) opacity vs. temperature (at $\rho_g = 1 \times 10^{-7}$ g cm^{-3}). The opacity is divided into eight temperature domains with four of those domains dependent on the mean gas density. Grey'ed lines indicate the trends toward lower and lower density.

equations simultaneously. First, the opacity, κ_R, depends on both the temperature and the mean density of the gas, the later of which I approximate with the disk-midplane density given in Equation (2.6) for a vertically isothermal disk, $\rho_{\rm g,mid} \propto 1/T$. Second, in the α-approximation given in Equation (2.9), the viscosity is also temperature-dependent, following $\nu = \alpha \Omega_{\rm K} H_g^2 \propto T$. Therefore, deriving an energy-balanced disk-temperature requires solving for $T_{\rm mid}$, κ_R (and $\rho_{\rm g,mid}$), and ν simultaneously. The numerical methodology for this is detailed in Appendix B.3.3.

By far, the most troublesome piece of the solution comes from the Rosseland mean opacity, for which I use the parameterization of *Bell & Lin* (1994). In this parameterization, the opacity is devided into eight regimes dependent on temperature. In each regime, a different mechanism dominates and

$$\kappa = \kappa_i \rho_g^{a_i} T^{b_i} \,, \tag{2.47}$$

where κ is defined in units of cm^2 g^{-1}. The boundaries between the different regimes are defined at $\kappa_i \rho^{a_i} T^{b_i} = \kappa_{i+1} \rho^{a_{i+1}} T^{b_{i+1}}$.

$$T_{\rm bound}\,(i \rightarrow i+1) = \left[\left(\frac{\kappa_i}{\kappa_{i+1}} \right) \rho^{(a_i - a_{i+1})} \right]^{1/(b_{i+1} - b_i)} \,.$$

Bell & Lin (1994) also use a smoothing technique to transition between each regime, but for a basic, 1D disk model, such refinement is not necessary, and my model simply divides the opacity

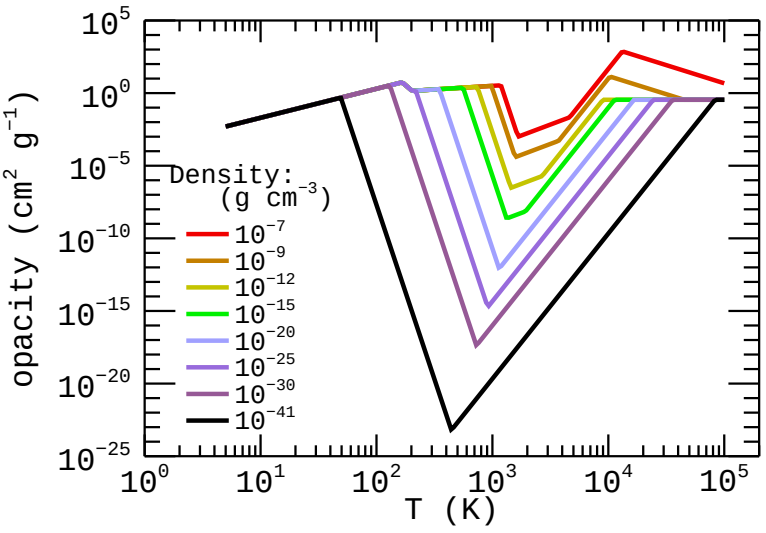

Figure 2.5: *Bell & Lin* (1994) opacities for a range of mean gas densities. Opacities divided into discreet temperature domains, rather than smoothed as in *Bell & Lin* (1994).

into discreet temperature domains. These domains are dominated, as defined by *Bell & Lin* (1994), by: ice grains; the evaporation of ice grains; metal grains; the evaporation of metal grains; molecules; H-scattering; bound-free and free-free processees; and electron scattering. Note that above $T \sim$ 2000K, the *Bell & Lin* (1994) are known to be consistently low. However, such high temperatures are almost always above the regime of those seen in my model disks.

In fact, not all of the opacity domains are dependent on the mean density, and Figure 2.4 plots a schematic of the opacity versus temperature, with grey'ed lines indicating the trends toward lower and lower gas density. As the trend lines shift, the transition points between some domains cross other domain boundaries. Where this occurs, the middle-most domain is discarded and a new domain boundary calculated using trend lines from the domains to either side. Figure 2.5 plots the *Bell & Lin* (1994) opacities vs. temperature for a range of mean-density values. Below $\rho \sim 10^{-10}$ g cm^{-3}, the bound-free–free-free domain is lost, as are the molecules domain below $\rho \sim 10^{-18}$ g cm^{-3}, the metal-grains domain below $\rho \sim 10^{-25}$ g cm^{-3}, and the evaporation-of-ices domain below $\rho \sim 10^{-26}$ g cm^{-3}.

The results of solving for the energy-balanced temperature at $t = 0$ in the fiducial disk model are shown in Figure 2.6. Note that in the inner regions the temperature is dominated by accretion (with lower temperatures for lower disk viscosity), while the temperature in the outer disk is dominated

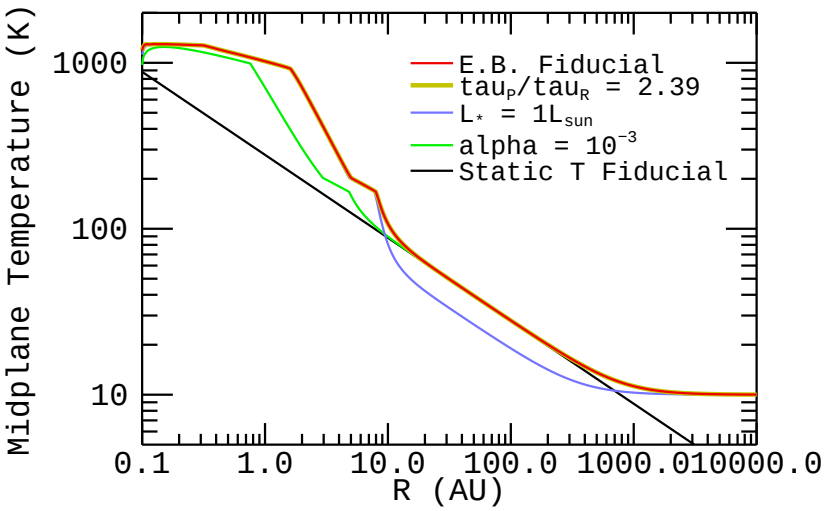

Figure 2.6: Midplane-temperature distribution at $t = 0$ calculated with the energy-balance–temperature code for the fiducial disk parameters ($M_{D,0} = 0.03 M_\odot$, $R_d = 20$, $\alpha = 10^{-2}$, $L_\star \simeq 5 L_\odot$) unless otherwise specified. The static temperature used for the fiducial disks of Chapters 4 & 5 is included for reference. Note that the test run with $\tau_P/\tau_R = 2.39$ is virtually identical to the $\tau_P/\tau_R = 1$ case.

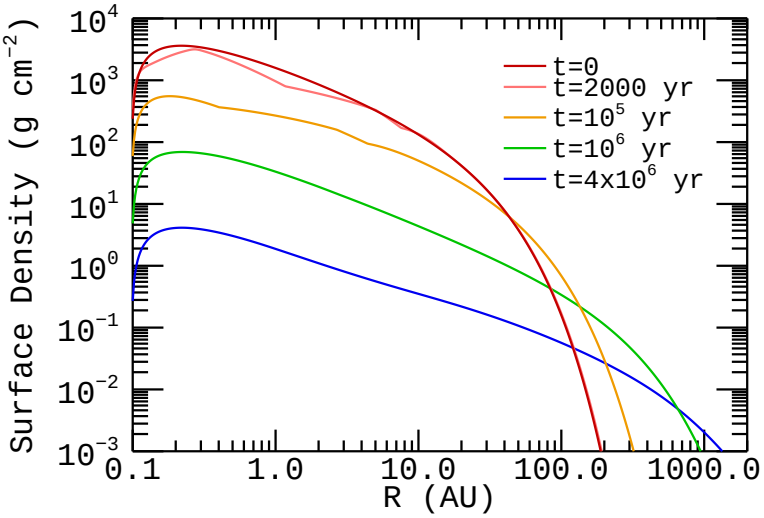

Figure 2.7: Surface-density profiles from running the disk-evolution code with an energy-balanced temperature distribution and the fiducial-disk parameters listed in Figure 2.6.

by stellar and background radiation. Such a non-smooth temperature distribution does have an observable effect on the evolving surface-density profile at early times, as shown in Figure 2.7 for the fiducial-disk model. Since (in the α-viscosity model) $\nu \propto T$, a greater inward flow of material occurs where the temperature is highest, and the inner disk quickly settles into a quasi-steady state with lower Σ_g in regions of high T and a mass flux that is roughly constant in R.

2.4.2 Calculating an Evolving Disk Temperature using a Power-law Parameterization

Converting the temperature evolution derived using the energy-balance method to a fitted, evolving, power-law distribution is a two step (two fit) process. First is to fit the temperature distribution at each time step with a power-law distribution:

$$T\left(R,t\right) = T_{AU}\left(t\right)\left(\frac{R}{1\mathrm{AU}}\right)^{q_T(t)} .$$

To make this fit, I have chosen to fix this first power-law fit to the modeled temperature distribution at the grid points for $R \sim 0.2$ & ~ 200 AU, as shown in Figure 2.8. Therefore,

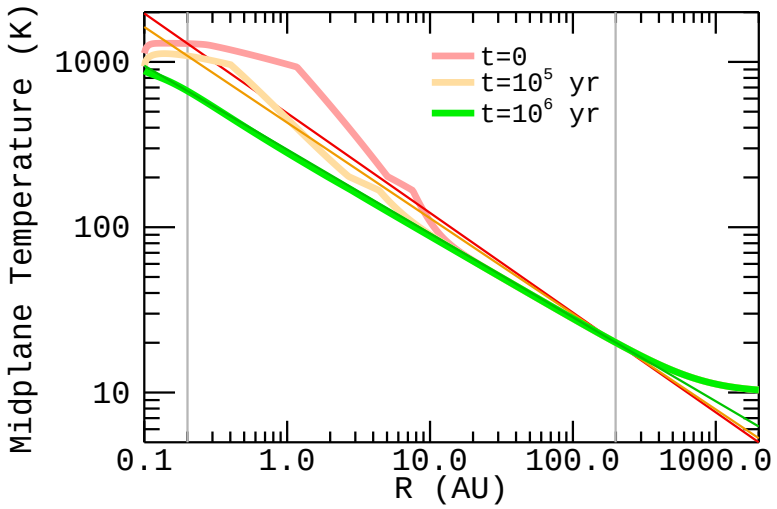

Figure 2.8: Plots energy-balanced disk temperatures (thick lines) compared to the first fit to an evolving power-law temperature (darker, thin lines) where the two are matched at $R \simeq 0.2$ and 200 AU at each time step.

$$q_T(t) = \ln\left(\frac{T_{0.2}}{T_{200}}\right) / \ln\left(\frac{R_{0.2}}{R_{200}}\right), \tag{2.48}$$

$$T_{AU}(t) = \frac{(T_{0.2} - T_{200})}{(R_{0.2}^{q_T} - R_{200}^{q_T})}. \tag{2.49}$$

Because of the complex structure of the energy-balanced temperatures, the q_T and T_{AU} functions derived this way are not entirely smoothly varying in time. In order to run simulations using an evolving power-law temperature distribution with my code, I next fit $q_T(t)$ and $T_{AU}(t)$ in t using a quasi-exponential decay toward a passive-disk temperature profile. For each power-law parameter $(q_T, T_{AU} \rightarrow x)$

$$x(t) = (x_0 - x_\infty) \exp\left[-\left(\frac{t}{t_x}\right)^{b_x}\right] + x_\infty . \tag{2.50}$$

The fit is made separately for $q_T(t)$ and $T_{AU}(t)$ for each disk-evolution model. x_0 and x_∞ are taken from the initial and final conditions provided by Equations (2.48) & (2.49) and the disk-evolution model, discounting sudden discontinuities near $t = 0$ when the disk surface-density at small R is first adjusting into a quasi-steady state. This fit is also made by matching the curves at two points (in t this time). However, these two points, (t_1, x_1) and (t_2, x_2), are chosen by inspection separately for each disk-evolution model to provide a nice fit. Using these points,

$$A_1 = \ln\left(\frac{x_1 - x_\infty}{x_0 - x_\infty}\right), \qquad A_2 = \ln\left(\frac{x_2 - x_\infty}{x_0 - x_\infty}\right),$$

$$b_x = \frac{\ln(A_1/A_2)}{\ln(t_1/t_2)}, \tag{2.51}$$

$$t_x = \left(\frac{t_2^{b_x} - t_1^{b_x}}{A_1 - A_2}\right)^{1/b_x}. \tag{2.52}$$

The fits for q_T and T_{AU} for the fiducial-disk model of Chapter 6 are shown in Figure 2.9, plotted beside the Equations (2.48)&(2.49)-derived values. The power-law fit parameters thus chosen for this disk-evolution model are shown in Table 2.1. Figure 2.10 plots and compares Σ_g contours for the fiducial-disk model using the original static temperature distribution, the energy-balanced temperature distribution, and the power-law fitted temperature distribution. Interestingly, despite the marked difference in temperatures (and therefore viscosities) in the inner disk at early times, the large-scale and long-term disk evolution are all quite similar (and the power-law–fitted temperature parameterization is a decent match for the energy-balanced model). This suggests that the outer

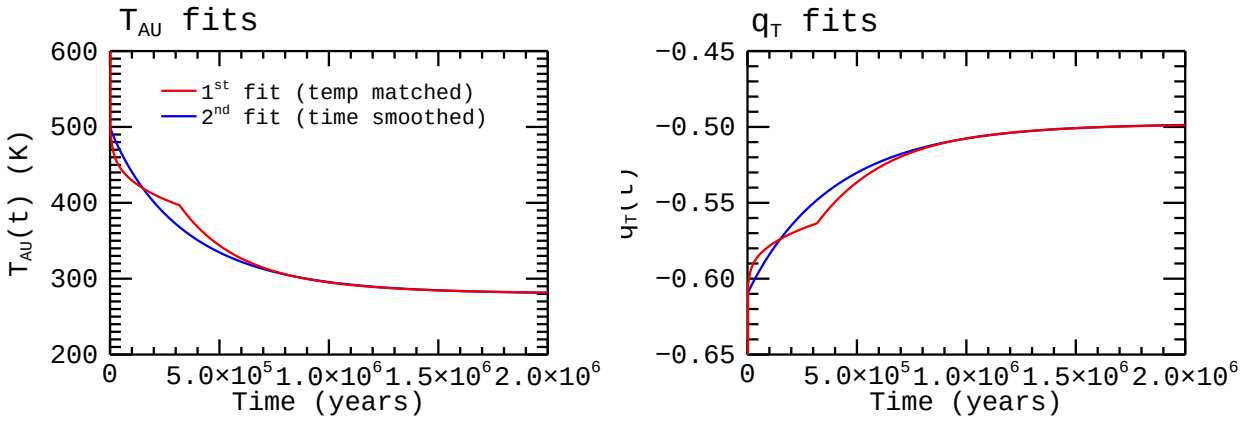

Figure 2.9: Plots the quasi-exponential fit in t (Equation (2.50)) against the initial fit at $R \simeq 0.2$ and 200 AU for the fiducial disk model.

$M_{D,0} = 0.03 M_\odot$, $R_d = 20$AU, $\alpha = 10^{-2}$:	
$T_{AU,0} = 500$K	$q_{T,0} = -0.61$
$T_{AU,\infty} = 279.94$K	$q_{T,\infty} = -0.497683$
$t_{T_{AU}} = 3.494091 \times 10^5$ yr	$t_{q_T} = 3.9992166 \times 10^5$ yr
$b_{T_{AU}} = 0.924903$	$b_{q_T} = 0.965539$

Table 2.1: Fitting constants for the evolving, power-law temperature distribution of the fiducial disk model. For fitting constants of the full set of disk models run with evolving temperature, see Table 6.1 in Chapter 6.

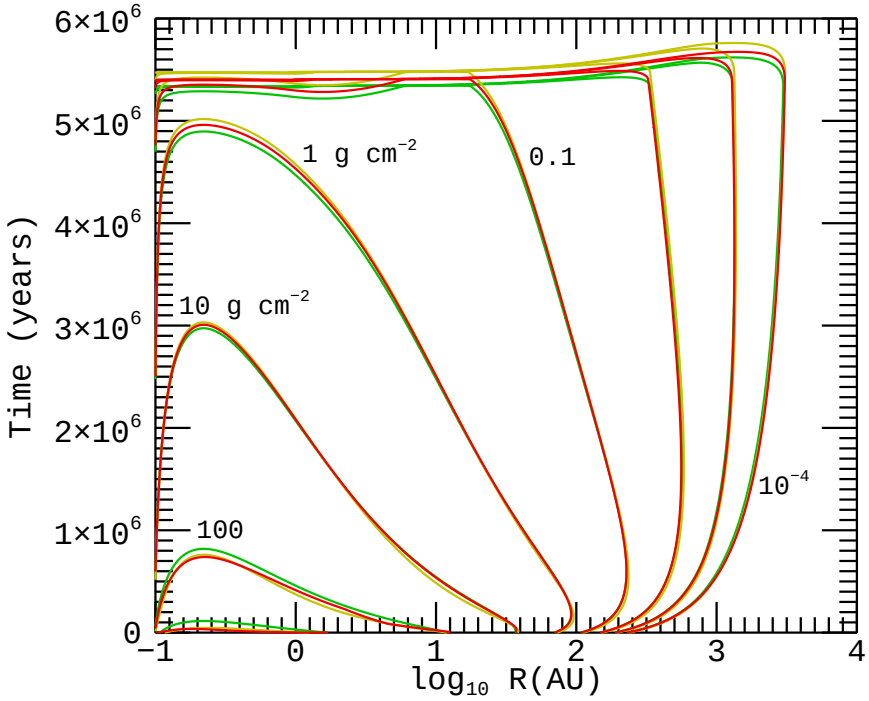

Figure 2.10: Surface-density contours for an evolving disks using the fiducial-disk-model parameters. Green contours plot the temperature-static disk (fiducial model for Chapters 4 & 5. Red contours plot the disk evolving with an energy-balanced temperature distribution. Yellow contours plot the disk with a power-law-fitted evolving temperature distribution (fiducial disk model for Chapter 6.

disk, housing most of the disk mass and where the temperature variations are smallest, holds primary control over the global, viscous disk evolution.

2.5 Observational Comparisons for Model Disks

Here I include a brief comparison of the model disks used in this thesis to the observational constraints laid out in §2.1, considering specifically: disk mass, mass-accretion rate, outer gas radius, and lifetime. The fiducial disk model uses $M_{D,0} = 0.03 M_{\odot}$, $R_d = 20$ AU (similar to a $t = 0$ characteristic radius of 20 AU), and $\alpha = 10^{-2}$. In Figures 2.11 & 2.12, I plot $R_{\rm out}$, the outer disk radius estimated based on CO emission, the total disk masses, and the total mass-loss rates as a function of time for model disks varying R_d, $M_{D,0}$, and α, as well as for the fiducial model evolved using each of the three disk-temperature models. Note that I have included an $R_d = 80$ AU case, and an $\alpha = 10^{-3}$ case, neither of which are used in my simulations, due to their longeivity.

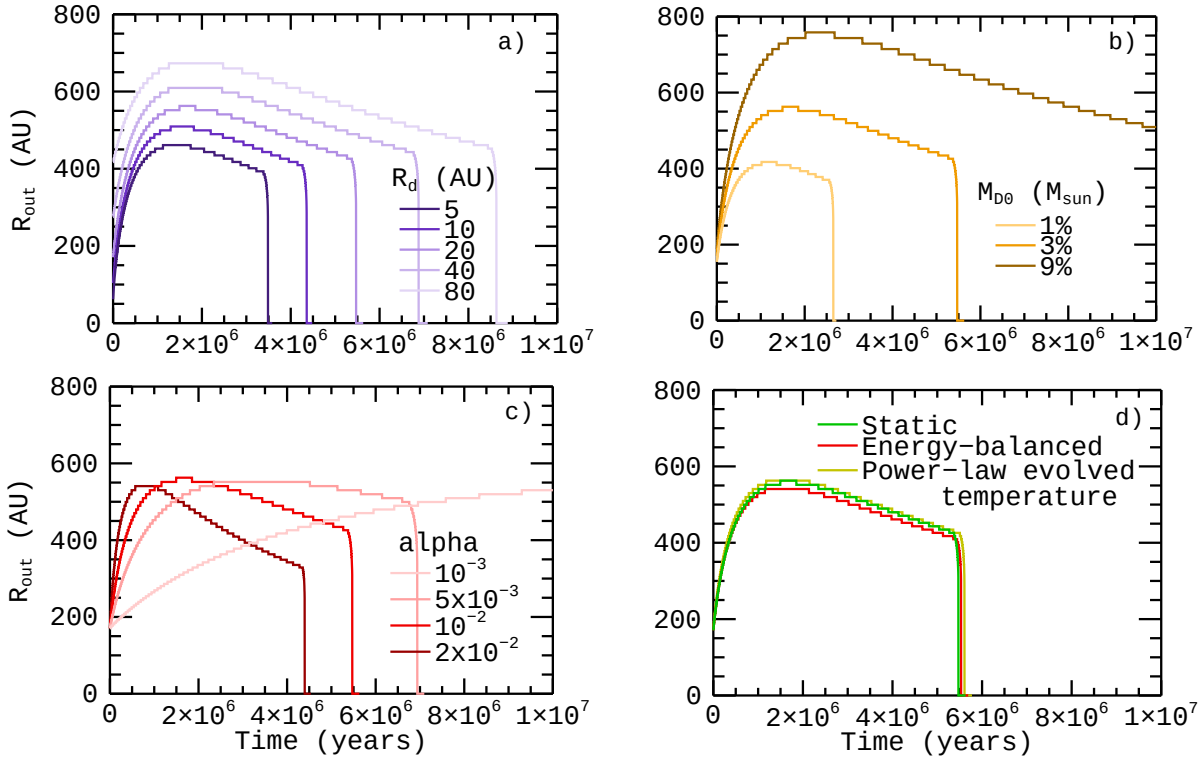

Figure 2.11: $R_{\rm out}$ for model disks using a range of disk parameters. The baseline model uses $M_{D,0} = 0.03 M_{\odot}$, $R_d = 20$ AU, and $\alpha = 10^{-2}$.

The $M_{D,0} = 0.09 M_{\odot}$ also has an over-long lifespan, but *has* been included in Chapters 5 & 6 as a test of the effect of the disk mass on the mixing and global distribution of dust solids in my simulations. The rapid loss of disk mass at the end of the disk lifetimes is due to photoevaporative clearing by EUV radiation, rather than accretion onto the central star, and occurs on a timescale consistent with observations (as these models do not allow for disk clearing by planet formation). The disk masses are generally consistent with medium-sized disks, and the mass-accretion rates fall comfortably within the range observed across the progression of disk ages.

To define $R_{\rm out}$ for Figure 2.11, I follow *M. Hughes et al.* (2008), who note that the outer radius as measured by CO emission appears to occur when the midplane surface density drops below the critical density for the rotational transition. At 20 K, the critical density is $\sim 4.4 \times 10^4$ CO cm^{-3}. This is a CO mass density of 2.06×10^{-22} g cm^{-3} and, using their interstellar value for the CO-to-H$_2$ mass ratio of 10^{-4}, this comes to a total gas density of 2.06×10^{-18} g cm^{-3}. Therefore, I have set the $R_{\rm out}$ plotted in Figure 2.11 at the boundary in the model disks where $\rho_{\rm g,mid} \geq 3 \times 10^{-18}$

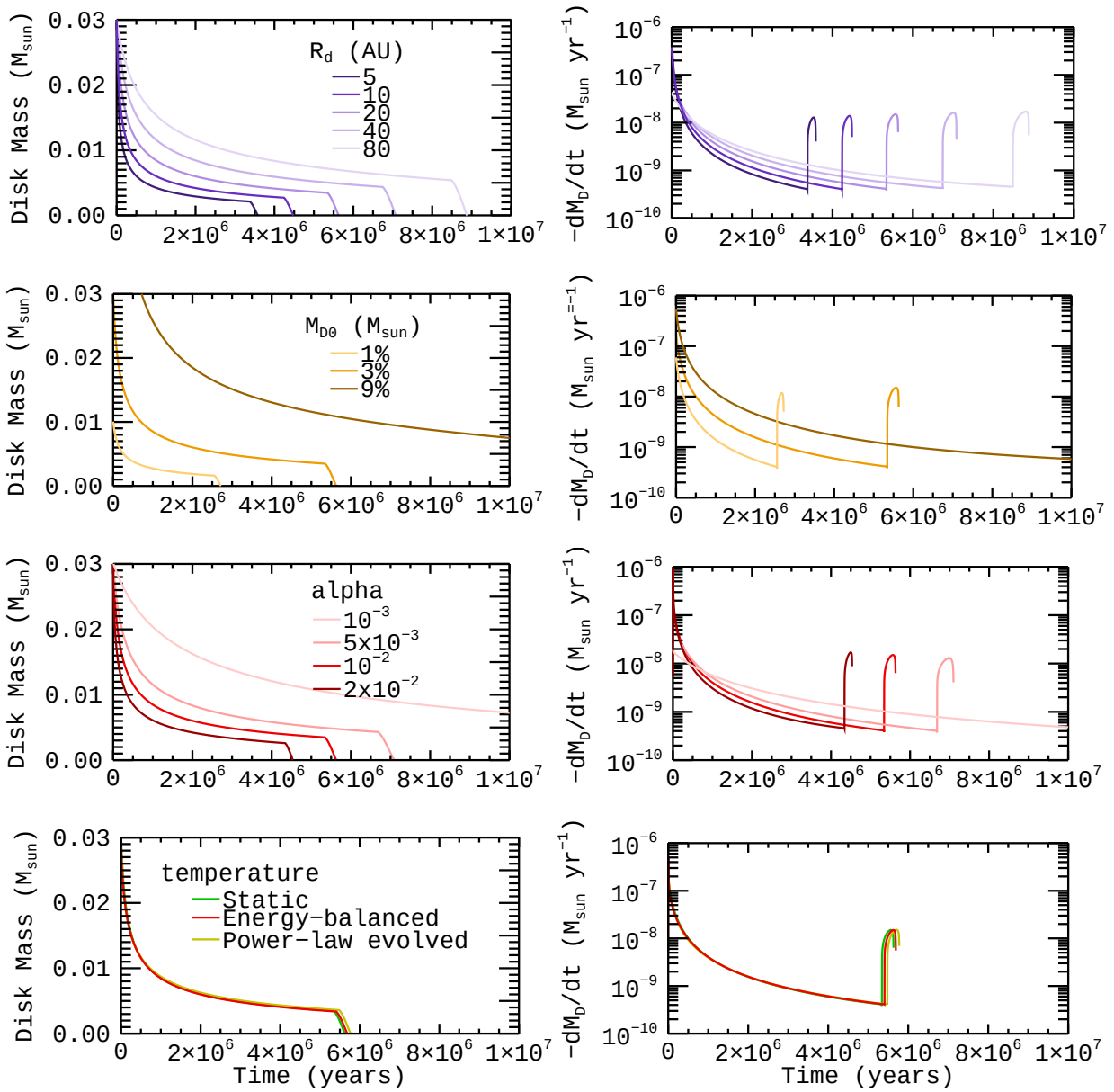

Figure 2.12: Total disk masses and mass-loss rates for models disks using a range of disk parameters. The baseline model uses $M_{D,0} = 0.03 M_{\odot}$, $R_d = 20$ AU, and $\alpha = 10^{-2}$.

g cm^{-3}, using Equation 2.6 for a vertically-isothermal disk structure. In all of my model disks, I find an outer gas radius of several hundred AU measured for the majority of the disk lifetime, with some fall-off with time as the disk accretes onto the star and thins.

2.6 Calculating Gas Velocities

In this section, I overview three calculations for the disk-gas velocities, $v_{\phi,g}$, $v_{r,\mathrm{acc}}$, and $v_{r,\mathrm{merid}}$. While the particle-transport simulations presented in this thesis are restricted to the midplane, I include the vertical dependence of these velocities (assuming a vertically isothermal disk) for completeness.

One of the most important velocities for studying small-particle transport in protoplanetary disks is the azimuthal (orbital) velocity of the gas. This velocity deviates from Keplerian due to the radial pressure gradient within the gas, which acts to somewhat offset the gravity of the central star. The gas orbital-angular velocity, Ω_g, is easily derived using radial force balance (*Takeuchi & Lin*, 2002) where

$$R\Omega_{\mathrm{g}}^2 - \frac{GM_\star R}{\left(R^2+z^2\right)^{3/2}} - \frac{1}{\rho_{\mathrm{g}}}\frac{\partial P}{\partial R} = 0\,. \tag{2.53}$$

At the midplane, the pressure gradient is outward, causing the gas to orbit at slower-than-Keplerian speeds, but in a flared disk, high above the midplane, or just outside a gap in the gas, the pressure gradient is inward and the gas rotation super-Keplerian.

Using $P = \rho_g k_B T/\mu m_H$ and the definition for ρ_g in a vertically-isothermal disk (Equation (2.7)), one can solve for Ω_g for any general disk surface-density and temperature structure:

$$\begin{aligned}
\Omega_g^2\left(R,z\right) &= \Omega_{\mathrm{K}}^2\left(z\right) + \Omega_{\mathrm{K,mid}}^2\frac{H_g^2}{R^2}\left[\frac{R}{\Sigma_g}\left(\frac{\partial\Sigma_g}{\partial R}\right) + \frac{R}{2T}\left(\frac{\partial T}{\partial R}\right) - \frac{3}{2}\right] \\
&\quad + \Omega_{\mathrm{K,mid}}^2\frac{z^2}{R^2}\left[\frac{3}{2} + \frac{R}{2T}\left(\frac{\partial T}{\partial R}\right)\right], \\
&\downarrow \\
\Omega_g^2\left(R,z\right) &= \Omega_{\mathrm{K}}^2\left(z\right) + \Omega_{\mathrm{K,mid}}^2\left(\frac{H_g^2}{R^2}\left[q_\Sigma + \frac{1}{2}q_T - \frac{3}{2}\right] + \frac{z^2}{R^2}\left[\frac{3}{2} + \frac{1}{2}q_T\right]\right),
\end{aligned} \tag{2.54}$$

where q_Σ and q_T are the local radial power-law slopes for the gas surface-density and temperature, respectively (see Appendix B.2.2 for the numerical calculation), $\Omega_{\mathrm{K}}\left(z\right) = \sqrt{\frac{GM_\star}{\left(R^2+z^2\right)^{3/2}}}$ is the general-Keplerian angular velocity, and $\Omega_{\mathrm{K}}\left(z=0\right) = \Omega_{\mathrm{K,mid}}$.

The actual orbital speed of the gas is given by $v_{\phi,g} = R\Omega_g$. Figure 2.13 plots the deviation between $v_{\phi,g}$ and v_{K}, the Keplerian speed, for several different vertical scale-height positions within the fiducial disk model of Chapter 6 at $t = 0$. Note that this variation is extreme near the outer

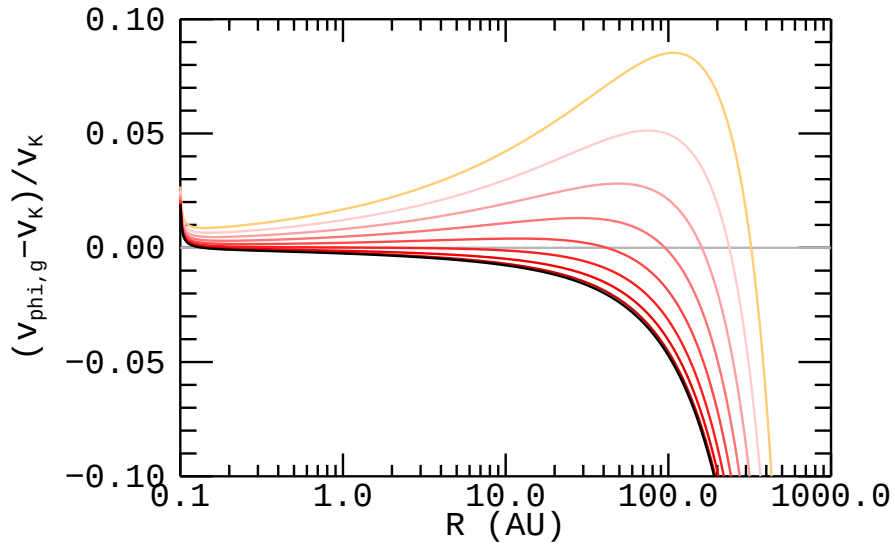

Figure 2.13: Plot of the difference between $v_{\phi,g}$ and $v_{\rm K}$ for several different heights above the disk midplane at $t = 0$ in the fiducial disk model of Chapter 6. Curves at half-scale-height increments from $z = 0$ (black) to $z = 4H_g$ (orange). My transport simulations take place at the midplane, where the gas almost always orbits at sub-Keplerian velocities.

edge of the disk where the surface density drops toward zero, and also that the gas velocity is greater than Keplerian at the very inner disk edge.

Because the radial-flow velocity of the gas depends on aspects of disk turbulence that cannot yet be predicted from first principles, my simulations consider two end-case calculations for $v_{r,g}$. The first is the 1D, vertically-averaged gas velocity, $v_{r,\rm acc}$, referred to as the accretion-flow velocity. This is the bulk radial flow required to maintain mass conservation for 1D viscous disk evolution. It is derived from the same equations as the basic form of the 1D disk-evolution equation (beginning of §2.3.1) using the same simplifying assumptions of $\Omega_g = \Omega_{\rm K,mid}$ and $\partial\Omega_g/\partial t = 0$. Combining Equations (2.13), (2.14), & (2.15) yields

$$v_{\rm r,acc} = -\frac{3}{\Sigma_{\rm g} R^{1/2}} \frac{\partial}{\partial R} \left(\nu \Sigma_{\rm g} R^{1/2} \right) , \tag{2.55}$$

which produces a gas flow that is predominantly inward. Importantly, however, there is a region of outward-flowing gas in the outer disk where the disk is expanding. The boundary of this region moves outward as the disk evolves and spreads.

Almost certainly, an accurate 2D (R, z) depiction of radial gas flow within a disk requires variation in that flow with height above the disk midplane. One model to calculate such variation assumes that the viscosity is constant in z and that there is no vertical mixing of angular momentum; all transfers take place in the radial direction only. The basic property of such a model in a flared disk is that there is rapid inflow of material in the surface layers of the disk, while at the midplane, for most disk radii, the flow is actually directed outward (*Urpin*, 1984; *Rózyczka, Bodenheimer & Bell*, 1994). To calculate this flow (the meridional gas velocity, $v_{r,\mathrm{merid}}$), I follow *Takeuchi & Lin* (2002) and use the azimuthally symmetric Navier-Stokes equation,

$$\begin{aligned} \mathbf{v_{r,g}}\, R\rho_g \frac{\partial}{\partial R}\left(R^2\Omega_g\right) + \mathbf{v_{z,g}}\, R\rho_g \frac{\partial}{\partial z}\left(R^2\Omega_g\right) \quad = \\ \frac{\partial}{\partial R}\left(R^3\nu\rho_g\frac{\partial\Omega_g}{\partial R}\right) + \frac{\partial}{\partial z}\left(R^3\nu\rho_g\frac{\partial\Omega_g}{\partial z}\right) - R\rho_g\frac{\partial}{\partial t}\left(R^2\Omega_g\right) , \end{aligned} \tag{2.56}$$

which at the midplane yields

$$v_{r,\mathrm{merid}} = \left[\frac{\partial}{\partial R}\left(R^2\Omega_\mathrm{g}\right)\right]^{-1}\left[\frac{1}{R\rho_\mathrm{g}}\frac{\partial}{\partial R}\left(R^3\nu\rho_\mathrm{g}\frac{\partial\Omega_\mathrm{g}}{\partial R}\right) + \frac{R^2\nu}{\rho_\mathrm{g}}\frac{\partial}{\partial z}\left(\rho_\mathrm{g}\frac{\partial\Omega_\mathrm{g}}{\partial z}\right) - R^2\frac{\partial\Omega_\mathrm{g}}{\partial t}\right]. \tag{2.57}$$

Note that while *Takeuchi & Lin* (2002) assume a power law for the gas distribution and use that to derive a simplified expression for the flow structure of the gas, I use the input of the disk surface density from my disk-evolution model to solve Equation (2.57) numerically by assuming vertically uniform temperature and viscosity, as in the expansion for Ω_g above. I discuss my numeric calculations for the R- and t-derivatives in Appendix B.2.2.

Figure 2.14 shows the accretion-flow velocity and the midplane-flow velocity at the midplane at $t = 0$ and at $t = 1$ Myr in the fiducial-disk model of Chapters 4 & 5. Note that the outward expansion of the disk dominates both velocity models at large disk radii.

In order to derive an expression of $v_{r,\mathrm{merid}}$ valid at $z > 0$, one must solve Equation (2.56) including some expression for $v_{z,g}$, the gas vertical velocity. Here I show one simple approach. If I assume that a given parcel of gas will tend to remain at it's original scale-height position within the disk such that $\frac{z_g}{H_g} = K =$ a constant, then I have

$$v_{z,g} = \frac{d}{dt}\left(z_g\right) = K\frac{d}{dt}\left(H_g\right) = K\left(\frac{dR_g}{dt}\right)\left(\frac{dH_g}{dR}\right) ,$$

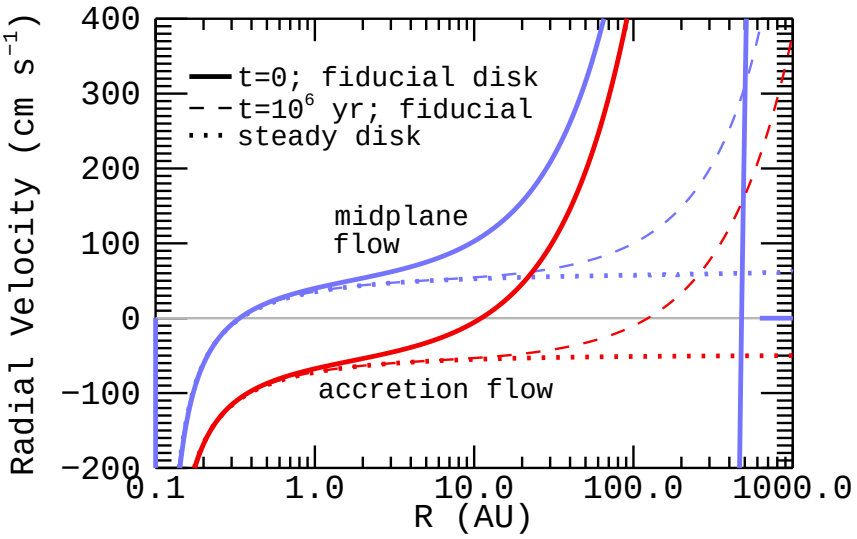

Figure 2.14: Radial velocities of the disk gas in the fiducial disk model of Chapter 4, as well as in the steady disk discussed in §4.5.4. Red curves plot the flow for the accretion-flow model. Blue curves plot the flow at the midplane in the meridional-flow model.

and

$$v_{z,g} = v_{r,g} \frac{z}{H_g} \left(\frac{dH_g}{dR} \right) . \tag{2.58}$$

Using the same vertically-isothermal expansion for ρ_g (and the z-derivatives of ρ_g and Ω_g), I can then write

$$\begin{aligned} \mathbf{v_{r,g}} \left[\frac{\partial}{\partial R} \left(R^2 \Omega_g \right) + \frac{R^2 z}{H_g} \left(\frac{\partial H_g}{\partial R} \right) \left(\frac{\partial \Omega_g}{\partial z} \right) \right] &= \\ \frac{1}{R} \frac{\partial}{\partial R} \left(R^3 \nu \frac{\partial \Omega_g}{\partial R} \right) + R^2 \nu \left(\frac{\partial \Omega_g}{\partial R} \right) \left[\frac{1}{\Sigma_g} \left(\frac{\partial \Sigma_g}{\partial R} \right) - \frac{1}{H_g} \left(\frac{\partial H_g}{\partial R} \right) \left(1 + \frac{z^2}{H_g^2} \right) \right] &+ \\ R^2 \nu \left(\frac{\partial^2 \Omega_g}{\partial z^2} \right) - R^2 \nu \frac{z}{H_g^2} \left(\frac{\partial \Omega_g}{\partial z} \right) - R^2 \left(\frac{\partial \Omega_g}{\partial t} \right) . \end{aligned} \tag{2.59}$$

2.7 Summary

In this chapter I have described the model I use for protoplanetary-gas-disk evolution, structure, and environment properties. This is a 1D (radial) model ultimately defined by radially gridded values for the disk surface density and temperature. My primary use for this model is to define the aerodynamic environment experienced by orbiting small grains in a typical Solar Nebula-analog

disk, and to explore the effects of disk evolution on aerodynamic particle transport.

These disks do not, unfortunately, include the very early stages of star formation and the build-up of the disk, but do allow for exploration of changes to the initial disk conditions. I use the *Shakura & Sunyaev* (1973) alpha-prescription to describe the disk viscosity and viscous evolution and use a somewhat narrow range for α and the base disk parameters, with a fiducial model of $M_{D,0} = 0.03 M_{\odot}$, $R_d = 20$ AU, and $\alpha = 10^{-2}$. This provides a model disk both of sufficient mass to act as a credible stand-in for our own Solar Nebula, and having a lifetime and mass-accretion rate consistent with observations of disks around other stars. While other disk-evolution/viscosity models do exist applicable within a 1D treatment, these models are often described in terms of alpha-parameterizations. Using an alpha-prescription, therefore, allows the greatest ease of comparison between my simulations and scenarios using others' disk models.

It is important to note that disks *do* change dramatically over the course of their lifetimes, having initially more compact configurations and high rates of accretion that also allow for massive outflow at the expanding outer edges. This early high accretion means that a substantial fraction of mass is lost early, and later disks are considerably more tenuous and spread out. While surface-density profiles in an alpha-model disk tend to approach an inverse with the viscosity profile, only in the very inner disk (inner few AU) do profiles match well with those of steady-disk models.

Chapter 3

Building the Particle Transport Model

The particle-transport model is built separately from the evolving gas-disk model described in Chapter 2, which is used to define the environment in which the simulation dust particles reside. While some studies have treated the dust as a fluid (*Gail*, 2001; *Bockelée-Morvan et al.*, 2002; *Dullemond, Apai, & Walch*, 2006; *Ciesla*, 2009), I have chosen to treat it as an ensemble of discreet particles and particle trajectories. This choice allows me to examine not only variations in the distribution of disk solids, but also in the mixing between solids that originate in vastly different regions of the disk. My particle-transport model tracks an ensemble of particles within the 1D (radial) gas-disk environment and subjects the particle orbits to two non-gravitational forces: aerodynamic drag against the mean gas flow, and turbulent diffusion of the ensemble within the disk gas. Coagulation and other grain-grain interactions are neglected, as are back-ractions of the solids on the disk-gas flow or collective effects in the grain motion. However, for some later simulations, I employ a simple model of early grain-growth processes to place rough constraints on the timescales for the appearance of larger particles (micron–centimeter sizes) within the disk.

The particle trajectories therefore consist of two components: mean radial motion assuming drag against the mean disk flow, and a random-walk component due to turbulent diffusion. These two physical effects are represented numerically by two components to the dust radial velocity: v_{srd}, the mean radial velocity induced by gas drag, and $v_{\rm turb}$, the turbulent random-walk velocity. These velocities are calculated at each evolutionary time step of the gas-disk model (defined in §2.3.2) for each grid point of the model disk; values between grid points are linearly interpolated

as necessary. Together, these velocities are used to integrate the dust-grain trajectory as:

$$r_d\left(t+\Delta t\right) = r_d\left(t\right) + \Delta t \times \left(v_{srd} \pm v_{\rm turb}\right) \ , \tag{3.1}$$

where r_d is the dust-particle radial position in the disk, and Δt is the time step. The time step is chosen locally, to insure accurate integration of particle trajectories, but is capped globally at the disk model's disk-evolution time step (or at the output time if the disk model is static).

In the following section, I outline the range of forces and effects a dust grain might experience within the environment of a protoplanetary disk, with special attention to the aerodynamic forces modeled by my particle-tranport model. In §3.2, I discuss the basics of gas drag and the advective component of the model, and in §3.3, I focus on the random-walk diffusive component. In §3.4, I discuss a set of simple models used to place rough constraints on grain growth in various regions of the disk, and in §3.5, I summarize the workings of this model.

3.1 Forces on a Dust Grain in a Gas Disk

While I focus in this thesis on aerodynamic effects to drive grain motions within protoplanetary disks, there are a number of other effects one may consider for their influence over grain transport. Figure 3.1 shows a schematic of a disk and some of the different regions and regimes where various transport processes might occur, and in this section, I briefly outline the range of forces acting on small grains in protoplanetary-disk environments.

Basics aerodynamics interactions, like advection within the bulk flow of the accreting disk and headwind drag, are familiar and tend to predominate throughout the dense-gas regions of the disk into which particles are intermixed, such as region E in Figure 3.1. However, gas-flow transport of grains is not necessarily restricted to the main disk. Some disks are known to exhibit jets or to experience photoevaporation of their bulk material. A well known model, termed the X-wind model, proposes that grains very near the central star may become swept up in a magnetocentrifugal outflow and deposited further out in the disk (*Shu, Shang, & Lee*, 1996), as depicted for region A of Figure 3.1.

As indicated by the X-wind model, most disks are believed to be threaded by large-scale magnetic fields. Indeed, one of the leading theories to explain disk accretion argues for instabilities in

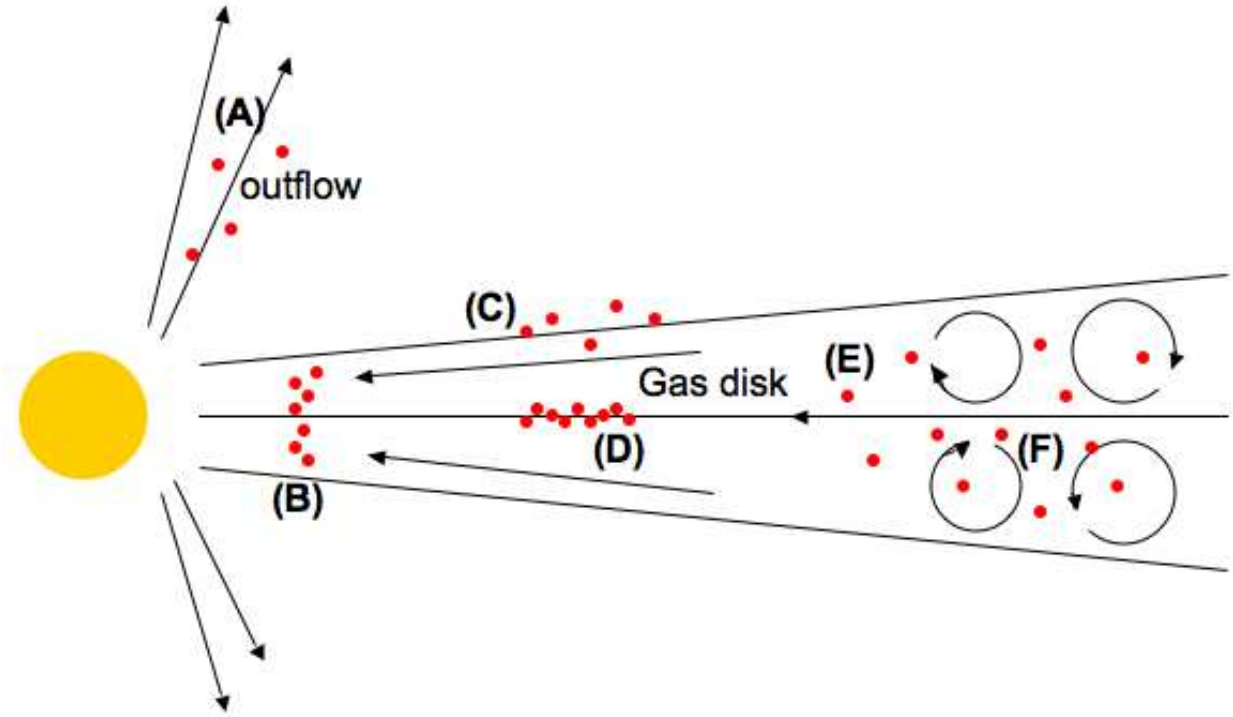

Figure 3.1: Disk schematic of a variety of different particle-interaction zones: A) within an outflow, B) at the edge of an inner cleared region, C) in the optically thin disk-surface layers, D) for settled particles at the midplane, E) within the main disk flow, and F) within disk-gas turbulent eddies.

the gas flow created by interaction with such a magnetic field (*Balbus & Hawley*, 1991). This then raises the question of whether grain charging and interactions with magnetic or electric fields play an important role in the transport of protoplanetary dust grains. This is known to be the case in the disk of ring material around Saturn. There, space-craft have captured images of features termed spokes, short-lived, dark smudges forming radial patterns of considerable extent over the surface of the B ring (*Grün et al.*, 1983). It is believed that these features form when collisional events produce a population of small particles that are then lofted above the surface of the rings within a photoelectrically created surface electric field (*Mitchell et al.*, 2006). One of the keys to making such a process efficient, however, is the extreme-vacuum environment. Grain charging and lifting is dependent on the particle's surface-area-to-mass ratio, which is highest for the smallest grains, which are therefore electrically transported the most efficiently (e.g., *Hughes, Colwell, & DeWolfe* (2008)). However, within a gas disk, it is this same high surface-area-to-mass ratio that most efficiently couples particles to the gas flow, as discussed in §3.2.1 below. Therefore, trans-

port of grains via electric or magnetic-field effects is likely potentially important only in the most tenuous regions of a disk.

In the tenuous surface layers of a disk (C of Figure 3.1), radiation effects become important because the gas here is optically thin to stellar illumination. This means that fine dust grains at the disk surface are efficiently heated (*Chiang & Goldreich*, 1997) and also that forces like radiation pressure become important. The force of radiation pressure goes as

$$F_{\rm rad} = \frac{\pi s_d^2 I}{c}\,, \tag{3.2}$$

(where s_d is the grain radius, and I is the intensity of the incident illumination) and is therefore most efficient at transporting small grains. Combining the radially outward radiation pressure from the central star with a buoyant force due infrared radiation from the heated disk, *Vinković* (2009) proposes that grains a few microns in size may be transported large distances outward along the disk surface due to radiation-pressure forces.

Equally restricted to low-optical-depth regions but also dependent on non-zero gas pressure, is photophoresis, which produces outward motion of a grain due to an illumination-induced temperature gradient over the grain surface. With photophoresis, gas particles absorbed and re-emitted from the hot side of a grain leave with a faster velocity than those from the cold side, thus imparting momentum away from the light source (*Krauss & Wurm*, 2005). This is depicted in Figure 3.2 panel-a opposite the standard picture for acceleration due to radiation pressure in panel-b. In the relatively cold environment of a protoplanetary disk, the force due to photophoresis goes as

$$F_{\rm ph} = \frac{\pi s_d^3 I J_1 P}{k_{\rm th} T}\,, \tag{3.3}$$

where J_1 is an assymetry parameter, P is the local gas pressure, $k_{\rm th}$ is the thermal conductivity of the grain, and T is the local temperature. This force can be orders-of-magnitude greater than radiation pressure and is more efficient for large grains as well as for porous agglomerates, which have lower $k_{\rm th}$ values, making them better at establishing strong thermal gradients over their surfaces. While the illumination requirement means that this effect will not operate throughout the bulk of a radially optically-thick disk, *Krauss & Wurm* (2005) predict that it may be responsible

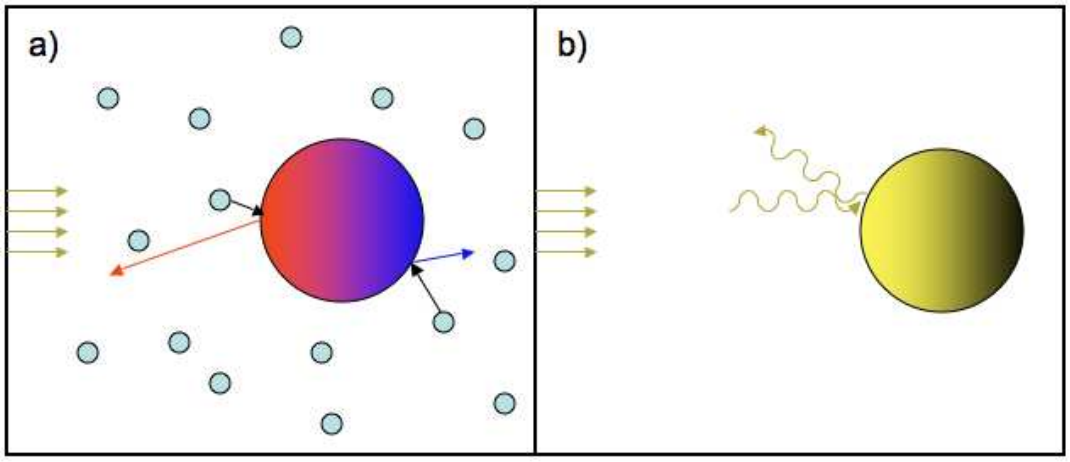

Figure 3.2: Diagram of the mechanics of the force of (a) photophoresis and (b) radiation pressure. Photophoresis depends on light heating a grain that then interacts with a pressurized gas, whereas radiation pressure is an interaction between the grain and incoming light directly.

for clearing out optically thin regions of some inner disks. Pushing back all the dust grains from some inner region would drastically lower the optical depth of that region, allowing photophoresis to operate at greater radius and push the grains still further out. This could lead to the pile-up of a sharp-edged dust ring at the radius where photophoresis balances inward drift due to headwind drag on the particles, as indicated for region B of Figure 3.1.

A somewhat less exotic effect is the settling, usually of larger grains, toward the disk midplane (D of Figure 3.1). If grains are allowed to settle out, then there is a whole host possible interactions that may occur, both collective and aerodynamic. Large dust-to-gas density ratios or collective motions of grains may lead to a slower infall of those grains than is otherwise experienced by individual particles (*Weidenschilling*, 2003; *Bai & Stone*, 2010a). Particles large enough to be only marginally coupled to the gas may excite streaming instabilities that can lead to particle clumping (*Johansen, & Youdin*, 2007; *Bai & Stone*, 2010a). Furthermore, increasing the density of dust grains will lead to more frequent collisions, accelerating grain coagulation and fragmentation processes (*Dullemond & Dominik*, 2005). While these processes are all interesting, none are explored directly in the transport simulations of this thesis. This is in part because they each represent separate disciplines into themselves, and in part because I have focused on the transport of small grains, which tend to be well-mixed vertically with the disk gas.

Turbulence is expected to be very efficient at mixing small grains to height above the disk

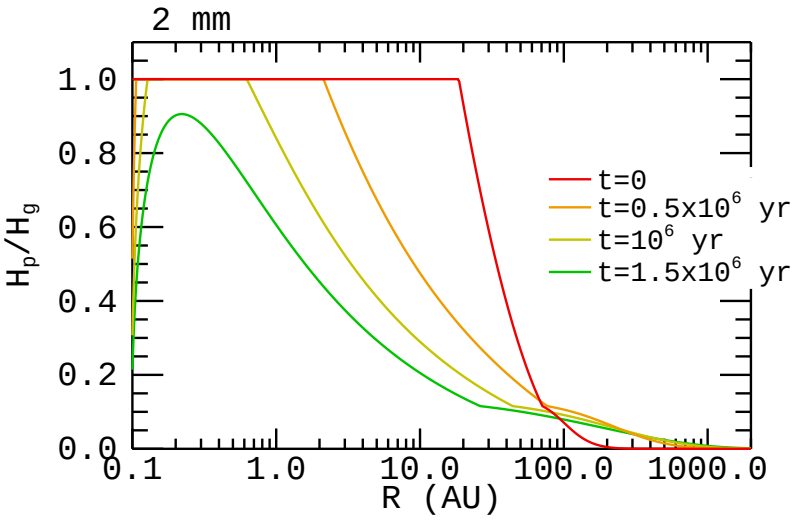

Figure 3.3: Particle scale-heights for 2 mm grains in the fiducial disk model of Chapters 4 & 5. Curves are truncated at 1.0 because the particle scale-height cannot be greater than the scale-height of the disk gas.

midplane. Using an alpha-model for disk turbulence (as described in §2.2), the scale-height of particles, H_p, in a disk is expected to go as (*Cuzzi et al.*, 2005)

$$H_p \simeq H_g \sqrt{\frac{\alpha}{\Omega_{\rm K} t_{\rm stop}}}, \tag{3.4}$$

where H_g is the gas scale-height, and $t_{\rm stop}$ is the gas-drag stopping time on the particle (discussed in §3.2.1). In Figure 3.3, I plot the predicted scale-height of mm-sized grains in the fiducial disk model of Chapters 4 & 5, which uses an alpha-scaling of $\alpha = 10^{-2}$. This is more than sufficient turbulence to produce efficient vertical mixing and even such relatively large dust particles are expected to be well-mixed throughout the disk structure for a substantial portion of the disk lifetime. Note that a wide spread in particle heights may have an appreciable effect on the net drag-induced flow experienced by particles. This effect is discussed in detail in, e.g., *Takeuchi & Lin* (2002) and *Ciesla* (2009). In Figure 3.4, I plot drift velocities for particles at different heights (in units of local disk-gas scale-height) above the midplane. In a flared disk model, gas actually orbits at super-Keplerian velocities near the disk surface, causing a tailwind drag that exerts a radially outward pull on particle orbits. The effect is strongest for slightly larger particles that are marginally coupled to the disk gas. While an exponential fall-off in the particle distribution with H_p means that few

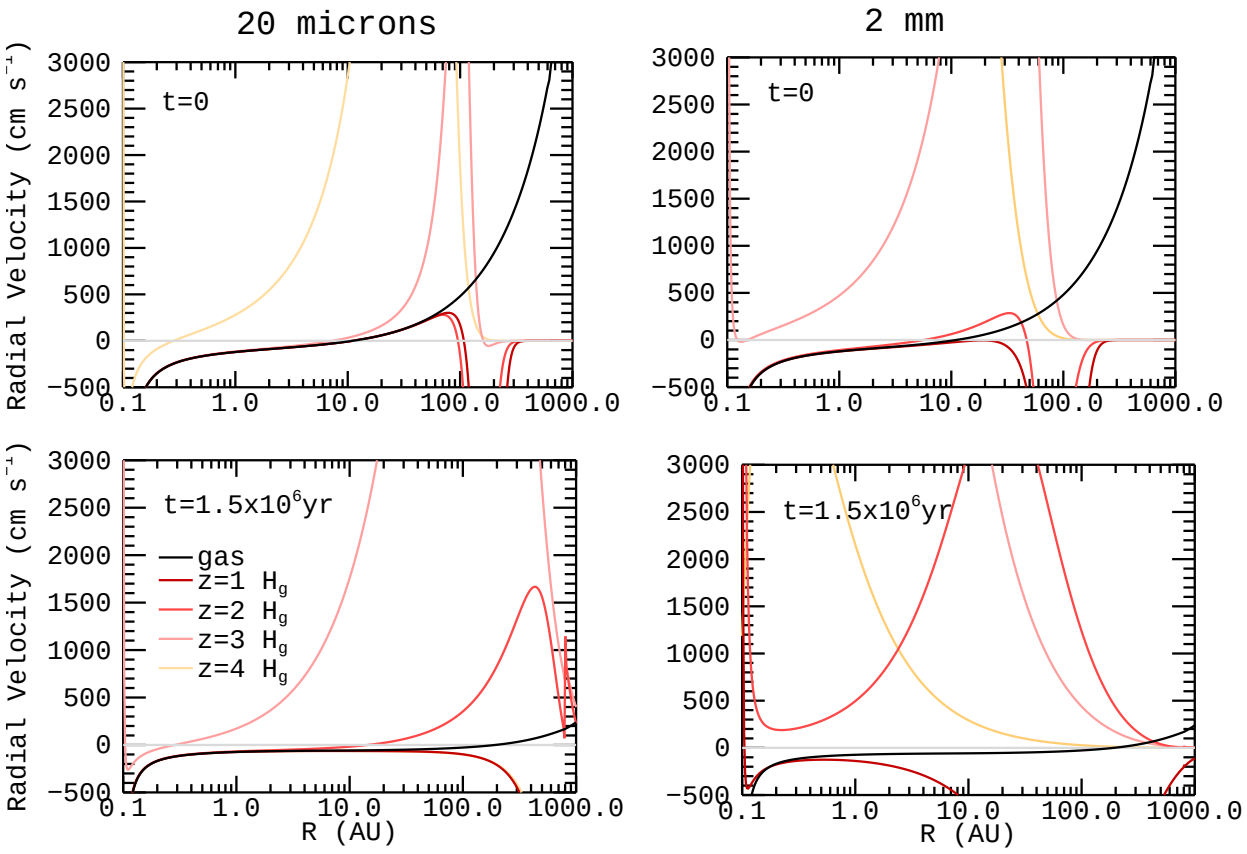

Figure 3.4: Drift velocities for grains at height z above the disk midplane in the fiducial disk model of Chapter 6 for two different times (top and bottom) and two different grain sizes (left and right).

particles will experience this effect, it does act as a caveat to my particle-transport simulations, which consider gas drag and particle transport only at the disk midplane.

While there are many varied and interesting effects operating to affect grain transport within protoplanetary disks, those that I am most interested in for the work of this thesis operate ubiquitously on the bulk of small-dust material to effect large-scale radial transport. Both gas-drag/advection and turbulent diffusion (just as, if not more, efficient radially as vertically) should be in effect throughout the bulk of the disk and provide the basic framework for dust-transport processes. Furthermore, these processes are equally important in the inner, planet-forming regions, as in the outer-regions best viewed by observations of disks around other stars.

3.2 The Advection of Particles Due to Gas Drag

In the particle-transport model, the advection of a dust grain is calculated dependent on the size of the grain and on the local temperature, density, and flow conditions of the gas disk. These conditions are used in the model to calculate a steady mean-radial velocity for the dust particle at each disk grid point, which is then used in Equation (3.1) to calculate the individual trajectories of each grain in the model ensemble. In this section, I first outline the physics of the radial and azimuthal gas drag acting on the particle orbit (§3.2.1), then discuss how those physics are translated into a steady mean-radial dust velocity at each grid point (§3.2.2). Finally (§3.2.3), I compare the particle-transport model trajectories to precision force-balance integrations of the particle motion to demonstrate the fidelity of my gridded velocities in capturing the radial-transport dynamics of particles advected within a laminar disk gas flow.

3.2.1 The Basics of Gas Drag in Orbit

The most familiar phenomenon concerning gas drag in a protoplanetary disk is headwind drag. Because the disk gas is radially pressure-supported, it orbits at a slightly lower velocity than the dust, which orbits closer to the Kepler velocity. This causes drag against the forward motion of the orbiting particle, sapping its angular momentum, so that it spirals inward onto the central star, sometimes quite rapidly (e.g., within $\sim 6 \times 10^4$ years for a 2 cm grain initiated at 1 AU in a typical disk and in $< 5 \times 10^3$ years if the inward accretion flow of the gas is included). There are instances where the gas pressure support may be reversed radially (such as just outside a gap in the disk surface-density profile caused by a massive planet or by photoevaporation), so that the gas orbits faster and causes a tailwind drag that boosts particles to wider orbits. However, this is essentially the same phenomenon as headwind drag, and from here on I use 'headwind drag' to refer to both. In many discussions of drag-induced radial migration [e.g., (*Youdin & Shu*, 2002)] the difference between the gas and dust *azimuthal* (orbital) velocities is considered the Δv of primary importance. However, as I will show, the difference in the gas and dust *radial* velocities can have a strong impact on the particle dynamics. Furthermore, in Chapters 4 & 5 I will highlight potential variations in the radial gas-flow velocity as a parameter-of-significance for the results of my outward-mixing simulations.

When the force of gas drag is linearly proportional to Δv (Epstein drag), the equations of motion for a particle in a laminar disk-gas flow, accounting for both the gas-drag force and the particle orbit, may be written as

$$\frac{dv_{r,\mathrm{d}}}{dt} = \frac{v_{\phi,\mathrm{d}}^2 - v_{\mathrm{K}}^2}{R} - \frac{(v_{r,\mathrm{d}} - v_{r,\mathrm{g}})}{t_{\mathrm{stop}}}, \tag{3.5}$$

$$\frac{dv_{\phi,\mathrm{d}}}{dt} = -\frac{v_{\phi,\mathrm{d}} v_{r,\mathrm{d}}}{R} - \frac{(v_{\phi,\mathrm{d}} - v_{\phi,\mathrm{g}})}{t_{\mathrm{stop}}}, \tag{3.6}$$

where $v_{r,\mathrm{d}}$ and $v_{\phi,\mathrm{d}}$ are the radial and azimuthal velocities of the dust particle; $v_{r,\mathrm{g}}$ and $v_{\phi,\mathrm{g}}$ are the local radial and azimuthal velocities of the disk gas; v_{K} is the local Keplerian velocity; and t_{stop} is the exponential-stopping time, the time over which a constant drag force brings v_{d} a factor of e closer to v_{g}. Comparing t_{stop} to the local Kepler time ($1/\Omega_{\mathrm{K}}$, where Ω_{K} is the Keplerian orbital angular velocity) provides an assessment of the relative importance between the gas motions and the Keplerian orbital motions on the particle dynamics, indicating whether a particle is well- or loosely-coupled to the gas motions. However, the more general form of the particle-motion equations is

$$\frac{dv_{r,\mathrm{d}}}{dt} = \frac{v_{\phi,\mathrm{d}}^2 - v_{\mathrm{K}}^2}{R} + \frac{F_{\mathrm{D},r}}{m_{\mathrm{d}}}, \tag{3.7}$$

$$\frac{dv_{\phi,\mathrm{d}}}{dt} = -\frac{v_{\phi,\mathrm{d}} v_{r,\mathrm{d}}}{R} + \frac{F_{\mathrm{D},\phi}}{m_{\mathrm{d}}}, \tag{3.8}$$

where $F_{\mathrm{D},r}$ and $F_{\mathrm{D},\phi}$ are the radial and azimuthal components of the force of gas drag; and m_{d} is the mass of the dust particle. Note: all of these are the equations in cylindrical coordinates and neglect motion in the vertical plane (normal to the disk and the particle orbit).

In general, for fine grains in a protoplanetary disk (up to a few centimeters at 1 AU or tens of meters at 10 AU), the force F_{D} is in the Epstein-drag regime. Unlike the more familiar Δv^2 drag laws, Epstein-drag is linear in Δv, because it applies when the radius of the dust grain, s_{d}, is less than the mean-free-path of the gas, λ_{mf} (and when $\Delta v \ll v_{\mathrm{therm}}$, the thermal velocity of the gas). In the Epstein-drag regime, the drag force is given by (*Weidenschilling*, 1977a)

$$F_{\mathrm{D}} = -m_{\mathrm{d}} \frac{C_R}{3} \rho_{\mathrm{g}} v_{\mathrm{therm}} (\vec{v}_{\mathrm{d}} - \vec{v}_{\mathrm{g}}) \tag{3.9}$$

where C_R is the particle surface-area-to-mass ratio; $\rho_{\rm g}$ is the local-gas volume density, and $v_{\rm therm}$ is the gas thermal velocity. Then the equations of motion for the particle may be written (*Takeuchi & Lin*, 2002)

$$\frac{dv_{r,{\rm d}}}{dt} = \frac{v_{\phi,{\rm d}}^2 - v_{\rm K}^2}{R} - \frac{1}{3} C_R \, \rho_{\rm g} v_{\rm therm} \left(v_{r,{\rm d}} - v_{r,{\rm g}} \right) , \tag{3.10}$$

$$\frac{dv_{\phi,{\rm d}}}{dt} = -\frac{v_{\phi,{\rm d}} v_{r,{\rm d}}}{R} - \frac{1}{3} C_R \, \rho_{\rm g} v_{\rm therm} \left(v_{\phi,{\rm d}} - v_{\phi,{\rm g}} \right) . \tag{3.11}$$

For larger particles or higher gas densities (closer to the star), Stokes drag applies, which resembles Epstein drag at low Reynolds number (Re) but transitions to the familiar Δv^2 drag force at $Re \geq 800$. Here (*Weidenschilling*, 1977a)

$$Re = \frac{2 s_{\rm d} \rho_{\rm g} \left| \vec{v}_{\rm d} - \vec{v}_{\rm g} \right|}{\eta} , \tag{3.12}$$

where η is the gas kinematic viscosity (equal to $\nu_{\rm m}/\rho_{\rm g}$, the molecular viscosity over the gas density). For gas particles modeled by hard spheres, η is given by (*Clarke & Carswell*, 2007)

$$\eta = \frac{5}{16} \frac{\sqrt{\pi \mu m_{\rm H} k_{\rm B} T}}{\sigma_{\rm cross}} , \tag{3.13}$$

where μ is the average mass of a gas particle in proton masses ($m_{\rm H}$); $k_{\rm B}$ is the Boltzmann constant; T is the local disk temperature; and $\sigma_{\rm cross}$ is the collisional cross section of a gas particle. For my simulations, I use $\mu = 2.34$ (*Nakagawa, Sekiya, & Hayashi*, 1986), and $\sigma_{\rm cross} \approx \sigma_{\rm H_2} = 2.4 \times 10^{-15}$ cm^2 (*Chapman & Cowling*, 1970). $\sigma_{\rm H_2}$ is the cross-section of molecular hydrogen, the dominant gas molecule in the disk, and, while slightly greater than the cross-section of a more-massive gas particle, is still sufficiently representative.

From *Weidenschilling* (1977a), in the Stokes-drag regime

$$F_{\rm D} = -C_{\rm D} \pi s_{\rm d}^2 \rho_{\rm g} \frac{\left| \vec{v}_{\rm d} - \vec{v}_{\rm g} \right|^2}{2} , \tag{3.14}$$

and the drag coefficient is given by

$$C_{\rm D} \simeq 24 Re^{-1} = \frac{12 \eta}{s_{\rm d} \rho_{\rm g} \Delta v} \qquad \text{for } Re < 1 ,$$

$$C_{\rm D} \simeq 24 Re^{-0.6} = \frac{24\eta^{0.6}}{2^{0.6} s_{\rm d}^{0.6} \rho_{\rm g}^{0.6} \Delta v^{0.6}} \quad \text{for } 1 < Re < 800\,,$$
$$C_{\rm D} \simeq \frac{24}{800^{0.6}} \quad \text{for } Re > 800\,.$$

Plugging these equations for Stokes drag into Equations (3.7) & (3.8) and using $\frac{\pi s_{\rm d}^2}{m_{\rm d}} = \frac{C_R}{4}$ yields the following full set for the Stokes-drag equations of particle motion:

$Re < 1$:

$$\frac{dv_{r,{\rm d}}}{dt} = \frac{v_{\phi,{\rm d}}^2 - v_{\rm K}^2}{R} - \frac{3C_R\eta}{2s_{\rm d}} \left(v_{r,{\rm d}} - v_{r,{\rm g}}\right)\,, \tag{3.15}$$

$$\frac{dv_{\phi,{\rm d}}}{dt} = -\frac{v_{\phi,{\rm d}} v_{r,{\rm d}}}{R} - \frac{3C_R\eta}{2s_{\rm d}} \left(v_{\phi,{\rm d}} - v_{\phi,{\rm g}}\right)\,; \tag{3.16}$$

$1 < Re < 800$:

$$\frac{dv_{r,{\rm d}}}{dt} = \frac{v_{\phi,{\rm d}}^2 - v_{\rm K}^2}{R} - \frac{3C_R\eta^{0.6}\rho_{\rm g}^{0.4}}{2^{0.6} s_{\rm d}^{0.6}} \left|v_{r,{\rm d}} - v_{r,{\rm g}}\right|^{0.4} \left(v_{r,{\rm d}} - v_{r,{\rm g}}\right)\,, \tag{3.17}$$

$$\frac{dv_{\phi,{\rm d}}}{dt} = -\frac{v_{\phi,{\rm d}} v_{r,{\rm d}}}{R} - \frac{3C_R\eta^{0.6}\rho_{\rm g}^{0.4}}{2^{0.6} s_{\rm d}^{0.6}} \left|v_{\phi,{\rm d}} - v_{\phi,{\rm g}}\right|^{0.4} \left(v_{\phi,{\rm d}} - v_{\phi,{\rm g}}\right)\,; \tag{3.18}$$

$Re > 800$:

$$\frac{dv_{r,{\rm d}}}{dt} = \frac{v_{\phi,{\rm d}}^2 - v_{\rm K}^2}{R} - \frac{3C_R\rho_{\rm g}}{800^{0.6}} \left|v_{r,{\rm d}} - v_{r,{\rm g}}\right| \left(v_{r,{\rm d}} - v_{r,{\rm g}}\right)\,, \tag{3.19}$$

$$\frac{dv_{\phi,{\rm d}}}{dt} = -\frac{v_{\phi,{\rm d}} v_{r,{\rm d}}}{R} - \frac{3C_R\rho_{\rm g}}{800^{0.6}} \left|v_{\phi,{\rm d}} - v_{\phi,{\rm g}}\right| \left(v_{\phi,{\rm d}} - v_{\phi,{\rm g}}\right)\,. \tag{3.20}$$

Note that while these equations for the acceleration in the radial and azimuthal directions require the respective r and ϕ velocity components as input into the drag, the Re value and regime-of-relevance must be calculated using the full magnitude of $\vec{v}_{\rm d} - \vec{v}_{\rm g}$.

The Stokes-drag and Epstein-drag forces are equivalent at $\lambda_{\rm mf}/s_{\rm d} = 64/45\pi \approx 4/9$ and Figure 3.5 plots the particle-size boundary where this occurs as a function of R for $t = 0$ of the fiducial-disk models used in Chapter 6. From this figure it is clear that Epstein drag usually applies. The exceptions occur for particles of about centimeter size and larger in the innermost regions of the disk. The simulations run for this thesis all assume Epstein-regime drag forces.

To investigate gas-drag induced transport of particles, I can consider the simplest case of laminar-gas flow with no turbulent forcing of the particle motions, and numerically solve for each particle trajectory directly. To do this, I use a Runge-Kutta-style integrator, where, in the Epstein-drag regime, Equations (3.10) & (3.11) are coupled with radial acceleration and the full-set of

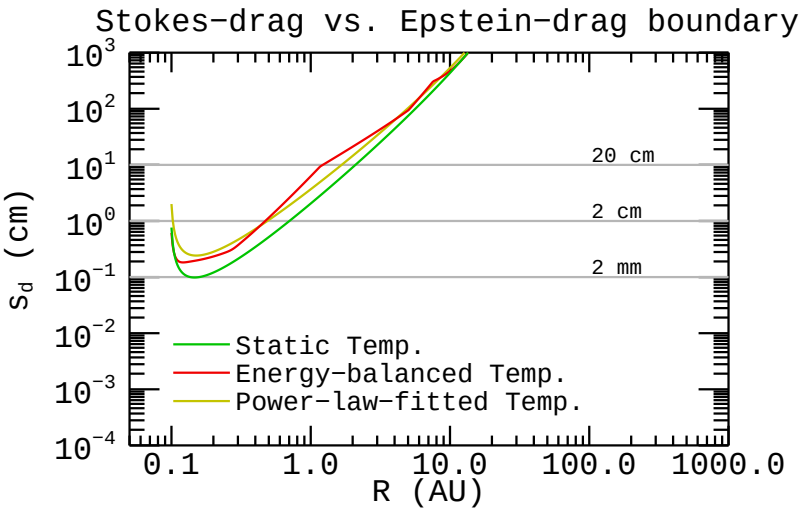

Figure 3.5: For the fiducial models of Chapter 6 ($t = 0$), a plot of the sizes at which the Epstein-drag and Stokes-drag forces are equivalent. Stokes(Epstein) drag for sizes above(below) the curve. Note that lower local temperature (like in the Static-temperature model) mean denser disk gas.

integrated equations is

$$\begin{aligned}
\frac{dr_d}{dt} &= v_{r,d}\,, \\
\frac{dv_{r,d}}{dt} &= \frac{\left(v_{\phi,d}^2 - v_K^2\right)}{r_d} - \frac{4\pi}{3}\frac{s_d^2}{m_d}\rho_g\, v_{\rm therm}\left(v_{r,d} - v_{r,g}\right)\,, \\
\frac{dv_{\phi,d}}{dt} &= -\frac{v_{\phi,d}\, v_{r,d}}{r_d} - \frac{4\pi}{3}\frac{s_d^2}{m_d}\rho_g\, v_{\rm therm}\left(v_{\phi,d} - v_{\phi,g}\right)\,,
\end{aligned} \tag{3.21}$$

defining the particle motion radially within the 1D disk, where $r_{\rm d}$ is the dust-grain radial location. The integrator uses step-size adjustment to reach a relative accuracy of 10^{-5}–10^{-6} in $r_{\rm d}$, $v_{r,{\rm d}}$, and $v_{\phi,{\rm d}}$. Note, however, that the integrator becomes numerically expensive when the individual terms in Equations (3.10) & (3.11) are large but sum to values that are small. Therefore, if the initially computed acceleration ($dv_{r,{\rm d}}/dt$ or $dv_{\phi,{\rm d}}/dt$ or both) is very small ($< 10^{-14}$ cm s^{-2}), the integrator sets the small acceleration equal to zero. Also, if $v_{\phi,{\rm d}} \sim v_{\rm K}$ (10^{-10} relative difference) then the $v_{\phi,{\rm d}}^2 - v_{\rm K}^2$-term in Equation (3.10) is set equal to zero, but only if $\frac{1}{3}C_R\rho_{\rm g}v_{\rm therm} \geq \frac{v_{\rm K}}{R}$. If $v_{\phi,{\rm d}} \sim v_{\rm K}$ but the second condition is not met, then the $v_{\phi,{\rm d}}^2 - v_{\rm K}^2$-term is still important and the integrator instead calculates the particle trajectory to the lower relative accuracy of 10^{-5}. To

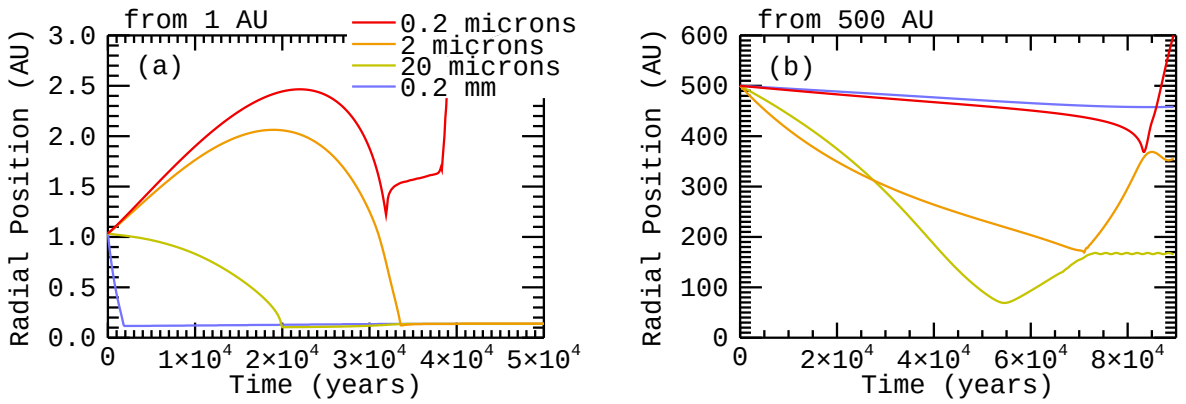

Figure 3.6: Particle trajectories within a tenuous, photoevaporating disk in the midplane-flow gas-velocity case for four different particle sizes. (*Alexander & Armitage* (2007) $\alpha = 10^{-2}$ disk; $\rho_d = 3$ g cm^{-3}.)

maintain stability in this dust-trajectory integration, I scale the called integration time-steps to $\leq 0.1 \times \dfrac{1}{\Omega_{K,mid}}$, which provides well-converged and stable output.

Figure 3.6 plots gas-drag trajectories for the case of outwardly flowing gas at the disk midplane in the $\alpha = 10^{-2}$ photoevaporating disk of *Alexander & Armitage* (2007) ($\dot{M}_0 = 10^{-10} M_\odot$, $R_d = 500$ AU) discussed in §2.3.3. The trajectories include two different starting locations and a range of particle sizes, and illustrate two important effects. First, for certain disk locations and particle sizes (changing in time) particle motion in radially outward, rather than inward. Second, depending on local conditions, the fastest inward radial-drift migration occurs for a particle of some intermediate size.

To examine the first effect, consider the case when the particle orbit is stable ($dv_{r,d}/dt = dv_{\phi,d}/dt = v_{r,d} = 0$). Plugging this condition into the Epstein-drag equations of motion (3.10) & (3.11) yields

$$C_{R,\text{steady}} = \frac{3\left(v_K^2 - v_{\phi,g}^2\right)}{v_{\text{therm}}\,\rho_g\,v_{r,g}\,R}\,. \tag{3.22}$$

$C_{R,\text{steady}}$ then defines a particle size (surface-area-to-mass ratio), as a function of R and the local disk conditions, for which the particle orbit is steady. Note that there are two important end cases:

1. If $v_{r,g} \to 0$ then $C_{R,\text{steady}} \to \infty$ ("inifinitely small" particles) because only massless particles will orbit at any forced non-Keplerian gas velocity without experiencing radial acceleration.

2. If $v_{\phi,g} \to v_K$ then $C_{R,\text{steady}} \to 0$ ("infinitely large" particles) because only the most massive

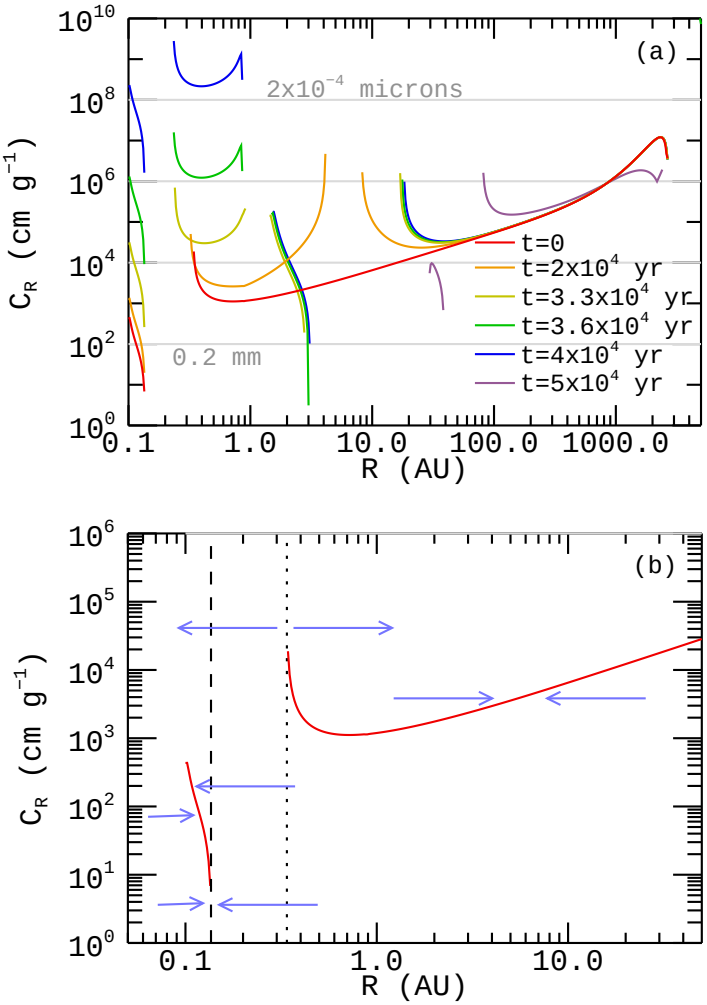

Figure 3.7: **(a)** Orbital stability boundaries in a photoevaporating disk (*Alexander & Armitage* (2007) $\alpha = 10^{-2}$) with outward-flowing gas, $v_{r,\mathrm{merid}}$. (See reference-Σ_g profiles in Figure 2.3.) **(b)** $C_{R,\mathrm{steady}}$ curve at $t = 0$ and a schematic of radial particle motions. Black-dashed line denotes $v_{\phi,g} = v_{\mathrm{K}}$. Black-dotted line denotes $v_{r,g} = 0$ (outward-flowing exterior, inward-flowing interior). Note, larger particle sizes = smaller values of C_R.

particles are impervious to radial gas drag, orbiting at v_{K} no matter what.

Figure 3.7 plots $C_{R,\mathrm{steady}}$ at the midplane for the photoevaporating disk of Figure 3.6, with $v_{r,g} = v_{r,\mathrm{merid}}$, at different times (panel-a). The curves are broken where $C_{R,\mathrm{steady}} < 0$ (negatively-massed particles). Including the boundaries where $v_{r,g} = 0$ and $v_{\phi,g} = v_{\mathrm{K}}$ in panel-b for $t = 0$, one sees that the steady-orbit curves divide the disk–particle-size parameter space into different transport zones. We know that very small particles (large C_R) can move outward with outward-

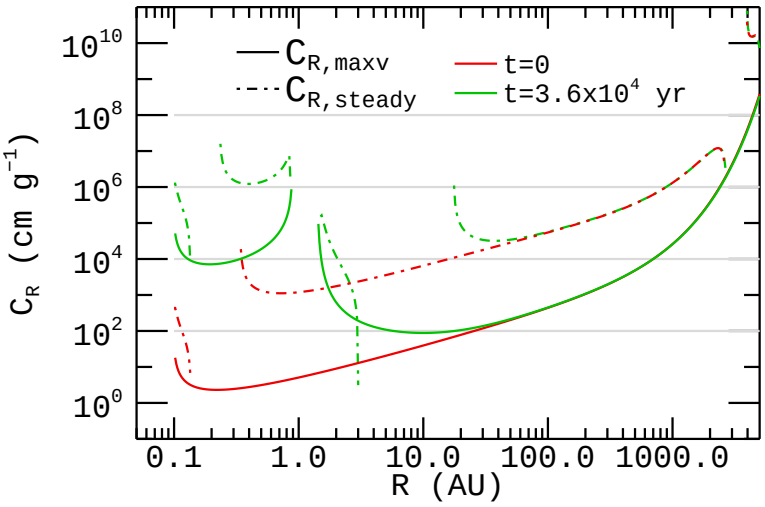

Figure 3.8: $C_{R,\mathrm{maxv}}$ curves (with $C_{R,\mathrm{steady}}$ curves for comparison) before and after gap opening by EUV photoevaporation in the *Alexander & Armitage* (2007) $\alpha = 10^{-2}$ disk. Note that $C_{R,\mathrm{maxv}}$ mirrors the disk surface-density profile.

flowing gas, and that super-Keplerian gas at the inner edge of the disk produces tailwind-drag that can move particles outward. Large particles are most influenced by the difference in $v_{\phi,g}$ and v_K (in more tenuous regions of the disk, the definition of large moves to smaller and smaller particle sizes), and small particles are more likely to be advected radially with the radial gas flow.

Next, to consider the second effect of particle motions demonstrated in Figure 3.6. *Weidenschilling* (1977a) notes that the greatest (azimuthal) drag-induced migration occurs when $\frac{t_{\mathrm{stop}}}{t_{\mathrm{orbit}}} \approx \frac{1}{2\pi}$. For Epstein drag, $t_{\mathrm{stop}} = \frac{3}{C_R \rho_g v_{\mathrm{therm}}}$. Assuming a Keplerian orbit for simplicity, then,

$$C_{R,\mathrm{maxv}} \approx \frac{3\Omega_{\mathrm{K}}}{\rho_g v_{\mathrm{therm}}}\,, \tag{3.23}$$

where $C_{R,\mathrm{maxv}}$ is the particle surface-area-to-mass ratio at which the maximum radial drift will occur. This particle-size is linked to the well-known radial-drift barrier in grain-growth and particle-transport studies where particles roughly centimeters to decimeters in size in a model Solar Nebula drift inward onto the parent star so rapidly that they quickly deplete the disk of solids. Figure 3.8 plots the $C_{R,\mathrm{maxv}}$ values for the disk of Figure 3.6 at the midplane at two times, compared with the $C_{R,\mathrm{steady}}$ values. Note that strong-drift forcing for the inner-disk region where the gas is super-

Keplerian allows particles of certain sizes to follow a photoevaporating disk edge outward (at least for a while) as is seen in Figure 3.6 at later times. Also, this strong-headwind-drag effect, as it depends on the local gas density, comes into play for smaller and smaller particles in more tenuous regions of the disk.

3.2.2 Calculating a Steady Radial Velocity

For my transport simulations, I solve for the mean radial velocity of the dust grains, v_{srd}, subject to Epstein drag against the mean gas flow. In my simulations, I assume that $\rho_{\rm g} = \rho_{\rm g,mid} = \Sigma_{\rm g}/\sqrt{2\pi}H_{\rm g}$, the gas density at the disk midplane. This means that the particle trajectories are calculated for the maximum coupling between gas and dust motions. While Equations (3.10) & (3.11) represent the precise equations of particle motion, including both orbital dynamics and gas drag, I follow *Takeuchi & Lin* (2002) and simplify these forces by assuming that the radial acceleration of the grain is zero, $dv_{r,{\rm d}}/dt \approx 0$, and that the azimuthal acceleration corresponds to a change in the Keplerian velocity with R, $dv_{\phi,{\rm d}}/dt \approx -v_{\rm K}v_{r,{\rm d}}/2R$. The equations for the radial and azimuthal motions of a grain now produce two equations for the steady mean radial velocity, v_{srd}, as a function of its steady azimuthal velocity, $v_{s\phi d}$,

$$\begin{aligned} v_{srd} &= v_{r,{\rm g}} + \frac{3\left(v_{s\phi d}^2 - v_{\rm K}^2\right)}{C_R R \rho_{\rm g} v_{\rm therm}} \\ v_{srd} &= -\frac{1}{3} C_R \, R \rho_{\rm g} v_{\rm therm} \frac{(v_{s\phi d} - v_{\phi,{\rm g}})}{(v_{s\phi d} - v_{\rm K}/2)} \, . \end{aligned} \tag{3.24}$$

I solve these equations iteratively for v_{srd} using the gas-disk bulk flow from my disk model at each radial grid point. (See Appendix B.3 for details.)

Figure 3.9 shows the mean radial velocities of the dust compared to the radial velocity of the gas. Very small grains ($\lesssim 1\mu$m) are well coupled to the gas flow, but for larger grains, at large distances from the star (tens of AU) and at late times in the disk evolution, the dust motion significantly departs from the gas flow.

There are a number of methods used in the literature to calculate or estimate the radial-drift velocities of particles in a disk. The simplest consider the difference between the gas and dust azimuthal velocities only, sometimes simply adding this drift velocity to the gas radial velocity assuming direct radial advection. This method can be effective in the inner, dense regions of a disk,

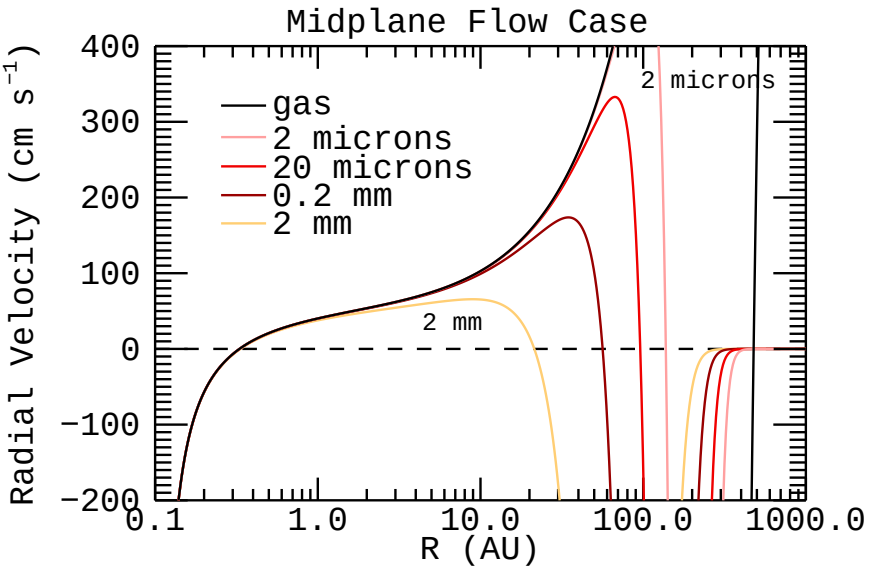

Figure 3.9: Steady mean-radial velocities for different grain sizes at $t = 0$ in the fiducial disk model of Chapters 4 & 5. Assumes gas flow at the disk midplane that is radially outward (see §2.6) and $\rho_d = 3$ g cm^{-3}.

but is much less so where the disk gas is tenuous. In Figure 3.10 panels-a1 and -a2, I plot radial-dust velocities for two cases according to my methods versus the azimuthal-only–drift limiting cases presented in *Weidenschilling* (1977a). The first limit is for $t_{\rm stop} \ll t_{\rm orbit}$ (well-coupled particles), and is given by (for Epstein drag)

$$v_{r,\rm drift} = \left(\frac{\rho_d s_d}{\rho_g v_{\rm therm}}\right)\left(\frac{1}{\rho_g}\frac{dP}{dR}\right) , \tag{3.25}$$

where ρ_d is the internal density of the grain and P is the local gas pressure. This is one of the most-commonly cited formulations for estimating particle drift lifetimes within a disk, the other being the same, but substituting c_s, the sound speed, for $v_{\rm therm}$, often preferred for order-of-magnitude estimates. The other limit shown is for $t_{\rm stop} \gg t_{\rm orbit}$ (large, decoupled particles), and is given by

$$v_{r,\rm drift} = \frac{1}{\Omega_{\rm K}^2}\left(\frac{\rho_g v_{\rm therm}}{\rho_d s_d}\right)\left(\frac{1}{\rho_g}\frac{dP}{dR}\right) . \tag{3.26}$$

The above limits can be combined into a continuous equation for $v_{r,\rm drift}$ across the range of particle stopping times, as given in, e.g. *Nakagawa, Sekiya, & Hayashi* (1986) and *Bai & Stone*

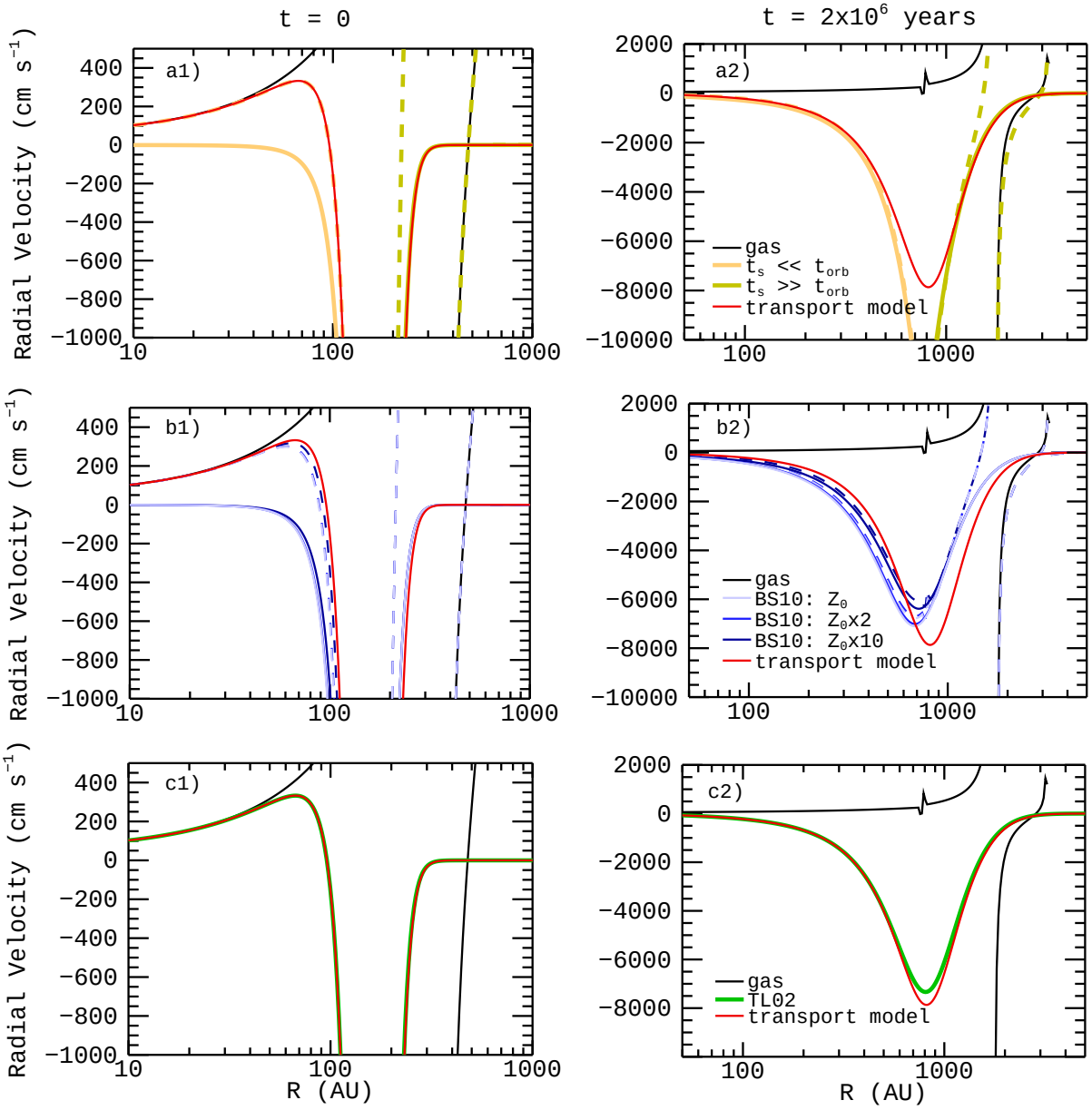

Figure 3.10: Plots of the particle-transport model calculations for radial drift of a 20 μm grain versus others' calculations for the drift velocity. Dashed curves denote the calculated velocity + the radial gas velocity for calculations that neglect the radial gas velocity. Curves shown for two times in the fiducial disk model of Chapters 4 & 5 for the case of outward-flowing gas at the midplane. Panels-a1 and -a2 consider the limits to drift velocity presented in *Weidenschilling* (1977a). -b1 and -b2 consider the velocity from *Bai & Stone* (2010a) (BS10) for three local dust-to-gas densities ($Z_0 = 0.015$. -c1 and c2 consider the velocity from *Takeuchi & Lin* (2002) (TL02).

(2010a). This combination produces

$$v_{r,\mathrm{drift}} = -\frac{2\tau_s}{(1+\epsilon_\rho)^2 + \tau_s^2}\eta_{\delta\phi} v_{\mathrm{K}}\,. \tag{3.27}$$

Note that the above equation also includes the effect that regions with high dust-to-gas ratios will experience slower particle drift (when $\epsilon_\rho = \rho_p/\rho_g$ is large, where ρ_p is the local volume density of solids), as shown in panels-b1 and -b2 of Figure 3.10. In Equation (3.27), $\tau_s = \Omega_{\mathrm{K}} t_{\mathrm{stop}}$ is the normalized stopping time, and $\eta_{\delta\phi}$ references the radial shearing within the disk, usually referenced as (approximations) $\eta_{\delta\phi} v_{\mathrm{K}} = v_{\mathrm{K}} - v_{\phi,g}$ or $\eta_{\delta\phi} = -\left(\partial P/\partial R\right)/2\rho_g R\Omega_{\mathrm{K}}^2$. However, perhaps because of the predominance of the order-of-magnitude limit for Equation (3.25), *Bai & Stone* (2010a) have chosen to specify τ_s of Epstein drag using c_s in place of v_{therm}: $\tau_s = \Omega_K \rho_d s_d/\rho_g c_s$. This has the effect of off-setting the $v_{r,\mathrm{drift}}$ curve from that calculated by my method, as shown in panels-b1 and -b2 of Figure 3.10, and calculating a somewhat larger inward drift for particles in the main part of the disk than necessary.

Finally, *Takeuchi & Lin* (2002) derive a widely used equation for the radial-drag velocity of particles that includes drag from the radial gas flow explicitly. It continues the simplifying assumptions used to arrive at Equations-set (3.24) to produce

$$v_{r,\mathrm{drag}} = \frac{v_{r,g}/\tau_s - \eta_{\delta\phi} v_{\mathrm{K}}}{\tau_s + 1/\tau_s}\,, \tag{3.28}$$

where *Takeuchi & Lin* (2002) derive their $\eta_{\delta\phi}$ directly from radial orbital-pressure balance: $\eta_{\delta\phi} = -\left(\partial P/\partial R\right)/R\rho_g\Omega_{\mathrm{K}}^2$. Plots of the *Takeuchi & Lin* (2002) radial-velocity values compared to my own are shown in panels-c1 and -c2 of Figure 3.10. Equation 3.28 provides radial-velocity values very similar to my own, if somewhat slower, along the range of disk-verus-gas conditions. However, my particle-transport model continues to use the itterative method to solve for dust radial velocities rather than this analytical expression largely because, as shown in the next subsection, my method has been tested and proven against direct-integration trajectories of gas-dragged, orbiting particles.

3.2.3 Fidelity of Transport Trajectories Compared to Force-Balance Numeric Integrations

The particle-transport model is constructed to use the gridded, steady-radial dust velocities discussed above, so that the trajectories calculated are a first-order approximation of the full gas-drag dynamics. Here I compare these trajectories to their corresponding precision-numerical integrations calculated as discussed in §3.2.1. Most of the comparison simulations presented below are run using the midplane-flow-velocity case, as defined in §2.6. I begin by presenting particle trajectories calculated within an initially tenuous disk (R_d = 500 AU, $\Sigma_{\rm g}$ (1AU) $\sim$ 1 g cm^{-2} at $t = 0$) that is photoevaporatively cleared within $\lesssim$10^5 years. Such tenuous disks provide loose particle-gas coupling. Combined with an outward-flowing gas velocity, the radial trajectories of the dust particles can be complex and so provide good tests of my particle-transport model. The dust-grain sizes quoted assume a rocky internal density of 3 g cm^{-3}.

Figure 3.11 plots, for both numeric integrations and particle-transport simulations, the trajectories and radial velocities of 0.2 mm-sized particles initiated at three different radial locations within this tenuous disk. Here, such large particles are only loosely coupled to the gas flow, with exponential-stopping times ($t_{\rm stop}$) at $t = 0$ of a few to greater than ten Kepler times (and of no shorter than 0.1 Kepler times throughout the simulations). Nevertheless, there is good agreement between my particle-transport simulations and the more precise numeric integrations.

However, the particle-transport model trajectories do lack certain details; as shown in the lower panels of Figure 3.11, they do not account for orbital eccentricity. Thus, the particle-transport simulations are limited in their depiction of complex gas-particle interactions. In panels-a2 and -b2, these interactions pertain to a particle disengaging from an outward-sweeping photoevaporation front. However, the results of interest to the studies of this thesis (as explored in Chapters 4, 5, & 6) are not sensitive to such a high level of detail. Most important, instead, are the broad effects pertaining to variations in particle size and the evolving disk surface density. As a test of these considerations, I ran simulations for particles of sizes 0.2 μm, 2 μm, 20 μm, and 0.2 mm in the tenuous disk, from 20 starting locations, 0.5–500 AU. Figure 3.12 compares the numerical integrations versus particle-transport simulations for those runs initiated at 1 AU and 500 AU. For the total run set, the exponential-stopping times ranged from less than 10^{-4} to greater than 10 Kepler times, and in general, the relative radial positions of the simulated trajectories agreed with

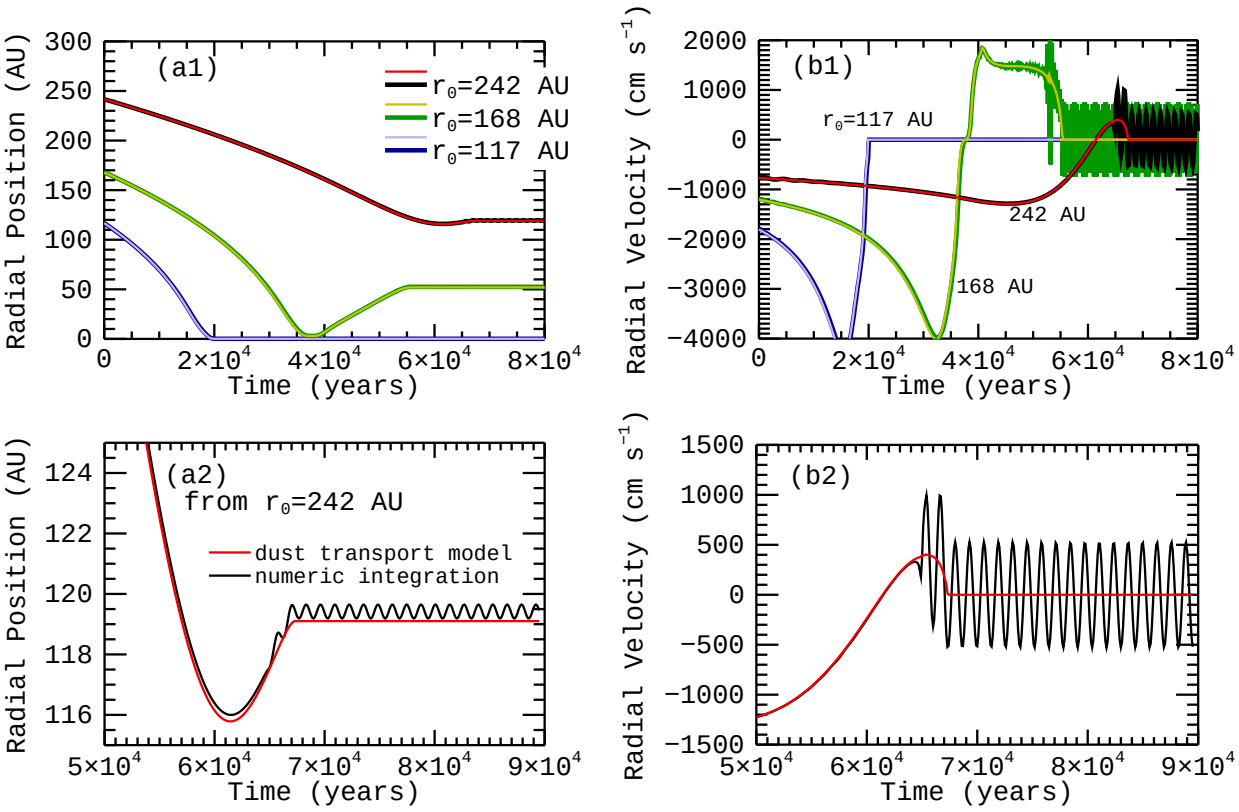

Figure 3.11: Radial position (a1, a2) and radial velocity (b1, b2) of simulated particle trajectories. Comparison between precision numerical integrations (heavy, dark lines) and the particle-transport-model trajectories (thin, pale lines). In this figure, 2 mm-sized particles were initiated at three different radial positions within a tenuous, evolving disk and were subject to the midplane-flow gas-velocity case. Lower panels show a zoom-in of the trajectory initiated at $r_0 = 242$ AU.

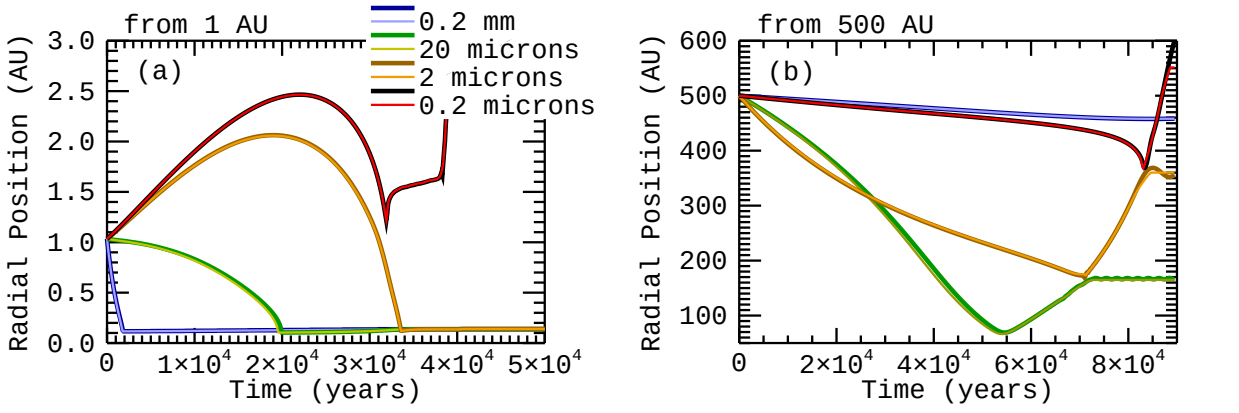

Figure 3.12: Particle trajectories within a tenuous, evolving disk in the midplane-flow gas-velocity case for four different particle sizes. Comparison between high-precision numerical integrations (heavy, dark lines) and particle-transport model trajectories (light lines). (a) Particles initiated at $R = 1$ AU. (b) Particles initiated at $R = 500$ AU.

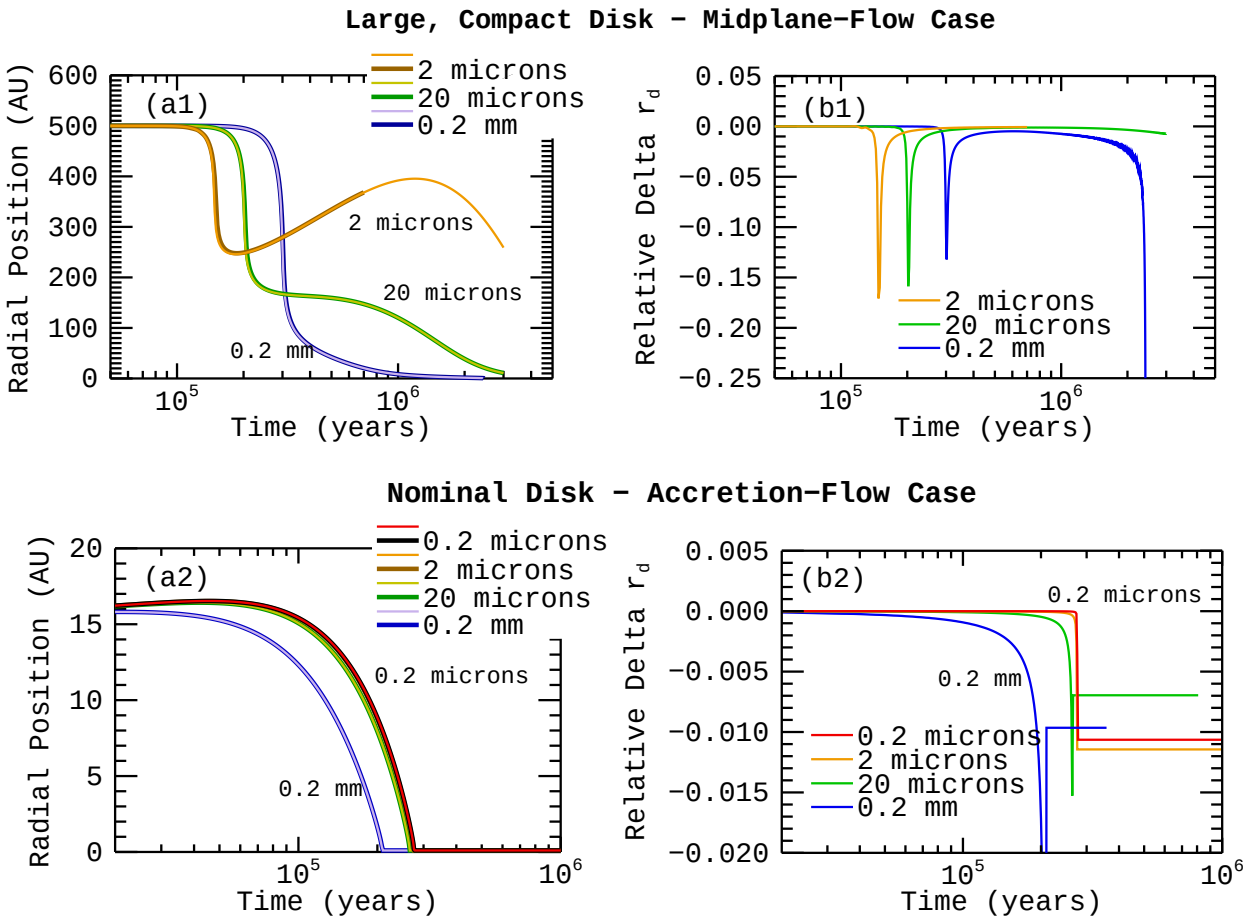

Figure 3.13: (a1, b1) Particles initiated at 500 AU within a massive, but initially compact disk for three particle sizes in the midplane-flow gas-velocity case. (a2, b2) Particles initiated at 15 AU within the fiducial-disk for four particle sizes in the accretion-flow gas-velocity case. Note that the two smallest particle sizes follow nearly identical trajectories. In the left panels, trajectories compared between high-precision numerical integrations (heavy, dark lines) and particle-transport model trajectories (light lines). In the right panels, the relative difference in the radial positions over time between the numerical integrations and the particle-transport simulations. [(simulated - integrated) / integrated] Note that the time-axes are in log-scale.

the numeric integrations to within 2% or better.

Where my particle-transport simulations deviate the most from the numeric integrations is for particles experiencing a long period of steady infall. This is true regardless of how well-coupled the particles are to the gas motions, and is an effect of the particle-transport model repeatedly overshooting the estimate of the infalling particle trajectory. Panel-a1 of Figure 3.13 plots trajectory comparisons for particles initiated at 500 AU in a massive, but initially compact disk ($M_{\rm D,0} = 0.05 M_\odot$ and $R_d = 10$ AU). In this scenario, the particles begin very decoupled from the

gas ($t_{\rm stop} > 10^3$ Kepler times), and after their initial infall toward the main disk they become moderately well-coupled ($t_{\rm stop} \sim 10^{-2}$ and smaller). In panel-b1 I plot the relative difference in the particle radial positions between the particle-transport model trajectories and the numerical integrations. Here one can see that for each infall (including the final infall of the largest particle) these two trajectory calculations diverge as the simulated trajectories outpace those of the numeric integrations. Therefore, exaggerated, rapid infall of particles may be a drawback of my particle-transport model. However, inspection of all of my simulated trajectories suggests that this exaggerated infall should have a negligible effect on my general understanding of the timing and trends of particle transport. As a check I have also run comparison integrations using the accretion-flow case in the baseline-disk model of Chapter 4. I ran four particle sizes (0.2 μm–0.2 mm) initiated at 15 AU and the results (trajectory comparisons and relative differences in radial positions) are plotted in Figure 3.13 panels-a2 and -b2. Initially the particles move outward with the outwardly expanding disk, but soon they are swept inward as the usual, steady, inward-accretion flow spreads throughout the main disk. There is good agreement between the simulations and the numerical integrations, with positional differences of less than 2% for all but the very final stages of infall.

Therefore, in the limit of zero turbulent diffusion, the simulated trajectories produced by my particle-transport model appear to be a sufficiently accurate representation of radial particle transport in an evolving disk under the influence of gas drag, due to both the pressure-supported–azimuthal and the radial gas flows.

3.3 Turbulent Diffusion of the Particle Ensemble

Turbulent diffusion of the particle ensemble in my particle-transport model is represented by a random walk added to the individual grain trajectories. The magnitude of this random walk is directed by the local radial diffusivity for a particle of a given size, while the inward/outward statistics of the walk also depend on the local disk-mass distribution and on the time stepping used in a given simulation. In this section, I first define the physical and numerical setup for effecting diffusion of the particle ensemble (§3.3.1). Next, I demonstrate the fidelity of my particle-transport model in reproducing analytical test-case solutions of radial diffusion within a gas disk (§3.3.2). Finally, I consider two different theories for the scaling of the dust to the gas diffusivities and compare the basic results of the standard-case simulations (of Chapters 4 & 6) using each (§3.3.3).

3.3.1 Numerical Calculation of Stocastic Integrations

To model the turbulent diffusion of the particle ensemble, I add a random walk to the individual grain motion via the addition of a turbulent velocity component, $v_{\rm turb}$, used in Equation 3.1. This turbulent velocity is set by the dust-particle diffusivity, $D_{\rm p}$, and by the time step of the random walk motion; it is given by

$$v_{\rm turb} = \pm\sqrt{\frac{2D_{\rm p}}{\Delta t}}\,. \tag{3.29}$$

In my particle-transport model, the time step of the random walk is limited by the time step of the gas-disk-evolution model, but is also allowed to be no greater than the local Kepler time, $1/\Omega_{\rm K}$ ($\Omega_{\rm K}$ is the Keplerian angular velocity), and no greater than either $\Delta R_5/v_{srd}$ or $\Delta R_5/v_{\rm turb}$, where ΔR_5 is the radial distance across five grid cells in the direction of particle motion.

For the bulk of my simulations, I follow *Youdin & Lithwick* (2007) in calculating the radial diffusion coefficient of the dust grains via

$$D_{\rm p} = D_{\rm g}\,\frac{1+4\tau_{\rm s}^2}{\left(1+\tau_{\rm s}^2\right)^2}, \tag{3.30}$$

where $D_{\rm g}$ is the gas diffusion coefficient, and $\tau_{\rm s} = \Omega_{\rm K} t_{\rm stop}$. (See §3.3.3 for a possible alternative to Equation (3.30).) In the Epstein-drag regime, $t_{\rm stop} = 3/\left(C_R \rho_{\rm g} v_{\rm therm}\right)$. The dust and gas diffusion coefficients are equal throughout most of the disk, except in the outermost regions where the gas surface density is very low, and the dust diffusion coefficient drops to zero. In my fiducial models, I assume that because the disk viscosity is derived from turbulence within the disk, $D_{\rm g} = \nu$.

While Equation (3.29) provides an accurate first-order representation of the particle diffusivity, it is not sufficient for producing accurate diffusion of the particle ensemble in my model gas disk. Among other things, it does not account for the mass distribution of the disk gas. In a real random walk, the time and distance of each step vary according to the local properties of the gas environment. In my model, however, the time step is fixed by other, mostly numerical, considerations. Therefore, to allow my particle ensemble to diffuse according to the actual gas distribution, I must calculate an appropriate probability for whether a given particle in the ensemble will step radially inward (p_{in}) or outward (p_{out}).

The proper weighting between p_{in} and p_{out} is a function of the imposed time step. Instanta-

neously ($\Delta t \to 0$), $p_{in}/p_{out} = 1$, because $\Delta t = 0$ represents only a single random walk encounter. However, for $\Delta t > 0$, the probability that multiple encounters will occur within that time step becomes nonzero. Furthermore, additional encounters will occur not at the initial position being considered, but either inward or outward of that location depending on the outcome of past encounters. Therefore, the properties of the diffusive medium (the gas) outside the local point of interest play a role in determining p_{in}/p_{out} for $\Delta t > 0$. The spatial extent of this region of interest is set by how far particles may travel for a given Δt. For the particle ensemble, this is the root-mean-square of the displacement of the diffusing particles, or

$$\Delta R_{rms} = \sqrt{\left\langle (\Delta x)^2 \right\rangle} = v_{\rm turb} \Delta t = \sqrt{2 D_{\rm p} \Delta t} \ . \tag{3.31}$$

The weighting for p_{in} is set by the gas properties between $R - \Delta R_{rms}$ and R; and for p_{out} by the properties between R and $R + \Delta R_{rms}$. Asymptotically, the diffusion must yield everywhere a uniform particles(dust)-to-gas ratio. Therefore, after an infinite time, the region with more gas mass must also have proportionally more dust particles. However, because regions of higher diffusivity reach the steady state of uniform concentration more quickly, for a finite time step, proportionally more particles will also mix into a region of higher diffusivity than into one of lower diffusivity. Therefore,

$$\frac{p_{\rm in}}{p_{\rm out}} = \frac{(M_{\rm g}\, D_{\rm p})_{in}}{(M_{\rm g}\, D_{\rm p})_{out}} = \frac{\displaystyle\int_{R-\Delta R}^{R} D_{\rm p} \Sigma_{\rm g} R \, dR}{\displaystyle\int_{R}^{R+\Delta R} D_{\rm p} \Sigma_{\rm g} R \, dR} \, . \tag{3.32}$$

To evaluate Equation (3.32) within my model gas disk, I assume uniform, mean values of the gas surface density and particle diffusivity between each grid point. Because I calculate $p_{\rm in}$ once at each disk-evolution time step, but Δt of the individual particle motions may vary due to local constraints, I calculate actually $p_{\rm in}$ at each grid point for both $\Delta t_{\rm evolve}$ and $\frac{1}{2}\Delta t_{\rm evolve}$, then interpolate parabolically for other time-step sizes as needed, using $p_{\rm in}\,(\Delta t = 0) = 0.5$.

Figure 3.14 plots the diffusion–time-step caps and corresponding $p_{\rm in}$ values for the static-disk models used to study mixing in Chapter 4. Both models have a maximum time-cap for data output of 5000 years, and the static0 disk model has an exponential fall-off of gas mass in the outer disk. Otherwise both have a roughly uniform mass distribution in radius. From this figure it is clear

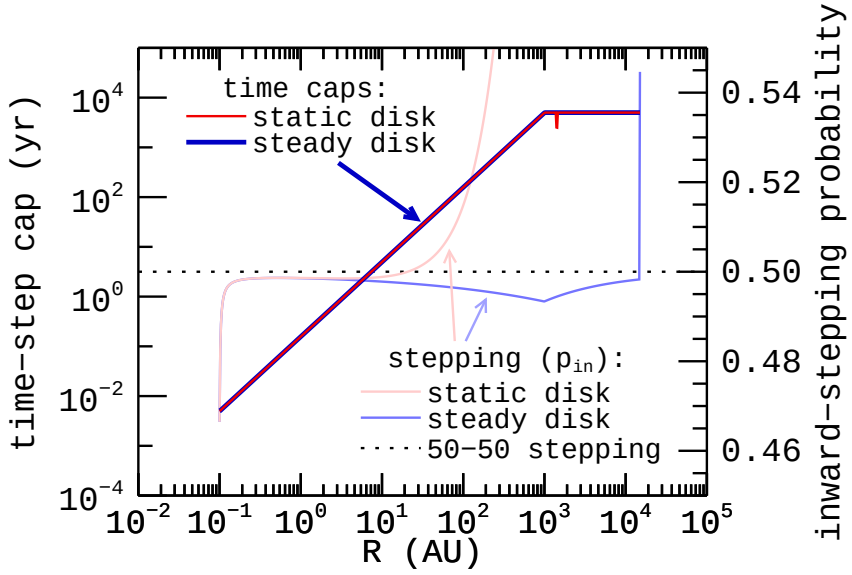

Figure 3.14: Curves of the maximum turbulent (random-walk) time step for particles in the static0 and steady disk models and the corresponding probablities for a particle to step radially inward. The global time step here is 5,000 years, setting the cap in the outer disk. Inward of the cap, the turbulent time-stepping in these models is primarily controlled by the local Kepler time ($1/\Omega_{\rm K,mid}$).

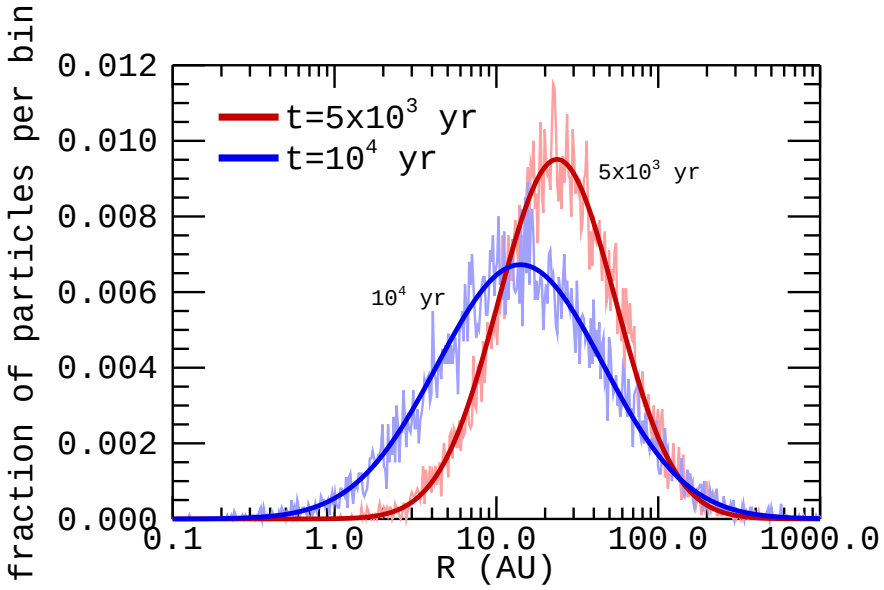

Figure 3.15: The fraction of particles per radial bin for my particle-transport simulations (pale lines) versus the analytical-expected values (dark lines). This figure corresponds to the *Clarke & Pringle* (1988) example where $\nu \propto \Sigma_{\rm g}^{-1} \propto R^2$ in a static disk with an accretion-flow velocity, $v_{\rm acc} = -1.5\nu/R$, and $\nu = 4.941 \times 10^{14}$ cm^2 s^{-1} at 1 AU. The simulation was initiated at $t = 0$ with 10^4 particles at 40 AU.

how, in general, the inward/outward-walking probabilities are close to equal, but that the particle ensemble will probabilistically avoid regions of very low mass density.

Figure 3.15 presents a comparison of the distribution of particles using my particle-transport model compared to the expected distribution for an analytical example derived by *Clarke & Pringle* (1988). While the discreet nature of my particle-transport simulations result in scatter on the distribution, the overall result is a good match to the analytical theory. In the following subsection, I compare simulated particle diffusion to other analytical test cases derived in Appendix A.

3.3.2 Fidelity of Model-Ensemble Diffusion

In this section, I present simulations of static-disk test cases of particle diffusion and compare these simulations to the analytical solutions obtained in Appendix A. I also discuss the effects of my choice of simulation time-step on the results. Analytical solutions can be found for a mass of contaminants (particles) given by a delta-function at $t = 0$ and for cases using fixed power-laws for the disk-gas surface density, Σ_g, the disk viscosity, ν, and the radial (advection) velocity of the diffusing contaminant, v_R, when those power-laws follow:

$$\begin{aligned} \Sigma_g &= \Sigma_0 R^{-a}\,, \\ \nu &= \nu_0 R^b \;\rightarrow\; D_{kg} = \zeta\nu\,, \\ v_R &= v_0 R^{b-1}\,. \end{aligned}$$

Σ_0, ν_0, v_0, ζ, a, and b are all constants and D_{kg} is the local diffusivity.

The analytic cases are solved for $C\,(R,t)$, the concentration of the contaminant, which is equivalent to σ/Σ_g, where σ is the local surface density of the contaminant. However, the particle-transport simulations output the number of particles per radial grid space, so I convert $C\,(R,t)$ into an expected mass distribution, $m_i/m_{\rm tot}$, where m_i is the contaminant mass in grid cell i, and $m_{\rm tot}$ is the total mass of contaminant in the disk at $t = 0$. This can then be directly compared to the distribution of particles in my simulations. Analytical solutions are given for three separate cases: simplest radial diffusion, with a constant disk-mass distribution ($a = 1$) and uniform diffusivity ($b = 0$); a steady disk with a logarithmic solution space ($a = b = 2$); and other random values of a and b and $b \neq 2$. Mass-distribution solutions for each of these are listed in Appendix A.

To compare my particle-transport model to the derived analytic test-case solutions, I have run simulations of 10,000 particles initiated at 40 AU. I consider cases for both $v_0 = 0$ and $v_0 = -3/2\nu_0$. The latter corresponds to the 1D gas-accretion velocity in the steady-disk cases ($a = b$), but is an artificially imposed velocity structure in the nonsteady disks. I vary the values of both a and b (the slopes of the disk surface-density (inverse) and disk-viscosity functions, respectively) to test my model in both steady and nonsteady-disk environments. All simulations use $\nu\,(1\mathrm{AU}) = 4.941 \times 10^{14}$ cm^2 s^{-1} and (unless otherwise stated) $\zeta = 1$. In these test-case simulations, the values of Σ_0 and the particle size are arbitrary, since the background velocity of the particles, v_R, is prescribed.

Panel-a1 of Figure 3.16 plots a comparison between my numerical simulations of particle transport and the analytically expected contaminant-mass distribution for the case of $a = b = 1.5$ and zero background velocity ($v_0 = 0$) at two different times. It shows that the overall, evolving distribution of the particle ensemble is in good agreement with the analytical solution. However, the scatter produced by the discreet nature of the particle simulations makes it difficult to judge the accuracy with which the simulations reproduce this analytical test case. Therefore, panel-b1 plots an alternate comparison of the simulated and analytical mass distributions. Here the values plotted correspond to a summing of the fractional-mass per grid space either from $R = 0$ outward, or from $R = R_0 = 40$ AU inward (for $R < R_0$) and outward (for $R > R_0$). Again, the simulations and the analytical solutions appear to be in good agreement.

I have simulated particle diffusion with zero background velocity in a steady disk for a range of $a = b$-values, and panels-a2 and -b2 of Figure 3.16 display the results at $t = 2 \times 10^4$ years. In general, my simulations agree well with the analytical solutions. The exceptions occur for very steep ($a = b = 3$), or very shallow ($a = b = 1$) disk profiles and are caused by the finite nature of my simulation space. The divergence is easy to see in the steep $a = b = 3$ case. A steep viscosity (diffusivity) profile that goes as R^3 leads to rapid transport of particles over very large distances in the outer disk. Therefore, the outer edge of my simulation space acts as a sink for particles. At early times, before a significant fraction of particles have been lost, the simulations and analytical solutions are in good agreement, as shown in the lower panels, (-a3 and -b3); they deviate from each other only at later times. In the shallow $a = b = 1$ case, it is loss past the inner boundary of the simulation space that causes the simulations to deviate from the analytical solutions (at later

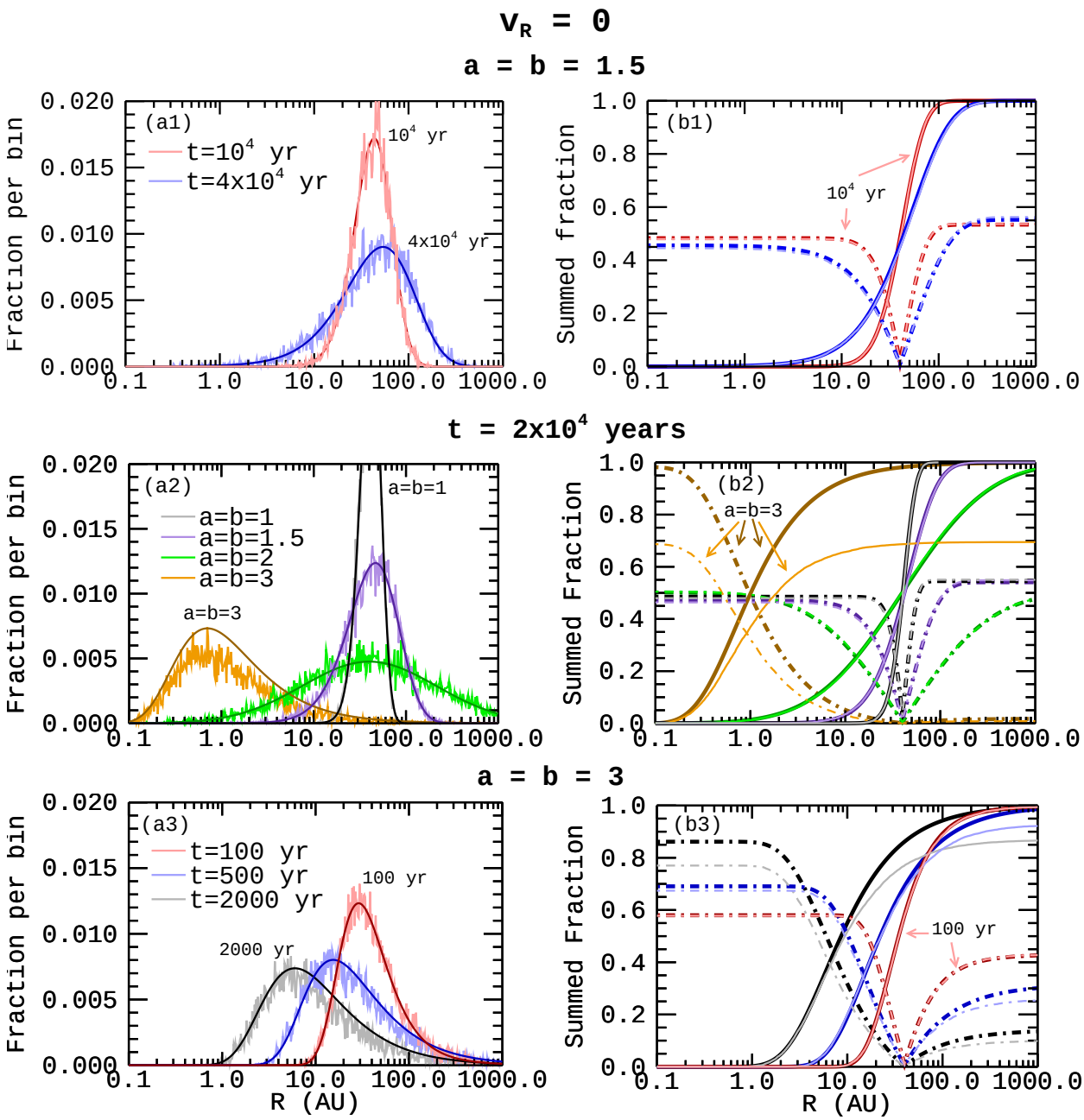

Figure 3.16: Steady ($a = b$ disks with zero background velocity. Left panels: comparison of the mass distributions of the particles (contaminant) between the particle-transport simulations (pale lines) and the analytical solutions (dark lines). The vertical axis is the fraction of total particles (total contaminant mass) per radial grid space. Right panels: comparison between simulations (pale lines) and analytical solutions (dark lines) of the summed-mass distributions. Solid lines represent the distributions summed from $R = 0$, and dashed lines represent the distributions summed from $R = R_0 = 40$ AU. Simulations run using 10,000 particles. For the cases of $a = b = 1$, 1.5, 2, and 3, simulations were run using global time-step sizes of $\Delta t = 2 \times 10^4$, 2000, 1000, and 2000 years, respectively. The $a = b = 3$ simulation for the lower panels-a3 and -b3 was run using $\Delta t = 100$ years. In this simulation at $t = 100$ years, 100% of the particles remain on the grid, but at $t = 500$ and 2000 years only 93% and 87% remain, respectively.

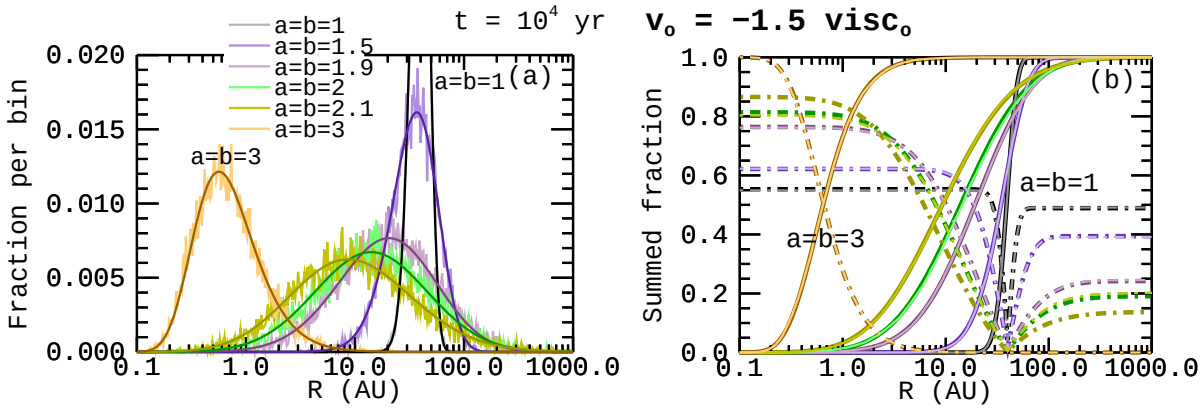

Figure 3.17: Mass-distribution profiles (a) and summed profiles (b) at $t = 10^4$ years for several $a = b$ cases with $v_0 = -1.5\nu_0$. Comparison between simulations (pale lines) and analytical solutions (dark lines). In (b) solid lines represent summing from $R = 0$, dashed lines from $R = R_0$. For the case of $a = b = 1$, the simulation was run using a global time-step size of $\Delta t = 10^4$ years. For $a = b = 1.5$ and 3, $\Delta t = 1000$ years. For $a = b = 1.9$, 2, and 2.1, $\Delta t = 500$ years.

times than the $t = 2 \times 10^4$ years shown in the Figure, due to the slower diffusive evolution).

Loss of particles past the simulation-space boundaries does not cause significant deviation from the analytical solution when I include a background-accretion velocity. In Figure 3.17, I plot the mass-distribution profiles at $t = 10^4$ years for a range of $a = b$ values (steady disks) with $v_0 = -3\nu_0/2$. Because the background velocity is inward, it keeps particles away from the outer boundary, and loss past the inner boundary is a part of the analytical solution as well as the simulations. All of these cases show good agreement between the simulations and the analytical solutions.

There is also good agreement for simulations run in non-steady disks ($a \neq b$). As examples, panels-a1 and -b1 of Figure 3.18 plot the mass-distribution profiles for the case of $a = 1$ (a uniform mass distribution in R), $b = 3$, and $v_0 = -3\nu_0/2$, which has a rapidly evolving distribution. And panels-a2 and -b2 plot the distributions for $a = 3$, $b = 0$ (uniform diffusivity), and $v_\circ = -3\nu_\circ/2$, which is slowly evolving. Simulations were also run for these $a \neq b$ cases with $v_\circ = 0$; they also agree well with their corresponding analytical solutions.

Next, as a check of the scaling between the diffusivity and the background particle velocity, I present simulations varying ζ (where $D_{kg} = \zeta\nu$). The results are plotted in Figure 3.19 for three disk scenarios, including zero and non-zero background velocity, and steady and non-steady disk

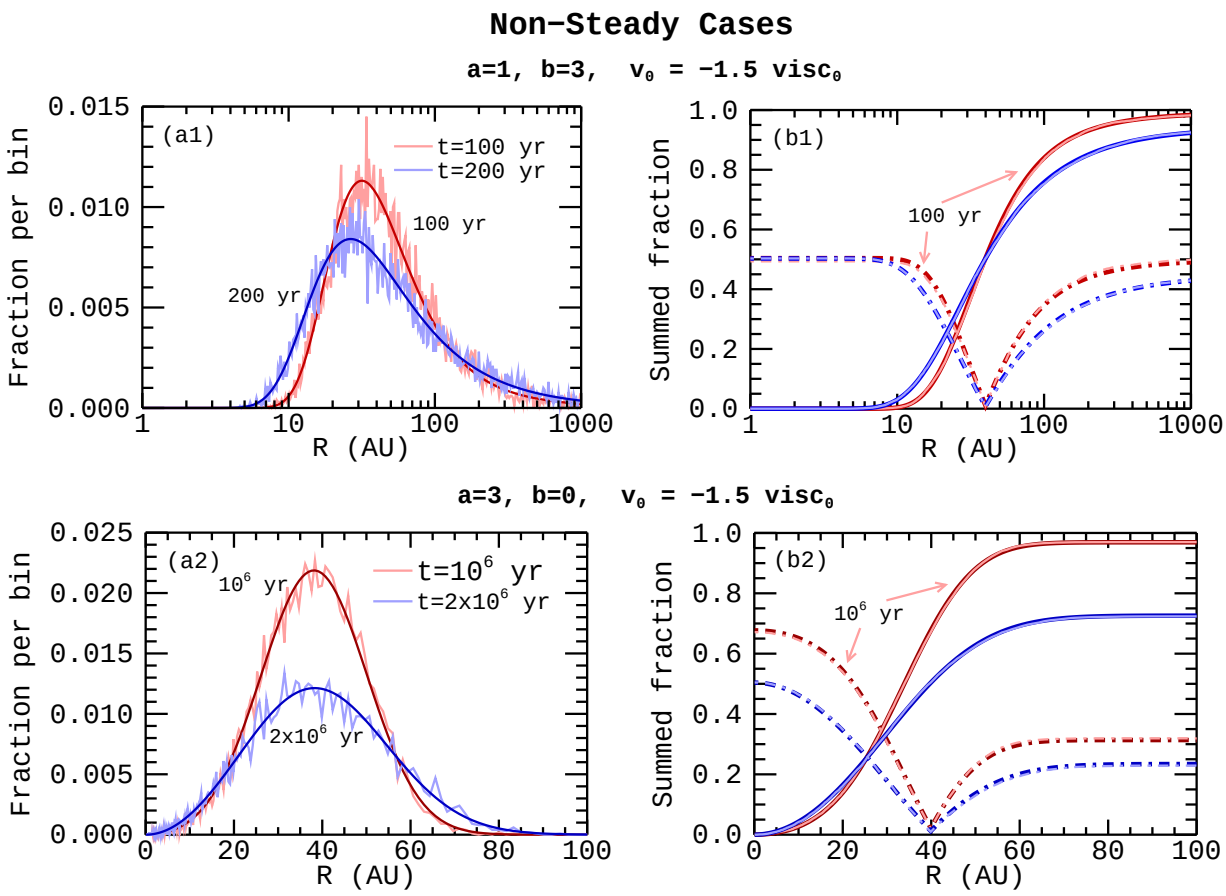

Figure 3.18: Mass-distribution profiles (a1, a2) and summed profiles (b1, b2) at two times for two non-steady-disk cases. Comparison between simulations (pale lines) and analytical solutions (dark lines). In (b1, b2) solid lines represent summing from $R = 0$, dashed lines from $R = R_0$. The simulation for (a1, b1) was run using a global time-step size of $\Delta t = 10$ years, and that for (a2, b2) was run using $\Delta t = 10^5$ years.

profiles. For all, I see good agreement between my simulations and the analytical solutions. The only noticable deviation occurs for the shallow disk case — panels-a1 and -a2 — with high relative diffusivity where there is excess loss of particles past the inner grid boundary.

Finally, I would like to be sure that my particle-transport model correctly simulates diffusion of the particle ensemble for the global time steps used in the static-disk simulations of Chapter 4 ($\Delta t = 2000$ years), as well as for the time steps required by the disk-evolution model in the evolving-disk simulations ($\Delta t \sim 0.05$ years). As was described in §3.3.1, maximum limits are placed on the particle time stepping to ensure that disk conditions local to each particle are obeyed. Panel-a of Figure 3.20 plots these time-step restrictions for a variety of disk scenarios and scaled diffusivities. The time-cap due to the simulation-output timestep is here set very high (10^4 years) in order to

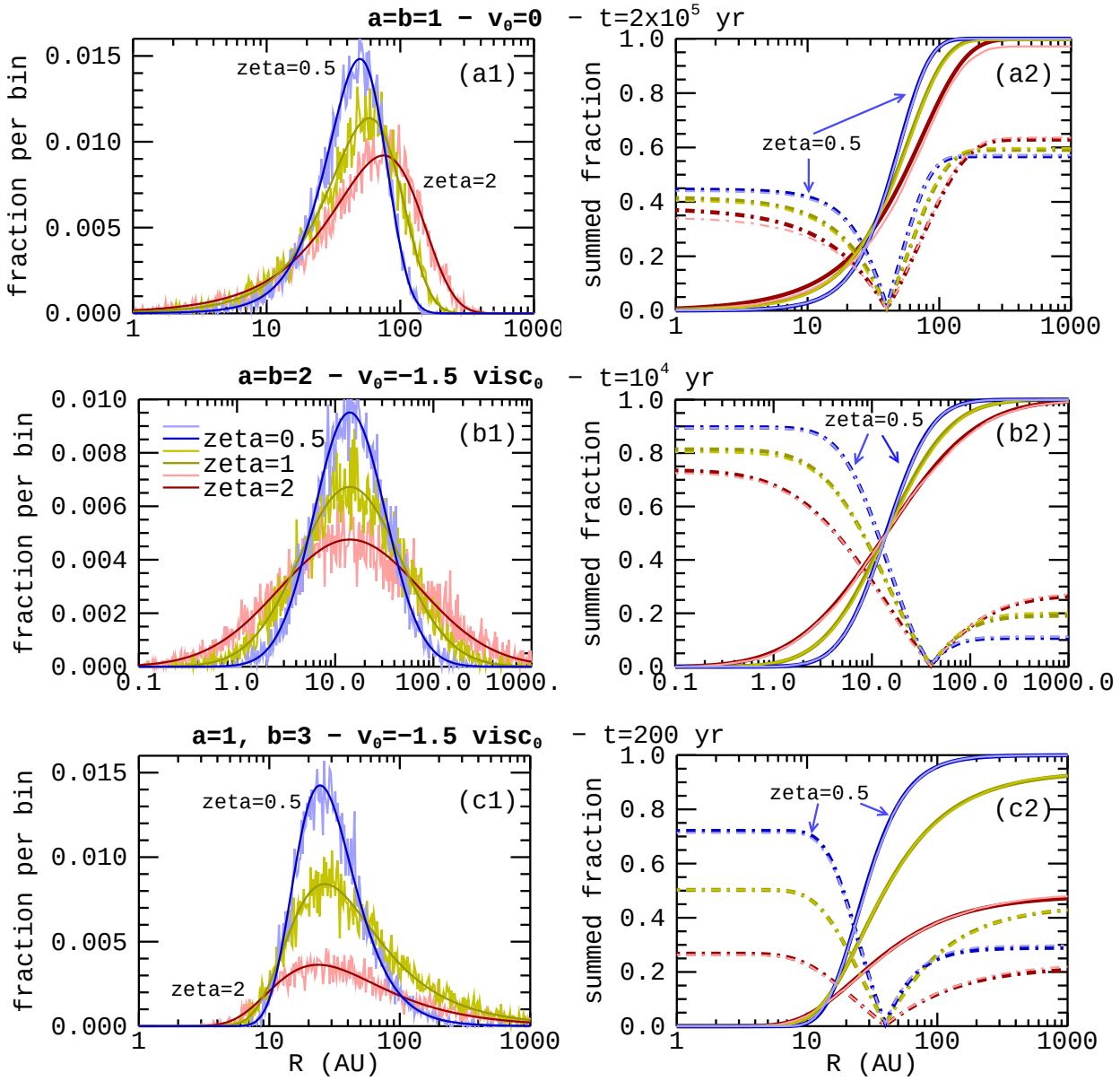

Figure 3.19: Mass-distribution profiles (a1, b1, c1) and summed profiles (a2, b2, c2) varying the contaminant diffusivity by a factor of ζ. The top panels are for the steady-disk case of $a = b = 1$ with $v_0 = 0$ at $t = 2 \times 10^5$ years run with a global time-step size of $\Delta t = 2 \times 10^4$ years for $\zeta = 1$ and $\Delta t = 10^4$ years for $\zeta = 0.5$ and 2. The middle panels are for the *Clarke & Pringle* (1988) standard steady-disk case of $a = b = 2$ with $v_0 = -\frac{3}{2}\nu_0$ at $t = 10^4$ years run with $\Delta t = 500$ years. The bottom panels are for the non-steady disk case of $a = 1$, $b = 3$, with $v_0 = -\frac{3}{2}\nu_0$ at $t = 200$ years run with $\Delta t = 10$ years.

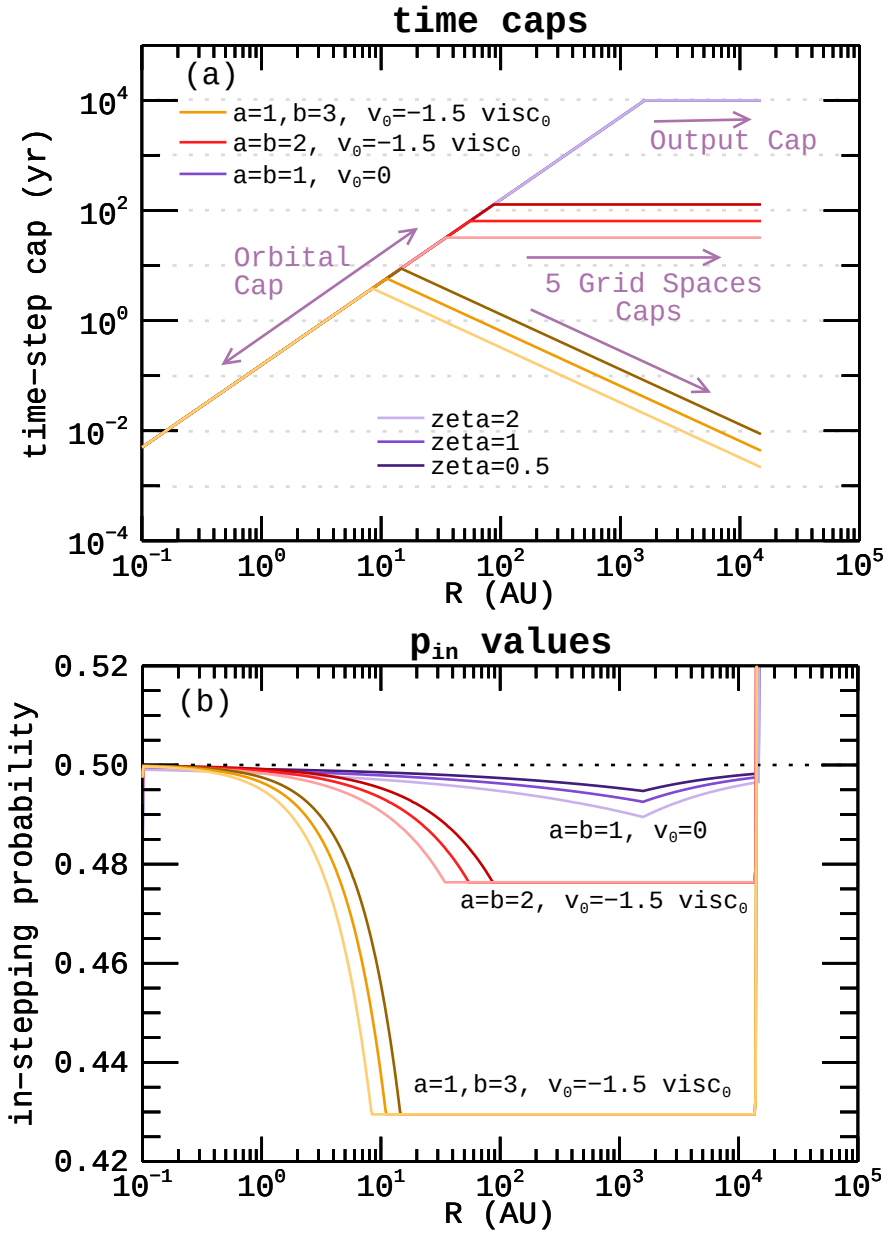

Figure 3.20: Turbulent (random-walk) maximum time steps (a) and the corresponding inward-stepping probabilities (b) for particles in a variety of disk models and for different scaled diffusivities. Time caps include all three forms of time-stepping restrictions: capping by the global time step of the simulation ($\Delta t = 10^4$ years here), capping by the local Kepler time ($1/\Omega_K$), and the restriction that a particle may not diffuse (or advect) more than 5 grid spaces in a single random walk. The inward-stepping probability is set by the integrated disk properties accessible within a single random-walk step, and changes for alterations in the random-walk time-step size.

show how the other constraints vary with R. A shorter output time or a cap due to an evolving disk scenario would truncate these curves above that time-step threshold and alter the requisite $p_{\rm in}$ values where that cap applied. The $p_{\rm in}$ values corresponding to the time-step curves shown are plotted in panel-b.

Smaller time steps mean more steps to simulate a given amount of time in the disk; therefore, the probabilities of a particle stepping inward versus outward grow ever closer to 50/50. Cumulatively, However, all time-step sizes used must evolve the distribution of the particle ensemble equally. Therefore, I have run a few test-case simulations using capped time-step sizes ranging from 10^{-3} years to 100 years. The resultant distributions versus the analytical solutions are plot-

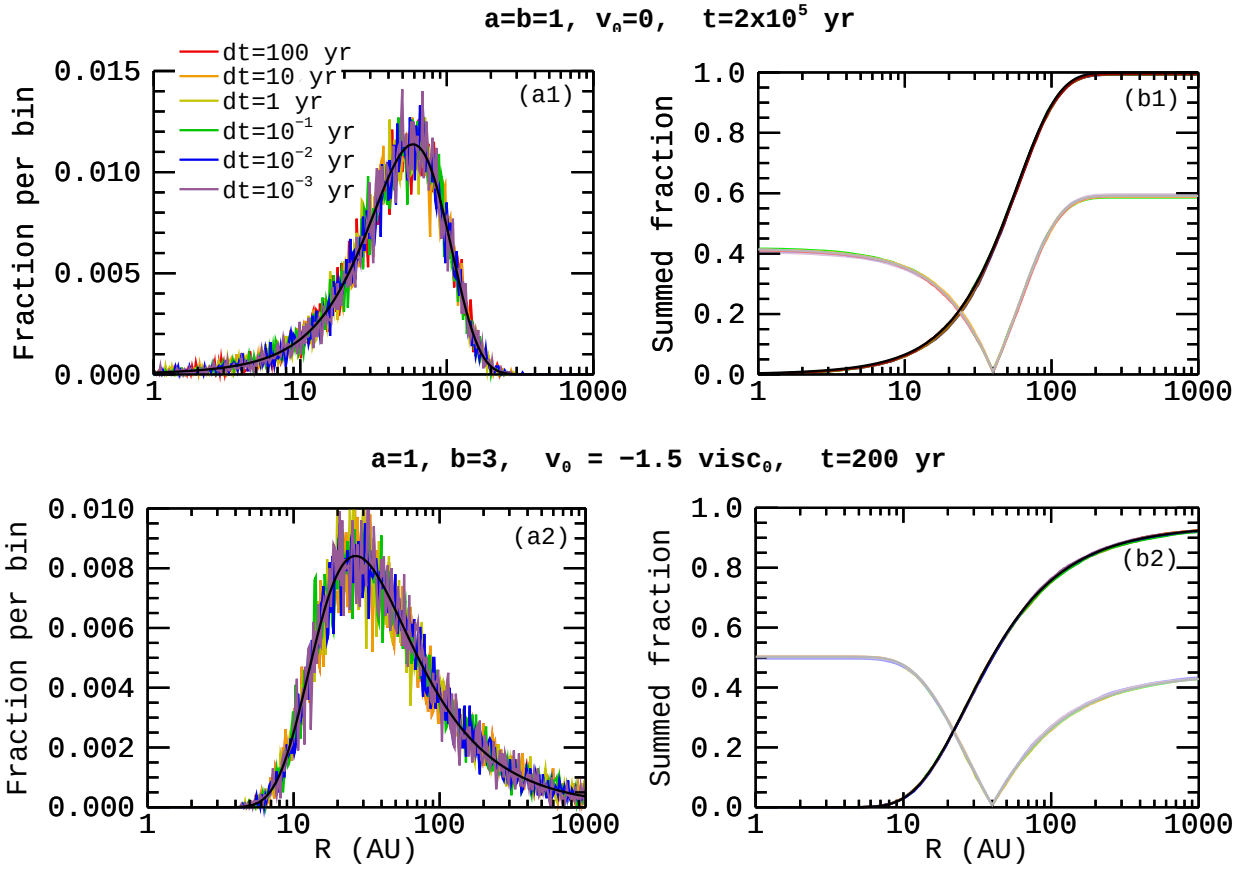

Figure 3.21: Mass-distribution profiles (a1, a2) and summed-profiles (b1, b2) for two disk cases: a steady case of $a = b = 1$ with $v_0 = 0$ shown at $t = 2 \times 10^5$ years, and a non-steady case, $a = 1$, $b = 3$, with $v_\circ = -\frac{3}{2}\nu_\circ$, shown at $t = 200$ years. Simulations were run for a range of global time-step sizes (colored lines) and are compared to the analytical solutions (black/grey lines). In (b1, b2) the dark lines represent summing from $R = 0$, and the pale lines summing from $R = R_0$. The colored lines of the simulations are largely obscured by the analytical solutions (black/grey) plotted over top.

ted in Figure 3.21 for the case of $a = b = 1$ and $v_0 = 0$ (panels a1, b1), and for the case of $a = 1$, $b = 3$, and $v_\circ = -3\nu_\circ/2$ (panels a2, b2). All of these simulations agree well with their corresponding analytical solution, and the scatter produced for simulations with different time-step sizes are all comparable.

However, while the agreement between simulations using different time-step sizes is good for almost all of the simulations I tested, one set of simulations shows a marked change in the scatter depending on the size of the time step used. Figure 3.22 plots simulations run for a range of time-step sizes for the case of $a = b = 2$ and $v_0 = -3\nu_0/2$ compared to the analytical solutions at two times. Looking at the summed-mass distributions (-b1 and -b2), it is clear that all of these simulations do distribute the particle ensemble appropriately for this diffusion test case. However, the mass-fraction-per-bin profiles show significant, resonant-like scatter in the $\Delta t = 10$ years and

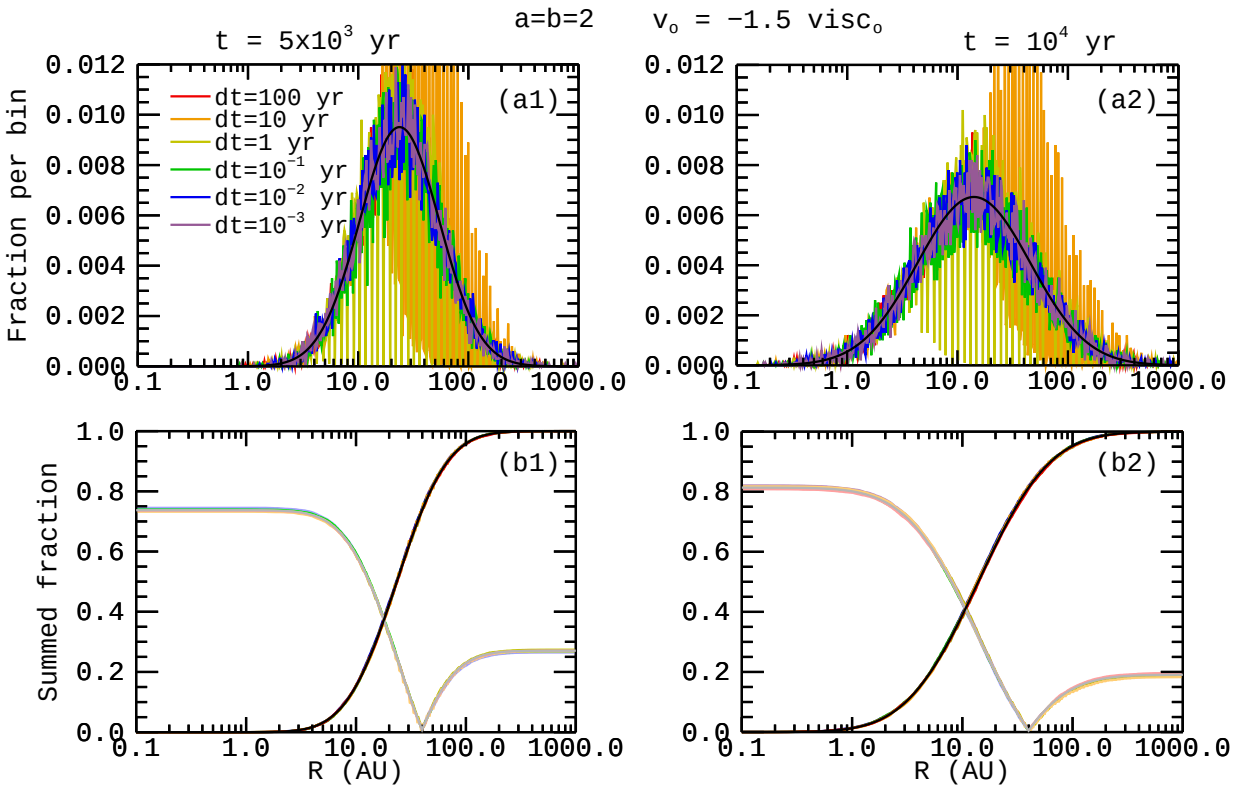

Figure 3.22: Mass-distribution profiles (a1 and a2) and summed-profiles (b1 and b2) at $t = 5 \times 10^3$ years (a1 and b1) and $t = 10^4$ years (a2 and b2) for the steady-disk case where $a = b = 2$, and $v_0 = -1.5\nu_0$. Simulations were run for a range of global time-step sizes (colored lines) and are compared to the analytical solution (black/grey lines). In (b1) and (b2), the dark lines represent summing from $R = 0$, and the pale lines summing from $R = R_0$. The colored lines of the simulations are largely obscured by the analytical solutions (black/grey) plotted over top.

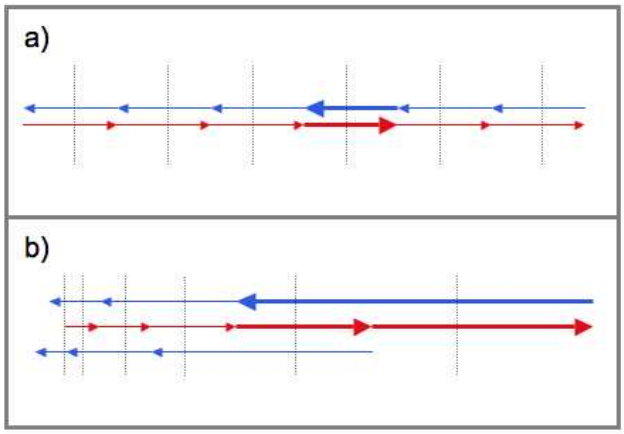

Figure 3.23: Schematics for producing resonant-like scatter of a diffused particle ensemble for (a) uniform diffusivity and (b) non-uniform diffusivity (increasing to the right). Vertical dotted lines represent the type of grid-spacing appropriate for observing resonant-like scatter in these systems.

$\Delta t = 1$ year simulations; the scatter also appears a bit higher than usual in the $\Delta t = 10^{-1}$ year simulation. Furthermore, the resonant-like-scatter region in the $\Delta t = 10$ years simulation is restricted to outward of about 15 AU, and this region moves outward with time. As shown above in Figure 3.20 panel-a, inward of 15 AU in these simulations the Kepler time ($1/\Omega_{\rm K}$) is less than 10 years and decreases toward smaller R; the time-step sizes of individual particles at small AU are restricted to smaller than the global 10-year time step. Therefore, the resonant-like-scatter behavior is only observable when the same local time-step size is used for the entire region and when the source of all the particles is a single point in R. Nonresonant-like scatter at small AU allows the particle distribution to spread out randomly, following the local diffusivity and removing the single-source-point condition first at small AU and then moving outward.

In the simplest diffusion scenario, it is easy to produce a distribution displaying resonant-like scatter. My model for diffusion does not simulate the spread in velocities/step-lengths that real diffusion produces, but rather uses a fixed diffusion step-length for a given time-step at a given grid-point (Equation (3.31)). If the diffusivity is spatially constant, there is zero background velocity, and diffusion occurs with the same time-step across a whole region, then particles from a single source will only occupy discreet locations within the simulations space, as shown in panel-a of Figure 3.23. While this will produce resonant-like scatter of the distribution, it will only be observed if the output grid onto which the grains are deposited is also appropriately spaced. This

case would require linear spacing in R. Also, the displacement of each particle has to be at least as long as the width of a grid-cell to be seen. Therefore, the effect should disappear for very small time-stepping/displacements.

The simulations of Figure 3.22 are not of simplest-case diffusion. There is a non-uniform background velocity, non-uniform diffusivity, and logarithmically spaced grid cells. However, this $a = b = 2$ case is special for two reasons: 1) The natural space for diffusion in this regime ($b = 2 \longrightarrow \ln(R)$-space) is the same as the space wherein my disk-model grid cells are equal width. Therefore we should be able to observe resonant-like scatter if it occurs. 2) Step-lengths for diffusion and advection both scale proportional with R: $\Delta R_{\text{turb}} \propto \sqrt{\Delta t \nu} \propto R^{2/2} = R$, and $\Delta R_{\text{advect}} \propto \Delta t v \propto R^{2-1} = R$. Therefore, if resonant-like scatter occurs, it should do so over a large portion of the simulation space.

Because of the non-uniform diffusivity, particles in Figure 3.22 cannot simply take one step forward and one step back to return to their starting location; they should end up interior to their starting location, even without background advection. They might, however, take two steps forward and one back, as depicted in the panel-b schematic of Figure 3.23, depending on the rest of the parameters of the system and the time-stepping. For the Figure 3.22 simulation, a particle that moves outward twice and inward once should be at a position:

$$R_{\text{fin}} = R_{\text{start}} \left[1 + \sqrt{2} \left(\Delta t \nu_0 \right)^{1/2} - \frac{13}{2} \Delta t \nu_0 - ... - \frac{27}{8} \left(\Delta t \nu_0 \right)^3 \right] ,$$

where R_{start} is the particle's starting location. Therefore, for $\Delta t \nu_0 \ll 1$, the system should approach a resonant-like scatter distribution. Also note that the offset of $R \times \sqrt{2 \Delta t \nu_0}$ is of the same order as for the scaling of a diffusive step-length, so characterizing a distribution is still rather messy. The grid spacing for my particle-transport simulations is $\Delta R_{\text{grid}} \sim 0.02R$, and $\nu_0 \approx 2.2 \times 10^{-12}$ s^{-1} for the Figure 3.22 simulations (so $\Delta t \nu_0 < 1$ for $\Delta t \lesssim 1.4 \times 10^4$ years). For $\Delta t = 0.1$, 1, 10, and 100 years, the offsets for resonant-like and diffusive stepping are $\sim 0.004R$, $\sim 0.012R$, $\sim 0.035R$, and $\sim 0.1R$ respectively. Therefore, we only see resonant-like scatter when the diffusive stepping and resonant-like offset are on the order of the width of a grid cell. (Recall from Figure 3.22 that resonant-like scatter is observed for $\Delta t = 1$ and 10 years.

While this resonant-like-scatter behavior is curious and somewhat vexing, it is also a special

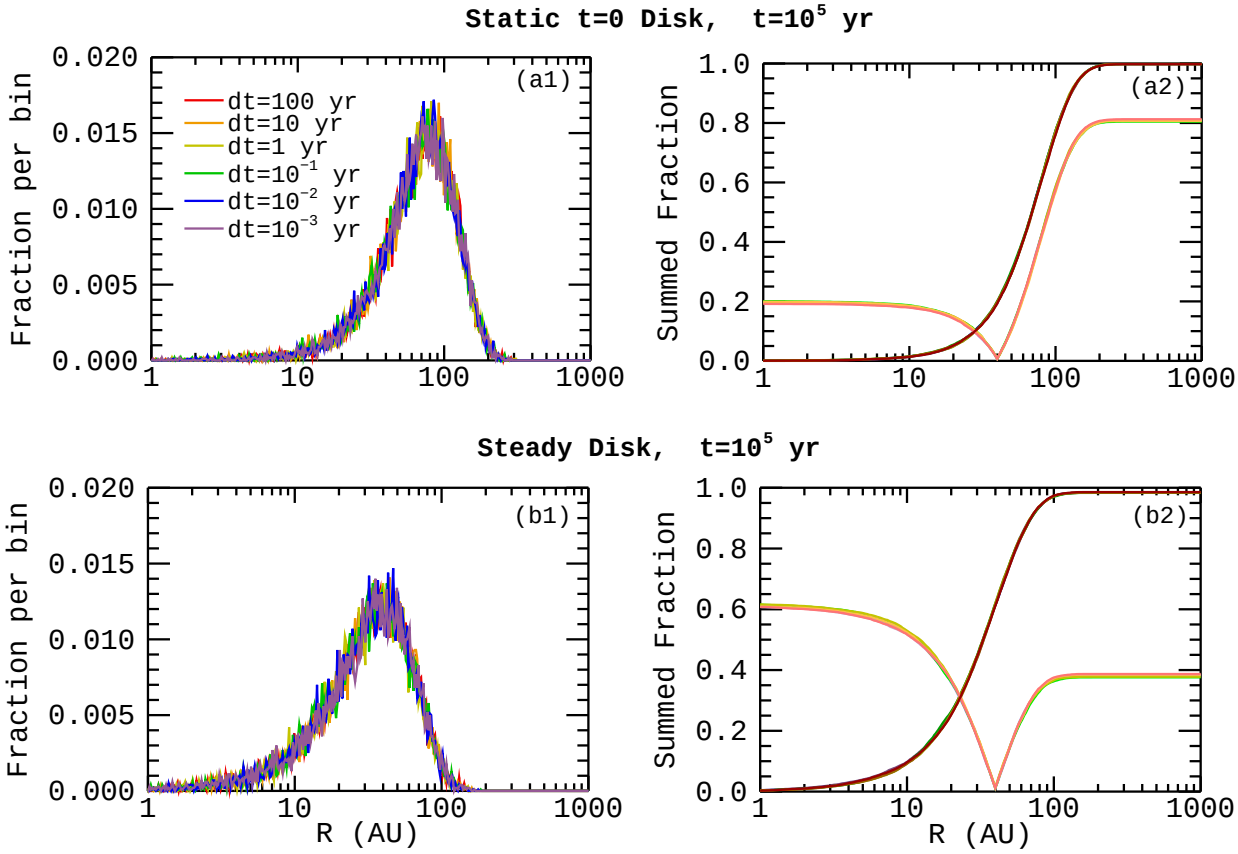

Figure 3.24: Mass-distribution profiles (a1, b1) and summed profiles (a2, b2) at $t = 10^5$ years for particles initiated at 40 AU in the two static disk models employed in Chapter 4 for a variety of global time-step sizes. These disk models do not have analytical solutions with which to compare the results, though the steady-disk has a form similar to the $a = b = 1$, $v_0 = 0$ disk case.

case and not a problem for the science simulations of this thesis. Figure 3.24 presents the results of time-step testing for particles in the two static-disk models used in Chapter 4; all timestepping produces essentially the same particle distributions (within the limits of the natural scatter of the discreet system).

3.3.3 Comparing Two Theories for Dust-Gas Coupling and Radial Particle Diffusion

In the simulations presented in this thesis, I use the most recent equations derived for the radial particle diffusivity respective to the radial gas diffusivity (*Youdin & Lithwick*, 2007). However, in the literature there is still contention over whether the older relation (*Cuzzi, Dobrovolskis, & Champney*, 1993) may not be the correct one. Therefore, in this section, I compare simulations using each of these diffusivity relations and show that for the results of Chapters 4, 5 & 6 the

specific relation for $D_{\rm p}$ is unimportant; headwind drag tends to exclude grains from regions where the two give noticeably different results.

In the papers that derive equations for $D_{\rm g}/D_{\rm p}$, the ratio is referred to as the Schmidt number, Sc. However, $Sc \equiv \nu/D_{\rm g}$ is the traditional fluid-dynamics definition, and is also an important parameter in my simulations. Therefore, I retain $Sc \equiv \nu/D_{\rm g}$ and simply refer to $D_{\rm p}$ and $D_{\rm g}$ explicitly. The most important parameters for relating particle and gas diffusivities are: $\tau_s = \Omega t_{\rm stop}$, which describes the relative importance of gas drag versus orbital motions on the particle motions; $\tau_e = \Omega t_{\rm eddy}$, which describes the frequency of turbulent kicks (one per eddy time) relative to the orbital timescale; and the Stokes number, $St = t_{\rm stop}/t_{\rm eddy} = \tau_s/\tau_e$, which describes the frequency of turbulent forcing relative to the gas-drag stopping time.

As given in Equation (3.30) above, the *Youdin & Lithwick* (2007) relation for radial diffusivity of particles in the case of isotropic turbulence is

$$D_{\rm p,YL2007} = D_{\rm g} \frac{\left(1 + 4\tau_s^2\right)}{\left(1 + \tau_s^2\right)^2} \,. \tag{3.33}$$

It is noteworthy that the result is independent of τ_e. *Youdin & Lithwick* (2007) point out that this may simply be consistent with long–stopping-time particles also having long mean-free-paths. The authors also describe the diffusivity for anisotropic turbulence and note that a larger proportion of azimuthal forcing leads to relatively more radial diffusion of particles. For all simulations, I have assumed isotropic turbulence.

The older relation for particle diffusivity is given by *Cuzzi, Dobrovolskis, & Champney* (1993).

$$D_{\rm p,CDC1993} = D_{\rm g} \frac{1}{(1 + St)} \,. \tag{3.34}$$

Not only does this relation depend on the eddy time, it also falls off more gradually as $D_{\rm p} \propto \tau_s^{-1}$, compared to the $D_{\rm p} \propto \tau_s^{-2}$ of Equation (3.33). The full equation in *Cuzzi, Dobrovolskis, & Champney* (1993) also finds a small decrease in diffusivity in the case of a non-zero mean vertical velocity for the particles. In my simulations, I assume that the mean vertical velocity is zero.

The two relations for $D_{\rm p}$ are plotted in Figure 3.25. Note that *Youdin & Lithwick* (2007) find a slight up-tick in diffusivity for marginal coupling ($\tau_s \sim 1$). This corresponds to a state of resonant

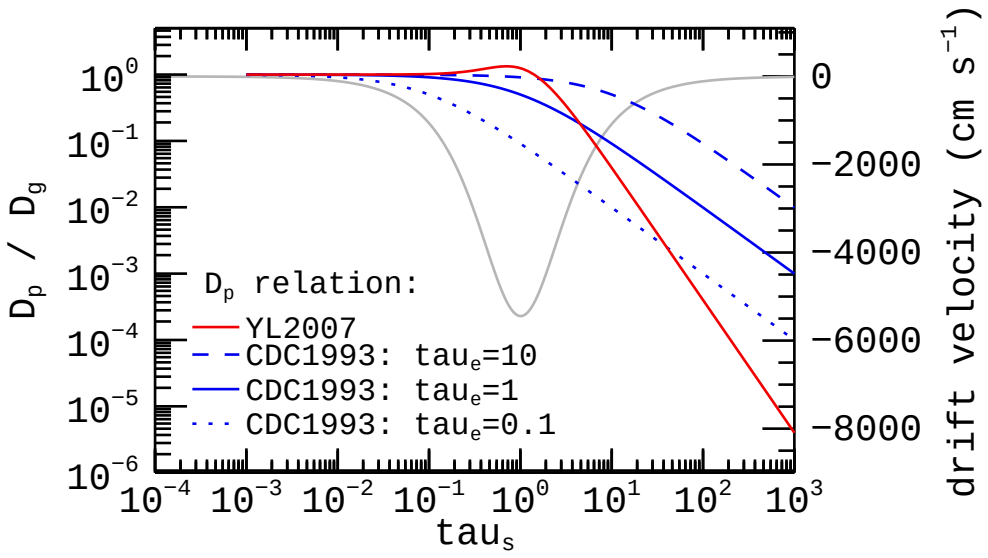

Figure 3.25: Comparison of the *Youdin & Lithwick* (2007) (red line) and the *Cuzzi, Dobrovolskis, & Champney* (1993) (blue lines) relations for the radial particle diffusivity in a gas disk as a function of the relative stopping time, τ_s. For isotropic turbulence, $D_{\rm p,YL2007}$ is independent of the eddy time, whereas $D_{\rm p,CDC1993} \propto \tau_e$. The grey curve plots an example of the radial-drift velocity of a particle (scale on the right-hand-side) as a function of $\tau_s = \pi s_{\rm d} \rho_{\rm d} / 2\Sigma_{\rm g}$.

forcing with the particle orbit. Figure 3.25 includes an example of the local mean-radial-drift velocity as a function of τ_s. Small τ_s occurs where the disk is denser, so toward smaller disk radii, and large negative values of the drift velocity correspond to rapid inspiral of the grain toward small R. Therefore, it is clear from this figure how grains may often be kept interior to regions of the disk where the two relations for $D_{\rm p}$ diverge.

Figures 3.26 & 3.27 demonstrate the negligible effect the difference between Equations (3.33) & (3.34) have on the results of my particle-transport simulations. Often, the eddy time is assumed to be equivalent to the orbital time, $\tau_e = 1$, and I have used this assumption for these simulations. Figure 3.26 plots $M_{\rm d,CDC1993}/M_{\rm d,YL2007}$, the ratio of the CDC1993-driven dust-mass distribution to the YL2007-driven distribution for the fiducial model of Chapter 6. The map is for R and t of the evolving disk, and the green regions correspond to $M_{\rm d,YL2007}/M_{\rm d,CDC1993} \sim 1$. The grey regions correspond to (R, t) with insufficient resolution to report results. Within the scatter of the simulations, the two diffusivity relations produce identical dust distributions. Figure 3.27 plots the average positions and fractions beyond 25 AU for the fiducial model of Chapters 4 & 5 for

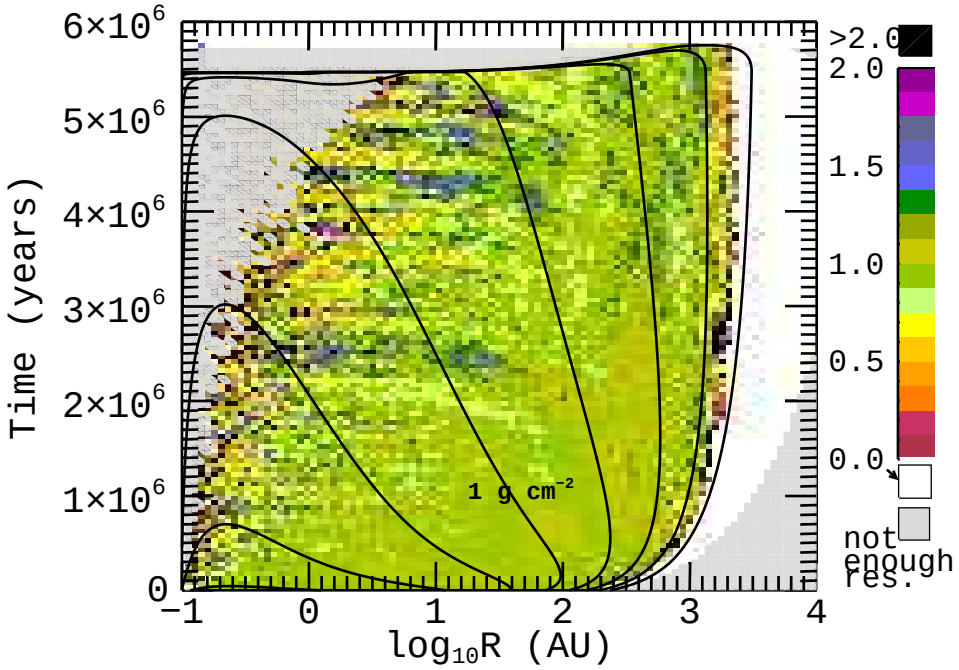

Figure 3.26: $M_{\rm d,CDC1993}/M_{\rm d,YL2007}$: A map in R and t of the ratio of the CDC1993-driven dust distribution to the the YL2007-driven distribution. Dust distributions simulated in the fiducial disk model of Chapter 6. Time-resolution of 25 points averaged per $\Delta t = 5 \times 10^4$ years. The black lines trace the evolving-disk gas–surface-density contours in orders of magnitude.

simulations using both diffusivity relations. Even for the largest particles, which are least-coupled to the gas motions, the two sets of results are identical within the noise. Therefore, while there is some disagreement over the correct relation to use for the particle diffusivity, for $\tau_e = 1$, the choice has no impact on the results presented in this thesis.

3.4 A Cartoon Model for Grain-Growth Constraints

Judging by observations, protoplanetary disks are sites for rapid growth of dust grains and also environments that harbor a significant small-grain population over a large fraction of their lifetimes (*Bouwman et al.*, 2003; *Kwon et al.*, 2009; *Sargent et al.*, 2009). Grains observed in the ISM are sub-micron in size (*Mathis, Rumpl, & Nordsieck*, 1977), while every disk for which we have observations shows signatures of grains that are microns, tens of microns, or even millimeters in size (*Testi et al.*, 2003). In the global-dust-distribution simulations presented in Chapter 6, I use a pair of cartoon

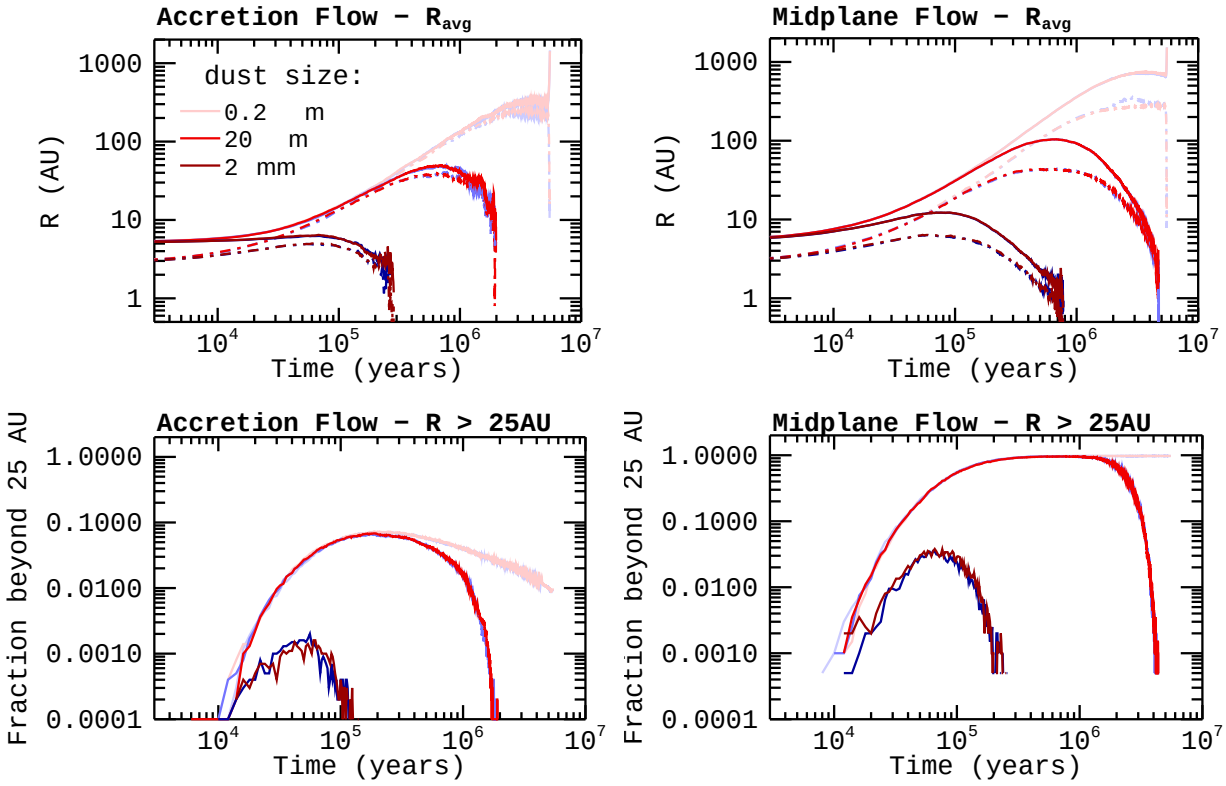

Figure 3.27: Simulations run for several particle sizes in the fiducial model of Chapters 4 & 5 for both the accretion-flow and midplane-flow gas-velocity cases. Red curves plot results using the YL2007-relation for $D_{\rm p}$ used throughout this thesis. Blue curves plot results using $D_{\rm p,CDC1993}$ with $\tau_e = 1$. Particles are initiated between 0.5 and 10 AU. Top panels show the average positions of particles (solid curves) and their RMS spread (dashed curves). Bottom panels show the fraction of the particles that are beyond 25 AU.

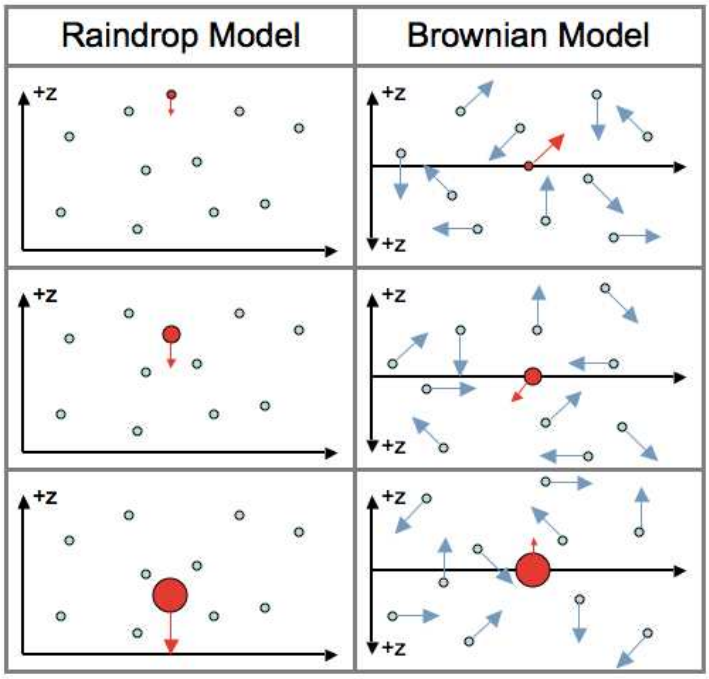

Figure 3.28: Depictions of grain growth in two cartoon models. The modeled, growing grain is highlighted in red, while the background grains from which it grows are shown in blue with black outlines. Arrows depict the relative magnitude and direction (random in the Brownian model) of grain motions. Growth in the raindrop model is dependent on grain height, z, above the disk midplane, while the grain growing in the Brownian model is assumed to exist always at $z = 0$.

models for the early stages of grain growth to place constraints on the timing for which larger particles (micron–centimeter sizes) may appear at various disk radii. The progression of grain growth for these two models is depicted in Figure 3.28, and in this section I outline how these models work, the physical mechanisms they do and do not describe, and how their depictions of grain-growth vary across different regions of the disk.

Aside from the supply of solid material from which to grow, the two most important parameters influencing grain-growth are the cross-sections for grain collisions, $\sigma_c\,(m_1, m_2)$, and the relative velocities of potentially-colliding grains, $\Delta v\,(m_1, m_2)$, (more generally, the velocity dispersion) (*Dullemond & Dominik*, 2005).

$$\frac{dm}{dt} \propto \sigma_c \Delta v\,. \tag{3.35}$$

For a solid-sphere representation of the dust grains, the collisional cross-section is given by *Dulle-*

mond & Dominik (2005)

$$\sigma_c = \pi \left(s_{d1} + s_{d2} \right)^2 \ , \tag{3.36}$$

where s_{d1} and s_{d2} are the radii of each of two colliding grains. Some sophisticated grain-growth models consider grain porosity and collisional compaction (e.g., *Ormel, Spaans, & Tielens* (2007)), but the cartoon models I use assume constant-density spheres.

Different regimes of grain-growth are largely described by the method that produces the colliding grains' relative velocity. My cartoon models for providing grain-growth/size constraints consider two methods separately. These methods are Brownian motion, where small particles have a large velocity dispersion due to their kinetic energy alone; and differential settling, where larger grains settle toward the disk midplane faster than small grains and so sweep up small grains in their path. For the cartoon models, I do not consider differential radial drift, turbulent coagulation, collisional fragmentation, or bouncing (collisions with zero-change in particle size). Many papers discuss these effects in detail (e.g., *Zsom & Dullemond* (2008); *Okuzumi* (2009); *Zsom et al.* (2010)). The main points to consider concerning their omission are:

* While the velocity dispersion due to **Brownian** motion decreases as grains grow, the dispersion due to **turbulent** motions increases for larger grain sizes (less well-coupled to the gas motions that are forcing them), allowing continued, efficient collision of equal-mass grains and rapid growth at larger sizes.

* Both fragmentation and bouncing lead to a maximum grain size above which particles do not grow. This tends to occur where grains are marginally coupled to the gas motions ($\tau_s \lesssim 1$).

* No single grain-growth process occurs in isolation. Therefore, models that consider only one type of coagulation will tend to underestimate growth rates, no matter the regime.

These are the limitations of using a cartoon-model for grain-growth. However, my needs for these models are only for setting relative thresholds for when larger grain sizes might appear in a disk, and so an efficient, simple model set is generally sufficient. They give me upper limits on the rapidity of grain-growth in the absence of turbulence.

The raindrop-growth model (so called because it mirrors the growth of raindrops falling through the atmosphere) has Δv due to differential settling and is described in *Dullemond & Dominik* (2005),

where its simplified nature is used to illustrate grain-growth processes. In true growth by differential settling, $\Delta v = |v_{\rm settle}\left(m_1\right) - v_{\rm settle}\left(m_2\right)|$ and so is strongly dependent on the local distribution (and vertical distribution) of grain sizes. However, the maximum rate of growth for a single dust grain via settling is easily defined by assuming that all other grains do not experience growth but remain small and perfectly suspended in (and mixed with) the disk gas ($\sigma_c = \pi s_{d1}^2$ and $\Delta v = |v_{\rm settle}\left(m_1\right)|$). In this limit, we have Equations (10) and (11) in *Dullemond & Dominik* (2005):

$$\frac{dz}{dt} = v_{\rm settle} = -\frac{3\Omega_K^2 z}{4c_s\rho_g\left(z\right)}\frac{m_1}{\sigma_c\left(m_1\right)} \tag{3.37}$$

$$\frac{dm_1}{dt} = Z\rho_g\left(z\right)\left|v_{\rm settle}\right|\sigma_c\left(m_1\right) \tag{3.38}$$

where z is the height above the midplane, ρ_g is the local gas density (vertically isothermal profile, as described in §2.2), $c_s = \sqrt{\frac{k_B T}{\mu m_H}}$ is the local sound speed, and Z is the assumed dust-to-gas mass ratio, set to $Z = 0.01$ for all runs of my cartoon grain-growth model. $v_{\rm settle}$ is defined for the case of Epstein drag. These equations are easily numerically integrated using the same integrator used for the force-balance–integrated radial dust-grain trajectories of §3.2.1. Figure 3.29 matches Figure 1 in *Dullemond & Dominik* (2005) and plots the change in z, s_d, and m for this raindrop–growth model using the parameters assumed in that paper. The initial grain size, $s_d\left(t=0\right)$, is varied, and while initially larger grains grow somewhat faster, the maximum size achieved by the time the grain reaches the midplane is the same for each $t = 0$ size.

For the Brownian-growth model, I use the same assumption that all background grains remain small, allowing only the particle-of-interest to grow. The collisional cross-section is defined as in Equation (3.36) (with $s_{d2} = 0.1\mu$m always) and the collisional velocity is set by Brownian motion:

$$\Delta v_{\rm B}\left(m_1, m_2\right) = \sqrt{\frac{8k_{\rm B}T\left(m_1+m_2\right)}{\pi m_1 m_2}}\,. \tag{3.39}$$

For this model, I keep the growing grain fixed at the midplane, where densities are highest and so growth is fastest, leading to

$$\frac{dm_1}{dt} = Z\rho_{\rm g,mid}\Delta v_{\rm B}\sigma_c\,. \tag{3.40}$$

Growth in the cartoon-Brownian-motion model is very rapid at small particle sizes when the velocity

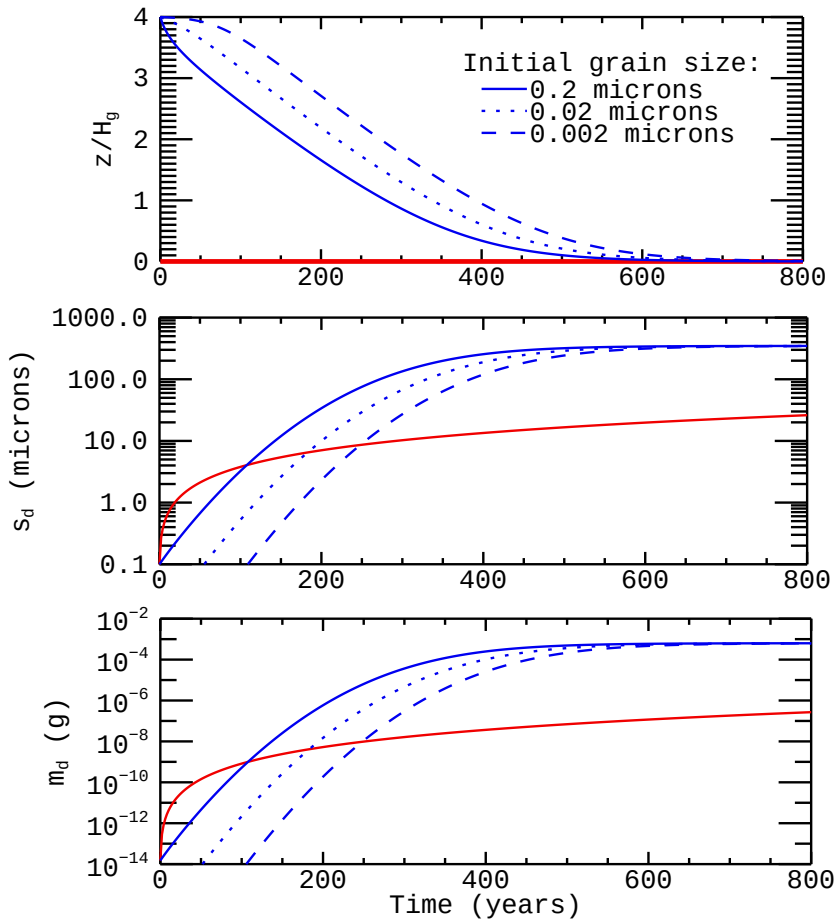

Figure 3.29: Grain growth in the simplified raindrop growth model depicted in Figure 3 of *Dullemond & Dominik* (2005) and using the simulation parameters of that paper: $z\,(t=0) = 4H_g$, $R = 1$ AU, $\Sigma_{\rm g} = 100$ g cm^{-2}, $T = 204$ K, $M_\star = 0.5 M_\odot$, $\rho_{\rm d} = 3.6$ g cm^{-3}, $\mu = 2.3$, and dust/gas-mass $= 0.01$. Raindrop-growth results are plotted for a range of initial particle sizes in blue. Growth with the Brownian-growth model ($s_{\rm d}\,(t=0) = 0.2\mu$m) for these models parameters is plotted in red for comparison.

dispersion is high and roughly equal-mass grains are colliding. However, even as the cross-section of the grain-of-interest grows, the mass flux continues to come from only very small particles. Therefore, Brownian-growth in this model is initially faster than raindrop growth. Raindrop growth tends to reach the larger sizes fastest, but ceases once the model-particle reaches the midplane, so if the cartoon-Brownian growth is allowed to persist for long periods of time, it will eventually surpass the raindrop model in maximum particle size.

In Figure 3.30, I plot raindrop growth and Brownian-motion growth using my cartoon models for a series of different parameters. For all, the initial particle size is 0.2 μm ($s_{\rm d,0} = 0.1\mu$m). My

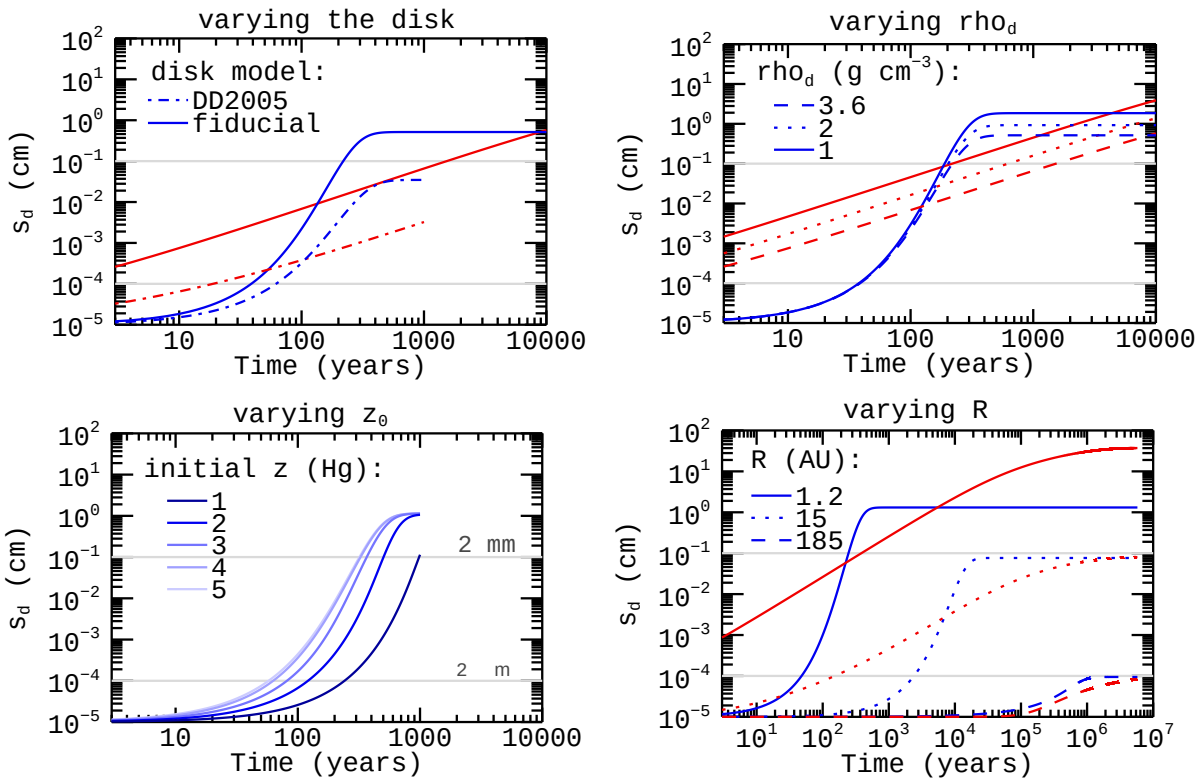

Figure 3.30: Grain growth using the two cartoon-grain-growth models. Blue: the raindrop growth model. Red: the Brownian-motion growth model. In the upper-left panel, I retain $\rho_{\rm d} = 3.6$ g cm^{-3} but compare growth in the *Dullemond & Dominik* (2005) setup to that in the evolving fiducial disk model of Chapter 6 at $R = 1$ AU. In that model (used in the rest of the panels), at 1 AU and $t = 0$, $\Sigma_{\rm g} = 1500$ g cm^{-2}, $T = 500$ K, $\mu = 2.34$, and $M_\star = 1 M_\odot$. In the lower panels, $\rho_{\rm d} = 1$ g cm^{-2}, and in the lower-left panel I plot only variations on raindrop growth as my cartoon Brownian-growth model assumes the particle remains at the midplane.

fiducial-model disks are denser and hotter than the disk model of *Dullemond & Dominik* (2005), and so grain-growth in them is faster. Like *Dullemond & Dominik* (2005), I find that fluffier particles ($\rho_{\rm d}$ smaller) tend to grow faster and larger due to larger collisional cross-sections. In the raindrop-growth model, grains grow the fastest and the largest if they are initiated at greater heights above the disk midplane, but this effect saturates at around $z\,(t = 0) = 4H_g$. And finally, because the inner regions of a disk are hotter and denser, they grow particles the fastest. In my Chapter 6 simulations, I combine runs of a number of different grain sizes. To do this, I define a series of radial zones and run these two cartoon-grain-growth models in each zone as the disk evolves. I then initiate each particle size of interest in each zone when either of the growth-models reaches that grain size or larger. Using this method, mm-sized grains are initiated no further out than 10 AU,

though they are observed in disks around other stars at hundreds of AU *Testi et al.* (2003).

3.5 Summary

In this chapter, I have outlined both the numerical setup for the particle-transport model that I use in my simulations, and the physical basis for its construction. This model operates by calculating the trajectories of an ensemble of simulation particles influenced by gas-drag advection and drift and by radial turbulent diffusion within the disk. My methods for calculating both radial-drift velocities and random-walk diffusion of the particle ensemble have been tested against direct force-balance integrations and analytical predictions, respectively, and have shown good fidelity to their test cases.

Considering radial transport of grains within a 1D disk model allows me to explore the interaction between disk evolution and the small-dust distribution without large computational expense. It does, however, require that I use single values (as a function of R) for the radial advection and gas-drag velocities, for which I have chosen the midplane values on the assumption that the bulk of both gas and solid material reside in the near-midplane zone. In reality, both the gas-velocity structure (likely) and the particle-drag velocities (definitely) vary with height above the disk midplane, possibly producing an outflow of some small fraction of larger grains near the disk surface layers. Taking a 1D (radial) modeling approach is considerably less computationally expensive than a 2D (radial,vertical) approach, but therefore probes only a subset of effects in terms of bulk gas-drag advection of particles.

Commonly, mixing simulations are performed in the fluid approximation for the dust distribution, so that the diffusion of individual grain populations is each modeled by a separate fluid-diffusion equation — much as the evolving disk surface-density is modeled as a viscously spreading fluid. This method makes it simpler to add source/sink terms to the dust distribution, but loses all information about the statistical history of individual grain motions and numerically must be carefully handled to avoid problems with mass conservation of the dust solids. By modeling the dust as an ensemble of particles, I am able to examine the spread of individual grain motions and to explore and compare mixing between populations originating in different regions of the disk within a single simulation calculation. This method also provides an additional check and perspective on results obtained using fluid-mixing calculations.

Chapter 4

Transport and Outward Mixing of Particles in Evolving Protoplanetary Disks: Implications for Results from *Stardust*

The majority of this chapter appears in *Hughes & Armitage* (2010).

Samples returned from comet 81P/Wild 2 by the *Stardust* mission confirm that substantial quantities of crystalline silicates were incorporated into the comet at the time of its formation. I investigate the constraints that this observation places upon protoplanetary disk physics, under the assumption that outward transport of particles processed at high temperatures occurs via a combination of advection and turbulent diffusion in an evolving disk. I also look for possible constraints on the formation locations of such particles. My results are based upon one-dimensional disk models that evolve with time under the action of viscosity and photoevaporative mass loss, and track solid transport using an ensemble of individual particle trajectories. I find that two broad classes of disk model are consistent with the *Stardust* findings. One class of models features a high particle diffusivity (a Schmidt number $\mathrm{Sc} < 1$), which suffices to diffuse particles up to 20 μm in size outward against the mean gas flow. For $\mathrm{Sc} \geq 1$ such models are unlikely to be viable, and significant outward transport appears to require that the particles of interest settle into a midplane layer that experiences an outward gas flow. In either class of models, the mass of inner disk material that reaches the outer disk is a strong function of the initial compactness of the disk. Hence, models of grain transport within steady-state disks underestimate the efficiency of outward transport. Nei-

ther model results in sustained outward transport of very large particles exceeding a millimeter in size. I show that in most circumstances, the transport efficiency falls off rapidly with time. Hence, high-temperature material must be rapidly incorporated into icy bodies to avoid fallback to small radii. I suggest that significant radial transport may only occur during the initial phase of rapid disk evolution. It may also vary substantially between disks depending upon their initial mass distributions. I discuss how my model may inform recent *Spitzer* observations of crystalline silicates in T Tauri star-disk systems.

4.1 Introduction

Comets are believed to be some of the most primitive bodies in the Solar System. As such, they preserve information about Solar Nebula conditions during the early stages of planet formation. Samples collected from the comet 81P/Wild 2 during the course of the *Stardust* mission show that the nonvolatile material of the comet is rich in relatively large grains (∼few–20 μm) of crystalline silicates (*Brownlee et al.*, 2006; *Zolensky et al.*, 2006; *Westphal et al.*, 2009). Crystalline silicates are not detected in the diffuse interstellar medium (ISM) and, although there is debate as to the formation mechanism of these grains in protoplanetary disks, they are not thought to form as far out in the disk as comet 81P/Wild 2 is believed to have originated. The *Stardust* results thus provide direct evidence for the outward transport of particles through protoplanetary disks. Spectroscopic observations suggest that similar processes may be widespread in T Tauri disks. *Spitzer* studies have revealed an apparent link between disk crystallinity, and grain growth and settling, but otherwise these disks exhibit a wide range of crystalline-to-amorphous silicate mass ratios and spatial distributions. This is suggestive of a great diversity in protoplanetary dust processing (*van Boekel et al.*, 2005; *Watson et al.*, 2009; *Olofsson et al.*, 2009).

Because no process has been proposed to form crystalline silicates out as far as the comet-forming regions, a mechanism is needed that can explain the presence of particles processed through high temperatures in cold regions of the Solar Nebula. One obvious possibility is radial mixing induced by turbulence. Turbulence is probably necessary for gas within the disk to accrete (*Shakura & Sunyaev*, 1973), and that same turbulence will result in diffusion of gaseous tracers and small particles coupled to the gas by aerodynamic forces (*Morfill & Völk*, 1984; *Clarke & Pringle*, 1988). It is unclear, however, whether turbulent transport suffices to explain the observations, or whether

other physical processes are also needed. Examples of such additional mechanisms include the ballistic launching of particles in a wind from near the inner edge of the disk (*Shu et al.*, 2001), photophoretic gas-pressure forces acting on grains in an optically thin disk (*Krauss & Wurm*, 2005; *Mousis et al.*, 2007), and radiation pressure on larger grains near the surface of the disk (*Vinković*, 2009).

The radial transport of both gaseous and particle species within a turbulent disk has been studied by several authors (*Gail*, 2001; *Bockelée-Morvan et al.*, 2002; *Keller & Gail*, 2004; *Boss*, 2004; *Dullemond, Apai, & Walch*, 2006; *Ciesla*, 2007; *Alexander & Armitage*, 2007; *Garaud*, 2007; *Boss*, 2008; *Dullemond et al.*, 2008; *Ciesla*, 2009; *Turner, Carballido, & Sano*, 2010). Here, I use a particle-based approach to model the advection and turbulent transport of non-interacting dust grains within evolving protoplanetary disks. My goals are to identify the conditions under which significant outward transport of particles can occur, bearing in mind the range of uncertainty in disk physics and evolution. I quantify the extent of radial transport as a function of the size of the grains, the initial compactness of the disk, the relative diffusivity of disk-gas tracers, and on the vertical profile of the gas flow and particle distribution. Initially compact configurations that expand rapidly appear to have the greatest promise to explain the *Stardust* results, though unambiguous predictions require accurate knowledge of the internal disk-flow structure and of crystalline-silicate formation mechanisms. I find that the importance of the advection of solids within the gas flow means that the outward transport efficiency drops significantly for larger particles (∼few millimeters), and at later times, thereby limiting the extent of mixing uniformity achievable within the disk.

In §4.2 I provide a summary of the relevant observations of silicates in both primitive Solar System bodies and in other protoplanetary disks. In §4.3 I describe the modeling setup used for these outward-mixing simulations. In §4.4, I step through a set of examples designed to illustrate the basic effects of various model parameters. In §4.5, I present and analyze results for a baseline case of particle transport in two scenarios of radial gas flow, then consider the effects of varying the size of the particles, the diffusivity, and the initial compactness of the disk. I present my conclusions in §4.6.

4.2 Observational Constraints

Observations of dust in the diffuse ISM show that the vast majority of silicates there are amorphous, with sub-micron grain sizes and a generally balanced Mg-Fe composition (*Molster & Kemper*, 2005; *Wooden et al.*, 2007). Therefore, the crystalline silicates that we observe in the Solar System and in disks around other stars are expected to have formed after the onset of the star-disk–system formation. Several mechanisms have been proposed: (1) The evaporation and condensation of silicate vapor, requiring gas heated to temperatures of $T \sim$ 1250–1450 K (probably at less than an AU from the parent star) (*Lodders*, 2003; *Gail*, 2004; *Wooden, Harker, & Brearley*, 2005; *Bell et al.*, 1997); (2) Annealing of amorphous silicate grains, requiring $T \gtrsim 1000$ K, (possibly occurring as far out as ∼2–3 AU in very hot, early disks) (*Nuth & Johnson*, 2006; *Wooden et al.*, 2007; *Westphal et al.*, 2009); and (3) Shock-heating and annealing in disk spiral arms. The first two of these are equilibrium processes, whereas the third relates to transient events that rely on the disk being massive enough to produce spiral arms. It may, however, result in the production of crystalline silicates out as far as 10 AU (*Harker & Desch*, 2002; *Scott & Krot*, 2005; *Wooden et al.*, 2007)[1]. These mechanisms have different chemical signatures. Grain formation in long-lived, high-temperature regions of the disk is most likely to produce Mg-rich silicates due to the low oxygen fugacity expected to prevail in those regions. Fe-bearing and Fe-rich crystalline silicates likely require a water-rich region of the disk in which to form, produced perhaps by migration and sublimation of icy bodies interior to the snow line, or in shocks in the outer disk (*Wooden*, 2008). They may also require transient heating mechanisms to form without evaporating, unlike Mg-silicates, which can crystallize below short-time-scale–evaporation temperatures (*Nuth & Johnson*, 2006). Pyroxene is thermodynamically favored over olivine when these minerals are formed by condensation, and, while annealing will tend to produce olivine from forsterite and pyroxene from enstatite, forsterite will convert to enstatite in long-lived ($\sim 10^6$ years to completion), high-temperature conditions (*Gail*, 2004; *Wooden, Harker, & Brearley*, 2005).

Observationally, it has been known for some time that Oort Cloud comets contain crystalline-silicate material (*Hanner et al.*, 1994; *Harker et al.*, 2002; *Honda et al.*, 2004; *Wooden, Woodward, & Harker*, 2004). These comets are believed to have formed primarily at distances of $\sim 5 - 10$ AU

[1]Note that although the strength of spiral shocks is expected to be greatest at many tens of AU (*Clarke & Lodato*, 2009), the gas in these regions is too tenuous and cold to anneal silicate grains.

from the Sun, in a region of the disk that may have overlapped that where in situ crystalline silicate formation was possible. The high amounts of crystalline silicates recovered by *Stardust*, nonetheless, came as a surprise, since 81P/Wild 2 is a short period comet, that most probably formed in the outer disk, around the current orbits of Uranus and Neptune (*Wooden, Harker, & Brearley*, 2005). This is beyond any plausible source region for crystalline silicates. Subsequently, observations of the comet 9P/Tempel 1 have confirmed crystalline silicates to be an important component of that Jupiter-family comet as well (*Lisse et al.*, 2006). The compositional evidence from the *Stardust* samples points to diverse formation environments for the high temperature materials (*Wooden*, 2008). A predominance of Mg-rich silicate grains, together with the recovery of three calcium-aluminum (CAI-type) minerals that almost certainly formed by evaporation and condensation at $T > 1400$–2000 K, suggest a substantial contribution from the innermost, hottest, disk regions. However, some Fe-bearing and Fe-rich crystalline silicates were also recovered. There are also hints of igneous and aqueous alteration among some grains (*Joswiak et al.*, 2010; *Stodolna, Jacob & Leroux*, 2010), which, if confirmed, would place additional constraints on the timing of the outward transport and incorporation of these materials into the 81P/Wild 2 cometesimals.

Direct comparison between the *Stardust* Solar System results and observations of other disks is difficult. Astronomical measurements are primarily sensitive to smaller orbital radii, and thus provide more important constraints on the degree and nature of processing than on radial transport. The observed mass ratio of crystalline-to-amorphous silicates varies greatly, both between disks (*van Boekel et al.*, 2005; *Watson et al.*, 2009; *Olofsson et al.*, 2009) and likely radially within a single disk (*van Boekel et al.*, 2004; *Olofsson et al.*, 2009). A study by *Watson et al.* (2009) measured crystalline mass fractions in the inner disks ($\lesssim$10 AU) of 84 classical T Tauri stars in the Taurus-Auriga star-forming region. The measured mass fractions ranged from less than 0.5% to more than 80% despite the fact that the systems were all of similar ages, 1–2 Myr, and all were observed within a single star-forming cluster. A significant correlation is observed between the crystalline mass fraction and the extent of dust settling toward the disk midplane. This may be related to the link other studies have found between disk crystallinity and grain growth (*van Boekel et al.*, 2005; *Olofsson et al.*, 2009), with characteristic crystalline grain sizes of a few microns. No correlations were found relating to the mass or luminosity of the star, the mass of the disk, or the mass ratio of the star-disk system, all properties expected to affect heating and thermal processing within the

disks. These results agree with a previous study of Herbig Ae-star disks by *van Boekel et al.* (2005) who found a correlation between disk crystallinity and stellar mass/luminosity that disappeared for $M_\star \lesssim 2.5 M_\odot$.

In terms of composition, silicates within other protoplanetary disks show the same predominance of Mg-rich grains as in the *Stardust* samples (*van Boekel et al.*, 2004, 2005; *Molster & Kemper*, 2005; *Watson et al.*, 2009; *Olofsson et al.*, 2009). There are also marginally significant correlations between crystallinity and stellar accretion rate. *Watson et al.* (2009) found that for pyroxene, the trend in crystalline mass fraction was inverse to the mass-accretion rate onto the star, whereas for olivine, the trend was proportional to the accretion rate. A study by *Olofsson et al.* (2009) found that disks of higher crystallinity tend to be dominated by enstatite (pyroxene-type) grains, and of lower crystallinity by forsterite (olivine-type) grains. *Olofsson et al.* (2009) also suggest very heterogeneous mixing of silicate particles in disks, reporting a higher rate of crystalline-feature detection for the cold ($\lesssim$10 AU) than the warm ($\lesssim$1 AU) spectral features. I will discuss later how some of these trends may be interpreted within the context of a turbulent transport model for grains within the disk.

4.3 Methods

The simplest model for studying the radial redistribution of particles within a disk assumes that the disk surface density is static and that the particles are small enough as to be perfectly coupled to the gas. Even in this limit, a range of other physical effects can be important and have been explored, e.g., mixing by (marginal) gravitational instability (*Boss*, 2004, 2008), the thermal evolution and production of annealed silicate grains (*Gail*, 2001; *Bockelée-Morvan et al.*, 2002), and vertical mixing and settling in an MHD model that includes dead-zone effects (*Turner, Carballido, & Sano*, 2010). Many of these studies agree that turbulent mixing can, in principle, be strong enough to explain the presence of crystalline silicates in comets.

My goal in this work is to systematically incorporate a range of additional physical processes into what is still a relatively simple one-dimensional model for the evolution of particles within a gas disk. I focus on three effects:

(1) Imperfect coupling of particles to the gas. The largest particles captured by *Stardust* (about

20 μm) may – depending upon the gas density – be only marginally well-coupled. Indeed, prior work that includes grain size and settling effects has found that large grains may settle out to the midplane and experience outward advection in a 2D stratified disk model (*Ciesla*, 2007, 2009). Here I consider imperfect coupling to examine the feasibility of transporting large grain sizes radially outward into the more tenuous outer disk and comet-forming regions.

(2) Disk evolution. The formation of material processed at high temperature almost certainly commenced early in the disk lifetime, when the disk would have been more massive, hotter, and more compact than the typical T Tauri disk. As I will show later, the evolution of such disks can have a substantial impact on the radial transport of particles. This has been demonstrated explicitly by *Dullemond, Apai, & Walch* (2006) and *Dullemond et al.* (2008), who found that disks that form in initially more compact configurations produce greater outward mixing of hot material.

(3) Uncertainties in the radial flow of gas at the midplane. Although the *vertically integrated* flow of gas in an active disk is assuredly inward at small orbital radii, the actual magnitude (and even direction) of flow at the midplane depends upon unknown aspects of the angular momentum transport within the disk. Indeed a flared viscous disk model with little to no vertical mixing yields an *outward* midplane flow (*Urpin*, 1984; *Takeuchi & Lin*, 2002; *Tscharnuter et al.*, 2009), which could be very important for the transport of particles large enough to have partially settled (*Keller & Gail*, 2004; *Ciesla*, 2007, 2009).

4.3.1 Model Disk Setup

For the work presented in this chapter, I implement these effects using the simplest-case–1D model for the gas-disk evolution. In this model, described in §2.2, the disk-temperature distribution is static, and everywhere $T \propto T_0 R^{-1/2}$ (T = 278.9K at 1 AU). This temperature structure is appropriate for a passive, flared disk after most of the gas infall has occurred and the initial rapid phase of accretion has slowed. Note that very-early disk temperatures are expected to be much higher (*Kenyon & Hartmann*, 1987; *Bell et al.*, 1997; *Tscharnuter et al.*, 2009). However, as described in §2.4, a more precise treatment of disk temperature requires models or assumptions involving, for example, disk chemistry and disk-forming infall rates. As described in §2.5, the

disk is chosen so as to be consistent with observational estimates of the lifetime and accretion-rate evolution of protoplanetary disks around low-mass stars, where final-stage clearing is effected by a 10^{42} photons s^{-1} EUV-flux-driven photoevaporation. I do not here study the evolution of particles *during* photoevaporation (long after the presumed epoch when crystalline material must have been incorporated into comets or their progenitor bodies); I include photoevaporation only because it is essential for providing reasonable model-disk lifetimes.

As discussed in Chapter 2, the disk-evolution model uses a non-steady $t = 0$ surface-density profile given by:

$$\Sigma_{\rm g}\left(R, t=0\right) = \frac{\dot{M}_0}{3\pi\nu}\left(1-\sqrt{\frac{R_{\rm in}}{R}}\right)\exp\left(-\frac{R}{R_{\rm d}}\right), \tag{4.1}$$

where where $\Sigma_{\rm g}$ is the surface density, t is time, R is radial distance from the central star, ν is the local disk viscosity, $\dot{M}_0$ is the $t = 0$ accretion rate onto the central star, $R_{\rm in}$ is the inner-disk boundary (set equal to the inner-grid boundary, $R_{1/2} = 0.099$ AU), and $R_{\rm d}$ is a variable controlling the compactness of the $t = 0$ profile. Having assumed $T \propto R^{1/2}$, Equation (2.9) for the disk viscosity leads to $\nu \propto R$. I adopt $\alpha = 10^{-2}$. This is also important for establishing the turbulent diffusion properties for the particle ensemble, as discussed in §3.3. In my fiducial-disk model, $R_{\rm d} = 20$ AU, and the initial disk mass of 0.03 $M_\odot$ dictates $\dot{M}_0 = 1.8 \times 10^{-7}\, M_\odot$ yr^{-1}. The evolution of this model is shown in Figure 4.1. Dissipation via photoevaporation occurs after ∼5.5 Myr.

In §4.5.4 I vary R_d (retaining $M_{\rm d,0} = 0.03 M_\odot$) to consider the effects of varied disk-forming conditions on the transport of particles. To facilitate a comparison with others' models, I also consider two models of dust motion within a static disk, including a steady-disk model where $R_{\rm d} = \infty$ (retaining $\dot{M}_0 = 1.8 \times 10^{-7}\, M_\odot$ yr^{-1}). As shown in Figure 4.1, this steady-disk model results in a disk profile that is matched to my $t = 0$ fiducial-disk profile in the inner-disk regions, but maintains a shallower profile and much larger gas surface densities in the outer disk.

The mean radial flow of gas experienced by solid particles within the disk depends on aspects of disk turbulence that cannot yet be predicted from first principles. The outward-mixing studies of this chapter maintain this uncertainty explicitly by considering two bounding cases for the gas flow, the predominantly inward "accretion-flow" case (Equation (2.55)) and the predominantly outward "midplane-flow" case (Equation (2.57)). Recall from §2.6 that the accretion-velocity case includes a region of outward-flowing gas in the outer disk where the disk is expanding, and that

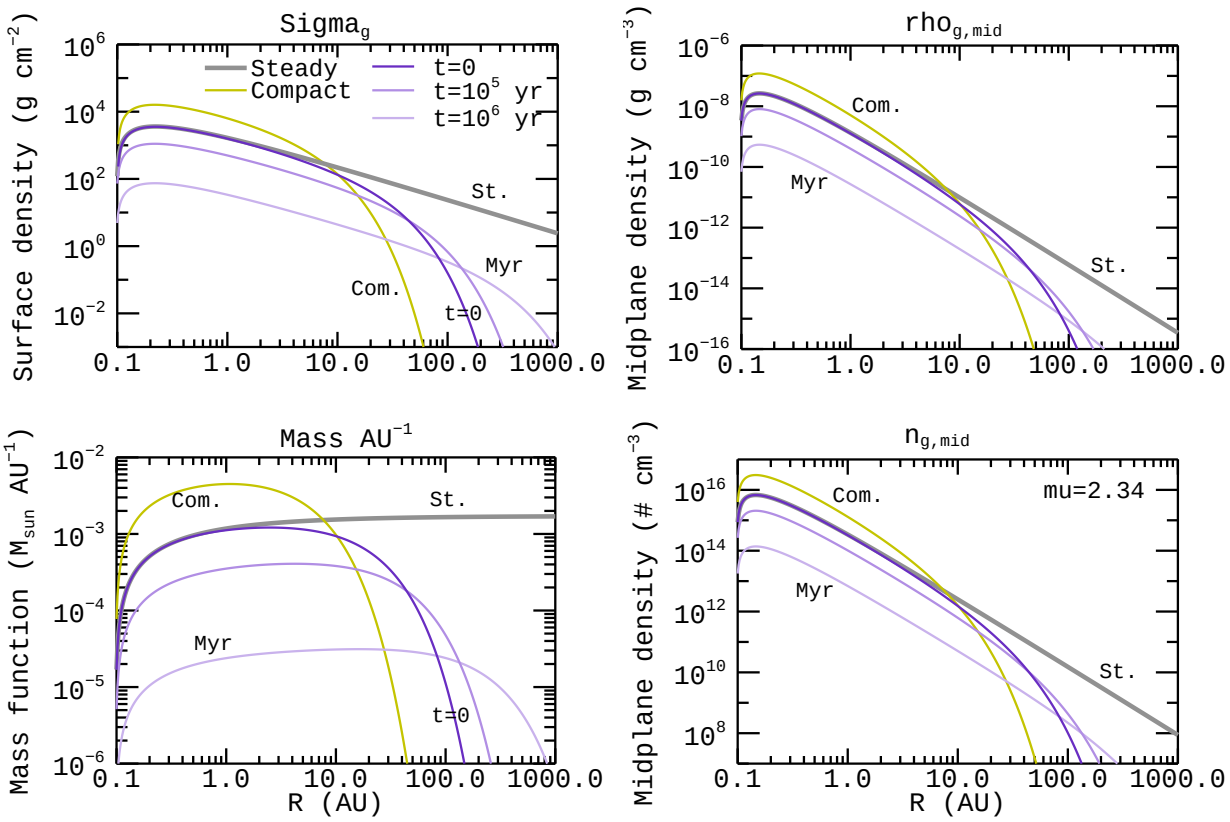

Figure 4.1: Plots of the local properties of the disk gas, including $\Sigma_{\rm g}$, the gas-mass distributions, $\rho_{\rm g,mid}$, and the local gas-particle number density at the disk midplane. The purple curves (A1, A2, A3) track the time evolution of the fiducial-disk model. The yellow curve (B) is the $t = 0$ profile for the most compact ($R_{\rm d} = 5$ AU) disk model. The thick grey curve (C) is the profile of the static steady-disk model.

the boundary of this region moves outward as the disk evolves and spreads. The transition from inward to outward flowing in the midplane-flow case, meanwhile, is roughly fixed at ~ 0.33 AU in the fiducial disk model. This flow is therefore highly conducive to the transport of inner-disk grains to the outer disk. Note, however, that the outward expansion of the disk dominates both velocity cases at large disk radii.

4.3.2 Particle Transport Setup

All of the particles run in these outward-mixing simulations are small enough that transport is calculated (following the methods outlined in Chapter 3) for the case of Epstein drag only. This does not, however, mean that the gas and dust motion are everywhere well-coupled; headwind drag dominates in the outer, tenuous regions of the disk.

The force of drag scales directly with the local gas density, ρ_g, and in my model, I assume that $\rho_g = \rho_{g,mid} = \Sigma_g/\sqrt{2\pi}H_g$, the gas density at the disk midplane. (H_g is the local scale-height of the disk gas.) In the accretion-flow case, inputting the midplane density into the drag-force equation is an approximation that selects for the tightest possible coupling between the gas and the particle ensemble at a given R; it leads to the most conservative estimate of outward mixing in this gas-flow case. However, the midplane density is the most appropriate choice for use in the midplane-flow case, which presupposes that the entire particle ensemble has settled to the disk midplane.

As discussed in §4.5.2 (and depicted in Figure 4.9), very small grains are well coupled to the gas flow, but the crystalline silicates larger than 10 μm associated with the *Stardust* collection are large enough that at large distances from the star (tens of AU) (and also at late times in the disk evolution) the dust motion significantly departs from the gas flow.

Turbulent diffusion of the particle ensemble is calculated as outlined in §3.3. In this chapter's fiducial models, I assume that because the disk viscosity is derived from turbulence within the disk, $D_g = \nu$, where D_g is the gas diffusivity. Recall that the dust (D_p) and gas diffusion coefficients are equal throughout most of the disk, except in the outermost regions where the gas surface density is very low, and D_p drops to zero. In §4.5.3, I vary $Sc = \nu/D_g$ to evaluate the impact of this assumption on the potential for the outward mixing of inner-disk grains.

4.4 Effects of Individual Transport Processes

To illustrate how each of the model components influences particle transport, I first consider a set of reduced models of successively greater complexity. I begin with a diffusion-only case for perfectly coupled particles, which I run keeping the gas disk profile fixed at its fiducial $t = 0$ form. I then add in the effects of radial gas velocity, particle size, and disk evolution. Unless otherwise stated, these simulations use 1000 particles initiated at 1 AU within the fiducial-disk model.

Figure 4.2 (a) displays an image of the relative number of particles in each radial bin over time for the diffusion-only simulation[2]. Diffusion results in rapid (within $\sim 10^5$ yr) radial spreading over tens of AU, such that the particle distribution closely approximates that of the gas within a fraction of the disk lifetime. While some particles become lost past the inner edge of the simulated

[2]Note that the bin size increases exponentially with R, so this representation looks somewhat different from a plot of the particle surface density or concentration.

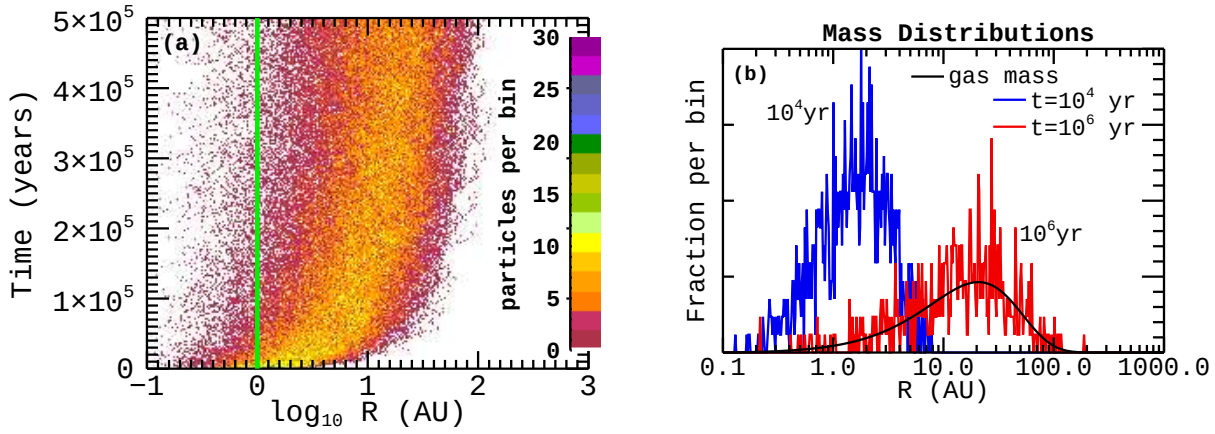

Figure 4.2: Basic diffusion: (a) Map of the number of particles per grid space as a function of radial position and time. I initiated 1000 well-coupled particles at 1 AU (denoted by the green line) in a static disk with zero radial-gas velocity. (b) The number of particles per radial grid space at two times, compared to the static gas-mass distribution ($t = 0$ profile of the fiducial-disk model). Vertical scale is arbitrary. Note that the gas-mass distribution appears to peak at a distance of several tens of AU from the central star. This appearance is an effect of grid spaces that increase exponentially in size with R. In fact, the gas-mass-per-AU function peaks slightly at around 2 AU, falls off gently in the main disk, and exponentially from beyond a few tens of AU

disk, the particle distribution comes to closely mirror that of the gas, as shown in Figure 4.2 (b).

Next, I include the effects of gas velocity by using the two cases for radial gas velocity, $v_{\rm acc}$ and $v_{\rm merid}$. The distribution maps for these simulations are shown in Figure 4.3 (a1, a2), and here the gross effects of mostly inward versus mostly outward gas velocities are clear. In the accretion-flow case, where most of the gas flow is inward, the majority of the particles are quickly lost onto the central star. Only ∼2% of the particles remain in the simulation after 10^4 years. However, the particles that do remain in the disk reach the outer-disk region and continue to move outward, because the steep gas distribution in the outer disk causes the accretion flow there to be outward. In the midplane-flow case, less than 10% of the particles are lost. Particles are instead swept rapidly outward with the gas flow and become trapped at the edge of the static disk-gas distribution, where the value of the disk surface density falls rapidly toward zero (at about 340 AU).

After turbulent diffusion and gas velocity, I add in the effects of particle size. The results of simulations using 20 μm particles are shown in panels-b1 and -b2 of Figure 4.3 . The effects of particle size are most clearly visible in the midplane-flow case where particles are still advected outward as before, but pile up at smaller radial distances (around 90 AU) than in the simulations with the well-coupled particles. What is happening here is that beyond ∼115 AU, the disk gas

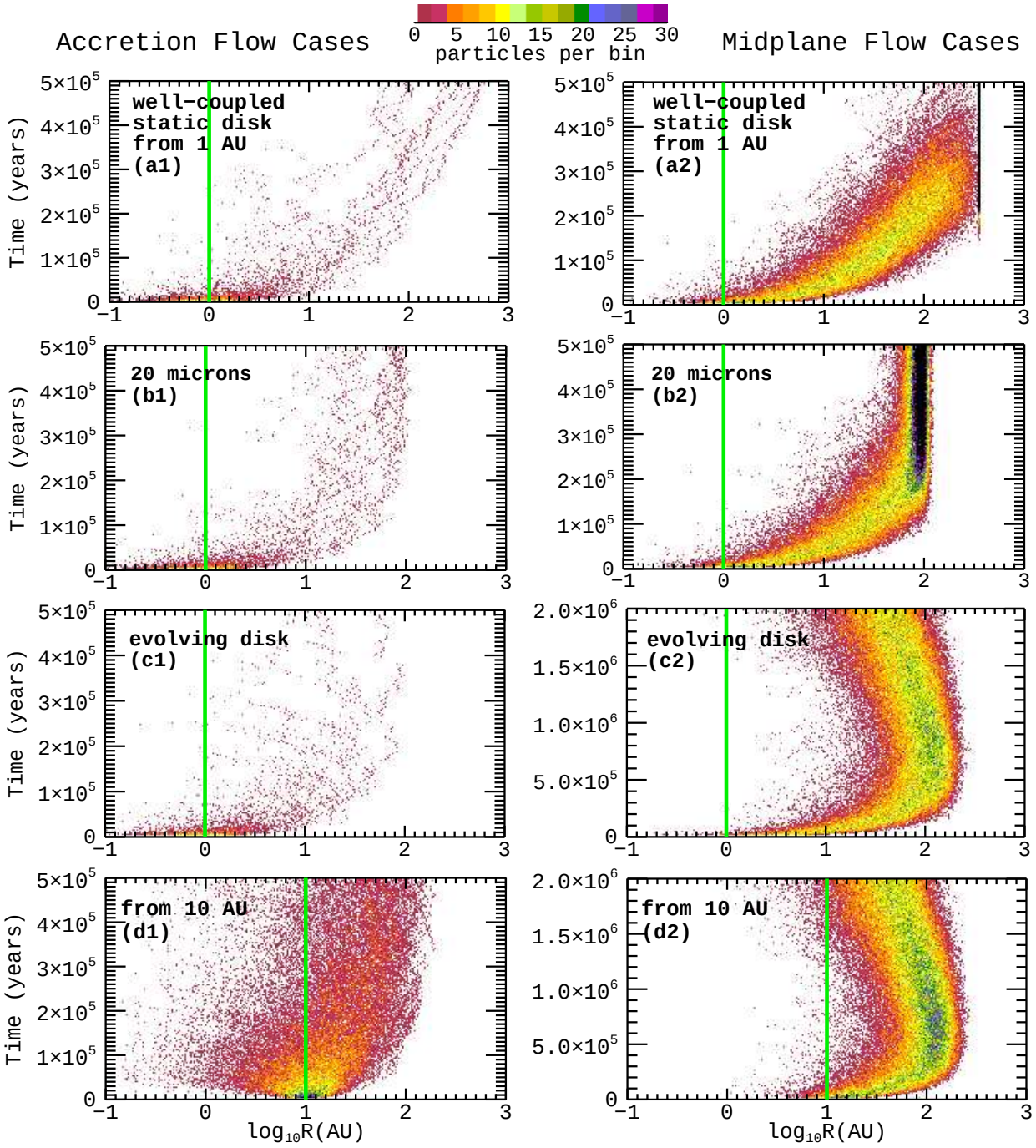

Figure 4.3: Diffusion scenarios: Maps of the diffusion of particles as in Figure 5.2(a) where the green line denotes starting location. The right-side panels all include gas velocity in the accretion-flow case, and the left-side are for the midplane-flow case. The simulations in (b1) and (b2) add in the effects of non-zero particle size. In (c1) and (c2) the disk surface density is also evolved with time, and the (d1), (d2) simulations are just like those above, but with the particles initiated at 10 AU.

is too diffuse to support the outward advection of particles of this size. Instead, headwind drag dominates the particle motion, pushing particles inward. In the accretion-flow case, the effects of a non-negligible particle size are similar. Though the dominant behavior of particle motion here remains the loss of most of the particles inward onto the parent star, those 20 μm particles that do reach the region of outward accretion flow are also confined to smaller radii than their massless counterparts.

Finally, I include the effects of disk evolution. As the disk evolves, the surface density drops. Panels-c1 and -c2 of Figure 4.3 show that in the accretion-flow case, this drop in density results in a sustained inward loss of the particles; in the midplane-flow case, the majority of particles are still retained and advected outward. In fact, some particles reach greater distances than in the static-disk model, because, as the disk expands, the surface density no longer drops off as steeply around 100 AU. However, after about $t = 0.5$ Myr, the decrease in disk surface density begins to dominate over the effect of the disk expansion. The gas can no longer support 20 μm particles at such large distances, and the particle distribution begins to move inward.

So far, I have presented simulations of particles initiated quite close to the parent star ($R = 1$ AU). In panels-d1 and -d2 of Figure 4.3 I see that if the particles are initiated further out in the disk, the particle motions are roughly the same, with the major exception that significantly more particles are retained in the accretion-flow case. For particles initiated at 10 AU in this case, about 60% remain in the disk after 10^5 years. In the midplane-flow case, particles initiated at 10 AU reach the furthest regions of the disk slightly faster, but otherwise behave the same as when initiated at 1 AU. Therefore, while both gas-flow cases can turbulently diffuse particles over wide regions of the disk, the accretion-flow case selectively retains particles initiated at larger radii and rapidly loses particles initiated at smaller radii.

To summarize, the basics of particle mixing in these transport simulations are that:

1. Turbulent diffusion rapidly spreads the particle distribution over many tens of AU.

2. Where advection tends toward the loss of particles inward onto the parent star, there will be a preferential rapid depletion in grains initiated close to the parent star.

3. Even in the case of outward-flowing disk gas (the midplane-flow case), small dust grains may still spiral inward at radii (or epochs) where the disk is locally tenuous.

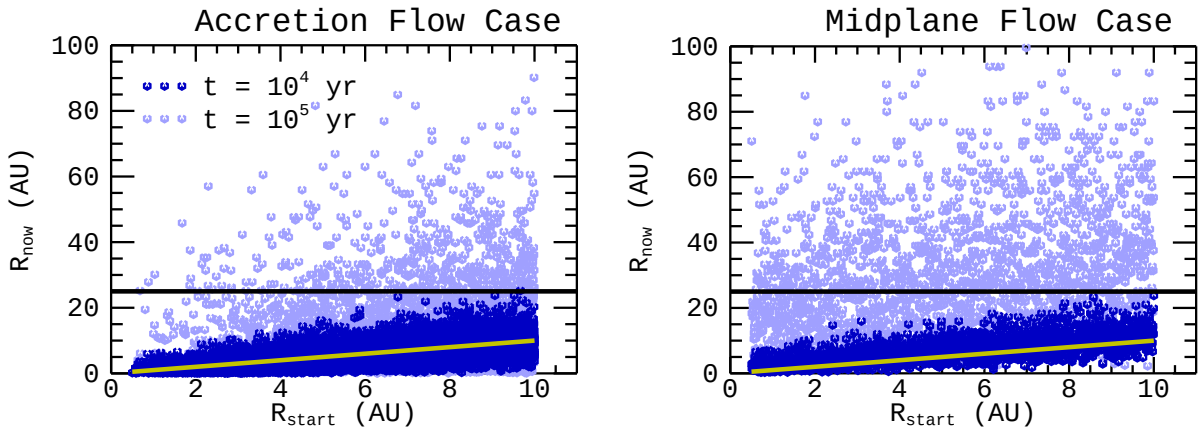

Figure 4.4: The position of 20 μm particles at two times in the fiducial-disk model plotted against their starting locations. The black line marks $R = 25$ AU, and the yellow line denotes the particle-starting locations (from 0.5 to 10 AU).

Figure 4.4, which plots particle positions versus their starting positions at two times, demonstrates how these effects will be reflected both in the availability of inner-disk particles in the comet-forming regions and in the source-region composition of those particles.

4.5 Results

In this section, I study how several parameters of the system affect the efficiency of mixing inner-disk particles out to large distances. The parameters examined include the structure/direction of the radial gas flow, the sizes of the dust particles, the diffusivity relative to the disk viscosity, and the initial distribution and evolution of the disk gas mass. I vary these parameters relative to a fiducial model that assumes 20 μm particles (all particle sizes assume a dust-particle internal density of 3 g cm^{-3}), a Schmidt number of $Sc = 1$ ($D_g = \nu$), and an evolving fiducial-disk model. The fiducial disk begins with a total gas mass of 0.03 $M_\odot$ and an exponential fall-off radius of $R_d = 20$ AU, so that at $t = 0$, 61% of the disk mass is concentrated within 20 AU of the star. All simulations presented here use $\alpha = 10^{-2}$.

In each model, the particles (10,000 for the accretion-flow runs, 2,000 for the midplane-flow) are initialized with a uniform radial distribution between 0.5 and 10 AU. Although this is not an exact match to the initial gas distribution at these radii, it allows me to fully sample the likely source regions for crystalline silicates within the disk. Figure 4.5 demonstrates how the evolution of the

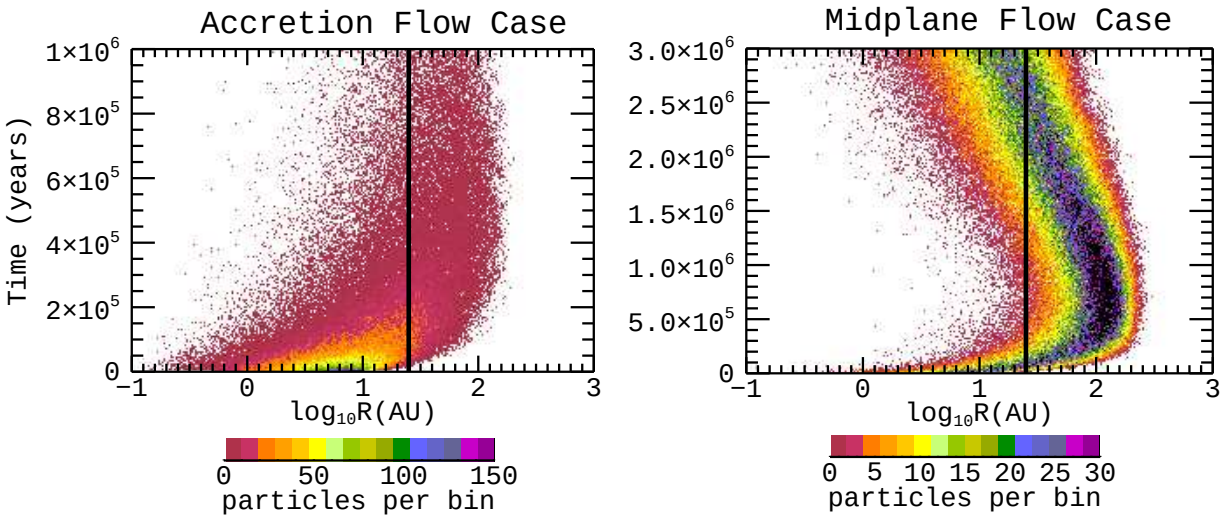

Figure 4.5: Map of 20 μm particles per bin for the fiducial disk simulations. Particles initiated between 0.5 and 10 AU. The black line indicates $R = 25$ AU. The accretion-flow simulations use five times as many particles as the midplane-flow simulations, so the color-scales have been adjusted accordingly.

particle distribution proceeds for this configuration of initial positions, in contrast to the R_0-fixed runs of Figure 4.3. I am interested, primarily, in the question of what fraction of these particles reach the "comet-forming region" (defined, for this paper, as the disk beyond 25 AU) at any time during the evolution of the disk. However, in some physical models, crystalline silicate formation is confined to smaller radial extents. Therefore, I also consider a subset of my simulation particles divided into three smaller source regions: the inner-quarter region (0.5–2.5 AU, 2106 particles in the accretion-flow simulations, 421 particles in the midplane-flow simulations), the inner-half region (0.5–5 AU, 4737 and 947 particles), and the outer-half region (5–10 AU, 5263 and 1053 particles).

The particle-transport simulations presented below were run on a 2.4 GHz Intel Core2Duo (used to run two simulations simultaneously when work-resource allocation permitted; my code does not use parallel processing). Run-time for a simulation depends primarily on particle size, as this affects the fraction and duration of simulation particles that persit within the disk throughout its lifetime. Runs with larger, 0.2 mm particles required roughly half-a-day of processing, while simulations of well-coupled, 0.2 μm grains required up to about five days. Simulations within a more-compact disk configuration run faster, roughly consistent with the shorter disk-lifetime of these systems. Also, particles persist for a smaller fraction of the disk lifetime in the accretion-flow cases simulations,

and so these simulations also tend to be slightly less computationally expensive.

4.5.1 Transport in Different Radial Gas-Flow Cases

Figure 4.6 shows the baseline results for particle mixing if the effective gas velocity seen by the particles is that of the accretion-flow case. I plot the fraction of 20 μm particles beyond 25 AU that originate from each of the source regions, together with the same quantity for perfectly coupled particles (i.e. of negligible size). I also show the *gas* fraction beyond 25 AU. As expected from the reduced models, diffusion is fast enough to mix some particles upstream into the comet-forming region. Indeed, the first particles pass 25 AU in less than 20,000 years. However, loss of particles by accretion onto the star is also rapid, especially close to the inner edge of the disk. After 10^5 years only ~30% of all 20 μm particles remain in the disk, and most of those originated in the outer half of my total source distribution (the peak fractions of particles in the comet-forming region are 2.6% from the inner-half zone, but 11% from the outer-half zone). The lifetime of particles that do manage to attain large radii is also limited, first by the fact that the transition radius that

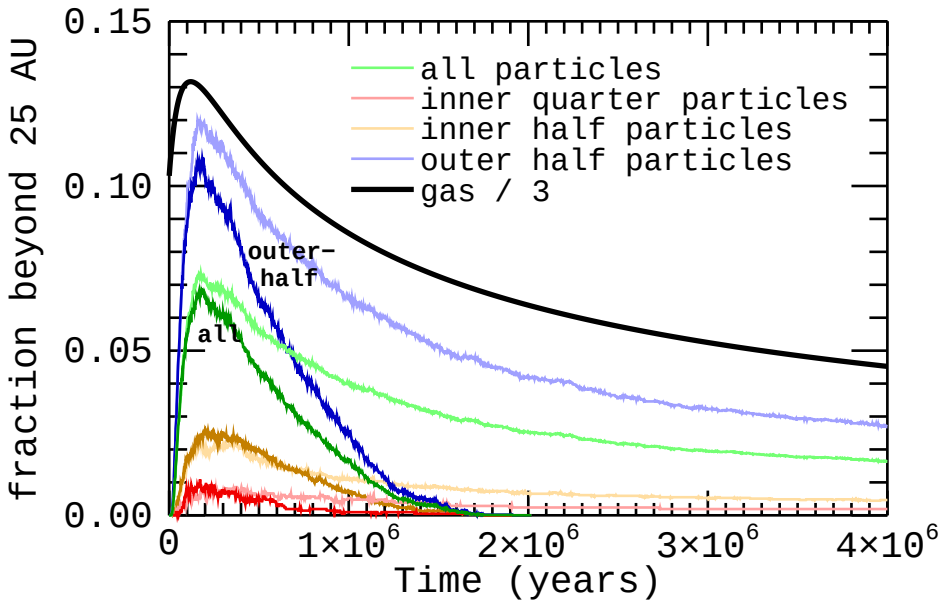

Figure 4.6: Fraction of simulation particles beyond 25 AU for different source regions compared to the fraction of the total disk gas mass currently beyond 25 AU (divided by three). Pale-colored lines denote particles well-coupled to the gas; dark colors denote 20 μm-sized particles. The inner-quarter source region is 0.5–2.5 AU; the inner-half source region is 0.5–5 AU; the outer-half source region is 5–10 AU. Simulation run in the fiducial disk model using the accretion-flow case.

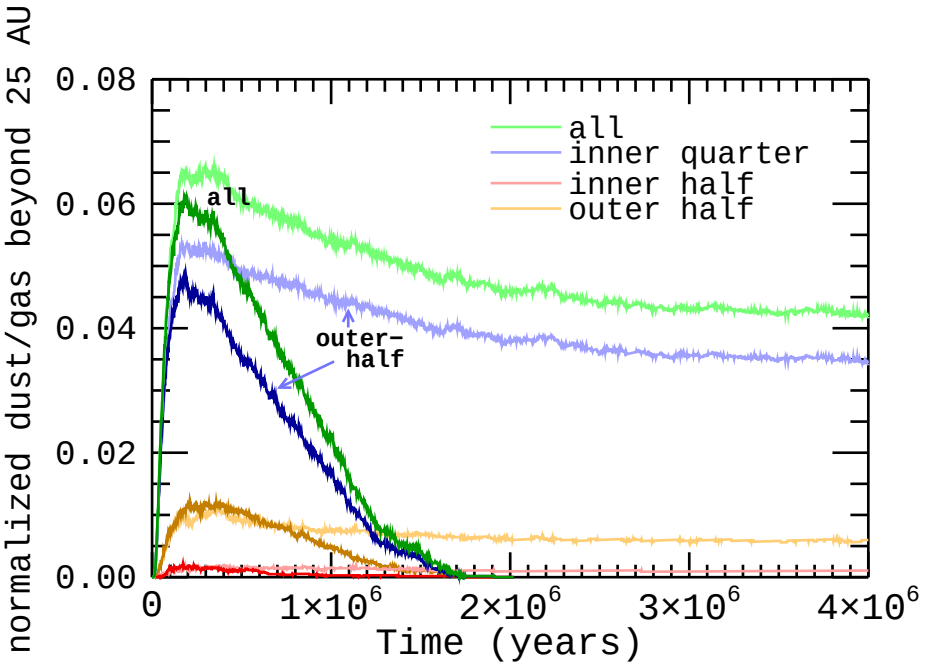

Figure 4.7: Normalized concentration of particles beyond 25 AU. [See Equation (4.2).] The pale-colored lines denote well-coupled particles. The dark lines are for 20 μm particles. Fiducial disk model. Accretion-flow case.

divides gas inflow from outflow itself moves out as the disk evolves, and second because declining gas densities in the outer disk eventually preclude retention of 20 μm particles. These effects mean that by $t = 10^6$ years, less than 1% of 20 μm particles exist in the disk beyond 25 AU, even if they started in the outer-half source region. By $t = 2.1$ Myr, all have been lost inward onto the parent star.

To quantify the effect of these mixing patterns on the abundance of hot, inner-disk grains in the comet-forming regions, I plot in Figure 4.7 the normalized concentration, C_N, of source-region particles beyond 25 AU as a function of time. I define the normalized concentration as the number of particles in a region divided by the gas mass in that region, then normalized by the initial number of source-region particles divided by the $t = 0$ gas mass of that source region:

$$C_N = \frac{(\text{number particles})_{\text{outer disk}} \,/\, (\text{gas mass})_{\text{outer disk}}}{(\text{number particles})_{\text{source},\, t=0} \,/\, (\text{gas mass})_{\text{source},\, t=0}} \tag{4.2}$$

With this definition, C_N is like a scaled dust-to-gas ratio, where $C_N = 1$ means that the ratio of

particles-of-interest–to–gas in the region of interest (the outer disk) is the same as where those particles originated at the time that they formed. I note that while the denominator of Equation (4.2) is almost constant across my source region (i.e. the initial dust to gas ratio is a fixed value to within 10%), the normalized concentration beyond 25 AU is an average over a broad region. The local values can vary widely, depending upon the parameters of the disk. For the accretion-flow case simulations, the highest local values of the normalized concentration typically lie just outside of 25 AU, with a lower local C_N in the regions hundreds of AU from the parent star.

From Figure 4.7, note that the peak values of the normalized concentration – and thus the maximum extent to which the outer disk can be contaminated by particles from the hot inner regions – is relatively modest. For 20 μm particles, the peak in C_N from the all source region is approximately 6%. This is actually higher than the value obtained from the outer-half source region, reflecting the fact that although a greater fraction of particles mix outward from the outer-half region, there is less total mass there to start with. Observe also that particle size strongly influences the lifetime of particles in the outer disk. For well-coupled particles, C_N declines only modestly from its peak at a few hundred thousand years out to several Myr. This reflects the fact that well-coupled particles that survive the initial evolution have thoroughly mixed with most of the entire disk gas mass, so that their subsequent loss is largely in proportion with the disk-gas accretion rate. By contrast, 20 μm particles are lost much faster, and only significantly contaminate the outer disk between $\sim 5 \times 10^4$ and 8×10^5 years.

Dramatically higher efficiencies of particle retention are obtained if, instead of experiencing the mean gas flow, $v_{\rm acc}$, the particles settle and experience an outward flow at the disk midplane (recall that this requires little or no vertical mixing of angular momentum, so that the steep radial density gradient at the midplane results in outflow). Results for this midplane-flow case are plotted in Figure 4.8. In this limit, few 20 μm particles are initially lost inward onto the parent star. 98% remain in the disk after 10^5 years, and around 90% of particles from each source region are transported to beyond 25 AU, with only a slight selection against particles from the innermost regions of the disk. This means that the normalized concentration curves for the different source regions are all nearly the same, only scaled relative to a given source region's innate ability to contaminate the outer disk - the relative fraction of $t = 0$ disk mass in that source region.

Because 20 μm and well-coupled particles are swept to large distances and remain there for

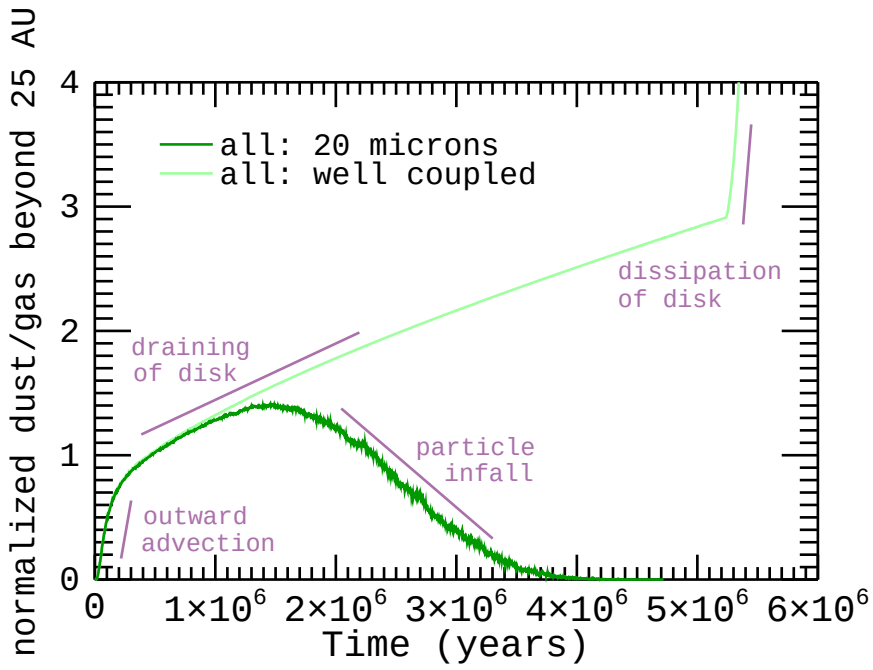

Figure 4.8: Midplane-flow case: Normalized concentration of simulation particles beyond 25 AU for all particles initiated between 0.5 and 10 AU. Fiducial disk model.

a long time, there is a period when the change of normalized concentration beyond 25 AU is a function solely of the loss of disk gas mass via accretion. Without the concurrent loss of accreting particles, the particle-to-gas ratio reaches values even higher than in the original 0.5–10 AU source regions. This is particularly so for the well-coupled particles, which never leave the outer disk once they have entered it. The normalized concentration of 20 μm particles drops to half-maximum at around $t \sim 2.6$ Myr, about three times the contamination time-window given in the accretion-flow simulations.

Note, however, that my model cannot account for the radial mixing that would occur in the presence of vertical mixing and a vertically stratified gas flow. If the gas flow is rapidly inward far from the midplane and outward near the midplane, then vertical mixing will lead to radial mixing, even in the absence of radial diffusion. *Ciesla* (2007, 2009) discusses in detail how a given degree of vertical mixing can lead to enhanced mixing of grain populations or to the partial segregation of inward-flowing and outward flowing populations. Therefore, the normalized concentration for the midplane-flow case merely represents the extreme upper limit on the extent and duration of the

contamination of the outer disk by inner-disk material.

The results imply that the efficacy of the fiducial disk model ($R_d = 20$ AU, Sc = 1) for outward transport of 20 μm grains depends upon both the location (and extent) of the the source region for crystalline silicates, and upon the radial gas flow experienced by the particles. In the accretion flow case, the peak of contamination of the outer disk (beyond 25 AU) would result in a crystalline-to-amorphous ratio of $\sim$6%. Attaining this limit requires that at $t = 0$ all silicate grains in the entire inner disk out to 10 AU were crystalline (and likewise assumes that all beyond that were amorphous). If, instead, the source of crystalline silicates is confined to inward of 2.5 AU then the peak C_N beyond 25 AU is only about 0.2%. Moreover, I find that even these modest degrees of contamination are relatively short-lived. 20 μm-sized grains (matched to the upper-size end of the *Stardust* grains) only have a contamination lifetime in the outer disk of $\lesssim 1$ Myr. Unless the timing of the epoch when grains became assembled into cometary material happened to coincide with the peak of the contamination, the crystalline fraction would be diluted, either by grains grown locally in the cold comet-forming region or by those raining inward from the even-colder outer regions of the disk. Finally, my results for the accretion flow case might be yet further reduced by the fact that some crystalline silicate formation mechanisms may not yield 100% crystalline fractions out to large radii. For example, if the primary source of crystalline silicates is shocks out to $\sim$10 AU, but a sizable fraction of silicates in that region remain amorphous, then that cuts into the potential maximum in the crystalline-to-amorphous ratio produced in the outer disk.

In the midplane-flow case, on the other hand, substantial outward transport can occur almost irrespective of the location of the source region. If there is an outward flow of gas at the disk midplane, then grains that are sufficiently well-settled will readily reach large distances (*Ciesla*, 2009). An outward-midplane flow also allows material that has been transported outward to persist there for a longer period of time. My midplane-flow simulations produce an upper-limit maximum C_N in the outer disk of 30% for the inner-quarter source region. Even if vertical mixing means that only a fraction of the maximum can be achieved, it is still plausible to believe that the CAI-like grains captured during the *Stardust* mission may have reached the outer disk via mixing within the disk gas alone. This scenario may also be consistent with the observations of *Watson et al.* (2009), who find higher crystalline-to-amorphous silicate mass ratios in disks where the grains appear more settled toward the disk midplane, and of *Olofsson et al.* (2009), who find that possibly a large

fraction of crystalline silicates exist in the outer regions ($\lesssim$10 AU versus $\lesssim$1 AU) of some disks.

4.5.2 Transport of Differently Sized Particles

In §4.4, I demonstrated that non-negligible particle size bars particles from the outermost regions of the disk, because at large distances, the gas is so tenuous that the particles decouple from the gas motions, and inward-pointing head-wind drag dominates. Figure 4.9 plots the dust-mean-radial velocities for several different particle sizes in the fiducial-disk model at $t = 0$ for the accretion-flow case. (In the midplane-flow case, the curves are similar, only shifted toward outward velocities, as in Figure 3.9 and following the pattern of Figure 2.14.) Though turbulent diffusion can send particles upstream of their average radial-velocity flow, grains are effectively barred from the regions of the disk beyond where their average-radial velocity falls to large, inward-pointing values. It is clear from Figure 4.9 that the range within the disk that dust grains may occupy depends strongly on the particle size, and that the mixing achievable out to the comet-forming regions will become sharply limited as one approaches millimeter particle sizes. Also, where this cutoff occurs varies, not only in time as the disk thins, but also from disk to disk depending on the total mass and mass distribution of each system.

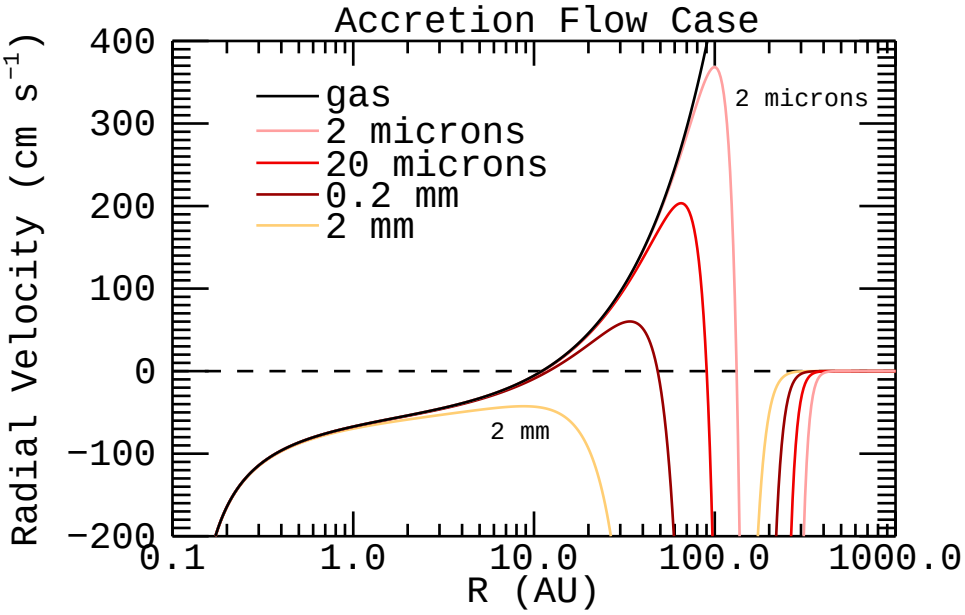

Figure 4.9: The mean-radial velocity of particles of different sizes in the fiducial disk model at $t = 0$, accretion-flow case. Sizes listed assume an internal-particle density of 3 g cm^{-3}.

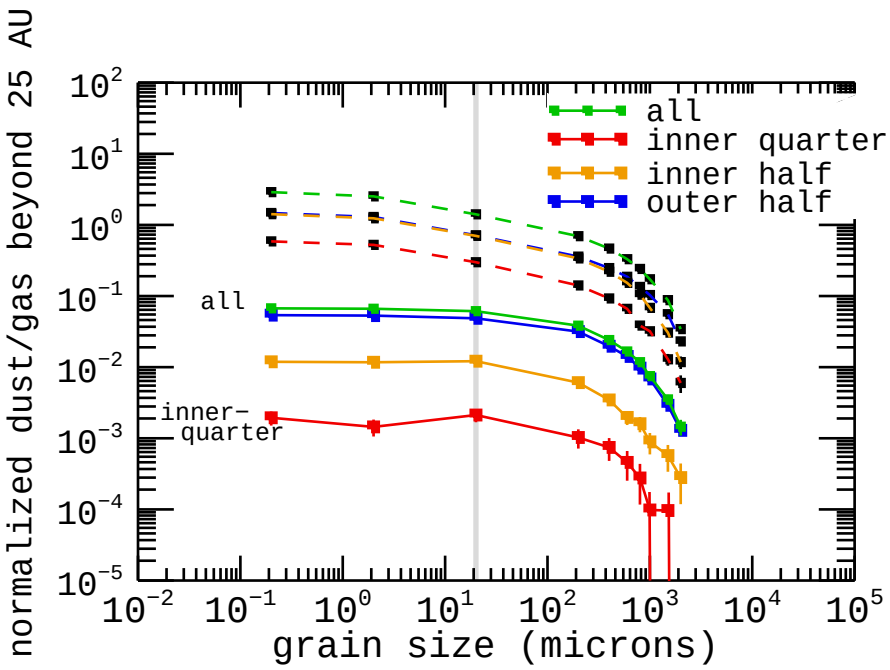

Figure 4.10: Maximum values of normalized concentrations beyond 25 AU as a function of grain size. Solid lines denote simulations run in the accretion-flow case; dashed lines with black markers denote the midplane-flow case. Error-bars mark the $\sqrt{N}$ noise of the peak values. Fiducial disk model. Grey line marks the baseline case of 20 μm-sized particles. In the midplane-flow case for the smallest particles, peak values shown are for $t = 5.2$ Myr, just prior to photoevaporative dissipation of the disk.

I parameterize the outward mixing of grains as a function of size by plotting in Figure 4.10 the peak values of the normalized concentration of grains beyond 25 AU as a function of grain size. The error bars show statistical errors based on the number of particles beyond 25 AU in each run. I plot the maximum values of C_N from each of the different source regions, as well as the upper-limit values provided by the midplane-flow simulations (dashed lines with black markers). While the magnitude of outward mixing varies by orders of magnitude across these populations, the trends with grain size are the same across all sets: as seen previously, the highest normalized concentrations of inner-disk particles in the outer disk occur for the smallest grain sizes, up to a few tens of microns, and the peak-C_N values drop off sharply at around millimeter grain sizes. The results of *Ciesla* (2007, 2009) for a vertically stratified disk flow suggest that the loss of larger grain sizes may be partially mitigated by settling toward the midplane, thereby increasing the relative outward transport and retention of these particles. Still, the concurrent drop in my midplane-flow upper-limit concentrations suggests that this can only hold back the loss of large grains from the

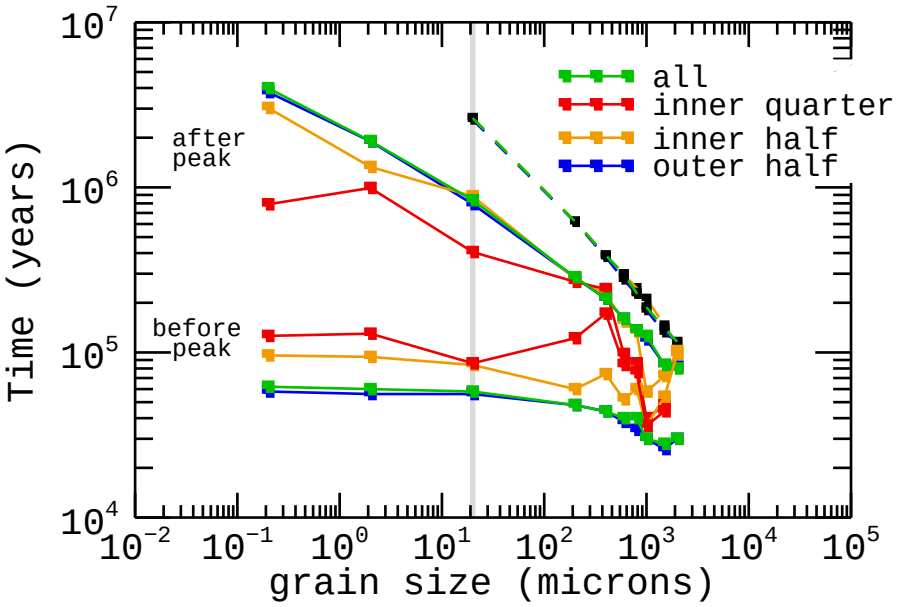

Figure 4.11: Time-windows for the peak values of normalized concentrations beyond 25 AU as a function of grain size and for different source regions. The lower set of solid curves mark the latest pre-peak time of half-maximum concentration in the accretion-flow case. The upper curves mark the earliest post-peak time of half maximum concentration for the accretion-flow case (solid lines) and the midplane-flow case (dashed lines with black markers). Fiducial disk model. In the midplane-flow case, the smallest particles remain in the outer disk longest and never drop below half-maximum concentration beyond 25 AU.

outer disk to a point. For 2 mm-sized particles, for example, even the midplane-flow runs yield a peak normalized concentration beyond 25 AU for all simulation particles of only ∼3.4%.

The other important variable to consider is the timing of these mixing events. In Figure 4.11, I depict, as a function of particle size, the time-frame over which the normalized concentration of inner-disk particles in the comet-forming region is at a value of half-maximum or greater. For each source region (for the accretion-flow case simulations) I plot the latest time of half-maximum concentration prior to the peak and the earliest time of half-maximum after the peak. (Due to limited particle statistics, some of these quantities are quite noisy.) I also include the boundary of post-peak half-maximum concentration in the midplane-flow simulations to illustrate when headwind-drag inspiral will overwhelm other physical effects even in the most extreme gas-flow scenario.

Figure 4.11 demonstrates that the smallest inner-disk particles remain mixed into the outer disk for millions of years, and that even inner-disk grains as large as 20 μm may be noticeably present at

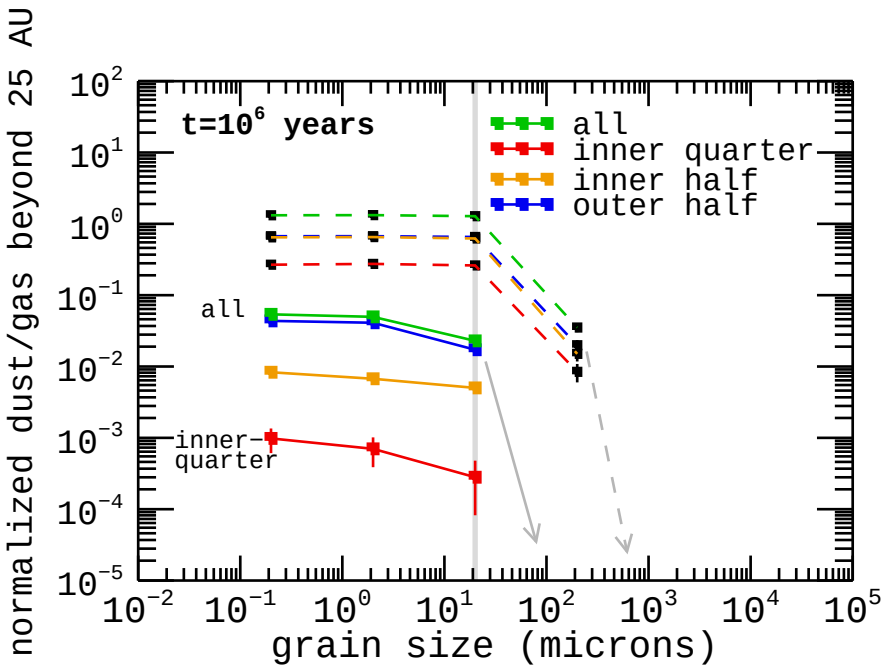

Figure 4.12: Normalized concentration beyond 25 AU at $t = 1$ Myr as a function of grain size. The largest particles are all depleted from beyond 25 AU by 1 Myr. Dashed lines with black markers denote the midplane-flow simulations. Fiducial disk model.

large distances for ∼1–2 Myr. However, while the mixing of all grains outward is relatively rapid in these simulations, not only do the larger particles experience relatively less outward mixing, but that mixing is similarly short-lived. Even in the midplane-flow simulations, post-peak half-maximum concentration is reached by $t \sim 6.2 \times 10^5$ years for 0.2 mm particles and as soon as $t \sim 1.1 \times 10^5$ years for 2 mm particles. The fact that larger inner-disk particles are short-lived in the outer disk is demonstrated more bluntly in Figure 4.12, where I plot the normalized concentration as a function of grain size at $t = 1$ Myr. While the mixing effects are relatively uniform for small particles at this time, no particles 0.2 mm and larger remain in the outer disk in the accretion-flow simulation, and the upper-limits of the midplane-flow simulations suggest that even in that extreme those large-grain populations are in rapid decline, if not already disappeared.

These results imply that it is the upper envelope of particle sizes recovered by *Stardust* that provides the most stringent constraints on disk evolution and particle transport. In my simulations, particles at least as large as 2 μm appear to behave as though well-mixed with the disk gas. Therefore, the presence of high-temperature particles in this size range within a Jupiter-family comet

can be largely explained by outward mixing of disk material aided by some disk expansion from an initially compact state. However, the particles recovered by *Stardust* include crystalline silicates as large as 20 μm. While the outward transport of 20 μm particles to the comet-forming region does occur in my models, these particles do not remain well coupled to the disk gas indefinitely. This suggests that either (1) mixing of particles and planetesimal formation in the Solar Nebula occurred in a disk massive enough for 20 μm particles to remain well coupled to the gas motions, or that (2) the formation of comets or cometesimals occurred within the first million years or so of disk evolution. This second constraint may be in agreement with *Stardust* results. Early studies found no aqueous minerals in the *Stardust* materials, suggesting that the outward transport and incorporation of these materials into the 81P/Wild 2 cometesimals occurred very early, before the primary accretion and fragmentation of the chondritic-asteroid parent bodies (*Wooden*, 2008). However, the possible identification of igneous materials in the *Stardust* samples may contradict this scenario or else put interesting time-line constraints on the formation time-scales of planetesimals and cometesimals across the range of Solar System radii (*Stodolna, Jacob & Leroux*, 2010; *Joswiak et al.*, 2010). Another constraint linked closely with time is the large-end grain size for which my model predicts measurable outward mixing. Not only do the peak (and midplane-flow–upper-limit peak) values of C_N beyond 25 AU drop off markedly for grains a few millimeters in size, but the time-frame for that outward transport is also restricted (to barely more than 10^5 years for 2 mm-sized grains), so that comet-formation would have to be quite rapid to capture such large inner-disk grains if they did appear in the comet-forming regions.

The transport of different-sized particles is also of interest for models that include the effects of grain growth. Some observational studies of disks suggest a link between disk crystallinity and grain growth (*van Boekel et al.*, 2005; *Olofsson et al.*, 2009), with characteristic crystalline grain sizes of a few microns (distinctly larger than typical ISM grains). At the very least, grain growth and crystallization likely occur on similar time scales. The results presented here suggest that as dust grains grow, they should become less likely to enter and more likely to leave the outer regions of the disk. Large grains become mostly confined to small disk radii where the disk gas is still dense enough to support them. We know that growth at centimeter and meter scales poses a constraint to disk models and planetesimal formation, because particles of this size are expected to fall inward toward the parent star very rapidly, depriving the disk of these solids. However, growth

to millimeter scales may also place constraints on cometesimal formation if the outer regions of the disk cannot support particles of even these sizes. At the very least, it could restrict the composition of bodies formed in the outer disk, if most of the particles available are those falling inward from large AU.

4.5.3 Transport Varying the Diffusivity

Next, I explore how the outward mixing of inner-disk grains depends on the Schmidt number, which is the ratio of the disk viscosity to the gaseous diffusivity (so that a lower Schmidt number means more relative diffusivity.) In *Pavlyuchenkov & Dullemond* (2007) the authors argue for an Sc lower-limit of 1/3. Therefore, I have run simulations of particle transport varying the Schmidt number by a factor of three, and in Figure 4.13 I plot the values of maximum normalized concentration beyond 25 AU for four particle sizes and two source regions as a function of Sc. The primary effect shown in Figure 4.13 is that a higher diffusivity can lead to a substantially higher degree of outward transport in the general accretion-flow case of my particle-transport simulations. Here there are variations of an order-of-magnitude or more in the peak outer-disk normalized concentrations between the

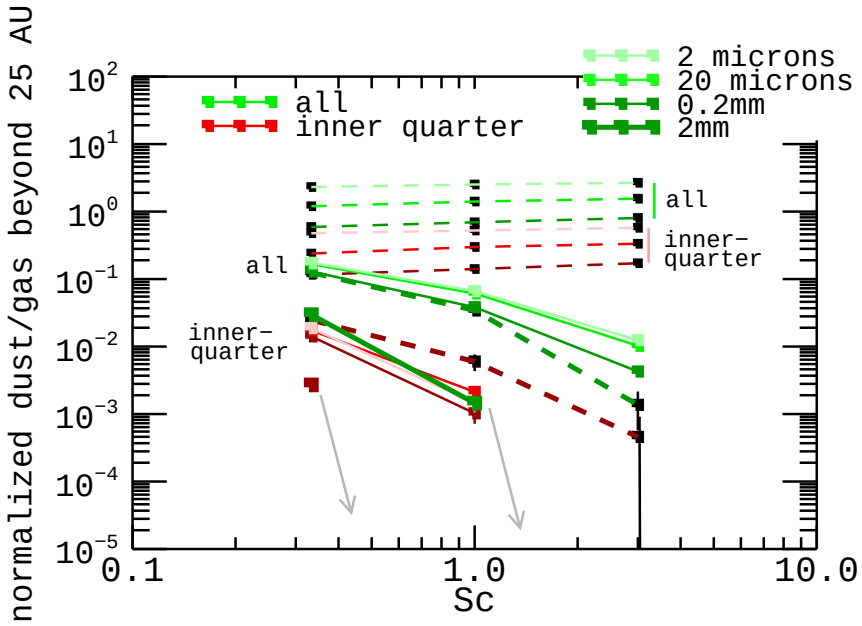

Figure 4.13: Maximum values of normalized concentration beyond 25 AU as a function of Schmidt number for a range of grain sizes and two source regions. Low diffusivity (large Sc) tends to restrict particles from reaching the outer disk. Dashed lines with black markers denote the midplane-flow simulations. Fiducial disk model.

highest ($Sc = 1/3$) and lowest ($Sc = 3$) diffusivity simulations across the range of particle sizes considered. This is less than the variation predicted in the model scenario of *Pavlyuchenkov & Dullemond* (2007) ($\sigma_{Sc=1/3}/\sigma_{Sc=3} \propto (R/R_{\rm source})^4$), but is still quite a substantial effect considering that my normalized concentrations are reported for the whole of the outer disk and that my pool of contaminants is limited to those present in the source regions at $t = 0$ only.

More generally though, the Schmidt number controls the relative importance of advection versus diffusion of particles. When the diffusivity is low, advection dominates, so that more grains reach the outer disk if the bulk flow is outward, and fewer do so if their bulk flow is inward (including the case of 2 mm particles in the outward-flowing–gas midplane-flow case whose radial advection is dominated by headwind drag). Conversely, high diffusivity pushes the system in the direction of a flow-independent state where diffusion, both within the disk gas distribution and inward onto the parent star, is the dominant term. The diffusivity can also have an important effect on outer-disk contamination from the inner-most source regions. For 20 μm-sized particles from the inner-quarter source region, $Sc = 1/3$ simulations produce a peak normalized concentration in the comet-forming region of 1.7%, up from 0.2% in the baseline $Sc = 1$ simulations. In the low-diffusivity simulations inner-quarter source grains of all sizes are completely absent from the comet-forming region unless directly advected there by outward-flowing gas in the midplane-flow simulations.

Finally, to some degree, the diffusivity also affects the timing of outward mixing. This is plotted for 20 μm-sized particles in Figure 4.14. The higher diffusivity simulations allow higher normalized concentrations in the outer disk to occur sooner and to last longer ($\sim 4 \times 10^4$–1.1×10^6 years half-max to half-max), whereas for lower diffusivity the outer-disk normalized concentration peaks later and more briefly ($\sim 9 \times 10^4$–5.5×10^5 years).

My results for the variation in transport efficiency with Schmidt number suggest that two distinctly different disk models could be consistent with observations. One possibility is that the diffusivity is high, as suggested by *Pavlyuchenkov & Dullemond* (2007). In this case, it seems plausible that a significant fraction of grains, formed in high temperature regions close to the star, can end up in the comet-forming region, even if the disk is highly turbulent and no significant settling occurs. The recovery of CAI-type grains by *Stardust* – whose condensation requires especially high temperatures – poses the strongest constraint on this scenario, and I have not demonstrated explicitly that it is possible. However, given that the early disk was certainly hotter than the disk

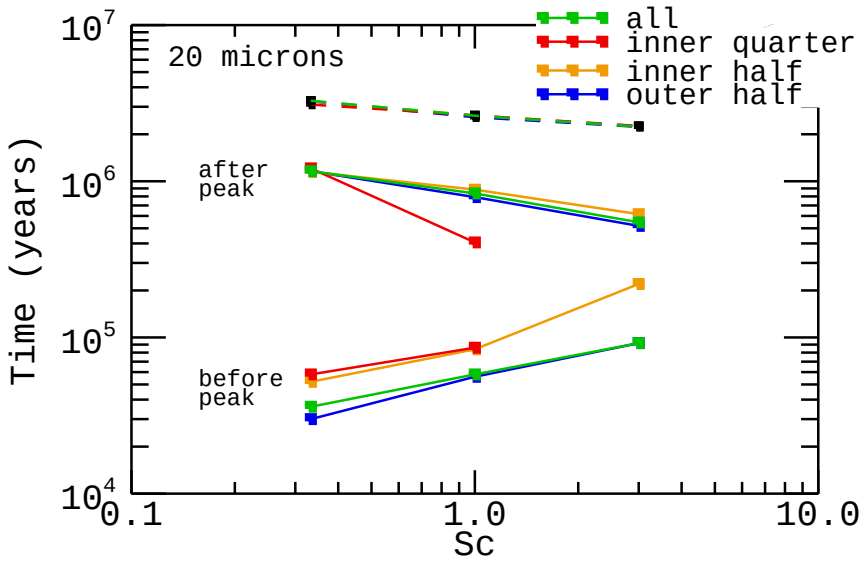

Figure 4.14: Time-windows for the peak values of normalized concentration of 20 μm particles beyond 25 AU as a function of Schmidt number ($Sc \equiv \nu/D_g$). Lower solid curves mark the lastest pre-peak time of half-maximum concentration in the accretion-flow simulations. Upper curves mark the earliest post-peak time of half-maximum concentration for the accretion-flow (solid lines) and midplane-flow (dashed lines) simulations. Fiducial disk model.

which I have modeled, it is plausible that enough material from the innermost disk could reach large enough radii. Hot outflows near the disk midplane, which *Tscharnuter et al.* (2009) find very early in the star/disk formation process, would assist outward transport from the innermost disk.

A qualitatively distinct disk model with low diffusivity is also conceivable. My results suggest that if Sc is significantly larger than unity, there is negligible transport of crystalline silicates subject to the accretion flow to the region where Jupiter family comets form. This is true even if silicates can form at radii as large as 10 AU. A low diffusivity disk, however, could potentially be favorable to the establishment of an outward midplane flow, which *is* able to move settled particles outward efficiently. *Ciesla* (2009) showed that a transport scenario dominated by high-altitude–inward and low-altitude–outward advection can lead to segregated grain populations with different processing histories. This is possibly compatible with disk observations of *Olofsson et al.* (2009) that suggest some disks are more crystalline at larger distances.

4.5.4 Transport in More/Less Compact Disks

Finally, I assess the role of the disk mass distribution and its evolution on outward transport. First, I contrast the results of runs assuming a static disk with those of the evolving disk, and then move on to exploring the effects of the initial compactness of the disk in the evolving-disk model. Of my two static-disk models, the first uses the $t = 0$ profile of the fiducial-disk held static (the static0-disk model). The second is the steady-disk limit of the $t = 0$ fiducial-disk profile, where the disk surface density follows Equation (4.1), with $R_d = \infty$ (the steady-disk model).

Results from the two static-disk models are shown in Figure 4.15, which plots in the top panel the total-fraction and in the bottom panel the normalized-concentration of 20 μm particles beyond 25 AU with time for two different source regions. The mass per AU of the gas disk does not drop off in the outer disk for the steady-disk model but is instead continuous out to the edge of my simulation space. Therefore, the normalized concentrations beyond 25 AU for this disk model are calculated using the disk gas mass only out to 100 AU (for a total 0–100 AU disk mass of 0.162 $M_\odot$; note that 0.03 $M_\odot$ of gas is contained within the first 21 AU in the steady-disk model). Figure 4.15 includes the results for the evolving fiducial-disk model for comparison. In a static disk, the upper-limit outward transport set by the midplane-flow case is that virtually all grains are advected out to the outer disk and remain there.

The most obvious result from Figure 4.15 is that the two static-disk models, together with the fiducial evolving-disk model, form a hierarchy in outward mixing that is based on disk structure. In the static0-disk model the region of outward-flowing accretion flow remains fixed relatively close to the central star, and those outward velocities are fairly rapid. Therefore, more than twice the peak fraction of fiducial-disk particles move to the outer disk (and stay there, as per the static-disk-model tendencies seen in §4.4). The surface-density structure in the steady-disk model means that in the accretion-flow case the gas radial-velocity is everywhere inward, and hence the number of 20 μm particles beyond 25 AU peaks at less than 40% of the value for the corresponding fiducial evolving-disk simulations, and those particles eventually all fall back inward onto the parent star, — and more rapidly than in the evolving disk simulations. Roughly 23% remain in the disk after 10^5 years (when 30% remain in the fiducial-disk accretion-flow simulations).

However, in terms of the normalized concentration of inner-disk particles in the outer disk, the

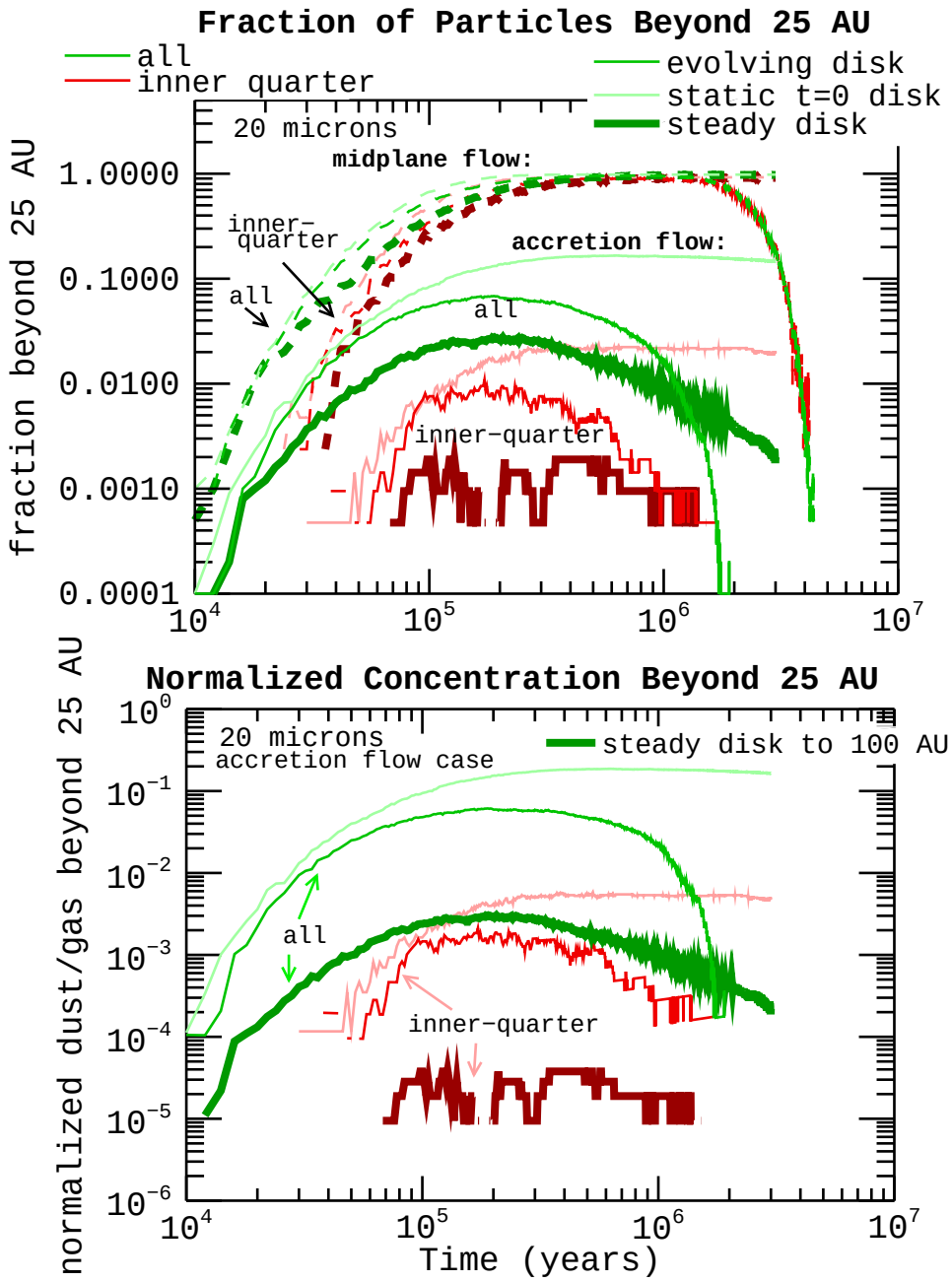

Figure 4.15: For the static disk models, (top panel) the fraction of 20 μm particles beyond 25 AU and (bottom panel) the normalized concentration of 20 μm particles beyond 25 AU for two source regions. Dark, heavy curves denote the steady disk model and assume an outer-disk gas mass truncated beyond 100 AU for the normalized-concentration calculation. The curves for the fiducial, evolving disk model are included for comparison. Solid curves denote the results for the accretion-flow gas-velocity case; dashed curves denote those for the midplane-flow case.

disk-gas mass distribution also really sets the steady-disk simulations apart from the rest. With so much more mass in the outer disk than the other two models, the steady-disk model is that much less intrinsically capable of contaminating the outer disk with inner-disk grains than are the disks with a more compact disk mass distribution. Finally, for the upper limits placed by the midplane-flow simulations both static-disk models send more than 90% of the simulation particles from all source regions to beyond 25 AU; the outward advection is only more rapid in the static0-disk model. Therefore, the upper bounds on the mixing in these models are set only by their relative source-region and comet-forming region disk-gas mass ratios.

Although some trends are the same for static as compared to evolving disk models, the results imply that the evolution of the disk – particularly at early times – has a substantial impact on particle transport. Steady-disk models tend to underestimate the degree of outward particle transport possible in protoplanetary disks in the early stages of disk evolution, when the most processing of high-temperature materials occurs. The outward transport of particles is substantially more efficient at early times, consistent with the results of *Bockelée-Morvan et al.* (2002) and *Ciesla* (2009), even here assuming a fixed diffusivity. How strong the effects of evolution are will depend, of course, on the details of the initial conditions for the disk. To examine this dependence, I vary the initial compactness of my evolving-disk model (parameterized by R_d in Equation (4.1)). I consider $R_{\rm d} = 5$, 10, and 40 AU, in contrast to $R_{\rm d} = 20$ AU in the fiducial-disk model. I retain 0.03 $M_\odot$ as the starting mass of the disk, so that the lifetimes of the model disks vary between 3.6–6.9 Myr, and the $t = 0$ mass accretion rates between 8.3×10^{-7}–$8.6 \times 10^{-8} M_\odot$ yr^{-1}. I do not consider possible variations in heating for disks forming in more or less compact configurations, retaining the static temperature profile described in §4.3.1[3].

Reducing the compactness of the model disk has two consequences: the disk initially expands more rapidly, and it does so from an initial state where a greater fraction of the mass is at small radii (and thus hot and potentially able to form crystalline material). The combined magnitude of

[3]I also continue to employ the same uniform radial distribution to initiate my simulation particles. One should note, however, that the gas-mass–per-AU is no longer roughly uniform across the source regions in the $R_d = 10$ and 5 AU disks, as shown in Figure 4.16. For $R_d = 10$ AU, the ratio of the average-gas-mass–per-AU for the inner-quarter source region to the outer-half source region is ~ 1.5, and for $R_d = 5$ AU it is ~ 2.6. This affects the accuracy of the normalized concentration values that I report for these disks (especially for the widest source regions), but it does not alter the trends with R_d repeated across source-region populations.

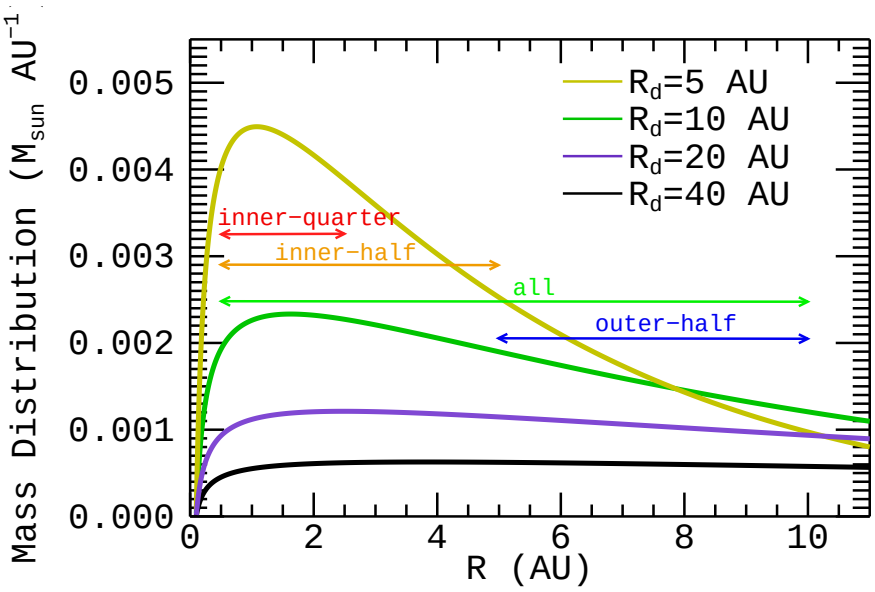

Figure 4.16: Gas mass distributions at $t = 0$ for different intial disk compactnesses (R_d). The different source regions considered are marked by colored boxes: green - all; red - inner quarter; orange - inner half; blue - outer half. Note that the fiducial disk model ($R_d = 20$ AU) has a mostly uniform distribution of mass across the different source regions, but that the more compact disk models contain significantly more mass per AU in the inner regions than out around 10 AU.

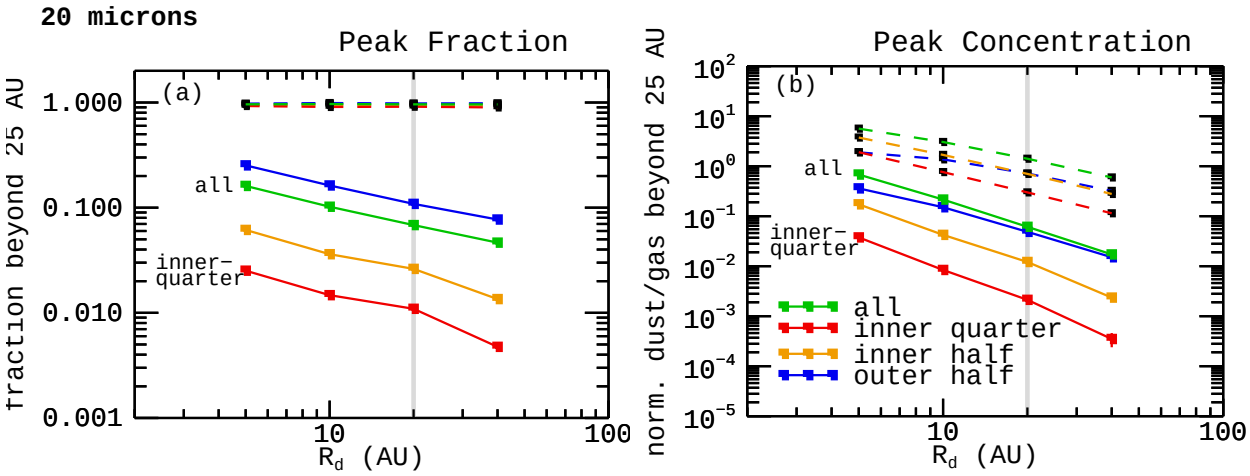

Figure 4.17: (a) Maximum values of the fraction of 20 μm particles beyond 25 AU and (b) maximum values for the normalized concentration of 20 μm particles beyond 25 AU as a function of initial disk compactness. Dashed curves with black markers denote the midplane-flow simulations. The grey line marks the baseline case of $R_d = 20$ AU. Note that the most compact disks both send a larger fraction of simulation particles beyond 25 AU and have a larger fraction of disk material in the source regions at $t = 0$.

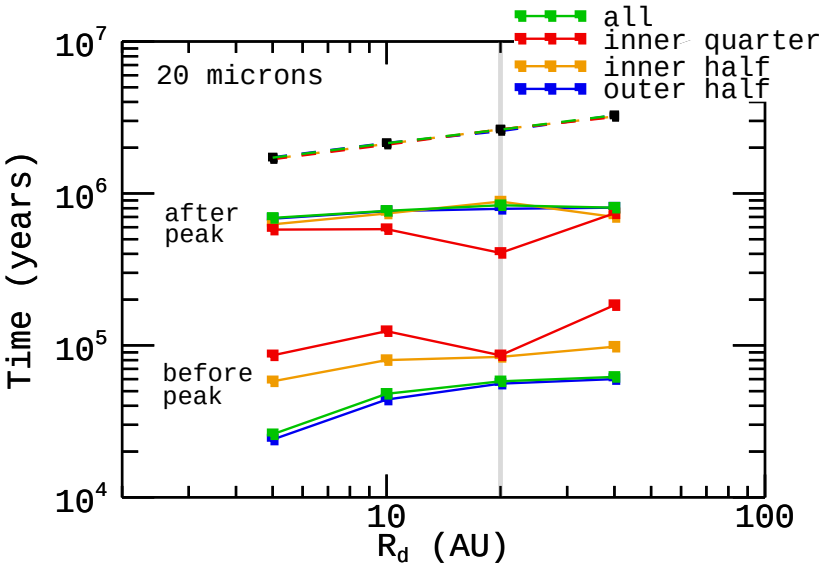

Figure 4.18: Time windows for the peak values of the normalized concentration of 20 μm particles beyond 25 AU as a function of initial disk compactness. Lower solid curves denote the latest pre-peak time of half-maximum concentration in the accretion-flow case. Upper curves denote the earliest post-peak time of half-maximum concentration for the accretion-flow (solid lines) and midplane-flow (dashed lines with black markers) simulations.

these effects is shown in Figure 4.17, where I plot first (a) the simple peak-fraction and second (b) the peak normalized-concentration of 20 μm particles beyond 25 AU as a function of R_d. Variations of approximately one order of magnitude in R_d result in nearly two orders of magnitude difference in the peak concentrations for each source region. For the smallest disk – with $R_d = 5$ AU – the normalized concentration of all simulation particles peaks at ∼68%, more than an order of magnitude in excess of the value for the fiducial simulations. A substantial part of this increase is due to the larger reservoir of mass that a compact disk has at small radii, which can potentially contaminate the (proportionally less massive) outer disk. That this mass-distribution effect is important is made clear by the fact that even the upper-limit concentrations from the midplane-flow simulations show a strong (order-of-magnitude) trend with R_d. However, as shown in Figure 4.18, there is little variation in the timing of outer-disk contamination with $R_{\rm d}$. The timing may be *slightly* faster for smaller $R_{\rm d}$. However, this is largely an effect of the disk lifetime, which is noticeably shorter for an initially more compact configuration.

The fact that the outer disks of the initially more-compact-disk models are less massive (and

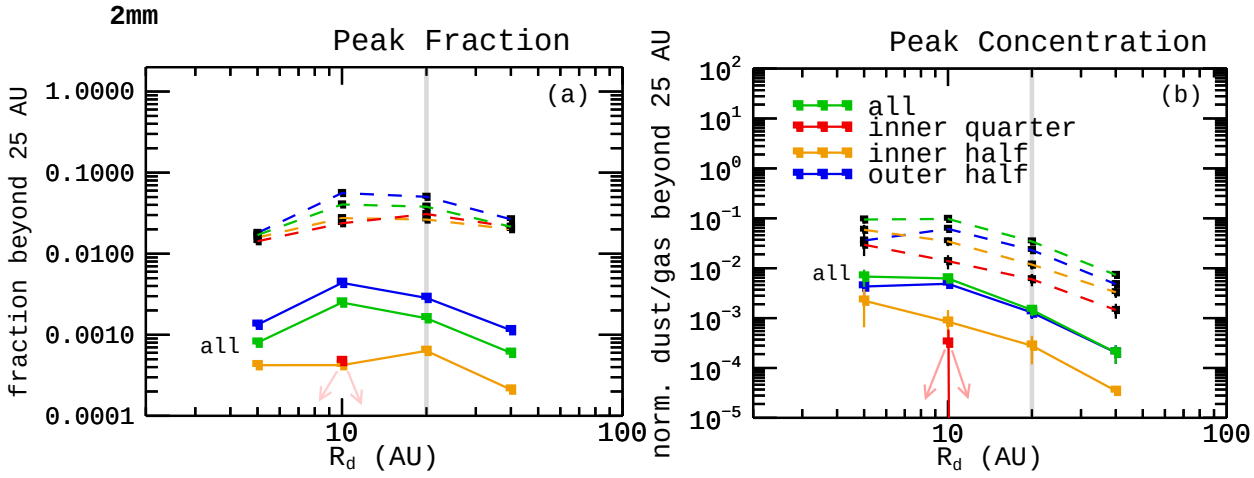

Figure 4.19: Maximum values for (a) the total-fraction and (b) the normalized-concentration of 2 mm particles beyond 25 AU as a function of initial disk compactness. Dashed curves with black markers denote the midplane-flow simulations. In the accretion-flow case, almost no 2mm particles from the inner-quarter source region reach beyond 25 AU.

more tenuous) does place some constraints on the outward mixing of large grains in my particle-transport simulations. In Figure 4.19 (b), I plot the peak normalized concentration of 2 mm particles beyond 25 AU as a function of R_d. All of the disks, of course, have less outward transport of these larger grains, but in my simulations, the peak in the fraction of particles sent to beyond 25 AU occurs for $R_d = 10$ AU (as shown in panel-a), which sends up to 0.25% of all 2 mm-simulation particles beyond 25 AU (4% in the midplane-flow case) compared to less than 0.1% for $R_d = 5$ AU (less than 2% in the midplane-flow case). Because of the larger source-region mass for $R_d = 5$ AU, this drop in fractional outward transport constitutes a leveling off in the maximum-achievable normalized concentrations of inner-disk particles in the outer disk.

Comparing these results to observations of crystalline silicates in other disks allows us to construct a possible scenario for the formation and transport of high-temperature minerals in those disks. In the *Watson et al.* (2009) survey, the disks observed were around T Tauri stars ∼1–2 Myr old and showed a slight correlation between the crystalline-silicate mass fraction and the measured accretion rate onto the star. As shown in Figure 4.20 for my model disks, $t = 1$ Myr corresponds to a time when those disks that were initially most compact (with high $t = 0$ accretion rates) now have lower accretion rates than the initially more-extended disks. Therefore, small grains that formed at small AU near $t = 0$ should be more broadly distributed in disks that now have lower accretion

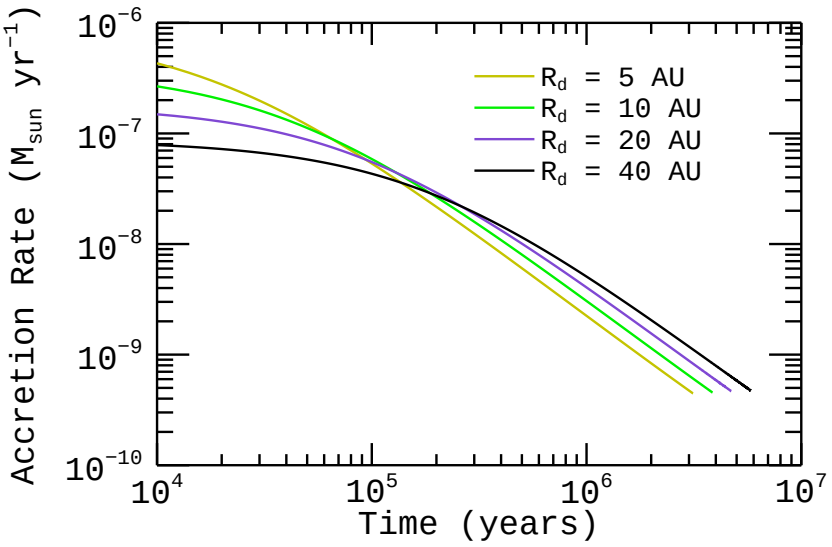

Figure 4.20: Mass accretion rates for disk models initiated with the same total disk mass, but with different initial exponential cutoff radii (R_d). Note the reversal in ordering from early to late times. All disks were initiated at $t = 0$ with a total mass of 0.03 $M_\odot$.

rates. However, lower accretion rates also mean disks that are more tenuous. The initially most compact disks lose mass the fastest, causing their outward transport efficiency to drop rapidly with time. Therefore, grains that formed at small AU after $t \sim 2 \times 10^5$ yr may be better distributed in the initially more-extended disks, which now have higher accretion rates.

These properties could potentially explain the opposing trends between crystallinity and observed accretion rate reported by *Watson et al.* (2009). Pyroxene is favored over olivine when the minerals are formed by condensation (*Gail*, 2004; *Wooden, Harker, & Brearley*, 2005). Therefore, a possible scenario is that pyroxene formed primarily at very early times when the disks were hottest and became most broadly distributed throughout the initially most-compact disks. Most of the olivine, on the other hand, may have formed over a longer period of time. It might, therefore, have become more broadly distributed within disks that retained significant surface densities for longer times (the initially more-extended disks). This hypothesis does not, however, explain why the *Watson et al.* (2009) survey found no correlation between crystalline mass fraction and disk mass.

4.6 Conclusions

Observations of comets (*Hanner et al.*, 1994; *Wooden, Woodward, & Harker*, 2004) and sample return from the *Stardust* mission (*Brownlee et al.*, 2006) suggest that outward transport of high-temperature solids to the comet-forming regions is a necessary component of any successful model of the early Solar Nebula. Some proposed mechanisms for such outward transport include the launching of grains from near the star out to large distances in a disk jet or wind (*Shu et al.*, 2001), the outward flow of mid-sized particles along the surface of the disk due to photophoretic heating and gas-pressure forces (*Mousis et al.*, 2007), and the outward diffusion of the hot grain population within the disk gas due to turbulent mixing. I have focused on this last mechanism, as turbulence is believed to be intrinsic to protoplanetary disks of all types, and therefore tubulent mixing of grain populations is likely important within all disks, reguardless of the degree of outer-disk contamination finally achieved. A turbulent mixing hypothesis is also free of concerns regarding grain survivability within potential wind launch flows initiated extremely closely to the central star, and of potential special-condition local optical-depth requirements for grains to reach large distances due to photophoretic forces. This is not to say, however, that these other mechanisms play no roles protoplanetary disk compositions; they are simply neglected here in favor of more univeral disk-turbulence and gas-drag effects.

I have constructed a 1D model of viscous disk evolution and particle transport that I use to study the relationships between the evolving disk mass distribution and the local conditions that are supportive of the aerodynamic outward mixing of grains, specifically including self-consistent treatment of the dust grains' surface-area-to-mass ratios in my aerodynamic transport terms. I have examined patterns of outward mixing considering variations in the radial gas-flow structure, the sizes of dust grains, the model's Schmidt number, and the initial compactness of the model disk's gas mass distribution. The differences in outward transport and outer-disk contamination according to these parameters are summarized in Figures 4.21–4.24 for both the 1D-gas-accretion-velocity and outward-midplane-flow scenarios.

I find that a range of disk models are able to account for the presence of high-temperature–inner-disk particles in the comet-forming region. As in *Dullemond, Apai, & Walch* (2006), the most favorable models involve rapid early expansion of initially quite compact disks. These conditions can

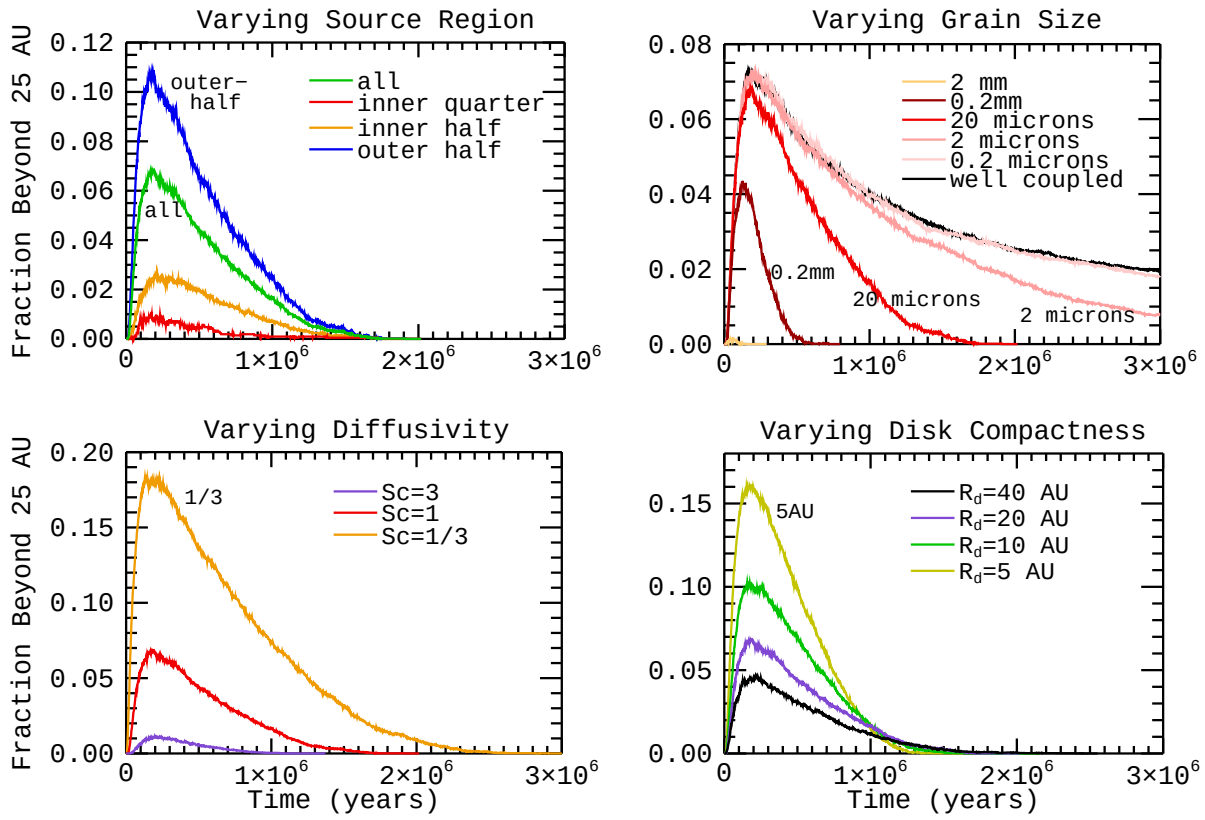

Figure 4.21: **Accretion-flow case; Total fraction beyond 25 AU**, each panel varying a different set of parameters. Unless otherwise marked, the baseline is: 20 μm particles from the "all" source region (0.5–10 AU) simulated in the fiducial (R_d = 20 AU) evolving disk model with diffusivity equal to the disk viscosity ($Sc = 1$).

result in inner-disk material flowing to the outer disk on a short time scale. In agreement with *Ciesla* (2009), I find that outward transport is more efficient at early times due largely to stronger gas radial outflows. Even more favorable are cases involving outward-flowing gas at the disk midplane (*Keller & Gail*, 2004; *Ciesla*, 2007, 2009), which are capable of delivering substantial fractions of grains inward of 1 AU to the outer regions of the disk. It is not known whether such outward flows exist in real disks (or, whether the particles are sufficiently settled to experience them consistently). Whether such midplane flows are *required* to explain the *Stardust* results depends upon the Schmidt number, which at its lower limit (highest relative diffusivity) could allow for a relatively high degree of general outward mixing, even from relatively near the parent star. While the mean accretion flow is less efficient at transporting particles outward, significant outward contamination by crystalline material would be possible if the disk were initially both compact and able to form silicates out to

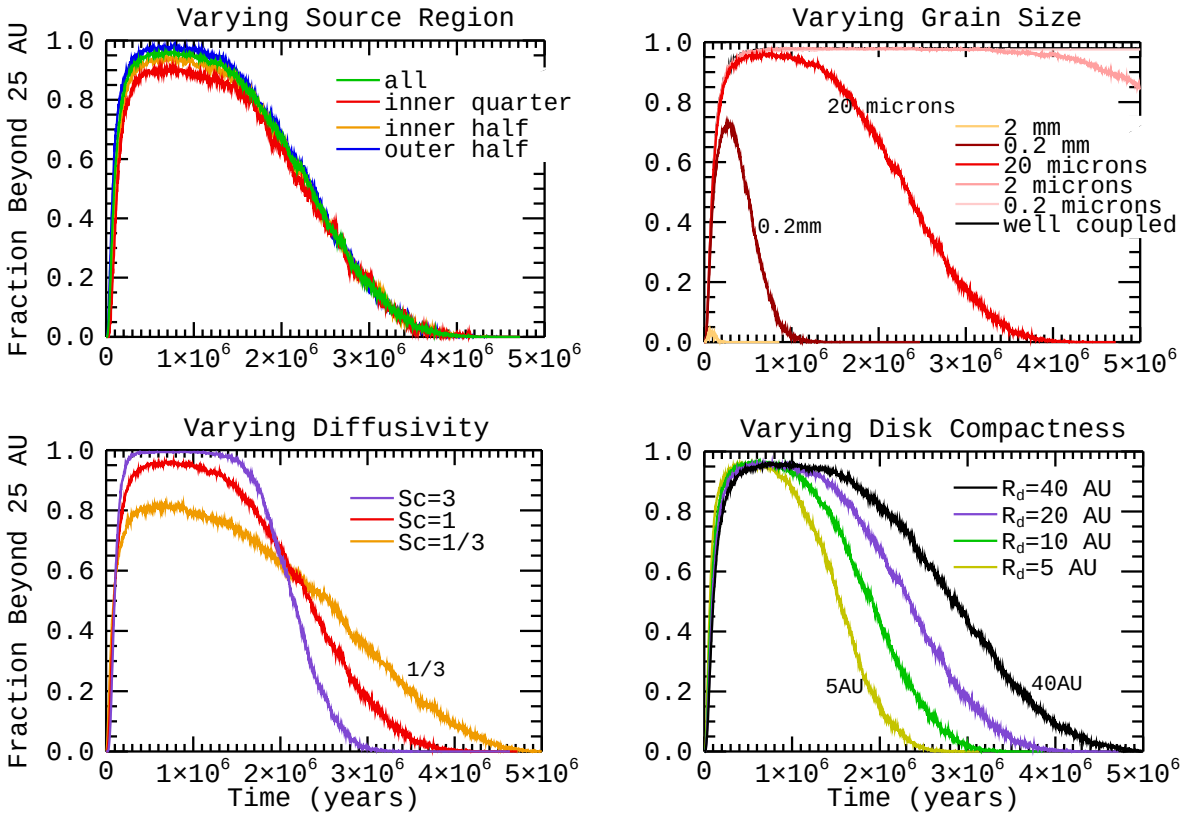

Figure 4.22: **Midplane-flow case; Total fraction beyond 25 AU**. Unless otherwise marked, the baseline is: 20 μm particles from the "all" source region (0.5–10 AU) simulated in the fiducial ($R_d = 20$ AU) evolving disk model with diffusivity equal to the disk viscosity ($Sc = 1$).

a distance of several AU.

My results suggest that it is the largest particles recovered by *Stardust* that place the tightest constraints on the evolution of the early Solar Nebula. Particles as large 2 μm are well coupled to the disk gas, and plausible levels of turbulent diffusivity allow them to reach the outer disk from small radii in a wide variety of models. My simulations show that 20 μm particles can also reach the outer disk — consistent with the *Stardust* results — as long as they were incorporated into larger bodies within the first 1–2 Myr of the disk evolution. For even larger particles, those of a few mm or larger, none of my disk models admit significant outward transport to the comet-forming region, regardless of the proposed source region. Even grains of a few hundreds of microns in size should be rare, since their residence time in the outer disk is very limited. Discovery of such grains would, within the context of the model developed here, require a more massive disk during the time

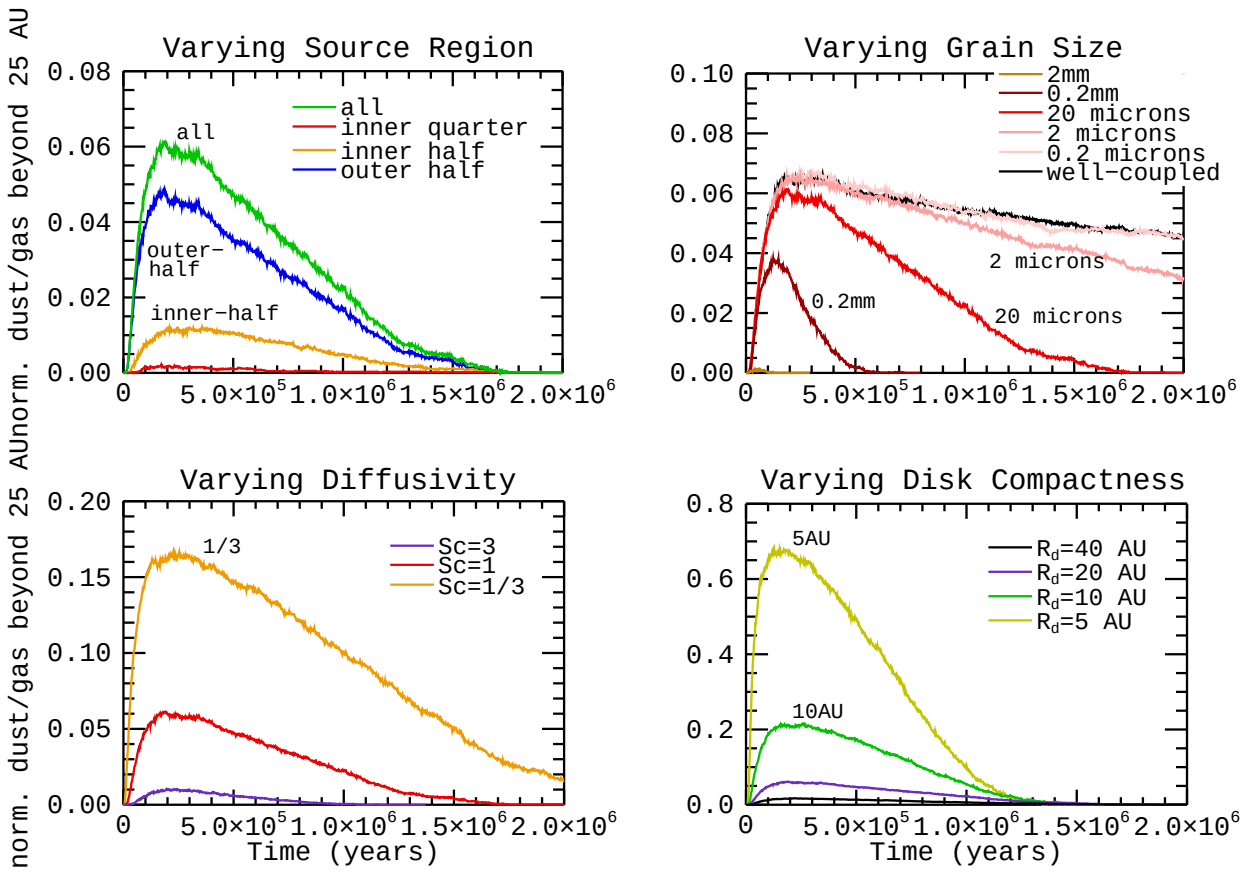

Figure 4.23: **Accretion-flow case; Normalized concentrations beyond 25 AU**. Unless otherwise marked, the baseline is: 20 μm particles from the "all" source region (0.5–10 AU) simulated in the fiducial ($R_d = 20$ AU) evolving disk model with diffusivity equal to the disk viscosity ($Sc = 1$).

of their formation, transport, and incorporation into cometesimals.

The existence of substantial uncertainties in the disk physics currently precludes an observational determination of the characteristic radii at which crystalline silicate formation occurs. The strongest constraints come from observations of CAI-like grains, which probably formed at fractions of an AU from the Sun. Only a subset of my accretion-flow simulations are likely compatible with this finding. A broader range of models in which the midplane gas flow is outward are viable, since these models retain particles in the disk for a longer period of time and facilitate the co-existence of grain populations of markedly different processing histories. Generically I expect that, provided sufficient outward transport is possible, turbulent diffusion will cause particles to become radially well-mixed over tens of AU, so that incorporation of CAI-like grains and Fe-rich crystalline silicates (possibly formed in water-rich shocks out to 10 AU) into the same body is plausible.

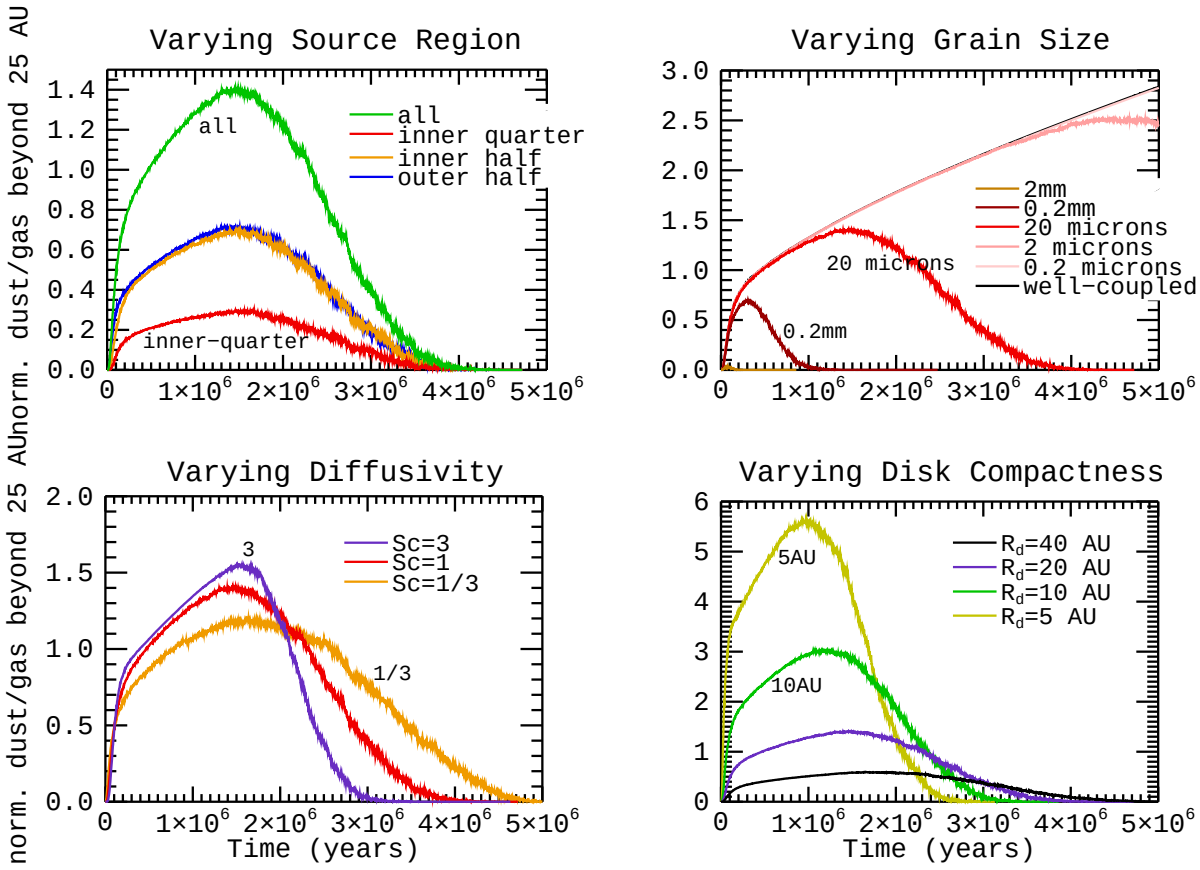

Figure 4.24: **Midplane-flow case; Normalized concentrations beyond 25 AU**. Unless otherwise marked, the baseline is: 20 μm particles from the "all" source region (0.5–10 AU) simulated in the fiducial ($R_d = 20$ AU) evolving disk model with diffusivity equal to the disk viscosity ($Sc = 1$).

For astronomical observations, my results suggest that the mass and size of the disk at an early epoch are critical parameters in determining the viability and extent of outward particle transport. These disk properties are inherited from the mass and angular-momentum structure of the cloud that collapses to form the star, and would vary from system to system. I expect this to result in variations in the crystalline fraction at large radii in disks around different stars. I have also noted that the time scale during which conditions allow substantial outward transport is only a small fraction of the disk lifetime. A limited time for outward mixing is both interesting and puzzling when paired with the emerging evidence for aqueous and/or igneous grains among the *Stardust* samples (*Wooden*, 2008; *Joswiak et al.*, 2010; *Stodolna, Jacob & Leroux*, 2010). However, it may allow the *Stardust* results to be reconciled with other observations that require compositional gradients within the disk to be maintained. A possible scenario is that an early stage of rapid

expansion drove particles into the outer disk where they were rapidly locked up into larger icy bodies. Once the disk had expanded, the gas flow became more uniform, limiting the outward transport of solids.

Chapter 5

Particle Mixing and Outward Transport: Extended Parameter Study

In Chapter 4, I explored the outward mixing of dust grains due to aerodynamic forces within a protoplanetary gas disk in the context of the *Stardust* results, specifically underlining the advantages and constraints imposed by protoplanetary disk evolution. I explored outward mixing as a function of some of the most obviously relevant parameters: the relative diffusivity of the particle ensemble, the particular sizes of transported grains, the relatively unknown gas-velocity structure of the disk, and the initial compactness (and subsequent expansion) of the evolving disk. All of these parameters are important to the outcome of outward mixing via gas-drag advection and turbulent diffusion. In this chapter, I use the same models and simulation setup to expand my exploration of parameter space in relation to outward mixing. Here, I consider those parameters not as immediately obvious to the basic question posed in Chapter 4, but equally fundamental to the efforts of modeling particle-transport within a gas disk. I find that constraints imposed by these new parameters on aerodynamic outward mixing of hot grains remain in keeping with the observations of disk crystallinity in disks around other stars. I also find that the results outlined in Chapter 4 are not unique to the disk models used in those simulations, and that my conclusions remain robust within the context of a one-dimesional, evolving-disk-model scenario: Disk mass distribution and contaminant production at the earliest times are the primary factors determining disk composition, and the process of disk evolution is tightly coupled to the outcome of particle transport within a protoplanetary disk.

5.1 Introduction

In this chapter, I continue to explore the outward mixing of hot grains in relation to the *Stardust* results and observations of disk crystallinity discussed in Chapter 4. Therefore, the simulations in this chapter are performed using the same disk-model and particle-transport setup as described for the Chapter 4 simulations. I continue to use a static, power-law disk-temperature profile and normalize my results to the same fiducial-disk model where $M_{D,0} = 0.03 M_{\odot}$, $R_d = 20$ AU, and $\alpha = 10^{-2}$. See §4.3 for details. In some instances, I also use the initially-most-compact disk setup as a baseline ($R_d = 5$ AU) but always in parallel with the fiducial model, and I include in this chapter results of varying $M_{D,0}$ and α explicitly. I use the same model-disk grid setup as in Chapter 4, except in §5.2.2, where I test the effect of moving $R_{\rm in}$ outward by removing grid cells from the inner edge of the grid (so that the grid as a whole is static for these tests).

As in Chapter 4, the primary measure I use to assess the degree of outward mixing in these simulations is the normalized concentration of source particles in the outer disk (beyond 25 AU), C_N, as a function of time, or as the peak value of that curve. Please refer back to §4.5.1 and Equation (4.2) for the definition and discussion of this quantity. Again, the source regions that I consider for outwardly-mixed grains are the inner-quarter source region, extending from 0.5–2.5 AU, the inner-half source region, 0.5–5 AU, the outer-half source region, 5–10 AU, and the all source region, 0.5–10 AU. Simulation particles are initiated evenly spaced between 0.5 and 10 AU, and I continue to assume a rocky internal density for the particles of $\rho_d = 3$ g cm^{-3}. Once again, I implement 10,000 particles within the mostly inward-flowing accretion-flow case, and 2,000 particles within the outward-flowing midplane-flow case. See §2.6 for details of the disk-gas radial velocities represented by these two cases. In general, the accretion-flow case should be thought of as providing the primary results of the simulations, tracing grain transport within the bulk flow of the disk, whereas the midplane-flow case provides the extreme upper limit on both the magnitude and temporal extent of grain transport to the outer disk.

Because I would like to test the results of outward transport not only on disk characteristics but also on my model setup, I begin in §5.2 by varying a couple (mostly) numerical parameters, namely the seed number used to initialize random-walk diffusion of the particle ensemble, and $R_{\rm in} = R_{\rm min}$, the inner boundary of both the model-disk grid and disk surface-density profile. In §5.3, I explore

outward transport as it depends on the time (according to the clock of my disk-model evolution) at which grains are initiated. In §5.4 and §5.5 I vary $M_{D,0}$ and α, respectively, and in §5.6 I explore outward transport as a function of the disk-temperature–model parameters. I provide conclusions in §5.7, tying the results of this chapter to those of Chapter 4, the compositions of extrasolar disks, and solar-system comets.

5.2 Some Numerical Considerations

While the simulations of Chapter 4 tested the results of outward transport on a number of different effects, they neglected to examine the effects of the simulation set-up itself. In this section, I test the results for outward transport under the influence of two effects: the random error introduced by using a relatively small particle sample, and the location chosen for the inner-disk edge, which is set to $R_{\rm in} = 0.1$ AU in the fiducial runs but which has a relatively minor effect on the evolution of the global gas disk.

5.2.1 Randomized Diffusion

To look for effects of statistical error on the output of my particle-transport simulations, I have run simulations in the fiducial-disk model varying the seed number inputed into the random-number generator that controls the random-walks for diffusion of the particle ensemble. In the fiducial simulations, I use an input seed of -34. For this section, I consider also runs with seeds of -33 and -35.

Figure 5.1 plots the normalized concentration beyond 25 AU as a function of time for 20 μm-sized grains from the all and inner-quarter source regions. From these curves, one can see that each of the separate runs produce qualitatively the same results, but that quantitatively the curves may differ by several percent at least at any given time-step. Unsurprisingly, this type of divergence is strongest for grains from the inner-quarter region in the accretion-flow case, for which the smallest fraction as well as the smallest total number of grains reach the outer disk (despite having five times more simulation particles initiated than in the midplane-flow case).

However, the primary quantitative result that I have used to characterize the outward-transport results of my simulations is the peak value of the individual C_N curves. As shown in the plots of Figure 5.2, this peak value is fairly well-characterized using the fiducial setup of my transport

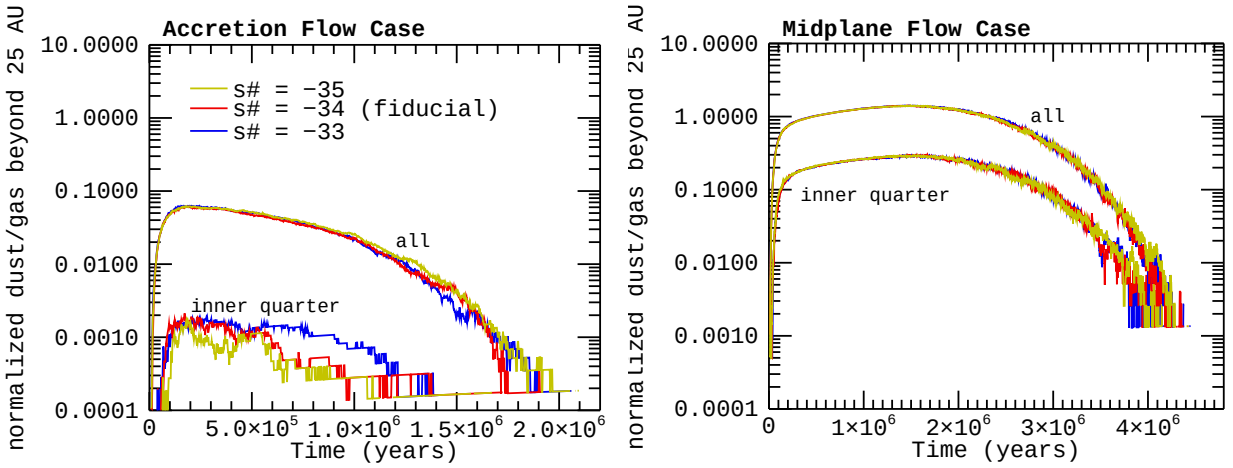

Figure 5.1: Normalized concentration beyond 25 AU for 20 μm grains in the fiductial disk model from the all and inner-quarter source regions. Three separater run-sets varying the seed number used to initialize random-walk diffusion of the particle ensembles.

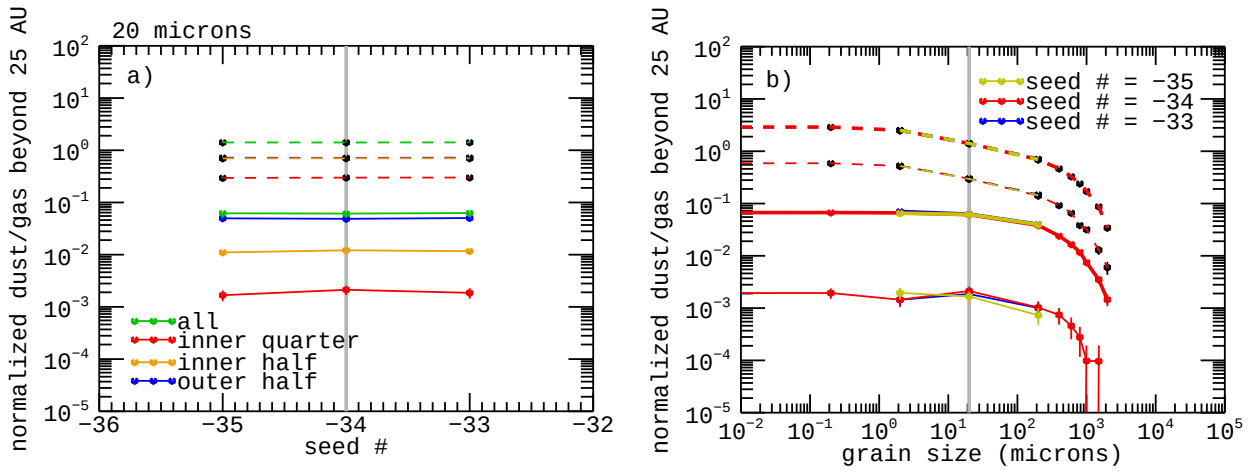

Figure 5.2: **Panel-a)** Peak C_N values for 20 μm particles in the fiducial disk model as a function of randomization seed number. **Panel-b)** Peak C_N values as a function of grain size for the three sets of initializing seed number. Thick lines plot values for the all source region, thin lines for the inner-quarter region. **Both panels)** Accretion-flow case: solid lines and colored markers. Midplane-flow case: dashed lines and black markers.

simulations. In panel-a, I plot the peak values for each of the source regions as a function of the simulation seed number and find that the spread in values is within the error-bars estimated using Poisson statistics. In panel-b, I plot the C_N-max curves as a function of grain size for each of the seed-number run sets, with results that suggest the peak C_N value I extract from a simulation is fully adequate for describing trends in outward grain-transport across simulation parameters.

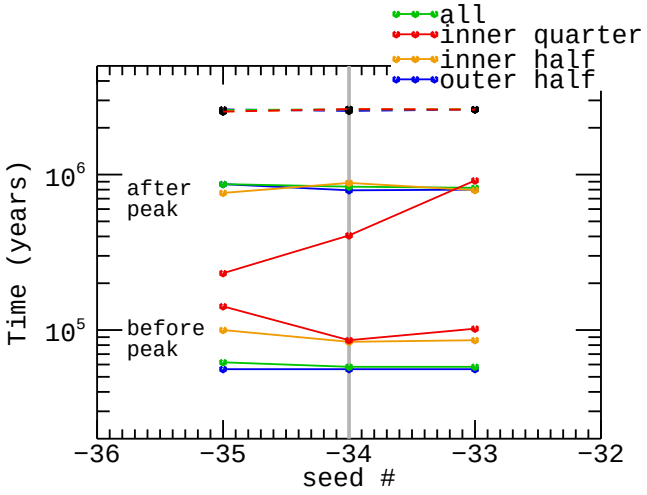

Figure 5.3: Times marking half-maximum C_N values for 20 μm grains before and after the peak for the accretion-flow case (solid lines, colored markers) and after the peak for the midplane-flow case (dashed lines, black markers), as a function of randomizing seed number.

Another measure I have used for examining outward transport in my simulations is the time-window between half-maximum values of the C_N curve. As the scatter in previous time-window plots has suggested, this measure is less well characterized in my simulations, and this is verified in Figure 5.3. While the source regions that send large fraction of grains to beyond 25 AU, such as those in the midplane-flow case, have well-characterized boundaries for the peak in outer-disk concentrations, small-number statistics in some other cases leads to extremely poorly characterized boundaries. The boundary for post-peak half-maximum for the inner-quarter region in the accretion-flow case ranges from $< 3 \times 10^5$ to nearly 10^6 years across the 20 μm-grain runs using three different seed numbers. Therefore, trends deduced from time-window plots should mostly consider the largest source-region sets in the accretion-flow case, and the upper-bounds given by the midplane-flow case.

5.2.2 Varying the Location of the Inner Disk Edge

The inner edge of the grid and model disk in my simulations is set, somewhat arbitrarily, to $R_{\rm in} = 0.1$ AU. As the mass flux from large AU has primary control over the disk evolution, varying this inner edge by a few tenths of an AU changes the computed disk lifetime by a percent or less. However, as I have set the inner edge of my total-particle-ensemble distribution to 0.5 AU, the

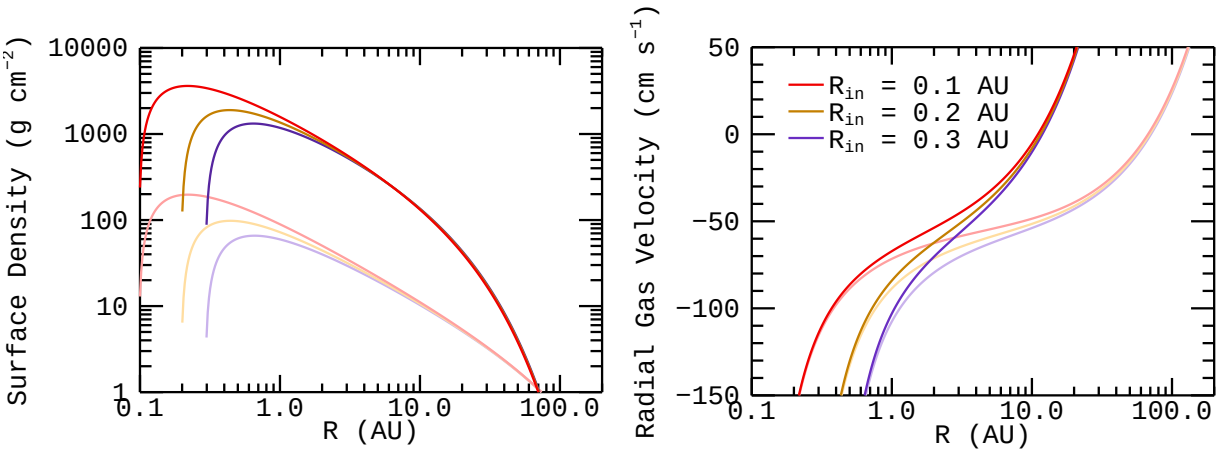

Figure 5.4: Surface-density and accretion-flow velocity curves for the disk gas in the fiducial disk model varying $R_{\rm in}$, the inner edge of the disk and simulation grid-space. **Dark curves** correspond to $t = 0$, **light curves** to t=0.5 Myr.

relative position of $R_{\rm in}$ may have a noticeable effect on the fraction of particles that reach large distances, particularly for the inner-quarter source region. In this section, I test outward mixing in both my fiducial-disk model and in the initially compact, $R_d = 5$ AU-disk model for cases when $R_{\rm in} = 0.2$ and 0.3 AU. (Note that shifting $R_{\rm in}$ outward is less expensive than inward because the disk-evolution time-step is controlled by the size and viscosity of the inner-most grid cell.) Figure 5.4 provides plots of the disk surface-density and accretion-flow velocities for $R_{\rm in} = 0.1$, 0.2 and 0.3 AU. Shifting $R_{\rm in}$ outward also increases the rate of inward-flow of the gas in the inner disk. It seems plausible, then, that for larger $R_{\rm in}$, the combination of a nearer sink boundary and faster inward advection should lead to faster inward loss of particles, to some degree, and that therefore larger $R_{\rm in}$ should correspond to somewhat less mixing to the outer disk. It is surprising, then, that this is not precisely the case.

In Figure 5.5, I plot peak C_N values as a function of $R_{\rm in}$ for the fiducial and $R_d = 5$ AU disks for 20 μm and 2 mm sized grains. Each simulation run in the accretion-flow case for each source region (except the inner-quarter region for 20 μm grains when $R_d = 5$ AU) shows a peak in outward transport for $R_{\rm in} = 0.2$ AU. Note that I plot here the C_N values for consistency with the results reported in other sections, but that this peak occurs equally if I plot the simple fraction of particles transported to beyond 25 AU; this is not an effect of disk-mass redistribution. Note also, that this peak-at-$R_{\rm in}$=0.2-AU effect is dominant for generally inward-flowing populations. It is more marked

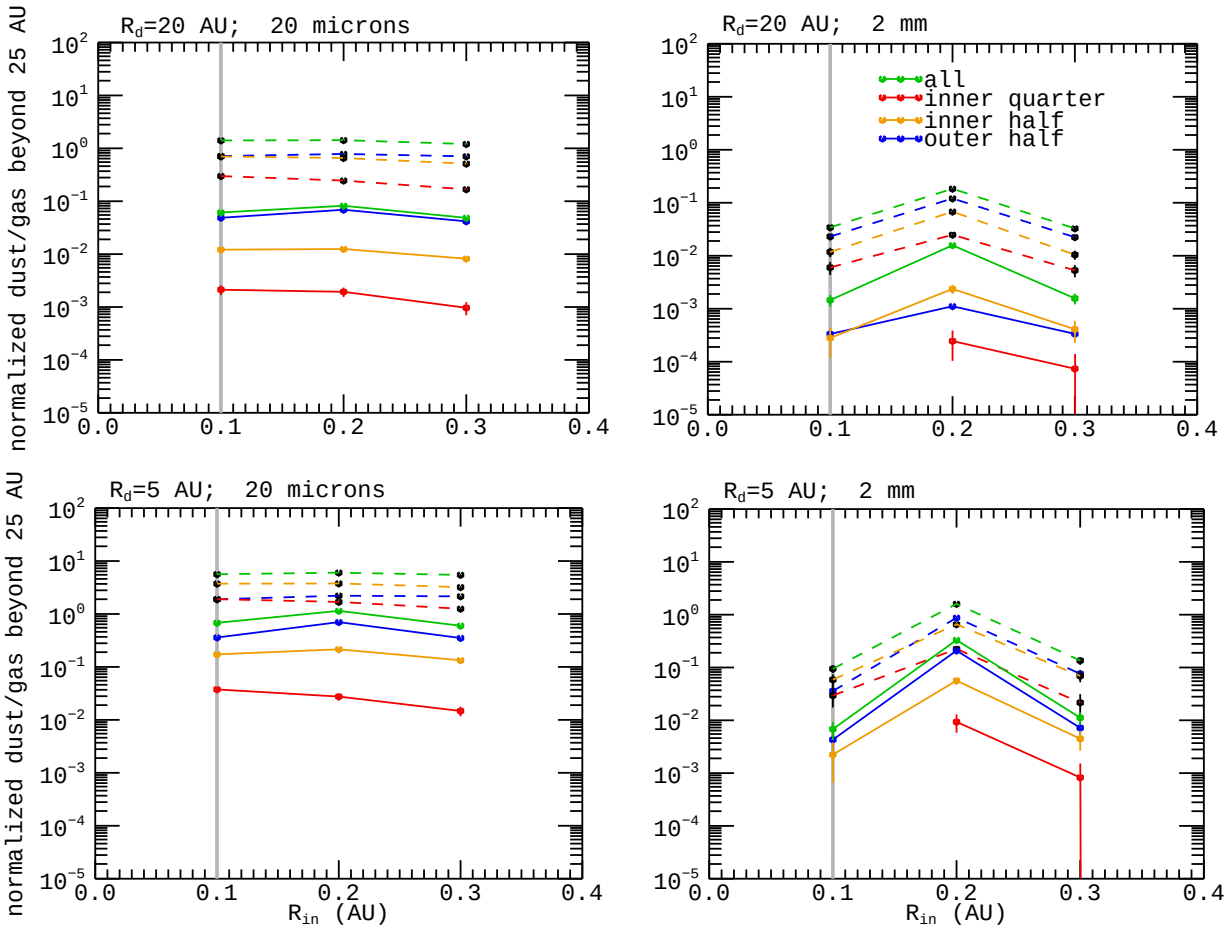

Figure 5.5: Maximum concentration beyond 25 AU as a function of $R_{\rm in}$ for the fiducial and $R_d = 5$ AU disk models and for 20 μm and 2 mm sized grains. Accretion-flow case: solid lines and colored markers; Midplane-flow case: dashed lines and black markers. Grey line marks the fiducial setup where $R_{\rm in} = 0.1$ AU.

for the 2 mm grains and is evident even in the midplane-flow case for these large grains. It is only for the dominantly outward-flowing populations (20 μm grains in the midplane-flow case) where intuition holds and increasing $R_{\rm in}$ provides a steady, if minor, decrease in peak outward transport.

One possible explanation for these results relates to the headwind drag experienced by particles in the inner disk. Headwind drag is strongest for the larger particle sizes (dominate over radial-advection drag) and could be lessened somewhat by shifting $R_{\rm in}$ outward (because this lowers Σ_g in the inner disk and also shifts azimuthal gas velocities to slightly closer to Keplerian at the inner edge of the particle-source region). Potentially, then, larger grains may be able to last slightly longer in the inner disk and so remain available for turbulent diffusion to the outer disk. Perhaps,

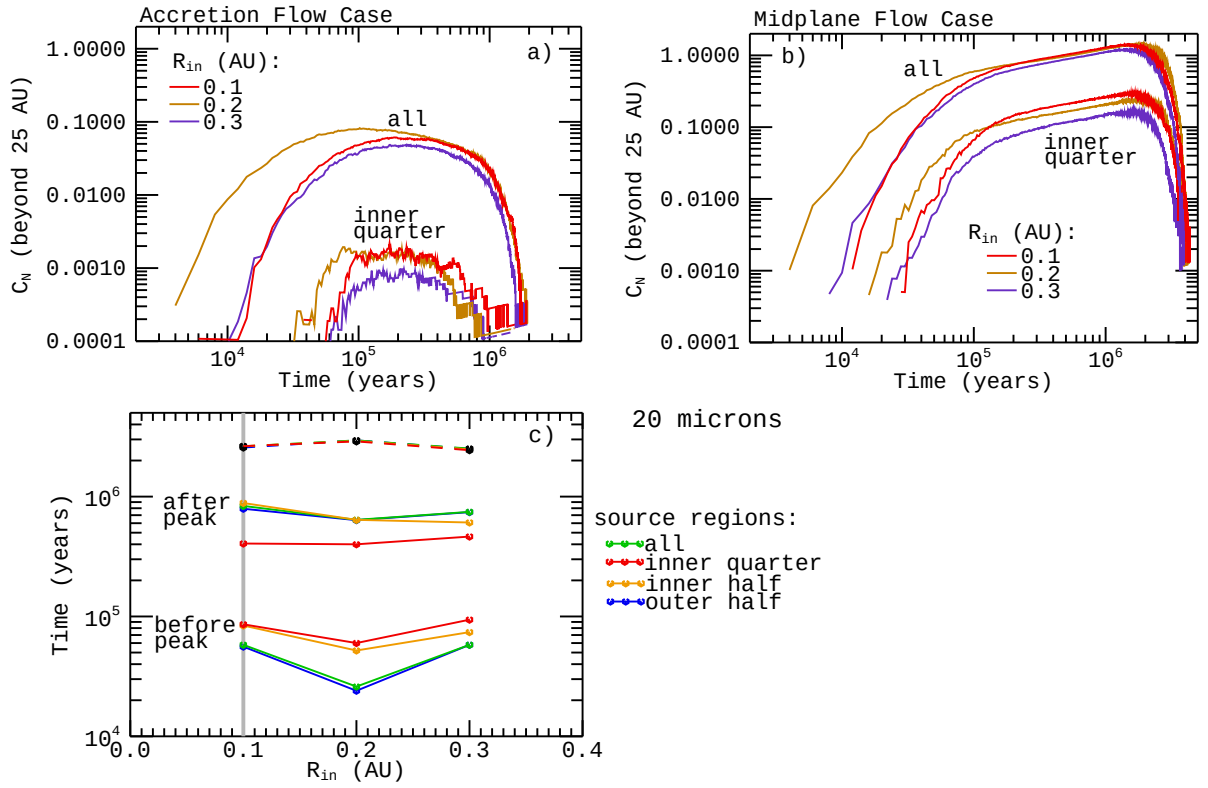

Figure 5.6: **Panels-a and -b)** C_N as a function of time for 20 μm grains in the fiducial disk model, varying $R_{\rm in}$, for the inner-quarter and all source regions - accretion-flow and midplane-flow cases, respectively. **Panel-c)** Times of C_N half-maximum before and after the peak for the accretion-flow case (solid lines, colored markers) and after the peak for the midplane-flow case (dashed lines, black markers).

then, the nearness of the innward-loss boundary in the $R_{\rm in} = 0.3$ AU case overcomes whatever advantage is presented by lessing this headwind drag.

This explanation is not entirely sufficient, however, to explane the results shown in Figure 5.6 that, even for the outward-flowing grains in the midplane-flow case, transport to beyond 25 AU is also markedly *faster* for $R_{\rm in} = 0.2$ AU than for the fiducial setup. Because the probability of outward versus inward diffusion is dependent on the gas mass available in both directions, it is possible that preferential outward diffusion is playing a role in the speed with which grains reach the outer disk. It is still surprising that such effects could be so strong for such a small redistribution to the disk mass, but for $R_{\rm in} = 0.3$ AU at least, faster inward advection does appear to dominate, allowing fewer particles to reach the outer disk, as expected.

As a summary, I plot in Figure 5.7 the peak C_N curves as a function of grain-size for the

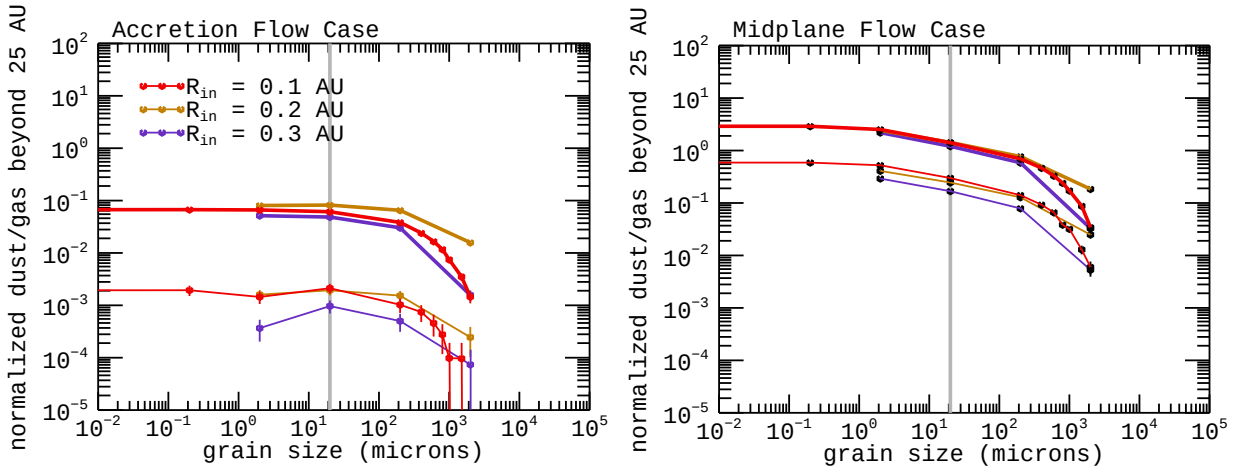

Figure 5.7: Maximum concentration beyond 25 AU as a function of grain size for the fiducial-disk model, varying $R_{\rm in}$, for the all and inner-quarter source regions.

different $R_{\rm in}$ cases of the fiducial-disk model. In general, $R_{\rm in}$ has a fairly minor effect on the trends for outward mixing simulated. However, $R_{\rm in} = 0.2$ AU seems to provide a peak in outward mixing for large grain sizes, therefore possibly shifting the cut-off grain size for outward transport to a slightly larger value. In general, this seems to be a "fine tuning" sort of effect, that is mostly mysterious but should not affect the larger-scale trends reported for these simulations.

5.3 Varying the Time of the Particle Initialization

In this section, I examine outward mixing of grains initiated at different times during the evolution of the fiducial disk model. Under the simulation setup used in Chapter 4, I essentially assumed that all crystalline silicates and high-temperature minerals were already formed in the disk at $t = 0$, with no further production at later times. While this assumption makes testing over a wide parameter set more tractable, it is flawed on a number of fronts, neglecting many of the nuances that make disentangling the compositions of bodies in our solar system such an interesting puzzle.

* First, of course, is that the creation of high-temperature minerals may have occurred over a relatively extended period, though still likely near the beginning of the disk evolution. Formation via condensation requires temperatures over 1000 K and so likely takes place only within the high-temperatures generated while the disk is initially forming. However, some theories predict the formation of crystalline silicates via annealing within disk shocks (*Harker*

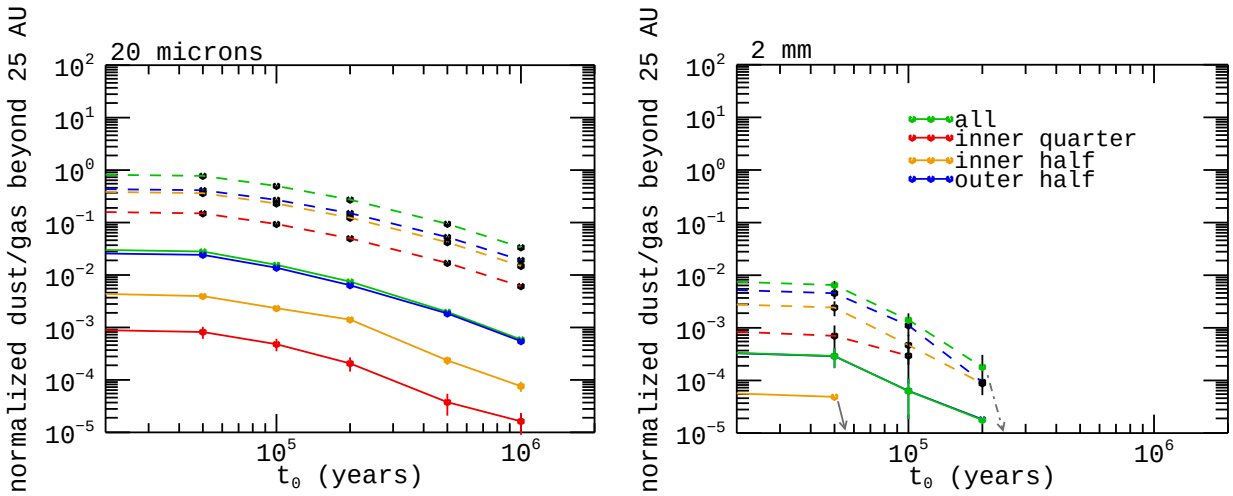

Figure 5.8: Peak outer-disk concentrations as a function of t_0 for 20 μm and 2 mm sized grains in the fiducial disk model. Solid colored lines and markers plot C_N-max for the accretion-flow case simulations, and dashed lines with black markers show the upper-limits from the midplane-flow simulations.

& Desch, 2002), and this could conceivably occur over a longer period.

* Next, when minerals formed and when they experienced transport to the outer disk may represent two different epochs. Some of the samples gathered from the comet 81P/Wild 2 show possible signs of minor aqueous processing (*Stodolna, Jacob & Leroux*, 2010), which would imply residence on an asteroid-like body, one both large enough and warm enough to contain liquid water. Depending on where and how such bodies may have formed and become disrupted, this could potentially represent a significant delay between the formation of the disk and the transport of some minerals out to the comet-forming regions.

* Finally, disk formation itself was not an instantaneous event, and by testing outward transport starting from $t > 0$, one may get a sense of how a disk's ($t < 0$) formation affects it's later composition. This is particularly important considering that the high temperatures providing some of the best conditions for forming crystalline silicates occur before the $t = 0$ of my model disks.

Figure 5.8 shows the primary results for outward transport of grains initiated at different times, $t_0 > 0$, during the model-disk lifetime for grains that are 20 μm and 2 mm in size. It plots the peak in the normalized concentration beyond 25 AU (defined in §4.5.1, Equation (4.2)) as a function

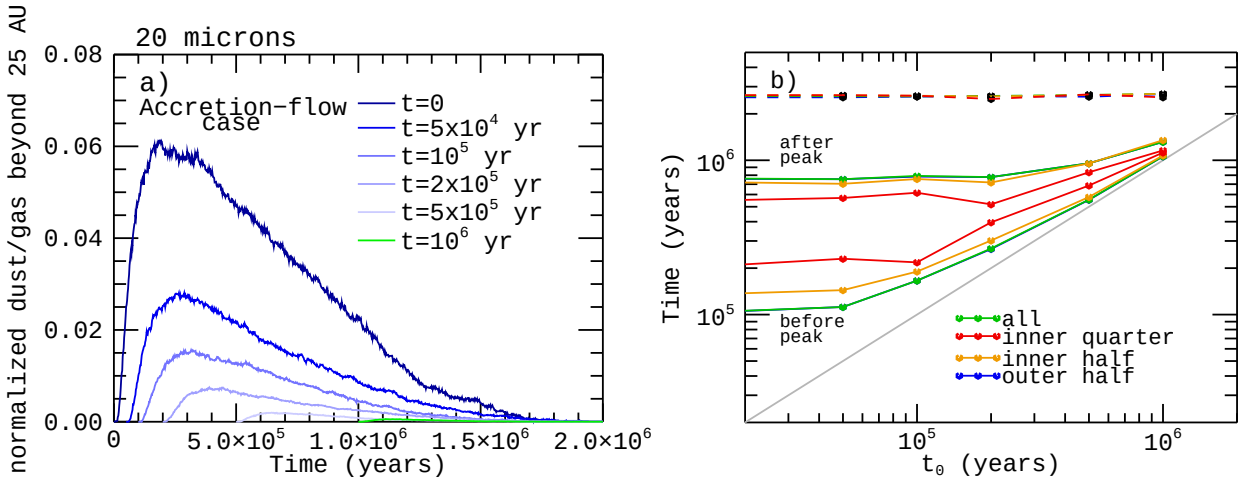

Figure 5.9: **Panel-a:** Normalized concentration beyond 25 AU as a function of time for particles in the all source region in the accretion-flow case of the fiducial disk model with different t_0s. **Panel-b:** Time windows for peak outer-disk concentrations as a function of t_0 - times of C_N-half-maximum both before and after the peak for the accretion-flow case (solid colored lines and markers) and half-maximum after the peak for the midplane-flow case (dashed lines and black markers). All curves reference the results for 20 μm sized particles.

of t_0 for the four source regions considered and for both gas-flow cases. From this, one can see a steady fall-off in outer-disk contamination achievable for grains formed/initiated at later times. There is more than an order-of-magnitude difference between peak contamination of 20 μm grains formed between $t = 5 \times 10^4$ and 10^6 years, and no transport of 2 mm grains to the outer disk after 2×10^5 years.

Furthermore, the window of time during which peak outer-disk contamination occurs shrinks as a function of t_0. In Figure 5.9 panel-a, I plot the C_N curves as a function of time for 20 μm grains in the general accretion-flow case. In panel-b, I plot the times of C_N half-maximum before and after the peak as a function of t_0, bounded by a grey line indicating the times of particle initiation. This time-window, for the accretion-flow case, narrows considerably for larger t_0, though the whole is shifted to slightly later times for $t_0 = 5 \times 10^5$ and 10^6 years. After-peak half-maximum for the maximum-transport, midplane-flow case, however, presents a fairly fixed barrier in time ($t \sim 2.6$ Myr for this disk model). Mid-sized dust grains do not remain in the outer disk once it has evolved (viscously accreted and thinned) past a certain state.

Finally, in Figure 5.10, I plot the C_N peak values as a function of grain size for three different t_0-simulation sets. The limited state of outward transport at late times in the fiducial disk model

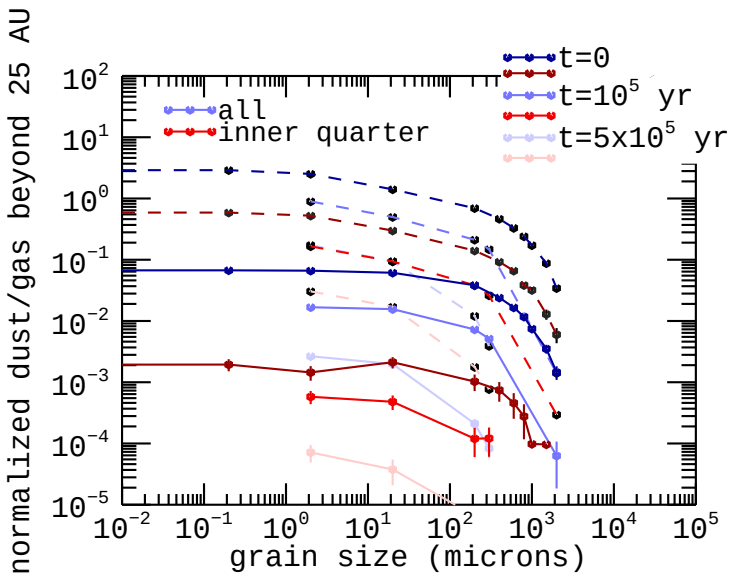

Figure 5.10: Peak C_N values as a function of grain size for the inner-quarter and the all source regions and for three different t_0 initialization times.

can best be summed up here, where one sees that by $t_0 = 0.5$ Myr the outer-disk contamination achievable by all grains initiated between 0.5–10 AU is about the same or less than the contamination from the inner-quarter region alone for $t_0 = 0$. Therefore, outward mixing at later times is still possible, but must be understood to be significantly less efficient.

These results agree with *Ciesla* (2010), who found that at some late time more CAI-type grains within a disk are those formed at earlier rather than later times. This is due to the greater prevalence of CAI formation at early times, but also to the stronger outflows produced in a hotter, expanding, young disk. In this way, comparing outward transport as a function of t_0 is similar to the study of §4.5.4 considering transport as a function of R_d, the compactness of the disk at $t = 0$; both greater source mass and outflow are in favor of greater outward mixing. The question, then, is how this might extend back in time to include the initial cloud collapse and formation of the star-disk system. *Dullemond, Apai, & Walch* (2006) found in their simulations of disk formation that heating and outflows were so extensive, they questioned primarily why not all disks aren't mostly crystalline, as opposed to the huge range (0–80%) of disk crystallinity observed (*Watson et al.*, 2009). *Ciesla* (2010) found the greatest outward mixing for the peak in disk mass, rather than the very earliest times, so the true answer, as indicated by observations, lies in some happy

medium. However, it is clear that disk formation and the earliest times likely play an important role in later-disk composition.

5.4 Varying the Initial Disk Mass

In this section, I consider the range in outward mixing achievable if I vary the initial mass of my model disk. For my fiducial model, I have used a disk with mass at $t = 0$ of $M_{D,0} = 0.03 M_{\odot}$. This is a reasonably average choice in terms of both the minimum-mass Solar Nebula (lower bound of $\sim 0.01 M_{\odot}$) and in terms of the masses of disks observed around other stars. Furthermore, my fiducial model has a disk lifetime, within the rest of the disk parameters I have chosen, that matches well the frequency of disks observed around stars of different ages. I have chosen such a disk as my fiducial model both in order to produce results widely applicable to observations of disks around other stars and because the prevalence of stars with debris disks and of stars found to host extra-solar planetary systems (*Currie, Plavchan, & Kenyon*, 2008; *Cumming et al.*, 2008; *Sierchio et al.*, 2010; *Wittenmyer et al.*, 2011) suggests a low probability that our own solar system formed under special-case circumstances.

However, the range and variety in disk masses observed is high, even for neighboring stars of similar ages (e.g., *Watson et al.* (2009); *Dahm* (2010)), and the gas mass of the early Solar Nebula cannot truly be known at this time. Furthermore, the study by *Watson et al.* (2009) found no correlation in a census of 84 classical T Tauri stars between the observed disk crystallinity and either the mass of the disk or the disk-star mass ratio. In order to offer aerodynamic mixing as a viable option to explain the crystalline compositions of disks, this mechanism must meet this non-correlation criterion, else invoke some counter-balancing mechanism, such as unknowns in the production rate of crystalline minerals. To study outward transport as a function of $M_{D,0}$, I have run simulations in the fiducial-disk setup and in the compact-$R_d = 5$AU setup for disk masses of $M_{D,0} = 0.01$ and $0.09 M_{\odot}$. For the fiducial setup, $M_{D,0} = 0.09 M_{\odot}$ produces a disk that is somewhat longer-lived than 10 Myr under the constant-viscosity processes modeled in my disk-evolution model. However, for the purposes of characterizing dependences observable for my simulation setup, it offers a decent range in the $M_{D,0}$ parameter space.

In Figure 5.11 panel-a, I plot the peak values of normalized contaminant concentration in the outer disk as a function of $M_{D,0}$ for 20 μm grains in the fiducial setup, where $R_d = 20$ AU and

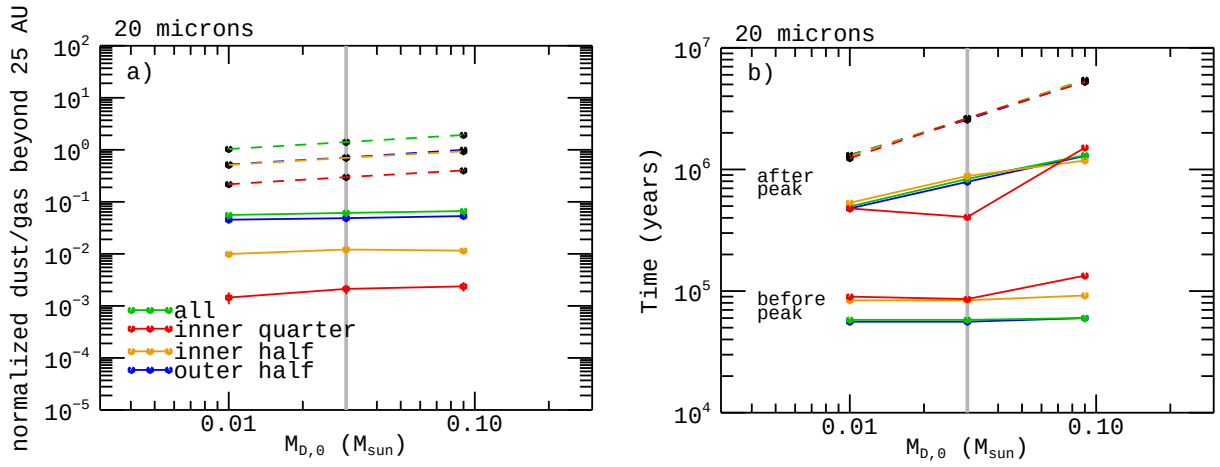

Figure 5.11: **Panel-a)** Peak C_N values as a function of $M_{D,0}$ for 20 μm particles and the four source regions. **Panel-b** Times of half-maximum C_N before and after the peak for the accretion-flow case (solid lines and colored markers) and after the peak for the midplane-flow case (dashed lines and black markers).

$\alpha = 10^{-2}$. From this plot, it is clear that outward mixing is largely independent of $M_{D,0}$. A slight slope toward higher peak C_N for higher $M_{D,0}$ is noticeable in the results of the midplane-flow simulations, but this represents less than a factor of two difference between transport in the $0.01M_{\odot}$ and $0.09M_{\odot}$ disks. The amount of time over which the disks experience high outer-disk contamination, however, is strongly dependent on the initial disk mass, as shown in Figure 5.11 panel-b. Initially more massive disks are longer lived, with similarly longer-lived conditions in which outer-disk surface densities are sufficient to sustain a population of mid-sized 20 μm particles.

Furthermore, when it comes to the large particle sizes, variation in outer-disk surface densities means there is a strong dependence of $M_{D,0}$ on outward mixing. This is shown in Figure 5.12 panel-a wherein I plot peak C_N values as a function of $M_{D,0}$ for 2 mm sized grains. For an initially 0.01 $M_{\odot}$ disk, these grains do not reach the outer disk at all, even under the influence of outward advection in the midplane-flow case. Therefore, the influence of $M_{D,0}$ on outward mixing is summed up in panel-b. Here, I plot maximum C_N for the all source region as a function of grain size for the three $M_{D,0}$ disk models in the fiducial setup. In general, small grains experience equal levels of mixing independent of the initial disk mass. However, the max-C_N curves diverge toward larger grain sizes and the upper-limit in grain size that can be transported to beyond 25 AU is notably smaller for the less massive disk than for the more massive one.

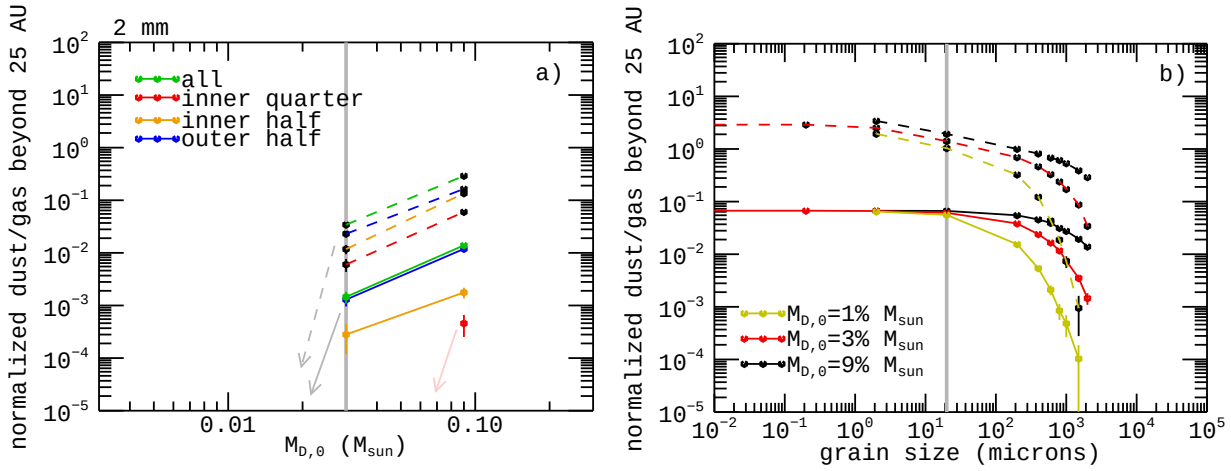

Figure 5.12: Peak C_N values as a function of $M_{D,0}$ for 2 mm particles (**panel-a**) and as a function of grain size in the all source region for different disk masses (**panel-b**). Accretion-flow case: solid lines and colored markers. Midplane-flow case: dashed lines and black markers.

The figures I have shown here are only for the fiducial disk setup with $R_d = 20$ AU, but the results of this experiment using a more compact disk configuration with $R_d = 5$ AU are essentially identical. These results suggest that a lower-mass disk with $M_{D,0} = 0.01 M_\odot$ should be equally consistent with the transport of 20μm sized grains to the comet-forming regions as the fiducial-disk model and so conform to the *Stardust* results equally well. This is reassuring given our uncertainties in the mass of the Solar Nebula, though this model cannot then offer new constraints to reduce those uncertainties. Holding the other disk-model parameters constant, a lower-mass disk offers a smaller window in time in which to form a comet enhanced in hot minerals via turbulent mixing. However, the disk lifetime as a whole is shorter and so a lower-mass disk offers a smaller window of time for forming most solar-system architecture.

Qualitatively, these simulation results are also a good match to the observed non-correlation between disk crystallinity and mass for systems around other stars, though there are a number of caveats. Using $M_{D,0}$ as a mixing measure presumes that the correlations that exist for that initial condition will hold for disk masses measured at a later given time, despite the fact that the rates of evolution and disk-mass loss between different-$M_{D,0}$ disks may vary. In the static-temperature viscous-disk model, at least, the rate of relative mass loss is set by the initial distribution of mass (R_d), rather than its sum ($M_{D,0}$). Also, because of the *Stardust* results with their clear constraints

on grain size, I have focused on transport of hot grains to the outer disk, defined as beyond 25 AU. However, observations of disk-composition for extra-solar disks tend to probe smaller distances, 10 AU or less. While this likely shifts the maximum grain size for which my results predict no-correlation to slightly larger sizes, it is still not known what grain-sizes transport and mix the bulk of material in disks around other stars. My simulations suggest that turbulent mixing is consistent with the compositions of extra-solar disks *if* most high-temperature material is held and transported within the small-grain population.

5.5 Varying the α-scaling of the Disk Viscosity

The most poorly constrained parameter of the disk-evolution model is the α-parameter of the disk viscosity, whose biggest effect is on the rate of mass transfer through the accreting disk. Assuming the *Shakura & Sunyaev* (1973) model to describe the viscosity, many attempts have been made to test and to measure α through observations and modeling of disk outburst events (e.g., *Pringle, Verbunt & Wade* (1986)) or through censuses of disk masses, ages, and accretion rates (*Hartmann et al.*, 1998; *Kitamura et al.*, 2002). In the simplest disk-evolution models, including the one used in this thesis, α is held spatially and temporally constant. However, some studies pairing disk-evolution–similarity-solution models and disk observations suggest α should decrease toward larger radii (*Isella, Carpenter, & Sargent*, 2009), while models involving episodic accretion events to explain rapid assmebly of stellar masses necessarily require short periods of time when the effective disk-evolution α is quite high relative to the mean (e.g., *Dunham et al.* (2010)). Models that attempt to replicate disk viscosity through phenomena such as the magneto-rotational instability (MRI) (*Balbus & Hawley*, 1991) sometimes predict αs that seem inconsistent with observations (*King, Pringle, & Livio*, 2007), but also predict phenomena such as time-variable turbulence (*Reyes-Ruiz*, 2007), and effective αs that varying with height above the disk midplane (e.g., *Flaig, Kley, & Kissmann* (2010); *Kretke & Lin* (2010)). The dead-zone model of MRI turbulence predicts a region near the midplane in the inner disk where the effective α drops toward zero (e.g., *Hasegawa & Pudritz* (2010)).

For the fiducial-disk model and the majority of simulations presented in this thesis, I have used an α-viscosity (always) with $\alpha = 10^{-2}$ (almost always). This value produces a relatively high level of turbulence which may or may not be compatible with grain settling observed in some disks (*Miyake*

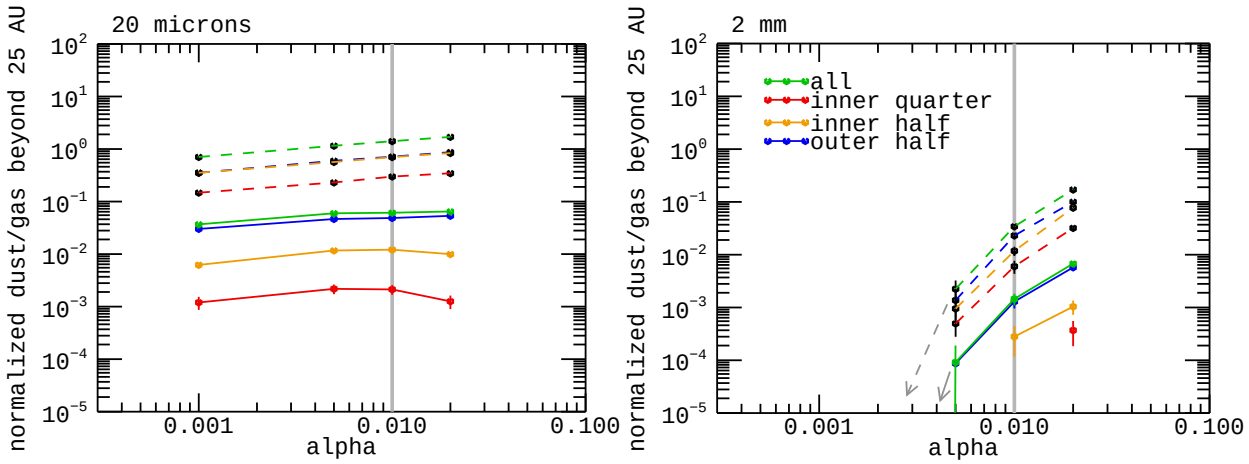

Figure 5.13: Maximum normalized concentration beyond 25 AU as a function of α for two grain sizes. Accretion-flow case: solid lines and color markers. Midplane-flow case: dashed lines and black markers.

& Nakagawa, 1995; *Dullemond & Dominik*, 2004) and that modeled for some particle-interaction-dynamics simulations (e.g. *Cuzzi, Hogan, & Shariff* (2008)). However, $\alpha = 10^{-2}$ is compatible with disk-census observations and produces a reasonable 5.5 Myr lifetime for my fiducial-disk model. On the other hand, my particle-transport model assumes that the diffusivity of the ensemble is directly proportional to the disk viscosity (meaning $D_p \propto \alpha$) and in §4.5.3, I showed that varying the magnitude of the diffusivity by less than half an order-of-magnitude produced strong variation in the outward mixing of the particle ensemble. Therefore, in this section, I test the dependance of outward mixing on α by running particle-transport simulations in disks with $\alpha = 10^{-3}, 5 \times 10^{-3}$, and 2×10^{-2} (and otherwise retaining $M_{D,0} = 0.03 M_\odot$ and $R_d = 20$ AU, as usual).

In Figure 5.13, I plot the peak outer-disk concentration for these simulations for 20 μm and 2 mm-sized grains as a function of α. For the 20 μm grains, the dependance on alpha is small. There is a slight increase in peak outward mixing for higher α, but it is less than a factor of two across more than an order-of-magnitude in α for the accretion-flow case and about a factor of two across one order-of-magnitude in the midplane-flow case. For 2 mm-sized particles, however, outward mixing depends strongly on α. In low-α disks, any particles from the inner source regions are less likely to reach the outer disk in the accretion-flow case, and no 2 mm particles in either gas-flow case reach the outer disk for $\alpha = 10^{-3}$. Therefore, as seen with the initial disk mass,

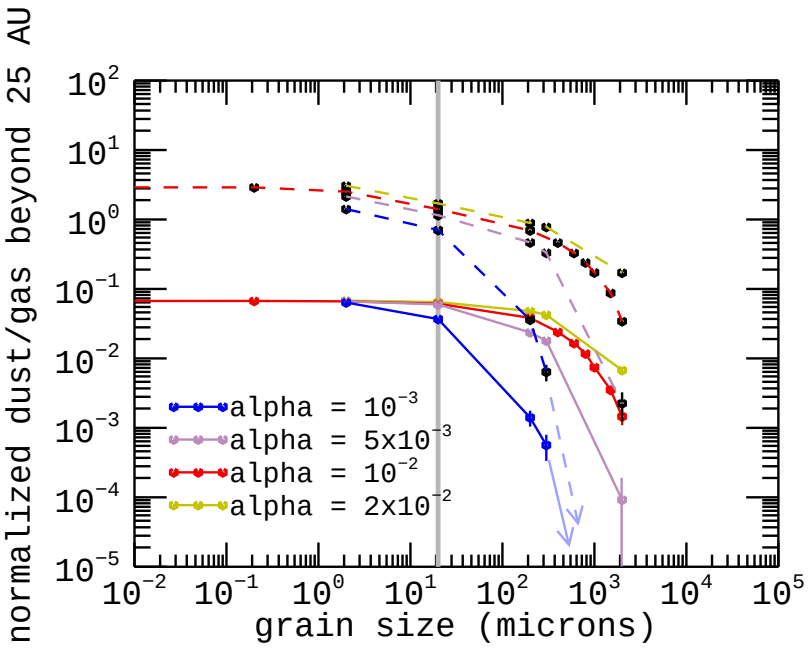

Figure 5.14: Maximum normalized concentration beyond 25 AU for the all source region as a function of grain size. Simulations run in the fiducial disk setup with $M_{D,0} = 0.03 M_{\odot}$ and $R_d = 20$ AU, but varying α. Accretion-flow case: solid lines and color markers. Midplane-flow case: dashed lines and black markers.

varying α primarily changes the upper-limit in grain-size that can be transported to beyond 25 AU, as summarized in Figure 5.14.

α is directly proportional to the diffusivety of the particle ensemble and also to the outward-flow velocity of the gas in the midplane-flow case. That the dependence on α of general outward mixing of well-coupled grains is so low then, suggests that these effects are largely counteracted by the more-rapid disk evolution that also takes place in higher-α disk models. Particles well-mixed with the gas will be rapidly accreted onto the central star at the rate of that disk mass. As with lower-mass disks, higher-α disks have shorter lifetimes and so the time-window for outer-disk contamination is also shorter. Unlike in low-mass disks, however, the high diffusivity that comes with high α means that outward mixing is also faster, so that the entire transport scenario shifts to earlier times for higher-α disks. This is shown in Figure 5.15, where I plot, for 20 μm sized particles, both the outer-disk contamination as a function of time, and the time-window for peak contamination as a function of α.

The primary conclusions, then, about outward mixing as a function of α are that the α-

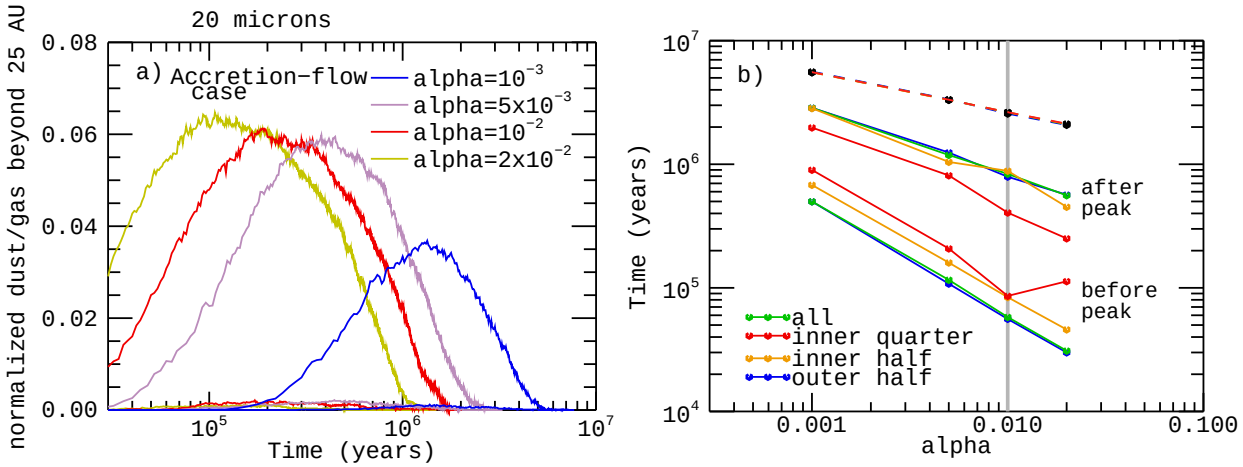

Figure 5.15: **Panel-a)** Normalized concentration beyond 25 AU for 20 μm particles from the all and inner-quarter source regions. **Panel-b)** Times of C_N half-maximum as a function of α before and after the peak in the accretion-flow case (solid lines and colored markers) and after the peak in the midplane-flow case (dashed lines and black markers).

dependence is small, but not non-existent. For the moment the α model for disk viscosity and diffusivity is likely sufficient for the purposes of particle-mixing simulations — as long as diffusivity and disk evolution are considered together. However, more complete models of disk viscosity will likely yield at least one or two interesting results from future work, perhaps particularly as researchers come to better understand the earliest, potentially outburst-driven stages of disk formation and evolution.

5.6 The Disk Temperature Distribution

For all of my outward-mixing simulations, including those discussed in Chapter 4, I use a static, power-law model for the disk temperature distribution that roughly corresponds to the temperature profile of a passive, flared disk around a 5 $L_\odot$ star (see §2.4). This temperature model has only two parameters, the temperature of the disk at 1 AU, $T_{\rm AU}$, and the slope of the disk-temperature as a function of R, q_T. In this section, I explore the dependence of the outward mixing of inner-disk grains on these two parameters.

5.6.1 Varying the Baseline Temperature

The primary reasons to consider varying the baseline disk temperature, $T_{\rm AU}$, are that: 1) disks around stars of various luminosity will be heated by stellar irradiation to various base temperatures; and 2) accretional heating in the disk at the earliest times when accretion rates are high tends to raise a disk's temperature, particularly in the inner disk (see §2.4). Varying $T_{\rm AU}$ is similar to varying the α parameter of the disk viscosity. Since, from §2.2,

$$\nu = \alpha \Omega_{\rm K,mid} H_g^2 \,,$$

where $\Omega_{\rm K,mid}$ is the Keplerian angular velocity at the disk midplane and H_g is the disk-gas scale-height:

$$H_g = \frac{c_s}{\Omega_{\rm K,mid}} = \frac{1}{\Omega_{\rm K,mid}} \sqrt{\frac{k_B T}{\mu m_H}} \,,$$

where c_s is the sound speed in the gas and μm_H is the average mass of a gas particle. Therefore,

$$\nu \propto \alpha T_{\rm AU} \,, \tag{5.1}$$

and it is the $\alpha T_{\rm AU}$ combined quantity (in the static, power-law–temperature disk model) that determines the rate of viscous evolution of the disk surface density.

Using Equation (5.1) and the results of §5.5, one might then predict that outward mixing depends on $T_{\rm AU}$ in the same way it depends on α: that generally mixing of well-coupled grains is mostly independent of $T_{\rm AU}$, but that a colder, more slowly evolving disk will mix fewer large grains to the outer disk. However, Figure 5.16, shows that this is not the case, that instead the outer-disk contamination achievable within a particle-transport simulation is essentially independent of $T_{\rm AU}$, no matter the particle size. $T_{\rm AU}$ affects disk evolution and particle diffusivity in the same way as α. However, disk temperature also plays an important role in the drag a particle feels against the gas flow, particularly in the Epstein-drag regime where (from §3.2.1)

$$F_D = -m_d \frac{C_R}{3} \rho_g v_{\rm therm} \Delta v \,,$$

where m_d and C_R are the particle mass and surface-area-to-mass ratio, ρ_g and $v_{\rm therm}$ are the local

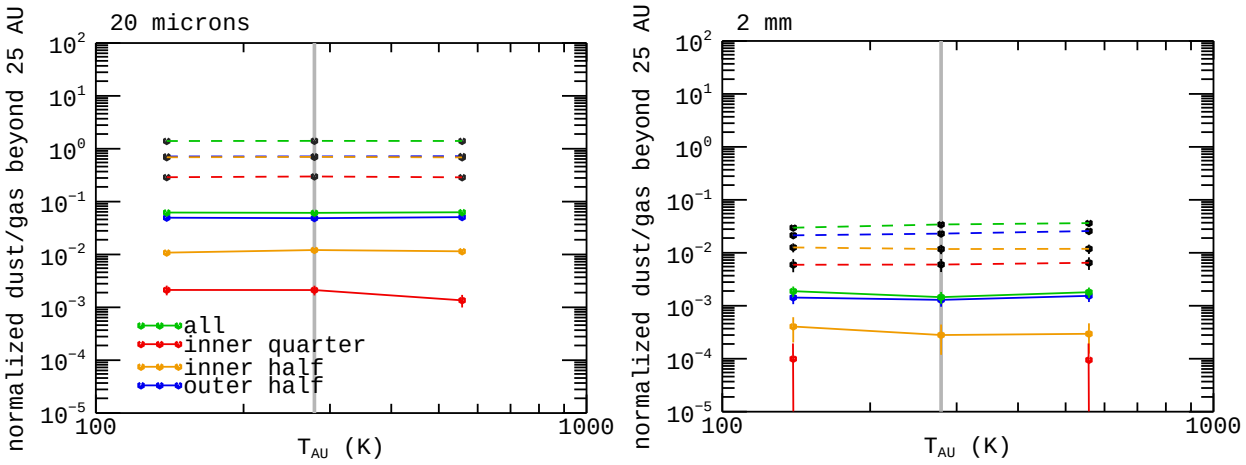

Figure 5.16: The maximum nomralized concentration beyond 25 AU as a function of the baseline disk temperature, $T_{\rm AU}$ for two particle sizes. In the fiducial disk model, $T_{\rm AU} = 278.9$ K. Accretion-flow case: solid lines and color markers. Midplane-flow case: dashed lines and black markers.

gas density and thermal velocity, and Δv is the difference between the particle and gas velocities. Next,

$$v_{\rm therm} = c_s \sqrt{\frac{8}{\pi}} \propto \sqrt{T}\,,$$

and, in a vertically isothermal disk like that used in my model,

$$\rho_g \propto \frac{\Sigma_g}{H_g} \propto \frac{1}{\sqrt{T}}\,.$$

Therefore, varying the disk temperature has no effect on the gas drag a particle feels in the Epstein-drag regime, so this aspect of the particle transport also remains balanced.

The balance, when varying $T_{\rm AU}$, between disk evolution, and particle advection and diffusion is shown in Figure 5.17, where I plot both the outer-disk contamination as a function of time varying $T_{\rm AU}$ and the time-windows for peak contamination as a function of $T_{\rm AU}$. Because disk evolution is faster in a hotter disk, the function for outward mixing is also shifted to earlier times, but the shape of that function remains essentially unchanged. The *timing* of outward transport still varies, but the net result is the same. This is a good illustration of why it is important to consider temperature/viscosity/diffusion and disk-evolution simultaneously. Higher disk temperatures should produce *faster* outward mixing, but not necessarily *more*.

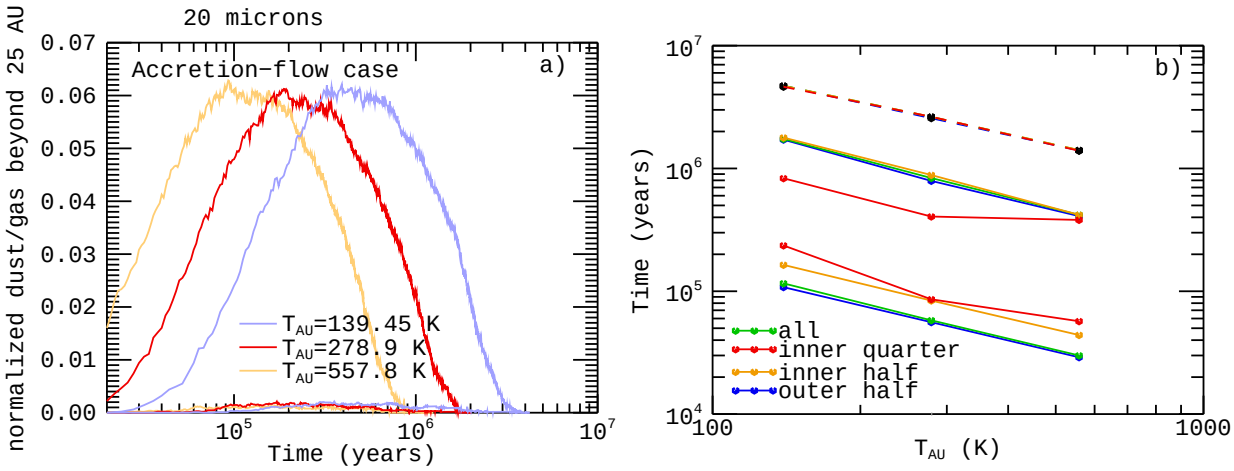

Figure 5.17: **Panel-a)** Normalized concentration beyond 25 AU for 20 μm particles from the all and inner-quarter source regions. **Panel-b)** Times of C_N half-maximum as a function of $T_{\rm AU}$ before and after the peak in the accretion-flow case (solid lines and colored markers) and after the peak in the midplane-flow case (dashed lines and black markers).

5.6.2 Varying the Radial-slope of the Disk Temperature

The fiducial, static-temperature model uses $q_T = -0.5$, which is appropriate for a simple passive model of disk temperature where the disk is heated only by intercepted radiation from the central star and where the disk flares, increasing scale-height with distance from the star so that the disk surface sees the starlight at the same interception angle for all disk radii (*Armitage* (2010), pp 45–47). (A flat disk structure where the incidence of starlight becomes ever shallower with increasing R has $q_T = -0.75$, *Armitage* (2010), pp43–45.) Even the energy-balanced temperature model discussed in §2.4.1 that includes accretional heating also includes a temperature-slope of $q_T = -0.5$ in the cold outer disk where stellar irradiation still dominates the temperature profile. However, as discussed in §2.4.1, how a disk is heated can be fairly complex and there are a number of reasons to consider variations in q_T. These include:

* Dominance of different heating mechanisms: As shown in the evolving-temperature models of §2.4.1, the dominance of accretional heating in the early, inner disk while the outer disk remains cold, can lead to relatively complex temperature structure. In these models, such as the one shown in Figure 2.6, both the innermost disk and the outermost disk heated by the ambient temperature of the parent molecular cloud have shallow temperature gradients,

while the transition region between accretion and radiant heating has a sharp fall-off in disk temperature and a steep q_T.

* Variations in types of disk opacity: As suggested by some of the complex temperature structure in the evolving temperature model (Figure 2.6), regional variations in disk opacity, largely dominated by dust opacities, can strongly affect the fall-off rate of disk temperature. For the models of *Keller & Gail* (2004) (assuming the flat disk-structure model normalized around $q_T = -0.75$), the authors report $q_T \approx -1$ where ice-coated grains dominate the opacity, and $q_T \approx -0.62$ where bare grains do so.

* Dust settling to the midplane: Many disk observations suggest that for some disks the dust-grain population has settled toward the midplane (e.g.,*Miyake & Nakagawa* (1995); *Furlan et al.* (2006); *Tsukagoshi et al.* (2011)). This is often attributed to grain growth, but could also occur if disk turbulence dropped to relatively low levels. In either case, the lack of small grains in a disk's atmosphere means that the disk structure flattens (*Dullemond & Dominik*, 2004) and less starlight is intercepted, providing a disk with a steep q_T.

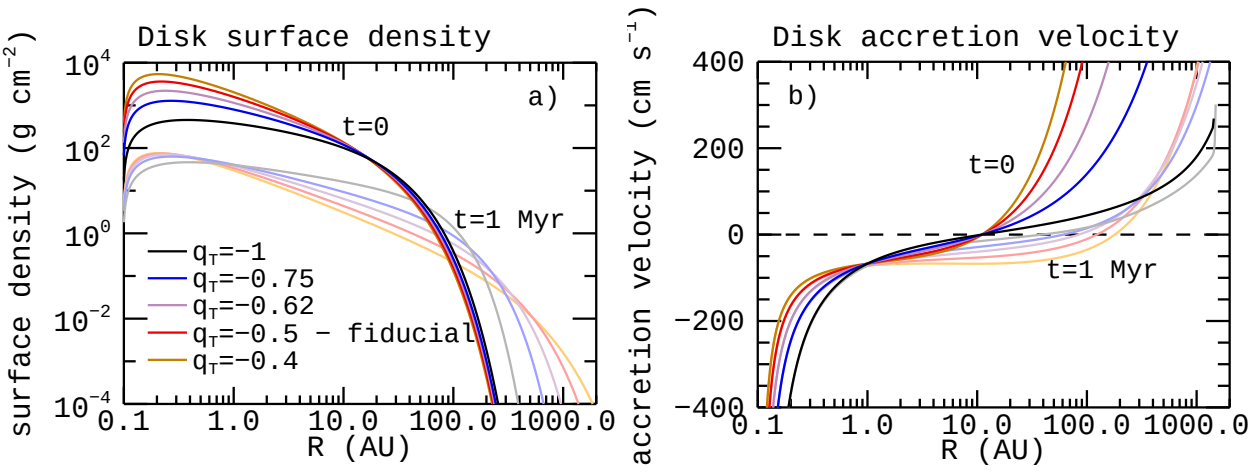

Figure 5.18: **Panel-a)** Surface-density profile and **Panel-b)** Gas radial-flow accretion velocity for disk models varying the radial slope of the disk temperature, q_T. Curves plotted for $t = 0$ (dark curves) and $t = 1$ Myr (light curves). Disk models using the fiducial model setup with $M_{D,0} = 0.03 M_\odot$, $R_d = 20$ AU, $\alpha = 10^{-2}$, and $T_{AU} = 278.9$ K.

To test the dependence of outward mixing in my simulations on q_T, I have run particle-transport simulations in disks with q_T ranging between -1 and -0.4. One important note is that varying q_T also varies the surface-density structure of the disk. In the α model for disk viscosity with a power-law disk structure, q_ν, the power-law constant of the viscosity, goes as $q_\nu = 3/2 - q_T$. And, in the steady-state approximation of disk structure, $\Sigma_g \propto 1/\nu$. Therefore, a steeper temperature profile leads to a shallower surface-density profile. This is illustrated in panel-a of Figure 5.18, where I plot the disk–surface-density profiles for these simulations at $t = 0$ and $t = 1$ Myr. In these disk models, I have left $T_{\rm AU}$ fixed to the fiducial value of 278.9 K. Therefore, the disks with steeper q_T are also generally colder and evolve more slowly than the fiducial model. This leads to both slower outward flow at the outer disk edge, and slower main-inward accretion, as shown in panel-b of Figure 5.18.

In some ways, varying q_T can be compared to varying the initial disk compactness, R_d, (discussed in §4.5.4). Both initially compact disks and disks with shallow q_T (steep q_ν and Σ_g) have more mass distributed at small disk radii and so have faster outer-disk outflows and evolve more rapidly. This can lead to a greater degree of outer-disk contamination, as shown in Figure 5.19 panels-b1 and -b2. However, while §4.5.4 showed that outward mixing is strongly dependent on R_d, Figure 5.19 shows that it is only moderately dependent on q_T. This is because q_T, also has a strong affect on the probability for a particle diffusing outward versus inward and on the relative strength of headwind drag on a particle orbit, both of which favor outward transport in steep, rather than shallow, q_T disks.

In the fiducial disk model with $q_T = -0.5$, the roughly $\Sigma_g \propto 1/R$ profile in the main, quasi-steady part of the disk produces an even distribution of mass per AU. This means that for a given diffusivity (proportional to the disk viscosity) a particle in the ensemble is equally likely to diffuse inward as outward. However, if Σ_g follows a shallower profile, as with steep q_T, then in the main disk there is locally more disk mass outward and a particle is more likely to be diffused outward. A steep q_T and cold outer disk do mean that diffusion in the outer disk is slower, but the mass distribution still strongly influences where well-mixed particles are held within the disk.

Also, if q_T is steep, leading to a shallow disk–surface-density profile, then the radial-pressure gradient is relatively more shallow as well. (Even if the surface-density profile is unchanged, colder temperatures still lead to denser gas at the disk midplane and a shallower radial pressure gradient).

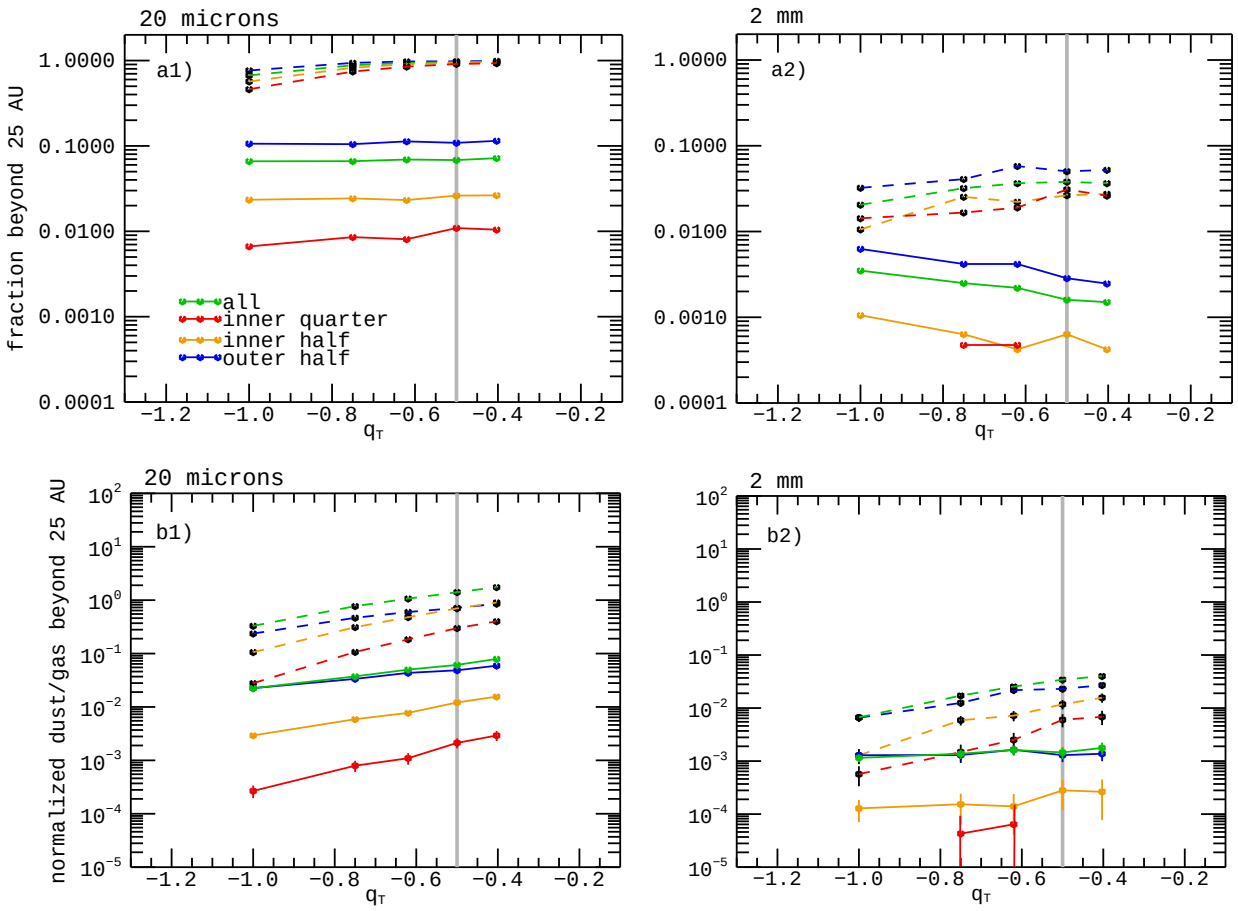

Figure 5.19: **Panels-a1 and -a2)** Maximum fraction of source particles mixed outward to beyond 25 AU as a function of q_T. **Panels-b1 and -b2)** Maximum normalized concentration of particles beyond 25 AU as a function of q_T. Accretion-flow case: solid lines and color markers. Midplane-flow case: dashed lines and black markers. Note that a steeper disk-temperature profile (q_T) corresponds to a shallower disk surface-density profile.

Steep radial-pressure gradients cause disk gas to orbit more slowly than Keplerian and lead to headwind drag, so steep q_T and shallower pressure gradients means a lessening of the headwind-drag effect. This is demonstrated most clearly in panel-a2 of Figure 5.19, plotting the peak fraction of 2 mm grains transported to the outer disk. In the accretion-flow case, a larger portion of these larger grains reach the outer disk for steep q_T because their range within the disk is less restricted due to headwind drag. This does not lead to more outer-disk contamination of 2 mm grains in the steep q_T cases, however, because shallow q_T, with more mass distributed into the hot, inner disk, still has a larger source mass with which to contaminate the outer disk.

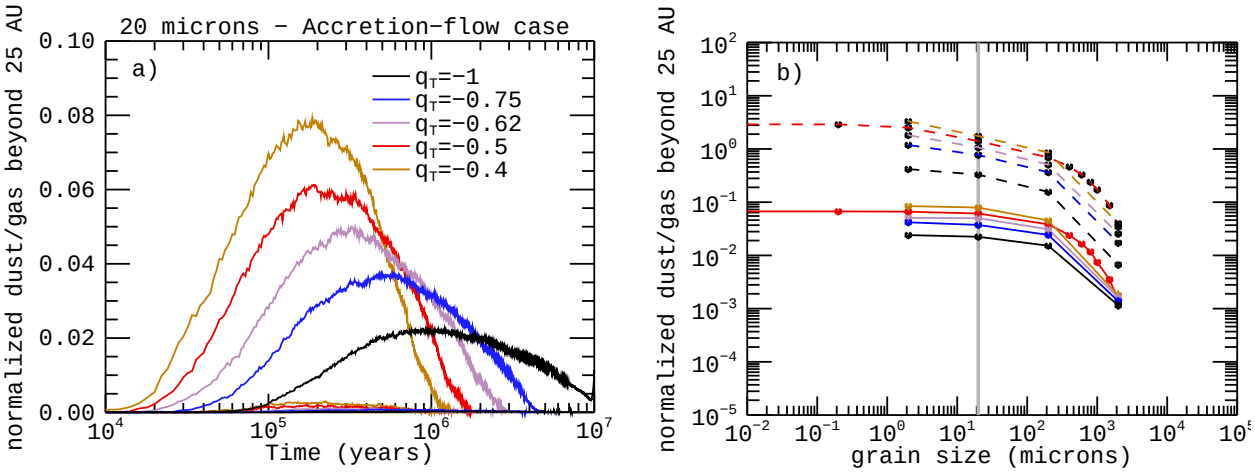

Figure 5.20: **Panel-a)** Normalized concentration beyond 25 AU of 20 μm particles from the all and inner-quarter source regions in the accretion-flow case in disks varying q_T. **Panel-b)** Maximum normalized concentration beyond 25 AU as a function of grain size for the all source region. Accretion-flow case: solid lines, colored markers; Midplane-flow case: dashed lines, black markers.

The results of the outward-mixing dependence on q_T are summarized in Figure 5.20. General outward mixing, particularly of small grains, is stronger for shallower disk-temperature profiles because a hotter disk has faster outflows and disk expansion and, importantly, because more mass is initially distributed toward small AU, creating a larger source mass for outer-disk contamination. However, the outward mixing of larger, more poorly coupled grains, is less dependent on q_T, because a cold outer disk has a shallower radial pressure gradient providing weaker headwind-drag confinement of the particle ensemble. Colder disks also evolve more slowly and may retain grains at large AU for longer periods of time. This suggests that disks with grains settled toward the disk midplane may retain a larger mass reservoir (of both gas and dust) in the outer disk, than hotter flared disks. However, in terms of the *Stardust* results, a hotter disk with a shallower q_T would be more likely to process a larger mass of grains at high temperatures and to send moderately coupled 20 μm grains out to contaminate the comet-forming regions.

5.7 Conclusions

The primary motivation for examining the aerodynamic outward mixing of dust grains in protoplanetary disks came from the results of the *Stardust* mission that found grains processed at high temperatures mixed within the material of a comet formed in the cold regions beyond the orbit

of Neptune. Another important motivation has been the large scatter and poorly defined trends in crystallinity (the relative fraction of observed silicates processed at high temperature) observed in disks around other stars. Therefore, the primary focus of these two chapters has been to systematically tie together aerodynamic transport processes with disk evolution in order to take into account the effect of the variable dynamic nature of disk systems on mixing-transport outcomes.

In Chapter 4, I examined the dependence of outward mixing on four parameters most directly tied to the questions of particle-transport and disk evolution. Two of the biggest unknowns tying protoplanetary disk models to particle-transport effects are (1) the velocity structures of evolving disks, directly important for the advection of grains, and (2) the portioning between diffusivity and viscosity within the disk. Next, (3) the actual physical sizes of dust grains not only help to tie transport results to the *Stardust* findings, for which real grain sizes are provided, but also link directly to disk aging; an older disk will no longer support larger grain sizes as it loses mass and becomes more tenuous. Finally, (4) the initial compactness of the disk is a direct example of variation between different disk systems that also has a strong influence on how disk evolution proceeds.

All four of the parameters explored in Chapter 4, were found to have important impacts on the degree of outward transport and outer-disk contamination achievable within a particle-transport simulation. This, then, begs the question of what other parameters might be equally important, both in terms of the physical properties of disks and of the particular model used to calculate the disk structure and evolution. Therefore, in this chapter, I have extended my search of parameter space to include other disk-model parameters of concern. My primary conclusions are these:

1. **The relative mass of source material is the primary factor controlling resultant outer-disk contamination.** In terms of the parameters tested, this source-mass importance is demonstrated relating to: the initial compactness of the disk, R_d, the timing of particle formation/initiation, t_0, the slope of the disk temperature (and therefore initial-mass) distribution, q_T, and, of course, the various possible source regions for hot grains transported within disks.

2. However, a number of disk-model and transport parameters are as yet poorly constrained and several of these also have a strong impact on simulated outward mixing. Therefore, **to**

rank the parameters I have tested that have the strongest impact on outer-disk contamination: The initial compactness of the disk has the strongest impact on the amount of hot material that may be mixed into the outer disk. Of next greatest importance are the uncertainly constrained diffusivity of a dust-grain population and the velocity structure of the disk gas. The most outward mixing occurs for an initially compact disk with regions of outward-flowing gas and high diffusivity relative to the disk viscosity. Finally, from this chapter, early-time ($t_0 \lesssim$ a few $\times 10^5$ years) production of hot minerals is also key to reaching high crystallinity fractions. Crystalline silicates formed at small AU at late times simply will not reach the outer disk in sufficient quantities to match observations.

3. **Finally, each parameter I have tested emphasizes the importance of including disk evolution along-side particle-transport and mixing calculations.** For example, my simulations measure faster outward mixing at $t = 0$ for both a more compact disk (small R_d) and a hotter baseline disk temperature (T_{AU}). However, I measure no dependence in *peak* outer-disk contamination on T_{AU}. A static-disk simulation would reveal only that increase in initial mixing rate and could lead to the conclusion that, for example, disks orbiting more luminous stars should experience a greater degree of outward mixing, when in fact more rapid disk evolution for higher T_{AU} entirely counter-balances the mixing-rate effect over the lifetime of the system.

Next, to specifically relate the parameters tested in this chapter to the results from *Stardust* and ongoing attempts to define our Solar Nebula, I find that:

1. The discovery of tens-of-microns crystalline silicates in comet Wild 2 material does not help to constrain α of our Solar Nebula (presuming the α-model of disk viscosity to be well representative of protoplanetary disks). The α parameter has a low impact on the outward mixing of grains, as long as a direct correlation between disk viscosity and dust-particle diffusivity is maintained, as the simulations presented here assume.

2. Outward mixing of 20 μm grains is compatible with a range of disk masses, down to at least $M_{D,0} = 0.01 M_\odot$. Outward mixing in my simulations is largely independent of initial disk mass. This means that one need not invoke a special case wherein our Solar System formed

from an unusually massive disk. However, aerodynamic mixing in this case also does not supply constraints as to what the mass of our Solar Nebula may have been.

3. In agreement with the findings of *Ciesla* (2010), high temperature minerals found within comet material are statistically more likely to have formed at the earliest times of Solar Nebula history. Not only does formation of the highest-temperature material (such as CAIs) require a young, hot disk, but transport of inner-disk material outward is significantly more efficient at early times.

These points are in addition to the Chapter 4 findings that: (1) outward transport of grains in the size-range relevant to the *Stardust* crystalline silicates (up to tens of microns) *is* feasible via aerodynamic mixing processes, but that (2) grains formed very near the sun, such as, probably, CAIs, likely require some outward gas flow for aerodynamic effects to explain their presence in a comet like Wild 2.

For comparison to observations outside our Solar system, the results of Chapter 4 found a potentially favorable comparison between increased outward mixing in more compact disks and the potential disk-crystallinity–accretion-rate correlation observed by *Watson et al.* (2009). Disk parameters tested in this chapter also show favorable comparisons between mixing trends and the *Watson et al.* (2009) survey results. Specifically, outward mixing appears largely independent of both the initial mass of the disk and the baseline disk temperature, while the *Watson et al.* (2009) survey found no correlations between disk crystallinity and either observed disk mass or stellar luminosity (which sets the baseline disk temperature in a passive-disk model). As discussed by those authors, such non-correlations are puzzeling, as both disk mass and heating by the central star are believed to be potentially important for the production of crystalline silicates. However, the results of my simulations suggest that the resolution of these puzzles should not require taking basic aerodynamics-mixing effects into account.

One note, however, is that comparing my simulation peak-mixing results to these survey results possibly may not properly account for timing effects present within the observations. The surveyed disks are observed at 1–2 Myr of age, which generally falls during the infall stage of 20 μm and larger grain sizes in my simulations. However, more massive disks, for example, support slower infall and higher outer-disk concentrations at a given time than simulated less massive disks. This

could have consequences for the relative observed crystallinities between different disk-mass cases, though the extent of the effect is unclear as crystalline and non-crystalline grains should experience infall roughly equally. However, my simulations do predict that the early-time outward mixing of the hot-grain population should proceed roughly identically for disks of different masses.

Whether or not aerodynamic mixing is *the* primary explanation for the existence of hot minerals in the cold outer-regions of disk systems, my simulations show that it is an important aspect determining the composition and compositional gradients found within a disk. Furthermore, through aerodynamic mixing, variation between the initial conditions found within young disks (e.g., mass distribution, timing and location of mineral formation) should lead to a wide range in disk compositional properties observed at later times. This prediction agrees well with studies that find wide scatter in observed disk compositions even within disk populations believed to have formed within relatively quiescent environments, such as those of the Taurus-Auriga young cluster (*Watson et al.*, 2009).

I have shown that the interactions between turbulence and evolving disk structure must have important consequences within a protoplanetary system. However, the precise outcome of mixing within a given, naturally evolving disk environment remains poorly resolved, largely due to presistent uncertainties concerning disk structure and mechanics. Nevertheless, there are a number of possibly important effects, not explored here, that should and can be pursued in future studies. Some specific avenues of research include:

* **Mixing within a 2D disk structure.** Mixing and transport of grains within a 2D (radial,vertical) disk structure have been explored by a number of authors (e.g., *Takeuchi & Lin* (2002); *Keller & Gail* (2004); *Ciesla* (2009)). However, these studies have either focused on the bulk transport of grains, or have neglected the specifics of grain-size effects. Of particular interest for the outward mixing of large grains is the outward "tail-wind" drag on particles high within a flared-disk atmosphere. Large grains are expected to mostly settle-out to the disk midplane, as discussed by *Ciesla* (2009). However, moderate to high turbulence (such as assumed in the $\alpha = 10^{-2}$ disk models used in my simulations) should allow a non-negligible fraction of grains at least tens-of-microns in size to experience outward drag at high z within the disk (§3.1). Turbulent *vertical* diffusion of grains should then lead to some degree of

circulation-style *radial* diffusion (*Pavlyuchenkov & Dullemond*, 2007) of grains in excess of the radial diffusion employed within my simulations. Whether such excess outward transport is significant remains to be tested.

* **Mixing during disk formation.** Work by, e.g., *Tscharnuter et al.* (2009), *Dullemond, Apai, & Walch* (2006), and *Ciesla* (2010), as well as simulations presented in this chapter, all suggest that the greatest outward transport should occur early in a disk's lifetime, possibly as the star-disk system is forming. Therefore, mixing of imperfectly coupled grains during disk formation merits further study. While disk-formation simulations tend to be computationally expensive, the window of interest for such a study would be on the order of 10^5 years, rather than the several 10^6 year disk lifetimes explored in my current simulations. Furthermore, current theories of star formation suggest that the birth of star-disk systems may be characterized by episodic-accretion events of high mass processing set within a more quiescent accretion environment. High-accretion events would provide periods of stronger gas inflow, but also higher disk temperatures and enhanced turbulent diffusion. Both the formation of crystalline silicates and the transport of grains within such a changeable early-disk environment are prime candidates for future study that could shed new light on dust processing with protoplanetary systems and our own Solar Nebula.

* **Mixing within new and alternative disk models.** While a large focus of my work has been the influence of disk evolution and a changing disk environment on grain transport, I have used a single, simple model (the α-disk model) to describe that evolution, and study of particle mixing within alternative as well as more-sophisticated disk models is warranted. For example, *Boss* (2004) considered the mixing of trace particles within a marginally self-gravitating disk, and disks involving the magnetorotational instability and possible dead-zones of low turbulence at the disk midplane are often discussed in the literature as, for example, structures that might preserve larger grain-sizes within the disk for longer periods of time (*Jacquet, Fromang, & Gounelle*, 2011). Dead-zone disk models, however, have yet to be fully explored in terms of their particle-transport properties. Also, it is likely that our own Solar Nebula was born within a rich star-cluster and experienced periods of strong external photoevaporation (*Throop & Bally*, 2005). As low surface-density in the outer disk can drive

outward gas flows, such episodes may have been important for the transport of Solar System minerals and should be explored in terms of their particle-mixing characteristics.

Limited understanding of disk structure is not the only obstacle to achieving a full understanding of the observed distribution of high-temperature grains within our own and other circumstellar systems. Formation mechanisms for high-temperature materials must also be more clearly outlined. Given the variety of material recovered by the *Stardust* sample-return mission, these processes likely relate not only to the local temperature evolution within a disk, but also to grain-growth and possibly even early planetesimal-formation processes. Furthermore, as will be discussed in the next chapter, our understanding of the transport of marginally-coupled grains remains incomplete. That mid-sized particles experience headwind-drag infall as a disk ages and thins is potentially in direct conflict with mm-sized grains observed at large distances within many extrasolar protoplanetary disks (*Testi et al.*, 2003). Until this conflict is resolved, mixing of large grains within a disk will remain an open area of study.

Chapter 6

The Necessity of Local Structure and Small-scale Concentration for Planetesimal Formation

Several recent theories of planetesimal formation (e.g., *Youdin & Shu* (2002); *Johansen et al.* (2007)) consider the formation of large bodies directly from the collapse of ensembles of small (millimeter–decimeter) dust grains and rocks. Some of these theories either require or are greatly aided by enhancements above solar composition in the local dust-to-gas ratio of the disk, and early calculations suggest that radial drift of small grains due to headwind drag against the disk gas might easily supply such an enhancement (*Youdin & Shu*, 2002). Here, I test the radial-drift hypothesis by running simulations of radial particle transport within a viscously evolving gas disk, including both advection with the gas accretion flow and turbulent diffusion of the particle ensemble. I find for a range of disk conditions (varying the disk mass, initial disk size, and α-scaled viscosity) that the dust-to-gas ratio throughout most of the disk remains roughly uniform for the first 40–60% of the disk lifetime, excepting a tapering-off depletion of solids in the outer disk. Enhancements, where they do occur, are generally insufficient to drive collapse of solids into large bodies, even considering recent evidence for possibly lower values of the critical Richardson number (*Lee et al.*, 2010). Therefore, enhancements necessary to drive planetesimal formation must come from local, non-axisymmetric disk structure and solids concentration. Furthermore, previous studies have noted that the rapid aerodynamic inspiral of large grains ($\sim$ 1mm) fits poorly with observations of large grains at large AU in disks around other stars (e.g., *Brauer et al.* (2007)). My simulations corroborate this result, and also indicate that combined advection and headwind drag lead to a rapid loss

of large grains from the inner disk as well. In my simulations, all mm-sized grains are lost onto the central star within half a million years, even though current understanding of chondrule-bearing meteorite parent bodies is that these bodies formed over a 1–3 Myr period, incorporating both calcium-aluminum-rich inclusions (CAIs) and chondrules with at least 1 Myr difference between their ages of formation (see, e.g., *Cuzzi, Davis, & Dobrovolskis* (2003)). I discuss the implications of these results for efforts of protoplanetary-disk modeling and the necessity of considering complex local structure and local concentration.

6.1 Introduction

Understanding the growth evolution of the small dust population in protoplanetary disks has long been troublesome, particularly for studies seeking to understand the formation of planetesimals, the building-blocks of planets, tens to hundreds of kilometers in size. Early research identified two primary problems: First, the headwind drag on particles of roughly meter size should cause these bodies to spiral in to the parent star on time-scales of a thousand years, and therefore growth across this size regime must be rapid to avoid large-scale depletion of solids from the early Solar Nebula. Second, the settling of solids toward the disk midplane where they might rapidly form large bodies via gravitational collapse will be stymied by the Kelvin-Helmholtz instability. This instability is created by the shear between a layer of solids (orbiting at Kepler velocities) and the disk gas, which is pressure supported and orbits at sub-Kepler velocities (*Weidenschilling*, 1995; *Youdin & Shu*, 2002).

Currently, many models of collisional grain growth find that often, around centimeter–meter sizes, colliding particles may not stick, or may collisionally fragment, leading to a bottleneck rather than rapid growth across this size range (e.g.,*Brauer, Henning, & Dullemond* (2008); *Zsom et al.* (2010)). However, recent refinements in the understanding of aerodynamics in disks have led to several theories of planetesimal formation via the concentration and mass collapse of small particles (millimeters–decimeters in size) into large bodies. These theories include turbulent concentration (*Cuzzi, Hogan, & Shariff*, 2008; *Johansen et al.*, 2007), shearing-instability binding of local clumps of solids (*Johansen, & Youdin*, 2007; *Johansen, Youdin, & Mac Low*, 2009; *Bai & Stone*, 2010a), and the precipitation of bound clumps at the disk midplane under conditions of solid over-density (*Youdin & Shu*, 2002). Planetesimal formation by these sorts of mechanisms is supported by

recent dynamical studies that suggest the asteroid-belt population formed at 100–1000 km sizes (*Morbidelli et al.*, 2009b), rather than building up incrementally, as in the traditional coagulative-accretion picture of planetesimal formation.

While not strictly a requirement for the *Cuzzi, Hogan, & Shariff* (2008) model of planetesimal formation, most of the formation-via-collapse models require local enhancement of the height-averaged dust-to-gas ratio (the local disk metallicity) above solar values in order for the clumping of solids to overcome the dispersive forces of the gas. These enhancement requirements vary between roughly 2–10 times standard metallicity (*Youdin & Shu*, 2002; *Johansen, Youdin, & Mac Low*, 2009; *Bai & Stone*, 2010a), though either a local buildup of solids or a local depletion of gas (such as by photoevaporation, as suggested for planetesimal formation by *Throop & Bally* (2005)) are often cited as equally effective. Furthermore, early calculations by *Youdin & Shu* (2002) suggest that headwind-drag infall of outer-disk solids could lead to large-scale radial-concentration of solids well above the threshold necessary to produce precipitation of bound solids at the midplane, thereby using the headwind-drag effect to advantage. However, this early calculation was performed within a static, steady-disk model, neglecting turbulent diffusion of small solids, which might counteract the inward sedimentation of the dust population, and neglecting any radial dependence on the initial grain-size distribution.

In this chapter, I test the hypothesis of large-scale dust concentration via headwind-drag infall by performing simulations of global particle transport within a viscously evolving protoplanetary disk model. My model for particle transport includes turbulent diffusion of the particle ensemble, as well as precisely-calculated radial velocities that account for both headwind drag and radial-advection drag within the flow of inwardly accreting disk gas. While each model run considers only a single grain size, I combine runs for a range of particle sizes into a composite map of the global evolving distribution of dust solids. For each grain size, I use a simplified model of grain growth to constrain the radial extent and the timing that grown solids will appear within the model disk.

In §6.2, I outline the specific models used in these simulations, including the disk-evolution and particle-transport models, as well as my method for combining simulations of individual grain sizes into a composite whole. In §6.3, I show the dust distributions resulting from my simulations and in §6.4 compare those distributions to the dust-to-gas enhancements thought necessary to lead to precipitation of large bodies. I find that dust particles in the larger size bins are lost inward onto

the parent star increasingly rapidly, and I discuss the implications of this effect and my results on the whole in §6.5, providing conclusions in §6.6.

6.2 Methods

Several previous studies have focused on a range of mechanisms for accomplishing large-scale enhancements of the dust-to-gas ratio that could potentially drive planetesimal formation. These include: headwind drag in a static disk (*Youdin & Shu*, 2002), infall of settled solids under the influence of collective effects (*Weidenschilling*, 2003; *Bai & Stone*, 2010a) (most important once dust-to-gas ratios are already high), and the photoevaporative loss of disk gas at large AU (*Throop & Bally*, 2005) (most important at the outer disk edge or near the end of the disk lifetime), with a range in potential outcomes reported. Because the focus of this chapter is to test radial dust concentration via aerodynamic forces within an evolving disk, I have focused my modeling efforts on three primary effects:

1. Self-consistent treatment of gas drag on particles of a specified size within the evolving protoplanetary disk structure. For this, I use the same particle-transport code described in Chapter 3 and employed in the outward-mixing studies of Chapters 4 and 5. I also use the updated model for the disk structure and viscous evolution that includes an evolving disk-temperature profile.

2. Diffusion of the particle ensemble. Turbulent diffusion can be important for moving grains both radially inward and outward within a protoplanetary disk structure. In the outward-mixing simulations of the previous two chapters, the degree of particle diffusivity was found to have an important impact on the large-scale mixing of grains. Likewise, diffusivity should not be neglected in calculations of the global dust-grain distribution, and I have included diffusion of the particle ensemble in the simulations of this chapter, using the random-walk method set up in my particle-transport model.

3. Placing constraints on grain-growth and allowing for a radial dependence to the grain-size distribution. While grain growth in disks is believed to be quite rapid, both theoretical models and observations (e.g., *Birnstiel, Dullemond, & Brauer* (2009); *Kwon et al.* (2009)) suggest that it is more rapid in the denser regions of the disk close to the central star. The

full treatment of coupled radial transport and grain growth is beyond the scope of this work. However, I consider that coagulation should produce the largest grains only at small disk radii, and that their appearance at larger radii must not occur until later than $t = 0$ times. I use the cartoon grain-growth model described in §3.4 to place constraints on the initiation timing and radial extent of the various grain sizes followed in these transport simulations.

Below I describe the specifics of the disk-evolution model used in these large-scale dust-distribution simulations, the setup of the particle-transport model and the initial distributions of simulation dust-grains of various sizes, and the method used to combine simulations of separate grain sizes into a composite map of the evolving dust-mass distribution.

6.2.1 Model Disk Setup

For the work presented in this chapter, I continue to use the 1D, viscously evolving model for the disk surface-density profile discussed in §2.3, but lift the static-temperature constraint of Chapters 4 & 5. As discussed in §2.4, I can calculate an energy-balanced temperature for the disk midplane that accounts for heating from both external illumination and energy dissipation by accretion. However, running the model to calculate this energy-balanced temperature is computationally expensive. Therefore, for the particle simulations run for this chapter, I run disk models using the time-evolving, power-law fit to the temperature distribution discussed in §2.4.2. For this fit

$$T\left(R,t\right) = T_{AU}\left(t\right)\left(\frac{R}{1\mathrm{AU}}\right)^{q_T(t)}, \tag{6.1}$$

(truncated to greater-than or equal-to the local-cloud background temperature, T_{cloud}) where $T_{AU}\left(t\right)$ and $q_T\left(t\right)$ both follow the functional form

$$x\left(t\right) = \left(x_0 - x_\infty\right)\exp\left[-\left(\frac{t}{t_x}\right)^{b_x}\right] + x_\infty\,. \tag{6.2}$$

The x_0, x_∞, t_x, and b_x constants for both $T_{AU}\left(t\right)$ and $q_T\left(t\right)$ are chosen to match the temperature evolution produced for disks run using an energy-balanced temperature. For the energy-balanced models, I assume that $T_{\mathrm{cloud}} = 10\mathrm{K}$, $L_\star = 5.0175 L_\odot$ (which, in the absence of accretional heating, matches the static-temperature value at 1AU used in the previous chapters), and that the starlight strikes the disk at an angle of $\phi = 0.05$ at all disk radii (see §2.4.1). Table 6.1 provides the

$M_{D,0}$ ($M_\odot$)	R_d (AU)	α	$T_{AU,0}$ (K) $q_{T,0}$	$T_{AU,\infty}$ (K) $q_{T,\infty}$	$t_{T_{AU}}$ (yr) t_{q_T} (yr)	$b_{T_{AU}}$ b_{q_T}
0.01	20	10^{-2}	458.184 -0.59066	279.94 -0.497683	1.9471788e5 2.2240062e5	1.02847 1.08899
0.03	5	10^{-2}	500 -0.61	279.94 -0.497683	2.3981058e5 2.7206114e5	0.966192 1.00691
0.03	20	2×10^{-2}	500 -0.61	279.94 -0.497683	2.2784514e5 2.6107508e5	0.917239 0.958942
0.03	**20**	$\mathbf{10^{-2}}$	**500** **-0.61**	**279.94** **-0.497683**	**3.494091e5** **3.9992166e5**	**0.924903** **0.965539**
0.03	20	5×10^{-3}	500 -0.61	279.94 -0.497683	5.066708e5 5.8107436e5	0.906569 0.942996
0.03	40	10^{-2}	472.431 -0.596439	279.94 -0.497683	5.0936365e5 5.8878103e5	1.0102 1.07481
0.09	20	10^{-2}	600 -0.65	279.94 -0.497683	7.2640871e5 8.1425523e5	1.00336 1.02683

Table 6.1: Disk parameters and power-law temperature fitting constants (Equations (6.1) & (6.2)) for the disk models used in this chapter. The $t = 0$ temperature is lower if there is initially much less disk mass at small AU. The time-scaling constants, $t_{T_{AU}}$ and t_{q_T} give a sense of the relative lifetimes of the various disk models, though the lifetimes are more than an order-of-magnitude longer than either of the scaling-constants. The parameters of the fiducial model are in bold.

values of the fitting constants used for each of the disk models run in the simulations of this chapter. While the disk surface-density evolution is very similar using either the energy-balanced or the parameterized-power-law temperature models, changes in disk temperature also correspond to changes in diffusivity for the particle ensemble. Therefore, in §6.3, I include for comparison a simulation of particle distributions run using the fully energy-balanced temperature disk model within the fiducial setup for $M_{D,0}$, R_d, and α.

As previously, I use $t = 0$ disk profiles that follow the form

$$\Sigma_g\left(R, t=0\right) = \frac{\dot{M}_0}{3\pi\nu\left(R\right)}\left(1 - \sqrt{\frac{R_{\rm in}}{R}}\right)\exp\left(-\frac{R}{R_d}\right), \tag{6.3}$$

where, for this initial profile, I use an assumed function for the $t = 0$ viscosity: $\nu\left(R\right) = \nu_0 \alpha R$.

With this $\nu\,(R)$ profile, I can constrain the initial mass of the disk as

$$M_{D,0} = \frac{2\dot{M}_0 R_d}{3\nu_0\,\alpha}\left(1 - \sqrt{\frac{\pi R_{\rm in}}{R_d}}\right), \tag{6.4}$$

and define the magnitude of the $t = 0$ surface-density profile appropriate to my chosen initial disk mass. In these simulations of particle (re)distribution, I consider results for a range in the disk-model parameters. From the fiducial state (fiducial-model parameters shown in bold), I vary the initial disk mass: $M_{D,0} = 0.09$, $\mathbf{0.03}$, and $0.01 M_\odot$, the initial disk compactness: $R_d = 5$, $\mathbf{20}$, and 40AU, and the alpha-scaling of the disk viscosity: $\alpha = 5 \times 10^{-3}$, $\mathbf{10^{-2}}$, and 2×10^{-2}.

Unlike in Chapters 4 & 5, I consider only the accretion-flow case for the radial velocity of the disk gas (§2.6) with gas-drag parameters set to the midplane values (as in Chapters 4 & 5). While the flow structure of both gas and dust is most certainly complex with height above the disk midplane (as discussed in §3.1), these choices represent the simplest with which to examine global dust distributions within a 1D disk model. Furthmore, as I am testing the hypothesis that headwind-drag infall of particles may trigger planetesimal formation, it is appropriate to consider gas drag at the midplane, where headwind-drag motions are most consistently inward and where said planetesimal formation takes place.

6.2.2 Particle Transport Setup

For the simulations of this chapter, I consider grain sizes of 0.2 μm – 2 cm (with $\rho_d = 1$ g cm^{-3}), meant to represent the general range of grain sizes produced by coagulative grain-growth processes. Above centimeter sizes, bouncing and collisional fragmentation represent possible barriers to further growth (*Brauer, Dullemond, & Henning*, 2008; *Zsom et al.*, 2010), and so I assume 2 cm as the upper-limit grain size for tracking a global dust distribution. Here, I continue to calculate grain trajectories based on Epstein-drag forces only, as described in Chapter 3, though there is a brief period near $t = 0$ where 2 cm grains for all disk models (and 2 mm grains for the initially most-compact disk model, $R_d = 5$ AU) are technically in the Stokes-drag regime (§3.2.1) for peak gas densities (at $\lesssim 1$ AU in the fiducial disk model) at the disk midplane. As I am here interested in global transport over much larger than AU scales, however, the use of Epstein drag throughout is taken as sufficiently accurate.

There are two primary differences between the simulations of this chapter and those of Chapters 4 & 5. The first is that here I consider motions of globally distributed dust grains, rather than only those initiated close to the parent star. The second is that, rather than examine the distributions of individual grain of a given size separately, here I build a simulation set from a compilation of simulations run for a a range of grain sizes: 0.2 μm–2 cm, spaced per decade in grain size. I describe the method for building these composites of the dust-grain distribution in §6.2.3. Here, I will elaborate on the initial distribution of dust grains in these simulations as it depends on particle size.

Both observations and models (e.g. *Kwon et al.* (2009); *Dullemond & Dominik* (2005)) support the idea that grain growth is more rapid in the inner, denser regions of a disk, than the outer, colder, more tenuous regions. Subsequently, one would expect a time lag in the formation of grains of a certain size as one moves out in the disk. In these dust-distribution simulations, I represent this lag to first order by dividing the model disk up into radial zones and initiating grains in each zone according to the cartoon model of grain-growth described in §3.4 (which predicts when grains of a given size should appear at a given location in the disk). I run this grain-growth model at a representative radial location for each zone for each simulated particle size from 2 μm to 2 cm; all 0.2 μm grains are initiated at $t = 0$, randomly distributed throughout the entire disk gas-mass distribution, under the assumption that 0.2 μm is the base size of the grains. I run a total of 20,000 particles for each grain-size transport simulation.

For the zone-initiated grain sizes, I consider 10 zones in the disk, with representative points spaced logarithmically from 0.5–1000 AU. The zone boundaries are places logarithmically between the representative points, though the inner-most zone boundary is extended to the full inner-boundary of the disk grid. The number of grains initiated in each zone, is taken as 20,000 divided by the number of zones used for that grain size. No growth to 2 μm or above is found to occur past zones 7 or 8 (depending on the disk model used), extending out to 121 or 282 AU, respectively. 2 cm-sized grains are initiated only out as far as zones 3 or 4, extending to 4.1 or 9.6 AU. The zone ranges used for each disk model and particle size (dictated by the grain-growth model of §3.4) are given in Table 6.2. Naturally, the smaller grain sizes are initiated the most quickly, with 2 μm-sized grains initiated out to 22 AU within the first 2000 years for the fiducial-disk model, and the full 121 AU within 4000 years. Alternately, in the fiducial-disk model, 2 cm grains aren't initiated into

$M_{D,0}$ ($M_\odot$)	R_d (AU)	α	2 μm	20 μm	0.2 mm	2 mm	2 cm
0.01	20	10^{-2}	1–7	1–6	1–5	1–4	1–3
0.03	5	10^{-2}	1–7	1–6	1–5	1–4	1–3
0.03	20	2×10^{-2}	1–8	1–7	1–6	1–4	1–3
0.03	**20**	$\mathbf{10^{-2}}$	**1–7**	**1–7**	**1–6**	**1–4**	**1–3**
0.03	20	5×10^{-3}	1–8	1–7	1–6	1–5	1–4
0.03	40	10^{-2}	1–8	1–7	1–6	1–4	1–3
0.09	20	10^{-2}	1–8	1–7	1–6	1–5	1–4

Table 6.2: Table of radial zones (right-hand columns) into which grains of different sizes were initiated for the different disk models used (parameters in left-hand columns). Ten zones are logarithmically spaced with representative points from 0.5–1000 AU. Parameters for fiducial model are presented in bold text.

zone 3 (out to 4.1 AU) before t =42,000 years.

6.2.3 Forming Composites of Multiple Single-grain-size Simulations

Here, I outline the method used to combine a set of particle-transport simulations for different grain sizes into a composite map of the distribution of disk solids. Because one cannot simulate the full number of particles expected to reside within a disk, this essentially comes down to a mass-allocation scheme, where each simulation particle represents a large mass of disk solids. Because the primary focus of this chapter is on changes in the dust-gas composition of the disk, when assigning mass to simulation particles, I use a gas-equivalent mass, $M_{\rm GE}$. Gas-equivalent mass can be compared directly to the disk-gas mass, M_g, in a given region to define the local disk metallicity, with $M_{\rm GE} = M_g$ for original (solar) metallicity and $M_{\rm GE} > M_g$ in regions enhanced in solids relative to the gas. For this work, I seek regions of the disk where the enhancement is above a certain threshold (usually about a factor of 2–10)[1]. I use $M_{\rm GE}$ to define the enhancement factor as

$$E = \frac{M_{\rm GE}}{M_g}\,. \tag{6.5}$$

For this work, I assume that at $t = 0$, the entire mass of disk solids is in 0.2 μm particles that

[1]The required enhancements quoted in the results of planetesimal-formation papers often fall between about 2–10. However, the specific requirements depend on both the planetesimal-formation model and the specific local conditions within a disk. Required enhancement factors are discussed in more detail in §6.4.

are evenly and randomly distributed throughout the entire disk mass (grains observed in the ISM are sub-micron in size (*Mathis, Rumpl, & Nordsieck*, 1977)). Radial transport of each dust size is simulated using an ensemble of 20,000 particles. Therefore, at $t = 0$, all of the 0.2 μm-sized particles are assigned $m_{\rm GE} = M_{D,0}/20,000$, where $m_{\rm GE}$ is the gas-equivalent mass assigned to an individual simulation particle, and $M_{D,0}$ is the total disk mass at $t = 0$, defined in §6.2.1.

Next, to add in the transport simulations for the larger particle sizes (binned logarithmically, with bin boundaries placed logarithmically between each size simulated), I consider that grain-growth occurs separately within the disk zones defined in §6.2.2. Each time new particles are initiated into a new size bin within a given zone, I first add up the total $M_{\rm GE}$ of the simulation particles currently located within that zone. I do this for particles up to and including the grain size that has just locally been initiated. I do not include the mass from any larger particles that may have been transported into that zone from one at smaller disk radii, as these large-particle interlopers are considered outside the grain-growth processes occurring within the zone of interest.

Next, I calculate the fraction of the total $M_{\rm GE}$ that should be portioned into each dust-size bin, based on a power-law distribution of particle sizes

$$\frac{dn_p}{ds_d} \propto s_d^{q_s} \, , \tag{6.6}$$

where n_p is the number density of grains of a given radius s_d, and q_s is the power-law index of the distribution. For the fiducial simulations, I take $q_s = -3.5$, corresponding to the size distribution of grains measured for the ISM (*Mathis, Rumpl, & Nordsieck*, 1977). However, flatter grain-size distributions are often observed in disks around other stars and interpreted as a sign of grain-growth within the disk (e.g., *Ricci et al.* (2011)), while collisional size-distributions tend toward steeper trends (*Dohnanyi*, 1969), often approximated as $q_s = -4$ (e.g., *Bai & Stone* (2010a)). Therefore, in §6.4, I also present composite simulations compiled with $q_s = -4$ and -2.5 for comparison with the fiducial q_s choice.

To continue, the volume mass density of particles may be found by (*Garaud*, 2007)

$$\rho_p = \int_{s_{\rm min}}^{s_{\rm max}} \frac{dn_p}{ds_d} m\left(s_d\right) ds_d \propto \left(s_{\rm max}^{4+q_s} - s_{\rm min}^{4+q_s}\right) \, , \tag{6.7}$$

where ρ_p is the local volume density of particles and $m\left(s_d\right) = \frac{4}{3}\pi s_d^2 \rho_d$ is the mass of a dust particle of radius s_d. Therefore, the fraction of dust mass in a given size bin can be calculated as

$$\frac{\rho_{p,s_d}}{\rho_p} = \frac{\left(s_{\mathrm{bmax}}^{4+q_s} - s_{\mathrm{bmin}}^{4+q_s}\right)}{\left(s_{\mathrm{max}}^{4+q_s} - s_{\mathrm{min}}^{4+q_s}\right)}, \tag{6.8}$$

where s_{min} and s_{max} are the lower and upper bounds, respectively, on the entire size distribution, and s_{bmin} and s_{bmax} are the bounds on a given size bin. I define size bins logarithmically, so that, e.g., redistributing mass between 0.2μm and 2μm size bins ($s_d = 0.1$ and 1μm) has bin boundaries at $s_d = 0.0316$, 0.316, and 3.16μm. Finally, note that $q_s = -4$ is a special case for which

$$\frac{\rho_{p,s_d}}{\rho_p} = \frac{\left[\ln\left(s_{\mathrm{bmax}}\right) - \ln\left(s_{\mathrm{bmin}}\right)\right]}{\left[\ln\left(s_{\mathrm{max}}\right) - \ln\left(s_{\mathrm{min}}\right)\right]}, \tag{6.9}$$

distributing an equal amount of mass into any set of logarithmically defined size-bins.

Once I know the fraction of gas-equivalent mass to be portioned into each size bin, I divide it up evenly between the particles of that size currently in the initialized zone, and allot the new m_{GE} to each particle. Note, that because of the wide range in the number of particles in a zone between different size bins (ranges as large as 230–6666 particles between bins) and the fact that successive size bins tend to have roughly half-an-order-of-magnitude difference in mass allotted to them, individual simulation particles may be allotted rather different values of m_{GE} to carry within the transport simulation. This effect is mitigated somewhat by the fact that the larger size bins receive a larger share of the mass but also tend to have more particles to distribute it amongst because their initialization range has a smaller radial extent, dividing 20,000 total particles between fewer zones.

Finally, once M_{GE} has been allotted among all the particles and particle sizes at each time step, I can calculate a map in time and disk radius of the local enhancement factor using Equation (6.5) by adding up the total M_{GE} and gas mass, $M_{g,i} = \pi\left(R_{i+1/2}^2 - R_{i-1/2}^2\right)\Sigma_{g,i}$, in each radial grid cell. I also combine E_i information in both radial and time bins (R_i and δt) in order to reduce the noise of this output. I consider the enhancement, E, averaged across (usually) 3 grid cells so that

$$E_{i'} = \frac{\left(M_{\mathrm{GE},i} + M_{\mathrm{GE},i+1} + M_{\mathrm{GE},i+2}\right)}{\left(M_{g,i} + M_{g,i+1} + M_{g,i+2}\right)}, \tag{6.10}$$

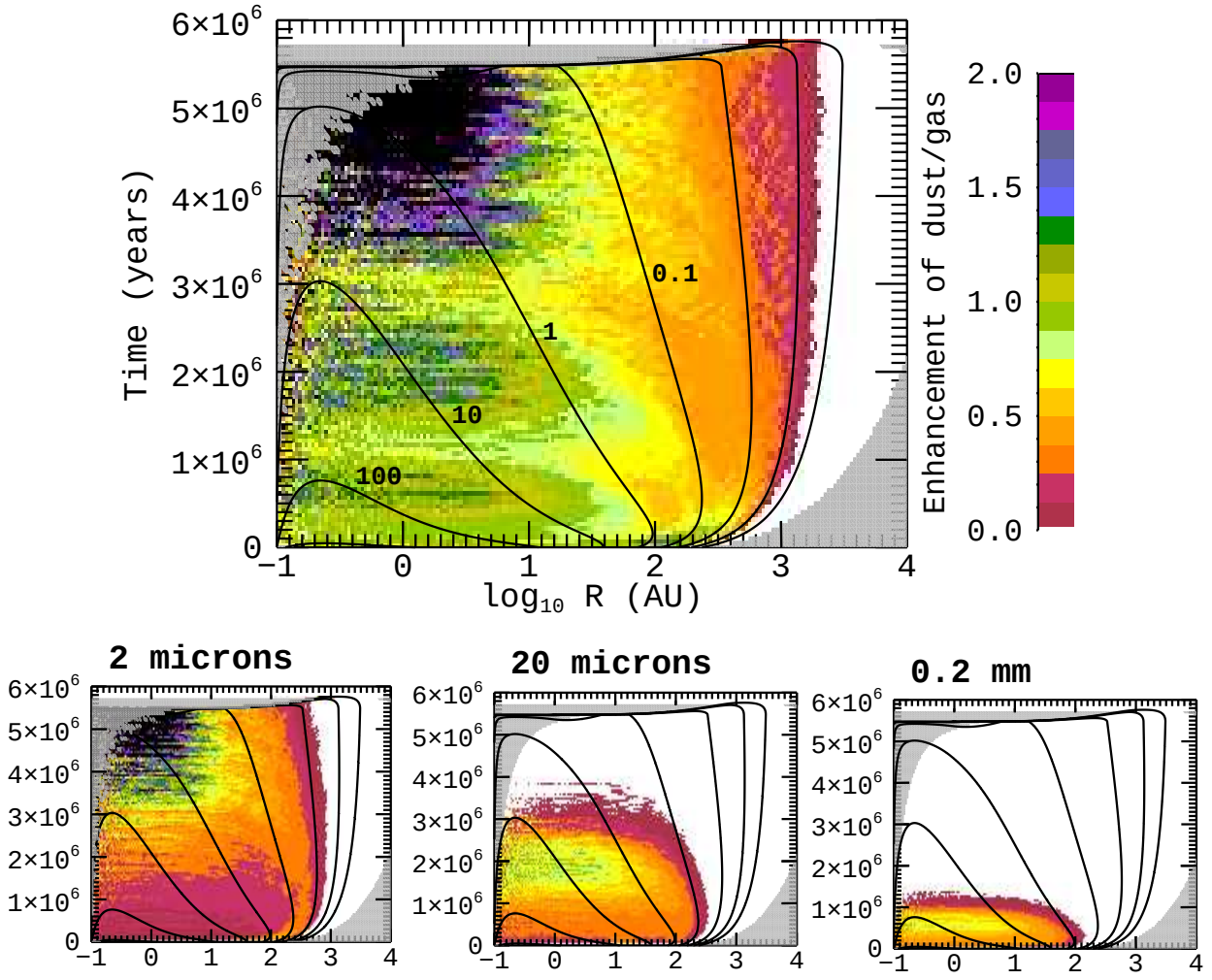

Figure 6.1: Example composite map of dust/gas enhancement factor (top panel) and maps of some of the contributing size bins (bottom panels). The black contours trace the evolving gas surface density spaced by orders of magnitude between 10^{-4} and 10^{3} g cm^{-2}. The grey regions mask out bins for which the particle statistics were too low to report dust/gas enhancement values.

where i' indicates the index value of the resolution-reduced grid, and I average over (usually) 250 output time-steps so that

$$E_i\left(\Delta t\right) = \frac{1}{\Delta t/\delta t}\sum_{j=1}^{\Delta t/\delta t} E_{i,j}\,. \tag{6.11}$$

The transport simulations for this chapter output particle positions every $\delta t = 200$ years, so the composite-enhancement maps in the fiducial case have a time resolution of $\Delta t = 5 \times 10^4$ years.

An example composite map of the enhancement factor is shown in the top-panel of Figure 6.1, overlain with disk-gas surface-density contours to provide context of the gas disk evolution. The

bottom-panels plot example maps of the individual grain-size components of the whole. Note that the scalloped artifacts visible in the composite map mark the boundaries of final particle infall for successive dust-grain sizes.

Last, while the enhancement factor is probably the more fundamental output of these simulation composites, it can also be translated into a value for the dust-solids surface-density, Σ_p, using the more general definition of the enhancement factor

$$E_{i,j} = \left(\frac{\Sigma_p}{\Sigma_g}\right)_{i,j} / \left(\frac{\Sigma_p}{\Sigma_g}\right)_{\odot} , \tag{6.12}$$

where $(\Sigma_p/\Sigma_g)_{\odot} = Z_{\odot}$ refers to the initial (solar) dust-gas composition of the disk, the baseline metallicity. $Z_{\odot}$ used in this work is taken from *Lodders* (2003) and is broken into two components:

$$Z_{\odot} = Z_0 Z_{\rm rel}\left(T\right) , \tag{6.13}$$

where $Z_0 = 0.0149$ is the total fraction of condensable material thought to be present in a solar-composition gas, and $Z_{\rm rel}\left(T\right)$ is the fraction of that material believed to actually be condensed based on the local gas temperature. The values of $Z_{\rm rel}$ used are

$$\begin{aligned} Z_{\rm rel} &= 0.3289 \quad \text{for} \quad T > 182\text{K} , \\ Z_{\rm rel} &= 0.7129 \quad \text{for} \quad 182\text{K} > T > 41\text{K} , \\ Z_{\rm rel} &= 1 \quad \text{for} \quad T < 41\text{K} , \end{aligned}$$

with transitions corresponding to the condensation of water ice (the snow line) and to the condensation of methane (and ammonia) ice. Therefore, from Equations (6.12) & (6.13),

$$\Sigma_{p,ij} = E_{ij}\Sigma_{g,ij} Z_{\odot}\, Z_{\rm rel}\left(T_{ij}\right) . \tag{6.14}$$

6.3 Results: The Global Distribution of Solids

Note that the simulations presented below were run (like the outward-mixing simulations of Chapters 4 & 5) on a 2.4 GHz Intel Core2Duo. A full set of simulations including runs with 0.2 μm – 2

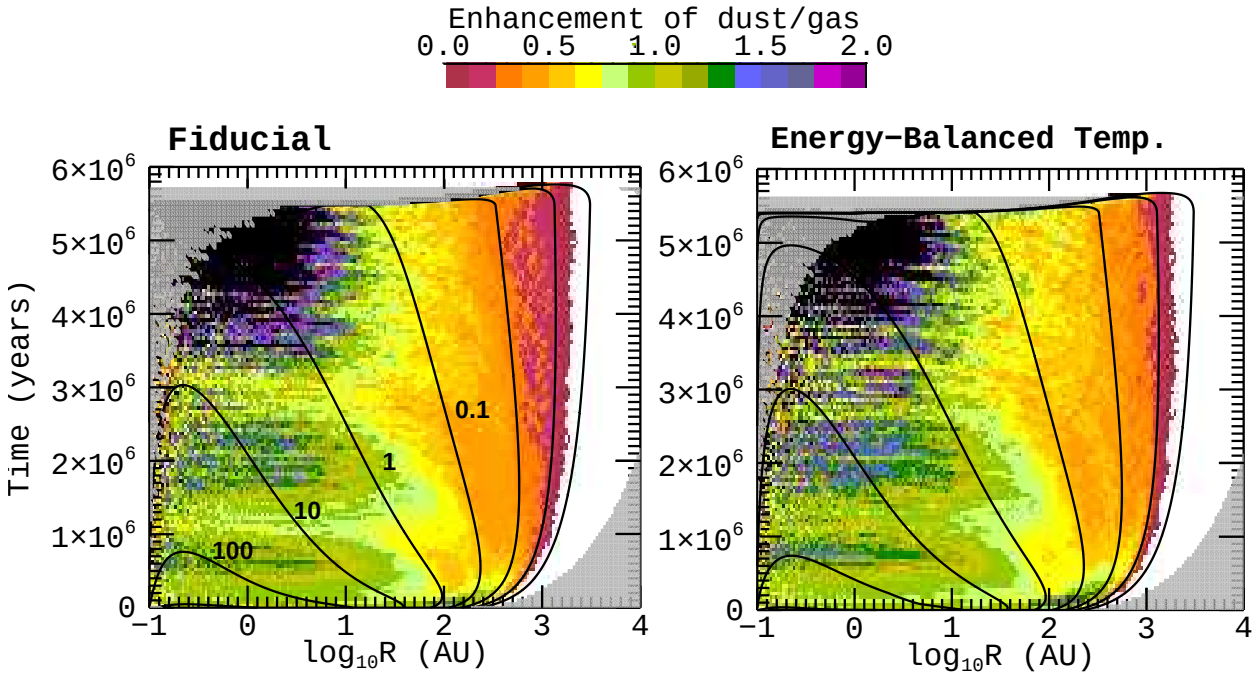

Figure 6.2: Enhancment maps for dust transport simulations within the fiducial disk model where $M_{D,0} = 0.03 M_{\odot}$, $R_d = 20$ AU, and $\alpha = 10^{-2}$. The fiducial-model setup uses a fitted–power-law temperature distribution during the grain-transport simulations. The results of simulations run using the energy-balanced temperature distribution are included for comparison. Both maps were compiled using three radial-grid-points for every radial-bin and averaging 250 time-points for every $\Delta t = 5 \times 10^4$ years time-bin. Black on the map indicates regions of $\times 2$ enhancement or greater. Grey indicates regions where the particle-to-gas resolution was too low to report results. Black contours range from 10^{-4}–10^{3} g cm^{-3}, tracing the gas-disk surface-density evolution.

cm-sized grains required roughly 2–2.5 weeks of computation time in the fiducial-disk setup. More massive disks required longer run times due to not only a longer disk lifetime but also to more extended retention of grains within the denser disk-gas medium. Runs using a larger value of α for the disk viscosity have model disks with shorter lifetimes (roughly as a function of $\sqrt{\alpha}$) but also take shorter disk-evolution time-steps ($\propto \alpha$), and are therefore more computationally expensive on the whole.

In Figure 6.2, I present the composite–enhancement-map results for the fiducial disk model as well as the map for the same disk model run using an energy-balanced temperature during the transport of the grains. The two are quite similar, providing reassurance that the fitted–power-law temperature distribution allows for the representation of global dust transport to sufficient accuracy within an evolving disk. In these maps, green areas represent no change from the initial

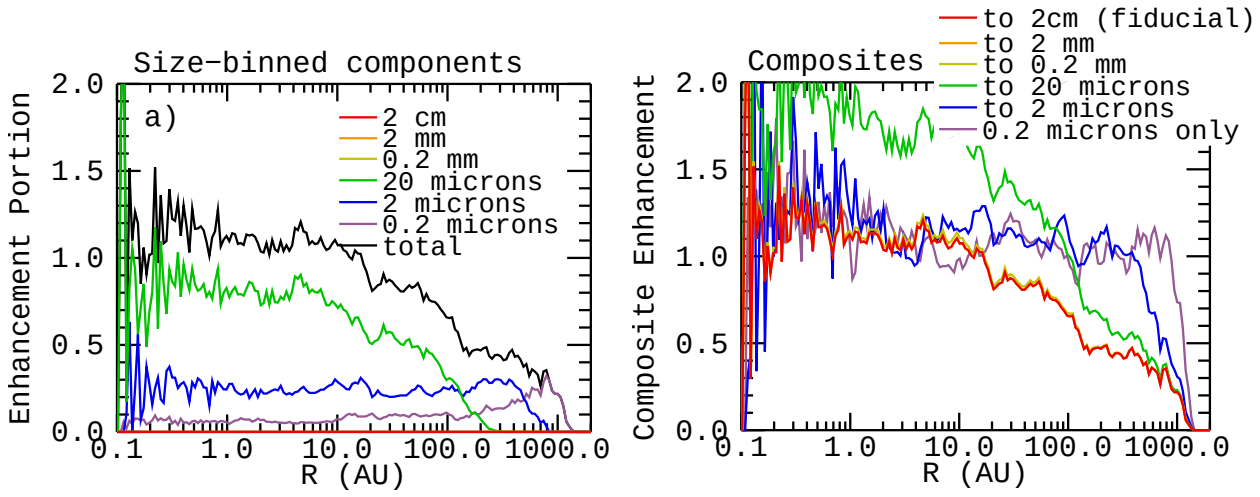

Figure 6.3: Measured enhancement of dust/gas for the fiducial-disk model simulations at $t = 1.5$ Myr. **Panel-a)** Portions of the enhancement factor contributed by each of the grain-size bins. **Panel-b)** Composite enhancements varying the largest grain size assumed for particle-size distribution. For no grain growth (0.2 μm grains only) the dust-to-gas ratio remains everywhere near unity. Allowing larger grain sizes also allows inward drift of the dust population.

dust-to-gas ratio, red areas represent depletion of dust relative to the gas, and black areas represent $\times 2$ enhancement of the dust or greater.

From these plots we see that the fiducial-disk simulations do not produce large radial concentrations of dust in the main and inner disks until near the end of the disk lifetime. In §6.4, I will compare these measured enhancement values to predicted requirements for models of planetesimal formation in more detail. Recall, however, that a common minimum requirement quoted to aid planetesimal formation is a doubling of the dust-to-gas ratio above solar metallicity and that the core-accretion scenario for giant-planet formation requires the formation of large cores when a substantial fraction of the disk gas yet remains. At very early times, some small grains are pulled outward with the outwardly expanding disk edge. Afterward, one sees that relative inward drift of the grain population does occur in these simulations, as marked by the depletion of solids in the outer regions of the disk. However, this influx of mass to the inner disk is simply offset by concurrent loss, particularly of the large particles, onto the parent star.

The importance of the large amount of dust mass contained in large particle sizes is shown in Figure 6.3 where, for $t = 1.5$ Myr, I plot in panel-a the portion of the enhancement corresponding to each grain-size bin, and (in panel-b) the compiled enhancement-factor for grain-size distributions

truncated at successively smaller particle sizes. From this second plot, one can see that grain-growth to roughly 20 μm sizes results in inward drift that depletes the outer disk of dust, and that growth to larger sizes subsequently depletes the inner disk of dust mass.

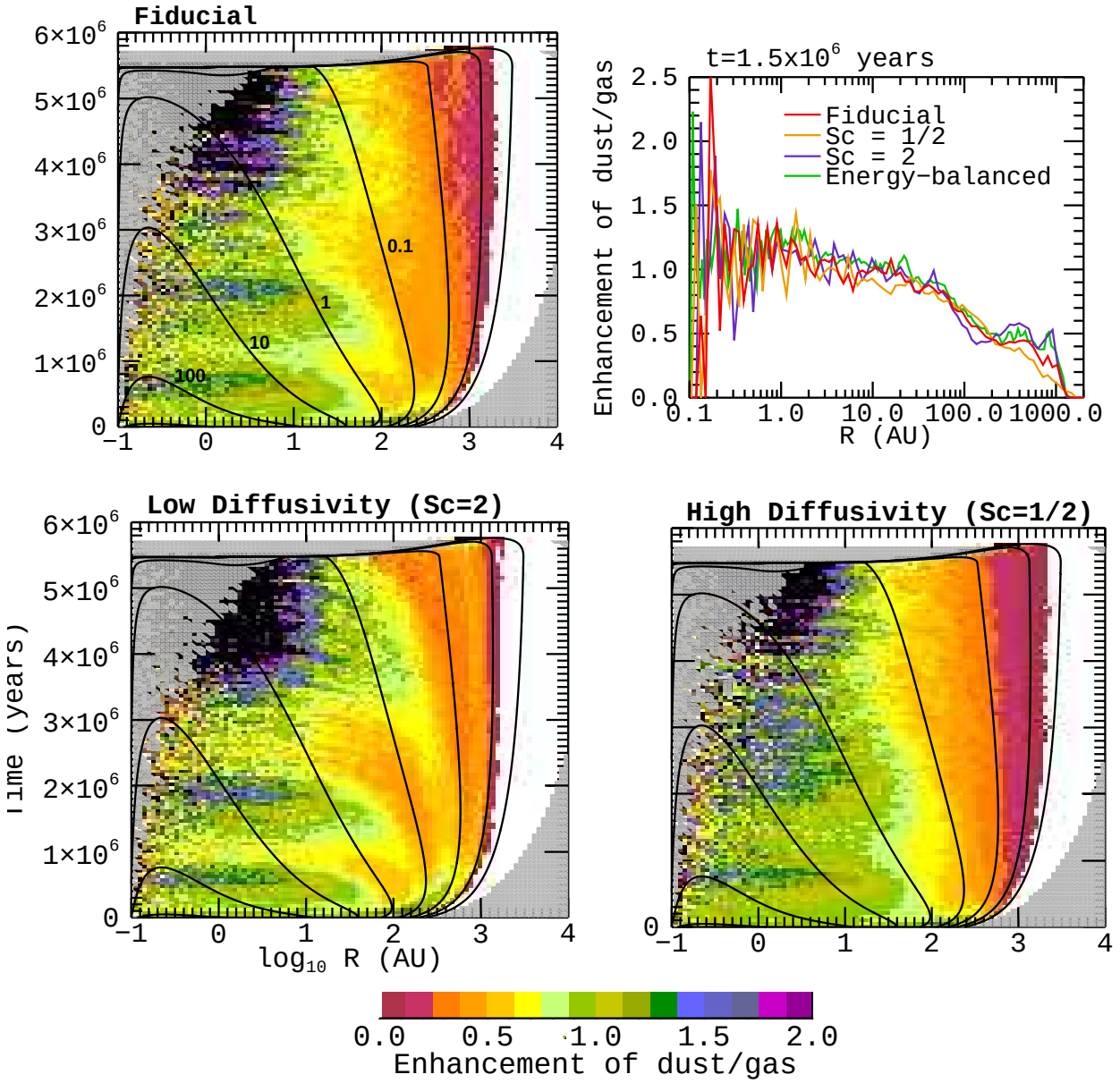

Figure 6.4: Enhancement maps from the fiducial simulations, as well as from simulations with $Sc = 1/2$ and 2. The simulations for different Schmidt number were run with output at lower resolution than the fiducial setup. All composite maps here were compiled using six radial-grid-points per radial-bin and averaging 25 time-points for every $\delta t = 5 \times 10^4$ years time-bin. Top-right panels plots the enhancement values as a function of R at $t = 1.5 \times 10^6$ years for these three cases, as well as for the energy-balanced-model simulations shown in Figure 6.2. Maps following the same conventions as in Figure 6.2.

Next, in Figure 6.4, I plot a comparison between the results for the fiducial simulations, and simulations run varying the diffusivity of the particle ensemble by a factor of 2 in either direction. Here one finds little difference between the global dust distributions produced for the different cases. A lower diffusivity leads to greater segregation of the particle-size distribution and emphasizes the discreet particle sizes used for these simulations. However, a real disk should have a mostly continuous particle-size distribution, and therefore the results for the global distribution of solids cannot be said to be qualitatively different from the other two cases. The higher-diffusivity case

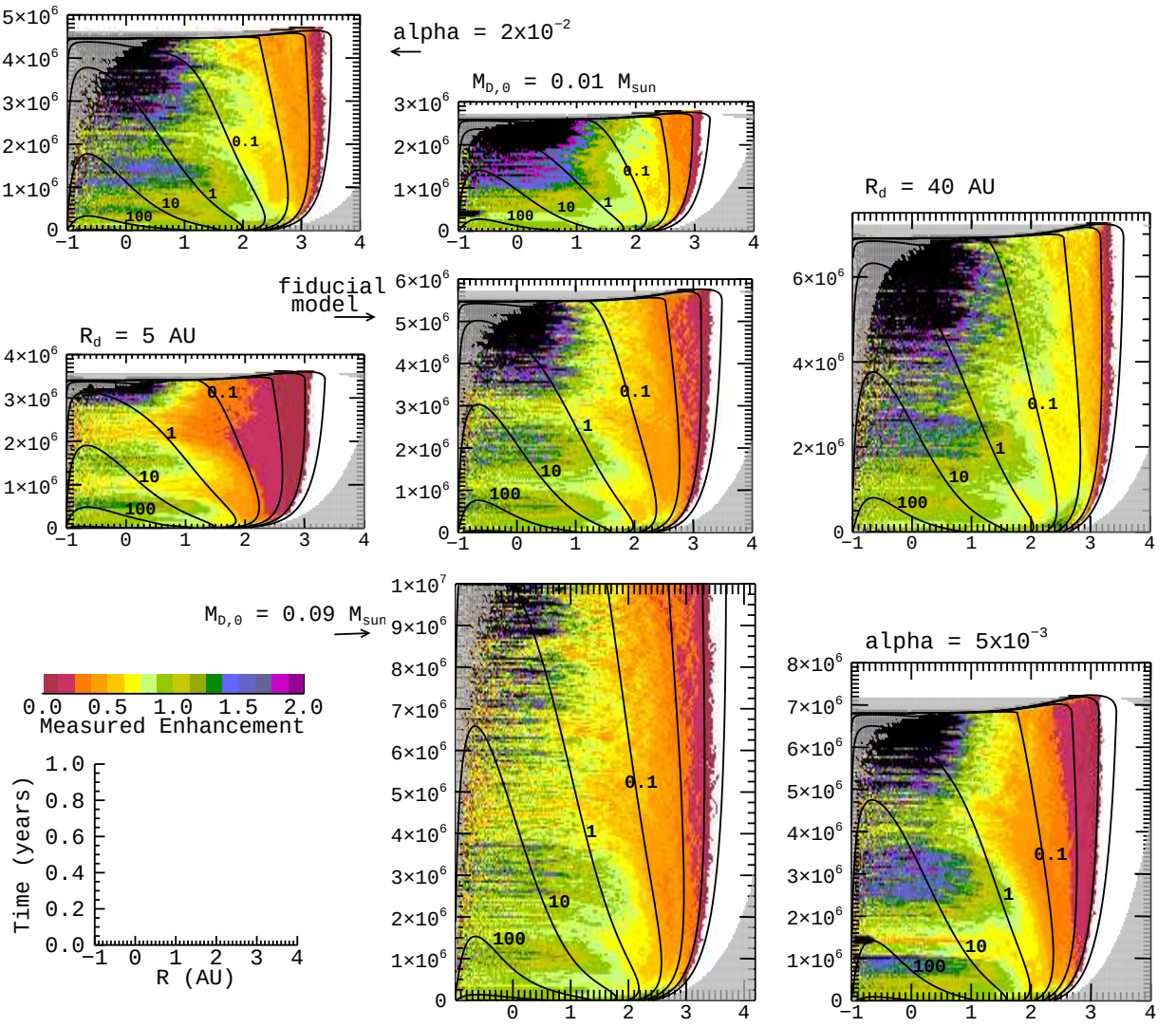

Figure 6.5: Enhancement maps for simulations run in several different disk models, separately varying R_d (horzontal), $M_{D,0}$ (vertical), and α (diagonal). Fiducial-model map ($M_{D,0} = 0.03 M_\odot$, $R_d = 20$ AU, $\alpha = 10^{-2}$) shown in the center panel. Maps follow the same conventions as in Figure 6.2.

allows large grains to remain in the disk slightly longer than usual (all 20μm grains are lost after 4.1 Myr rather than by 3.8 Myr as in the fiducial simulations), but again, this is insufficient to substantially impact the global distribution of solids. That the diffusivity plays such a small role in the global solids distribution suggests that, on this scale, the outward boundary defined by headwind drag for each particle size is the stronger of the two effects.

Finally, in Figure 6.5, I plot the composite enhancement maps for simulations run varying the disk-model parameters, $M_{D,0}$, R_d, and α. Qualitatively, the patterns of evolving global enhancement are roughly constant across the different disk-model setups. The infall of the smaller grain sizes causes depletion in the dust relative to the gas at the outer edge of the disk, while in the main disk enhancement values remain near unity for somewhere between 40 and 60% of the total disk lifetime. The initially more compact disk shows somewhat greater outer-disk depletion because a larger fraction of grains are processed to larger sizes at early times, while the disk using $\alpha = 5\times10^{-3}$ shows some of the enhanced segregation of the binned particle sizes typical of the lower-diffusivity simulations. But the basic shape of dust-to-gas values within the disk as controlled by aerodynamic

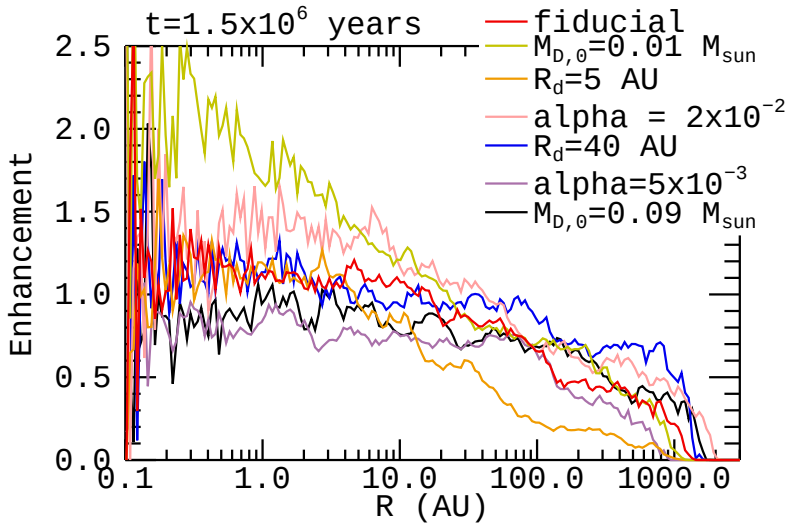

Figure 6.6: Radial enhancement profiles at $t = 1.5$ Myr for the different disk models shown in Figure 6.5. The enhancement profiles all follow the same general trend. The greatest deviation from that trend here is seen for the most-quickly evolving systems. In particular, the $M_{D,0} = 0.01M_{\odot}$ system is aged more than 50% of it's lifetime at $t = 1.5$ Myr and so has some concentration of the smaller grain sizes as small AU, while the $R_d = 5$ AU system has a larger fraction of it's dust mass processed at small AU to larger grain sizes and so experiences greater dust depletion in the outer disk.

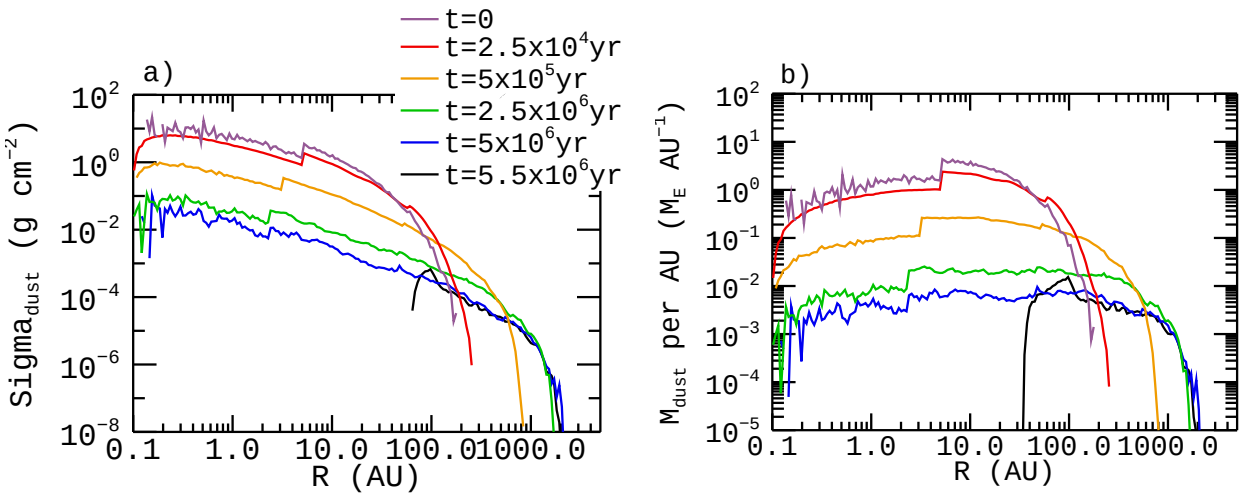

Figure 6.7: Dust surface-density (a) and mass-per-radius (b) distributions for the fiducial disk simulations.

forces appears fairly universal, and in Figure 6.6, I plot the radial cross-section of E at $t = 1.5$ Myr for each of these disk models for comparison. The primary result, of these simulations then, is that a smoothly-defined, azimuthally-symmetric, evolving disk model tends to lose dust-mass smoothly inward onto the parent star at a rate that generally keeps pace with the loss of accreting disk-gas mass, and that variety in basic disk properties/parameters does not tend to produce special-case disks with respect to this process.

The results presented above all look at the distribution of the dust-to-gas ratio in evolving protoplanetary disks, which is an important parameter for certain models of planetesimal formation. However, important to any study of planetary-system formation is simply the distribution of the solid material itself. In Figure 6.7 panel-a, I present surface-density profiles for the dust solids in the fiducial-disk simulations at several times. In panel-b, I translate those profiles into distributions of solid-mass per AU. Jumps in the distributions at around a few AU correspond to the snow-line, beyond which more material should be condensed into solids for a given disk metallicity. At $t = 0$, my fiducial disk has just over 100 Earth-masses of solid material spread throughout the entire disk, with the greatest concentration just beyond the snow line at around 5–10 AU. As the disk evolves, the solids distribution spreads outward with the disk and decreases in total quantity, to 40 $M_{\rm Earth}$ at $t = 5 \times 10^5$ years, and 10 $M_{\rm Earth}$ at $t = 2.5$ Myr. Presumably, planetesimal formation at some earlier time would allow for the retention of a larger fraction of this solid material. However, my

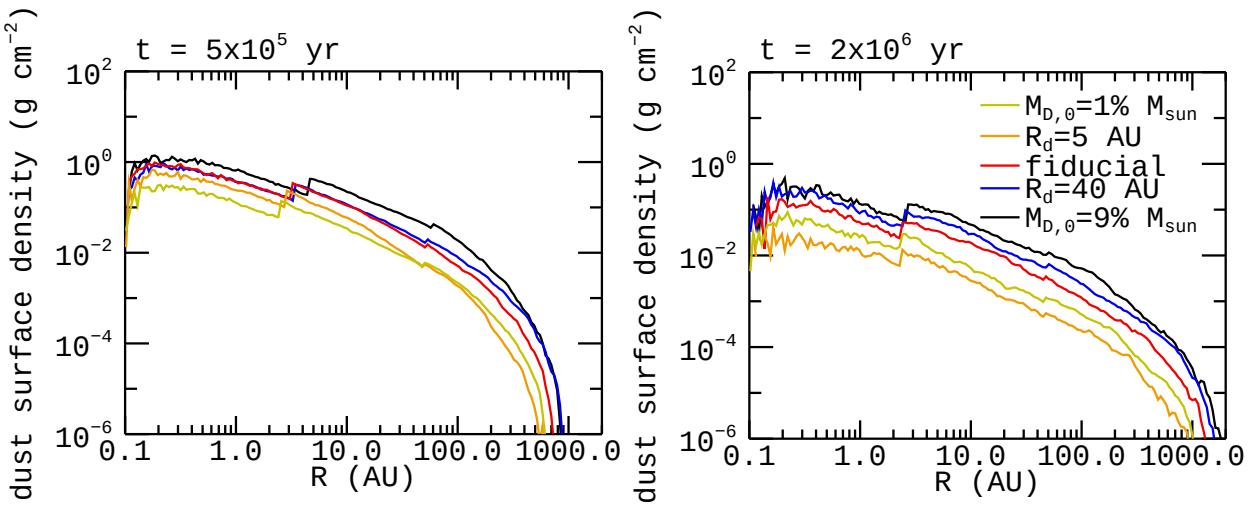

Figure 6.8: Dust surface-density profiles at two times for variations on the disk-model physical characteristics. The fiducial model has $M_{D,0} = 0.03 M_\odot$ and $R_d = 20$ AU.

particle-transport simulations record only the loss of material as fine grains along with the accreting disk gas itself. Of course, different disk models must, by their nature, exhibit different Σ_p profiles, and a few of these (corresponding to different disk models of Figure 6.5) are shown in Figure 6.8.

6.4 Comparison with Required Enhancement Factors

While the enhancement factors for the dust-to-gas ratio produced by my transport simulations are mostly fairly low, there are a number of different factors affecting the enhancement required under different models of planetesimal formation so that, in *Youdin & Shu* (2002) for example, very low to no enhancement may be required for certain disk types and conditions to produce planetesimals. In this section, I compare my simulated enhancement factors to those required by theories of planetesimal formation, with emphasis on the *Youdin & Shu* (2002) collapse/precipitation model, which has relatively straight-forward theoretical requirements. In §6.5, I include discussion of some of the specific requirements of the streaming-instability model for planetesimal formation. For the moment, note that there are multiple parallels between the two and that, for example, both models require increasingly large enhancement factors to accomplish planetesimal formation in regions of the disk that have a steep pressure gradient.

In the *Youdin & Shu* (2002) model, planetesimal formation is accomplished by the gravitational collapse of solids settled out to the disk midplane. It assumes that the disk is quiescent, with no

global turbulence to stir the particles upward, but also that, as particles settle, shear between the mostly Keplerian dust layer and the more slowly rotating gas will produce Kelvin-Helmholtz instabilities that *will* tend to mix particles upward. A dust disk in equilibrium with Kelvin-Helmholtz effects should then settle out only to a degree, characterized by the critical Richardson number, Ri_c, where the Richardson number in general characterizes the balance between buoyancy and shearing effects across the vertical profile with $Ri \propto \rho_g z / (\partial \rho_p / \partial z)$ (*Youdin & Shu*, 2002), and the critical value is typically assumed to be $Ri_c \approx 1/4$ by inspection of conditions for instability (see *Pringle & King* (2007) pp144–145). *Youdin & Shu* (2002) point out, however, that for midplane dust densities in this regime above a certain mass threshold, the gravity of the dust sub-disk should dominate and lead to the collapse of solids at the midplane. The criteria for this collapse, given in their Equation (15), is

$$\Sigma_{p,c} = 2\sqrt{Ri_c}\eta_{\delta\phi} R \rho_g s\left(\psi\right) \,, \tag{6.15}$$

where $\Sigma_{p,c}$ is the critical surface density of the solids for collapse, $\eta_{\delta\phi}$ relates the radial pressure gradient in the disk and the shear between gas and dust, and $s\left(\psi\right)$ is a correction factor accounting for the self-gravity of the gas. In the paper, these later two variables are defined as

$$\eta_{\delta\phi} \equiv -\frac{\left(\partial P / \partial R\right)}{2\rho_g R \Omega^2} \,, \tag{6.16}$$

and

$$\begin{aligned} s\left(\psi\right) &\equiv \left(1+\psi\right) \ln\left[\frac{\left(1+\psi+\sqrt{1+2\psi}\right)}{\psi}\right] - \sqrt{1+2\psi} \,; \\ \psi &\equiv \frac{4\pi G \rho_g}{\Omega_{\rm K}^2} \,. \end{aligned} \tag{6.17}$$

Assuming a gas density of $\rho_g \approx \Sigma_g / 2H_g$, where $H_g = c_s \, R / v_{\rm K}$ in a vertically isothermal disk model, I can convert Equation (6.15) into a critical dust-to-gas ratio:

$$\left(\frac{\Sigma_p}{\Sigma_g}\right)_c = \sqrt{Ri_c}\eta_{\delta\phi} s\left(\psi\right) \frac{v_{\rm K}}{c_s} \,. \tag{6.18}$$

Finally, to report this as a required enhancement factor, I must include the values for solar (initial)

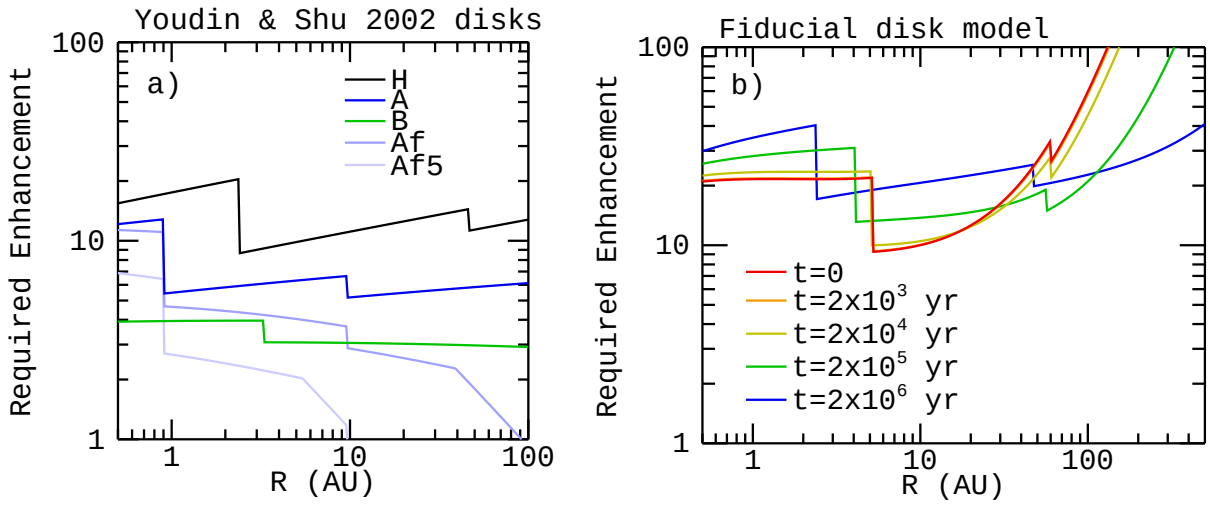

Figure 6.9: Required Enhancements for midplane precipitation with $Ri_c = 1/4$ for the disks of *Youdin & Shu* (2002) and my fiducial-disk model.

metallicity and the fraction of solids condensed out at different disk temperatures.

$$E_{\rm precip} \geq \frac{\left(\Sigma_p/\Sigma_g\right)_c}{\left(\Sigma_p/\Sigma_g\right)_\odot} = \sqrt{Ri_c}\frac{v_{\rm K}}{c_s}\frac{\eta_{\delta\phi} s\left(\psi\right)}{Z_0 Z_{\rm rel}\left(T\right)}\,, \tag{6.19}$$

where my conventions for Z_0 and $Z_{\rm rel}\left(T\right)$ are defined in §6.2.3.

This collapse criterion is separate from the simpler gravitational-collapse criterion using the Toomre-Q parameter, $Q_p < 1$. From *Youdin & Shu* (2002),

$$\begin{aligned} Q_p &\approx \frac{\Omega^2 H_{p,c}}{\pi G \Sigma_{p,c}}\,; \\ H_{p,c} &\equiv \sqrt{Ri_c}\eta_{\delta\phi} R h\left(\psi\right)\,; \\ h\left(\psi\right) &= \sqrt{1+2\psi} - \psi \ln\left[\frac{\left(1+\psi+\sqrt{1+2\psi}\right)}{\psi}\right]\,. \end{aligned} \tag{6.20}$$

The enhancement criterion for Q-collapse is then

$$E_{Q_p} \geq \sqrt{Ri_c}\frac{v_{\rm K}^2 \eta_{\delta\phi} h\left(\psi\right)}{\pi G R \Sigma_g Z_0 Z_{\rm rel}\left(T\right)}\,. \tag{6.21}$$

In Figure 6.9, I plot the required enhancements calculated using Equations (6.19) & (6.21) ($Ri_c = 1/4$) for the disk models considered in *Youdin & Shu* (2002) (panel-a) and for my fiducial

model	$\Sigma_{\rm AU}$ **(g cm^{-2})**	$\mathbf{q_\Sigma}$	$\mathbf{T_{AU}}$ **(K)**	$\mathbf{q_T}$
H	1700	$-3/2$	280	$-1/2$
A	1700	$-3/2$	170	-0.63
B	1700	$-3/2$	100	$-3/4$
Af	1700	-1	170	-0.63
Af5	8500	-1	170	-0.63
fiducial	**1176**	**-1**	**278.9**	$-1/2$

Table 6.3: Parameters for disk models used in *Youdin & Shu* (2002) compared to rough steady-disk equivalents for $t = 0$ of my fiducial model. In general, $\Sigma_g(R) = \Sigma_{\rm AU}(R/1{\rm AU})^{q_\Sigma}$ and $T(R) = T_{\rm AU}(R/1{\rm AU})^{q_T}$. "H" designates the minimum-Solar-Nebula model of Hayashi-1981 (see *Armitage* (2010) pp 4–5).

disk model at several times (panel-b). Panel-a does not provide a perfect replica of the *Youdin & Shu* (2002) results, in part because I've used my conventions for Z_0 and $Z_{\rm rel}(T)$, taken from *Chiang & Youdin* (2010) and *Lodders* (2003). In Table 6.3, I list the main parameters defining the different *Youdin & Shu* (2002) disk models, as well as the roughly-corresponding values (at $t = 0$) for my fiducial disk model (*Youdin & Shu* (2002) use simple power-law disk models while my models have both a roll-over in Σ_g at the inner disk edge and an exponential tail-off of the outer disk).

Figure 6.9 demonstrates several interesting features of these enhancement requirements.

* First, note that my fiducial model calls for remarkably high $E_{\rm precip}$ in the outer disk, particularly at early times. This is due to the strong dependence of $E_{\rm precip}$ on the dust-gas shearing term, $\eta_{\delta\phi}$. When the radial pressure gradient is steep, as near the outwardly expanding disk edge, this shearing is strong, requiring large dust-to-gas ratios to be overcome. The similar importance of $\eta_{\delta\phi}$ in streaming-instability models (e.g., *Bai & Stone* (2010b)) is discussed in §6.5.

* Second, while the *Youdin & Shu* (2002) paper de-emphasizes the roles of the disk gravity, represented by $s(\psi)$, the time-series for $E_{\rm precip}$ of my fiducial model, particularly in the inner disk, demonstrates the importance of the local disk mass for meeting dust/gas-precipitation requirements. $s(\psi)$ (and therefore $E_{\rm precip}$) becomes large, when ψ is small, which may occur for either a low local disk surface density, or for a locally hot disk.

* Finally, the $E_{\rm precip}$ curves for both sets of disk models emphasize the importance of the

ice lines, particularly the snow line, as places of potential local minimum in metallicity requirements for planetesimal formation. While my particle-transport model does not treat evaporation and vapor-transport effects, the simulations of *Ciesla & Cuzzi* (2006) do show an additional peak in the dust population just outside the snow line due at least partially to local concentration of diffused and recondensed vapor. This also corresponds to a peak in the disk opacity and heating, however, so it is not clear what the degree of advantage the region just outside the snowline lends to planetesimal formation via gravitational precipitation.

Next, while the calculations above assume $Ri_c = 1/4$, it is not entirely clear what the proper value should be. Lower values of Ri mean that the dust is settled more densely toward the midplane. Therefore, lower Ri_c would mean that greater settling was allowed to take place, without stirring by Kelvin-Helmholz instabilities, thereby increasing the mass of the dust sub-disk and the importance of its gravitational influence. *Lee et al.* (2010) ran 3D simulations of vertically-stratified disks with well-coupled dust particles to test for physical variables of Ri_c. From these simulations, they find the onset of Kelvin-Helmholtz instability at

$$Ri_c \approx \frac{\epsilon_{\rho,0}}{36}\,, \tag{6.22}$$

where $\epsilon_{\rho,0}$ is the dust-to-gas volume-density ratio at the disk midplane. This means that for many values of disk metallicity, the critical Richardson number could potentially be much lower than 1/4, and possibly that the dust/gas requirements for planetesimal formation could be lower as well. $\epsilon_{\rho,0}$ can be written as $\epsilon_{\rho,0} \approx (\Sigma_p/\Sigma_g)\,/\,(H_g/H_p)$ and, assuming H_p follows from $H_{p,c}$ in Equation-set (6.20),

$$Ri_c \approx \frac{c_s\,(\Sigma_p/\Sigma_g)}{36 v_{\rm K}\eta_{\delta\phi}\sqrt{Ri}h\,(\psi)} = \frac{c_s E Z_0 Z_{\rm rel}\,(T)}{36 v_{\rm K}\eta_{\delta\phi}\sqrt{Ri}h\,(\psi)}\,. \tag{6.23}$$

This describes a critical Richardson number that is specific to the midplane density produced for a given enhancement factor, E, with a vertical dust distribution specified by a given Ri. If, for fixed E, the dust distribution settles further toward the disk midplane, Ri decreases and Ri_c given in Equation (6.23) increases. At some point, defined by $Ri_c = Ri = Ri'_c$, this effect should balance out. One may then define a critical Richardson number based on the *Lee et al.* (2010) simulations

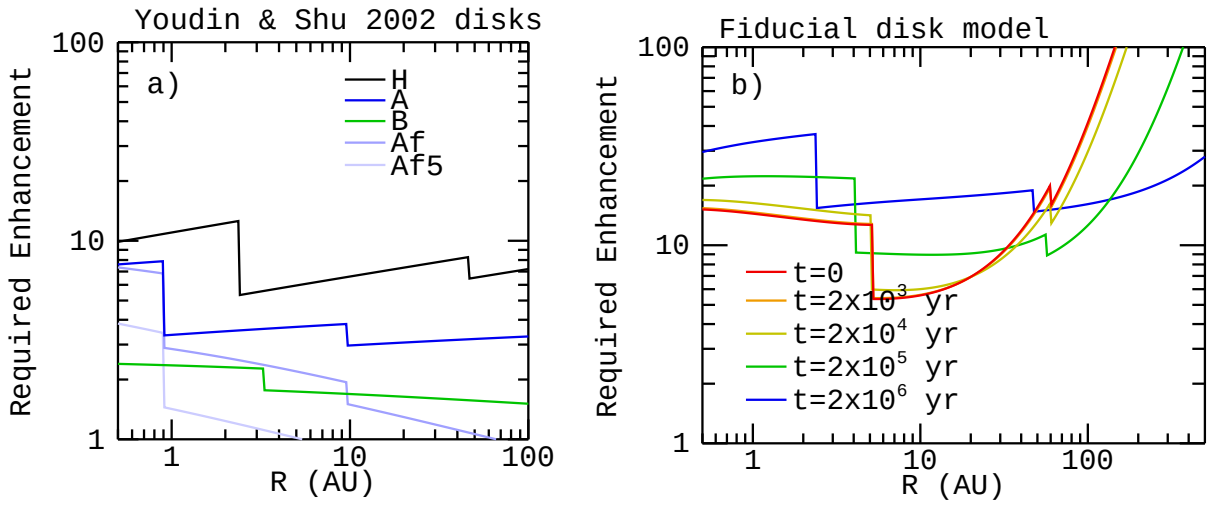

Figure 6.10: Required Enhancements for midplane precipitation using the results of *Lee et al.* (2010) and Equation (6.24) to calculate Ri_c for the disks of *Youdin & Shu* (2002) and my fiducial-disk model.

as a function of the enhancement factor alone:

$$Ri'_c = \left(\frac{c_s E Z_0 Z_{\rm rel}\left(T\right)}{36 v_{\rm K} \eta_{\delta\phi} h\left(\psi\right)} \right)^{2/3} . \tag{6.24}$$

Using Ri'_c in Equations (6.19) & (6.21), I define alternate enhancement criteria for precipitation/collapse of solids at the midplane:

$$E'_{\rm precip} \geq \frac{v_{\rm K} \eta_{\delta\phi} s\left(\psi\right)^{3/2}}{6 c_s Z_0 Z_{\rm rel}\left(T\right) \sqrt{h\left(\psi\right)}} , \tag{6.25}$$

and

$$E'_{Q_p} \geq \frac{\sqrt{c_s}\, v_{\rm K} \eta_{\delta\phi} h\left(\psi\right)}{6 Z_0 Z_{\rm rel}\left(T\right)} \left(\frac{\Omega_{\rm K}}{\pi G \Sigma_g} \right)^{3/2} . \tag{6.26}$$

Figure 6.10 plots the required enhancement factors using these new definitions for the same disk models considered in Figure 6.9. The result is enhancement requirements that are generally somewhat lower than those assuming $Ri_c = 1/4$ (about a factor of 2 lower at the snow-line), particularly at early times. However, in the very-outer-disk regions where radial pressure gradients are high, Equations (6.25) & (6.26) actually produce somewhat higher enhancement requirements. The enhancements required for precipitation in the expanding outer disk are so high in under both Ri_c

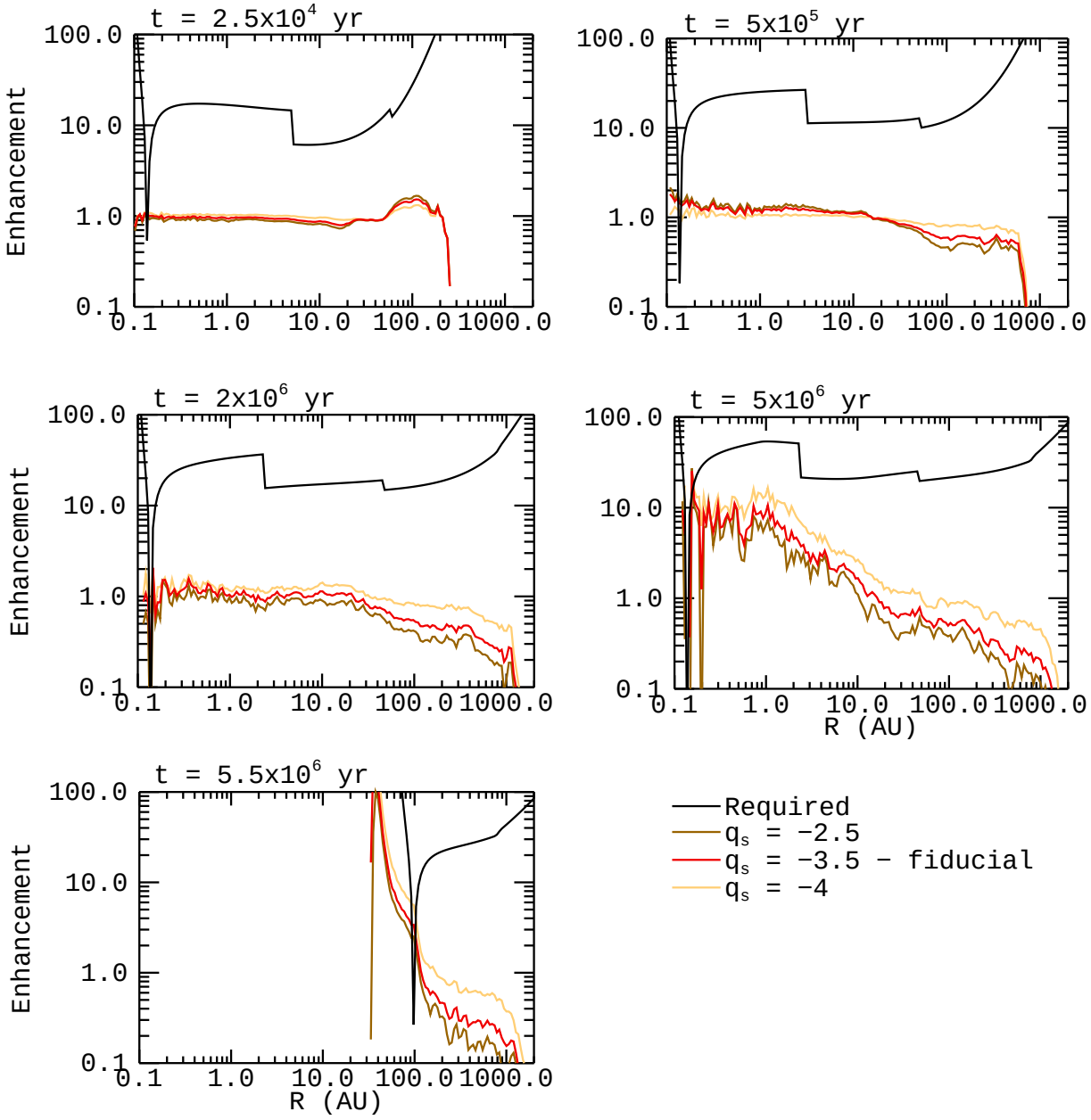

Figure 6.11: Measured, compiled enhancement values for the fiducial-disk model at several times and using several particle-size distributions compared to enhancement factors required for precipitation/collapse as given by Equations (6.25) & (6.26).

assumptions, however, as to be virtually unobtainable. Therefore, for the rest of this section, I compare the dust/gas enhancements produced by my particle-transport simulations to the slightly more forgiving requirements from Equations (6.25) & (6.26).

The first such comparison is shown in Figure 6.11 for the fiducial-disk model at several times. In

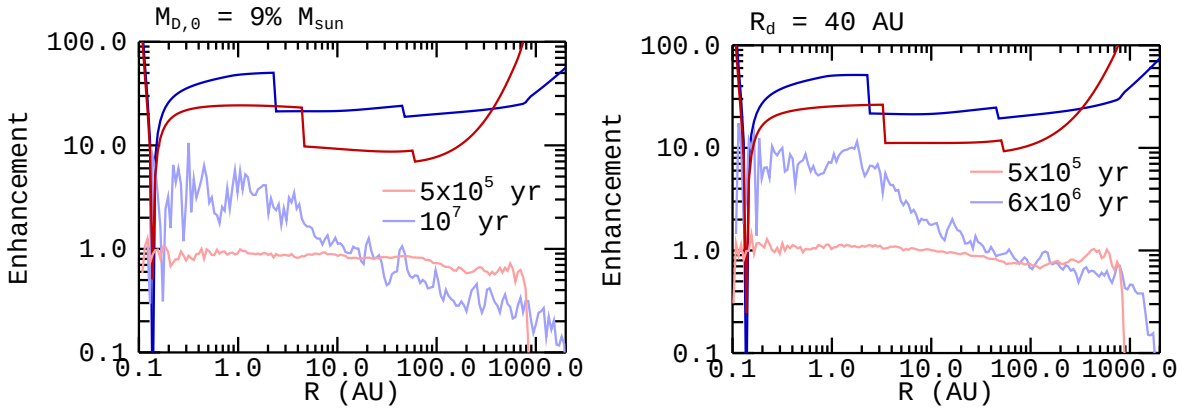

Figure 6.12: $E_{\rm precip}$ (dark lines) and measured E (light lines) for two larger disks at early and late times. Left side: $M_{D,0} = 0.09 M_\odot$, $R_d = 20$ AU, $\alpha = 10^{-2}$. Right side: $M_{D,0} = 0.03 M_\odot$, $R_d = 40$ AU, $\alpha = 10^{-2}$.

this figure, I compare enhancement factors required for planetesimal precipitation to enhancement results from my simulations compiled using three different assumed particle-size distributions. The fiducial distribution, with $q_s = -3.5$, uses the particle-size distribution measured for the ISM (*Mathis, Rumpl, & Nordsieck*, 1977), whereas $q_s = -4$ is often used for a collisional size distribution (e.g., *Bai & Stone* (2010a)), and $q_s = -2.5$ corresponds to shallow distributions, used as indicators of grain-growth, measured in some protoplanetary-disk systems (*Ricci et al.*, 2011). From Figure 6.11, it is clear that the size distribution used to compile my simulation results has little impact on the conclusions of the fiducial runs. Radial drift of particles does not produce enhancement sufficient to lead to planetesimal formation via precipitation for this model disk. The exception occurs at the very end of the disk lifetime when photoevaporative clearing of the disk leads to an outward-sweeping pressure-maximum point at large AU where $\eta_{\delta\phi}$ goes to zero and $E_{\rm precip}$ drops to small values.

The enhancement maps of Figure 6.5 show that the dust-to-gas distributions for the more extended or more massive disk models are qualitatively like that of the fiducial model. However, the enhancement criteria for these disks should differ from the fiducial case and, perhaps, be more favorable to collapse. In Figure 6.12, I plot measured versus required enhancements for the larger ($M_{D,0} = 0.03 M_\odot$, $R_d = 40$ AU, & $M_{D,0} = 0.09 M_\odot$, $R_d = 20$ AU) disk models at two times. While the collapse criteria are slightly less stringent than in the fiducial case, this is generally insufficient to allow the simulated enhancement factors to cross the threshold for precipitated planetesimal

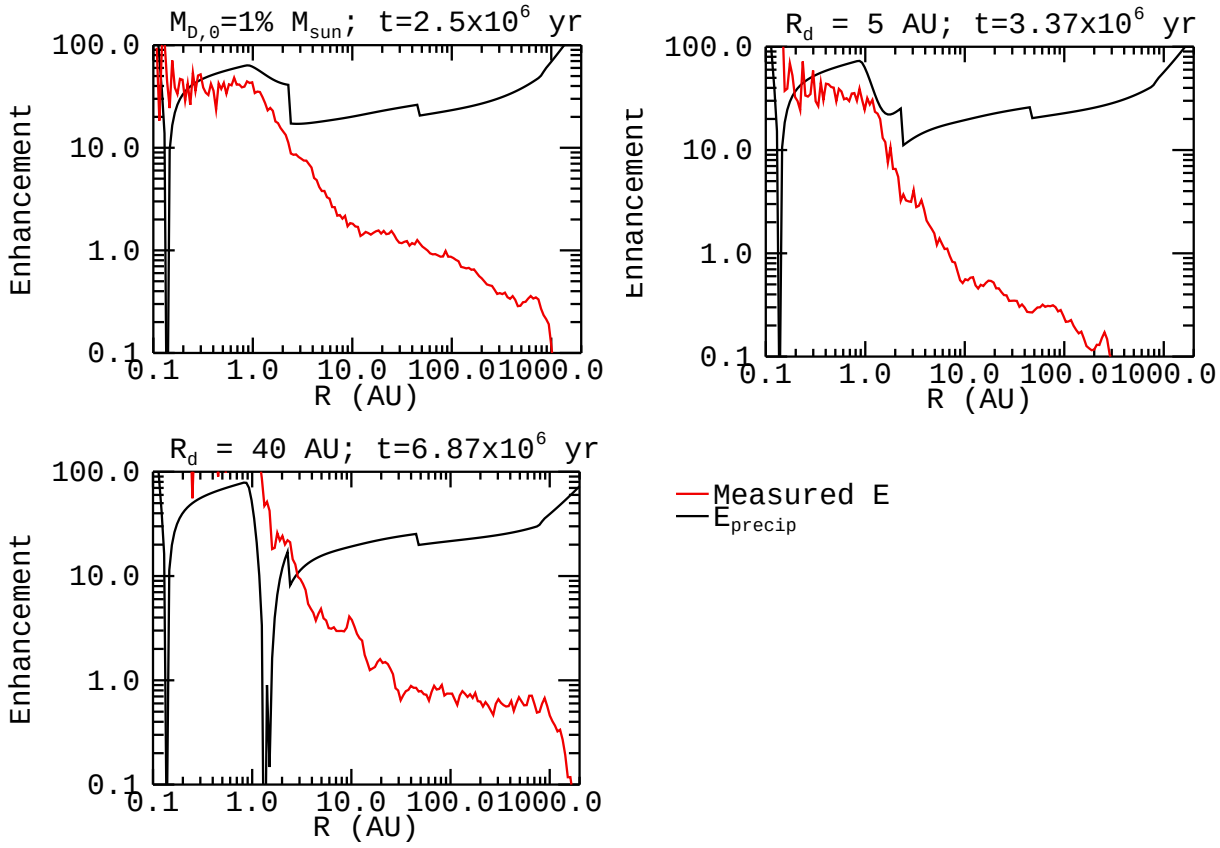

Figure 6.13: $E_{\rm precip}$ versus measured E in three non-fiducial disks close to the onset of gap opening via EUV photoevaporation. Top-left: $M_{D,0} = 0.01 M_{\odot}$, $R_d = 20$ AU, $\alpha = 10^{-2}$. Top-right: $M_{D,0} = 0.03 M_{\odot}$, $R_d = 5$ AU, $\alpha = 10^{-2}$. Bottom: $M_{D,0} = 0.03 M_{\odot}$, $R_d = 40$ AU, $\alpha = 10^{-2}$.

formation. At early times, measured E is still close to unity, and near the end of the disk lifetime both $E_{\rm precip}$ and measured E show similar behavior to the fiducial case. Once again, it is just before and during disk clearing by photoevaporation that precipitation criteria are the closest to being met, with equally strong potential for this to happen in the smaller-disk cases, as shown in Figure 6.13. In fact, near the end of the disk lifetime, the smaller disks have a slight advantage in that the more rapid loss of disk gas allows for infall of the smaller dust-grain population.

Of course, it can be difficult to rapidly pile-up large grains via radial drift when most of those grains originate at small AU. The observations of *Kwon et al.* (2009) of a collapsing cloud suggest that grain-growth may be very rapid indeed, and so the restrictions I have placed on the extent and timing of the large particle sizes may be too conservative. Furthermore, observations of protoplanetary disks tell us that large grains do exist at large AU (*Testi et al.*, 2003). Therefore,

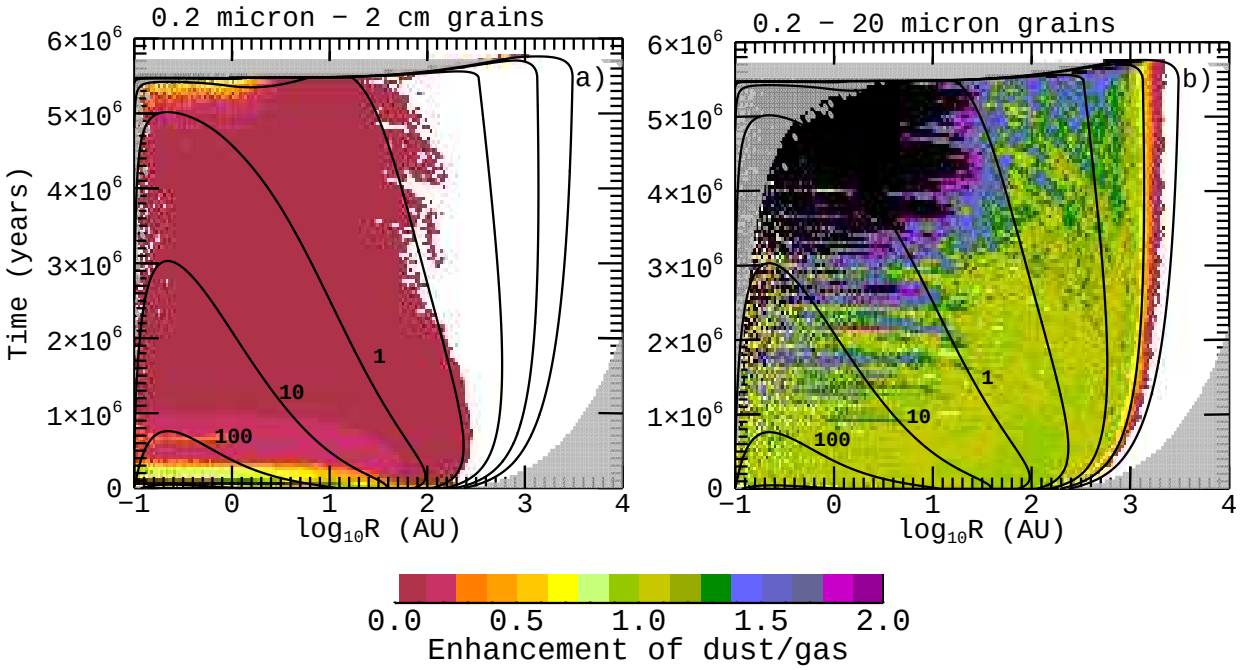

Figure 6.14: Enhancement maps for the case when all particles are initiated at $t = 0$ randomly distributed throughout the entire $t = 0$ disk-gas mass distribution. **Panel-a)** composite assuming the entire 0.2 μm – 2 cm grain-size set. **Panel-b)** composite using grains only up to 20 μm in size. Maps follow the same conventions as in Figure 6.2.

I next present a simulation set in which all grain sizes were initiated at $t = 0$ and entirely randomly (evenly) distributed throughout the mass of the $t = 0$ gas disk so that the initial grain-size distribution is entirely independent of R.

In Figure 6.14, I plot composite enhancement maps from this $t_0 = 0$ simulation for two cases: one in which the particle-size distribution extends from 0.2 μm to 2 cm, and one in which only the smaller 0.2–20 μm grains are included. Because $q_s = -3.5$ distributes more mass into larger sizes than small, in the first case, most of the dust-mass in the disk rapidly falls inward to small AU. It is thus quickly lost onto the parent star, but not before creating a period if distinct enhancement in the dust-to-gas ratio in the inner-main disk. This enhancement is plotted in Figure 6.15 panel-a relative to $E_{\rm precip}$. While the enhancement peaks around $\times 5$ at $t \sim 4 \times 10^4$ yr, this is still insufficient to cross the threshold of $E_{\rm precip}$ in the fiducial-disk model. The infall of smaller particle sizes can also be seen at larger disk radius in the $t = 4 \times 10^4$ year panel, but the *net* enhancement in the disk still declines swiftly after the $t = 4 \times 10^4$ year peak, and by $t = 5 \times 10^5$ years the metallicity across the whole disk is at a fraction its initial value.

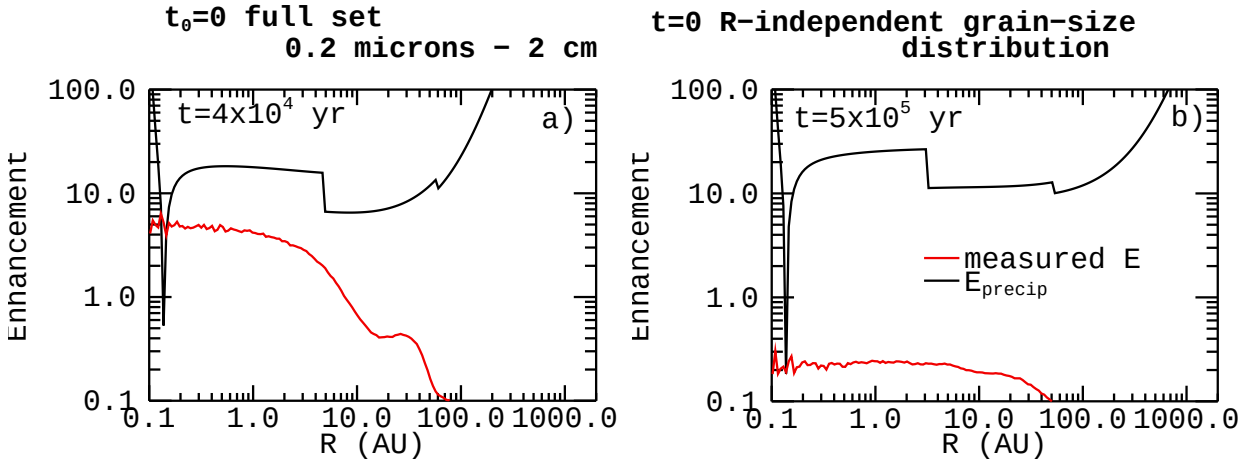

Figure 6.15: $E_{\rm precip}$ versus measured E at two times for the case when all particles were initiated at $t = 0$ equally distributed throughout the gas disk. The peak in measured E (occurring at $t = 4\times10^4$ years) is shown using a composite made with only 25 time-outputs per time-bin with $\Delta t = 5 \times 10^3$ years.

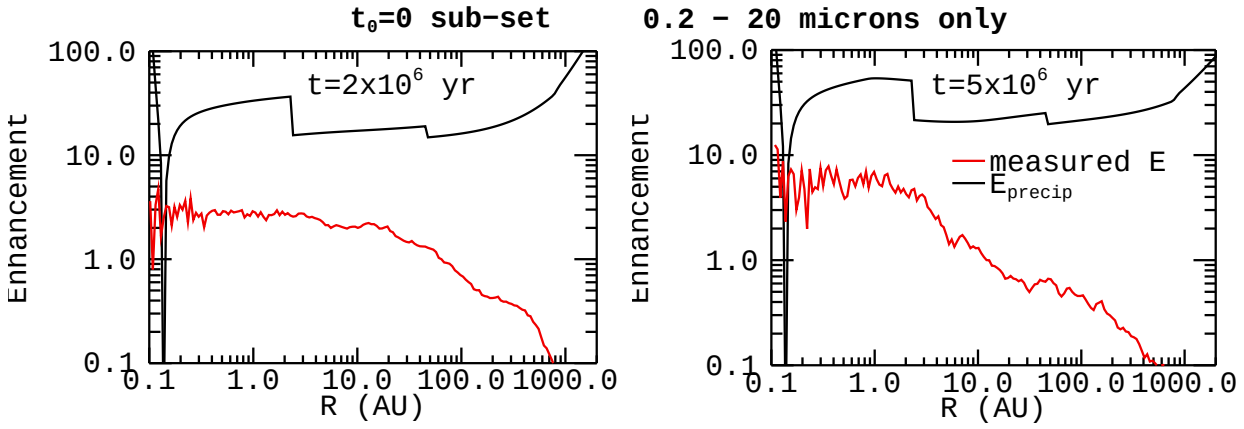

Figure 6.16: $E_{\rm precip}$ versus measured E at two times for the case when $t_0 = 0$ for all grain sizes, having a radially independent grain-size distribution at $t = 0$. Composite made using grains only up to 20 μm in size.

For the smaller-maximum–grain-size t_0=0 case shown in the second panel of Figure 6.14, substantial dust mass remains in the disk for a longer period of time and is not concentrated toward small disk radii until the disk is tenuous enough for 20 μm sized grains to experience substantial infall. Again, this infall does cause a distinct increase in the inner-disk metallicity, but again, as shown in Figure 6.16, it is insufficient to reach the requirements of $E_{\rm precip}$. At later times, more dust mass in small particle sizes remains in the disk, but peak enhancements toward the end of the disk lifetime of $E_{\rm max} < 10$ remain below $E_{\rm precip}$. Therefore, the potential of dust in these $t_0 = 0$

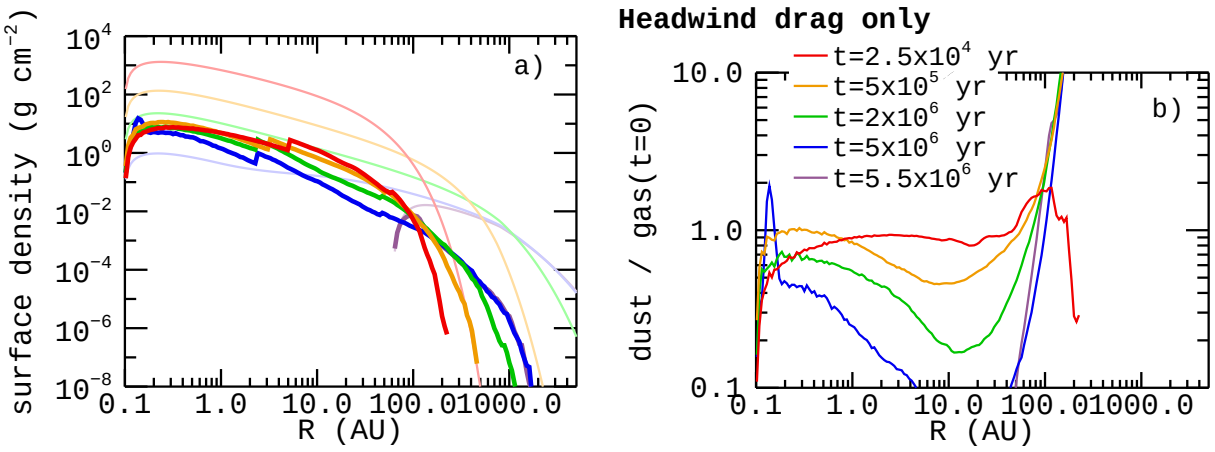

Figure 6.17: Dust distributions for the case where particles fall in due to headwind drag only, without radial gas-drag advection. **Panel-a)** Surface-density profiles of the dust (thick lines) and gas (pale, thin lines). **Panel-b)** Enhancement of dust relative to the $t = 0$ dust distribution. Simulation includes only grain sizes 0.2μm–2 mm.

simulations to reach $E_{\rm precip}$ concentrations are qualitatively the same as in the fiducial simulations with large grain sizes confined to smaller disk radii at t_0.

Finally, in my particle-transport simulations, the majority of dust mass is lost onto the parent star via simple advection within the accreting disk gas. In order to examine whether the pattern of this accretion inflow has an important impact on the relative distribution of grains, particularly on the rapid loss of the large grains, I present in Figure 6.17 a simulation in which particles were initiated in the standard way based on their grain size, but were then allowed to undergo inward drift based only on the difference between the dust and gas azimuthal velocities (just due to headwind drag by itself). The gas disk is evolved as normal so the dust distribution diffuses outward as the disk expands, as shown in panel-a. However, because the gas disk is rapidly losing mass while the dust disk is not, the standard measure of E, of course, reaches values of tens and even hundreds. Therefore, in panel-b, I do not plot the standard E measure. Instead I plot the distribution of dust mass relative to its $t = 0$ distribution. This produces extreme enhancement in the outer disk due to the outward diffusion relative to the $t = 0$ distribution (though not relative to the evolving gas distribution), and the mid-disk does show inward drift of the dust. However, this inward drift does not correspond to a relative increase in solids at small AU. The effects of headwind drag alone appear sufficient to preferentially remove mass from the inner disk. Radial advection only normalizes the dust distribution to the gas-disk evolution.

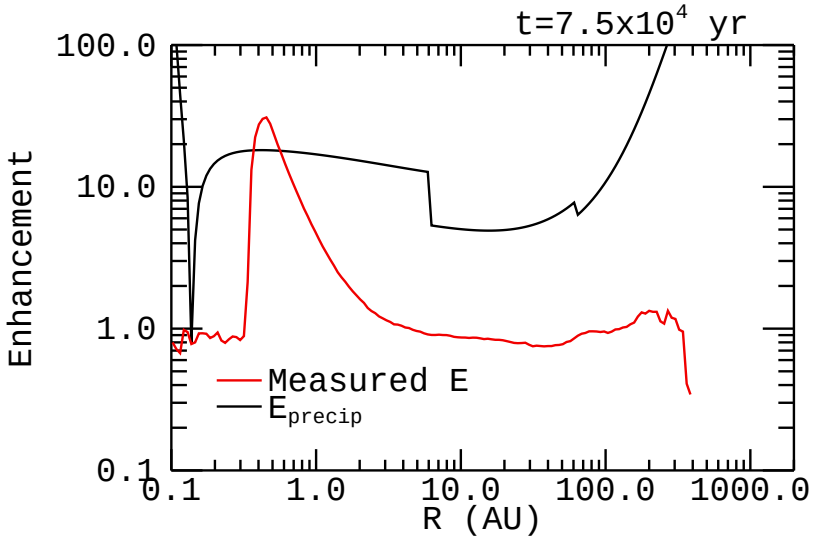

Figure 6.18: $E_{\rm precip}$ versus measured E at $t = 7.5\times10^4$ years for a simulation in the $M_{D,0} = 0.09M_\odot$ disk model in which the 2 cm-sized particles were barred from reaching the inner disk edge.

6.5 Discussion and mm-size Grains

In all of my simulations, it is the rapid loss of the largest grain sizes that stymies significant enhancement of the dust-to-gas ratio. Therefore, as in the mixing simulations of Chapters 4 & 5, the transport processes for large grains at small AU have an important impact on the dust-solids population as a whole. In Figure 6.18, I plot a simulated enhancement distribution at $t = 7.5 \times 10^4$ years in the $M_{D,0} = 0.09M_\odot$ disk for a case wherein the 2 cm-sized grains are given an artificial barrier to inward drift at small AU. In less that 10^5 years, they pile up so much mass in the inner disk as to cross the precipitation threshold of $E_{\rm precip} > \times10$. Without such a barrier, however, mm–cm sized grains are rapidly lost from the disk, as demonstrated in the fiducial simulations. This rapid loss of large grains presents problems on two fronts: that of observations of disks around other stars, and that of theories of planetesimal formation.

In terms of the observations, numerous observational studies of disks around other stars find evidence for rapid grain growth within disks (e.g., *Rodmann et al.* (2006); *Kessler-Silacci et al.* (2006); *Kwon et al.* (2009); *Ricci et al.* (2010a)). Furthermore, observations in the (sub-)mm bands see evidence for mm-sized grains, not just within disks, but out to 100 AU or farther within those disks (*Testi et al.*, 2003; *Ricci et al.*, 2010b). The cartoon grain-growth model I use to constrain

the radial extent of simulation particles does not allow mm-sized grains to be initiated beyond 22 AU an any of the disk models I've run, and the inward flow from both accretion and headwind drag certainly precludes any simulated mm grains from reaching 100 AU. Furthermore, the mixing simulations run for Chapters 4 & 5 include simulations of particles experiencing outward-flowing gas at the disk midplane, but less than 6% of mm-sized grains in that gas-flow case reach even 25 AU, and then only for a brief period of time, before the disk experiences substantial accretional evolution and thinning.

That headwind drag tends to bar large grains from the outer disk, in contradiction with observations, has been noted and studied by several authors (e.g., *Weidenschilling* (1977a); *Takeuchi & Lin* (2005); *Brauer et al.* (2007)). *Brauer et al.* (2007) specifically focus on attempting to solve the radial-drift problem by including more and more detailed physics into the transport calculations, including dust settling and collective effects, and angular momentum exchange between a dust sub-layer and the main gas disk. The authors find these effects in general insufficient to slow radial drift of mm-sized grains to velocities compatible with their observed persistence in disks that are generally 1 Myr old or older. *Brauer et al.* (2007) relate the problem of the survival of mm-sized grains in the outer disk to the problem of the survival of m-sized grains in the inner-main disk. However, one point in this puzzel that my global-dust-distribution simulations emphasize is that aerodynamic effects not only keep mm-sized grains from the outer disk, but lose them rapidly from the main and inner disks as well.

It is in the main and inner disks that loss of large grains is problematic for theories of planetesimal formation. In streaming-instability models of planetesimal formation, clumping and collapse of particle ensembles is not only strongly dependent on above-solar disk metallicities (*Johansen, Youdin, & Mac Low*, 2009), but occurs specifically for particles that are marginally coupled to the gas motions (*Johansen et al.*, 2007; *Johansen, & Youdin*, 2007; *Bai & Stone*, 2010a). This means particles with normalized stopping times, τ_s, preferentially near 1 (though *Bai & Stone* (2010a) report that grains as small as $\tau_s \sim 10^{-2}$ still participate in the streaming instability), requiring at least cm-sized grains at around 1 AU. Furthermore, chondrules (∼mm in size) make up a large fraction of most meteorites (*Cuzzi, Davis, & Dobrovolskis*, 2003), implying that planetesimals in the inner-main disk of the Solar Nebula were largely built from mid-to-large sized grains (see, e.g., *Cuzzi, Hogan, & Bottke* (2010) for a discussion). Therefore, planetesimal formation models using

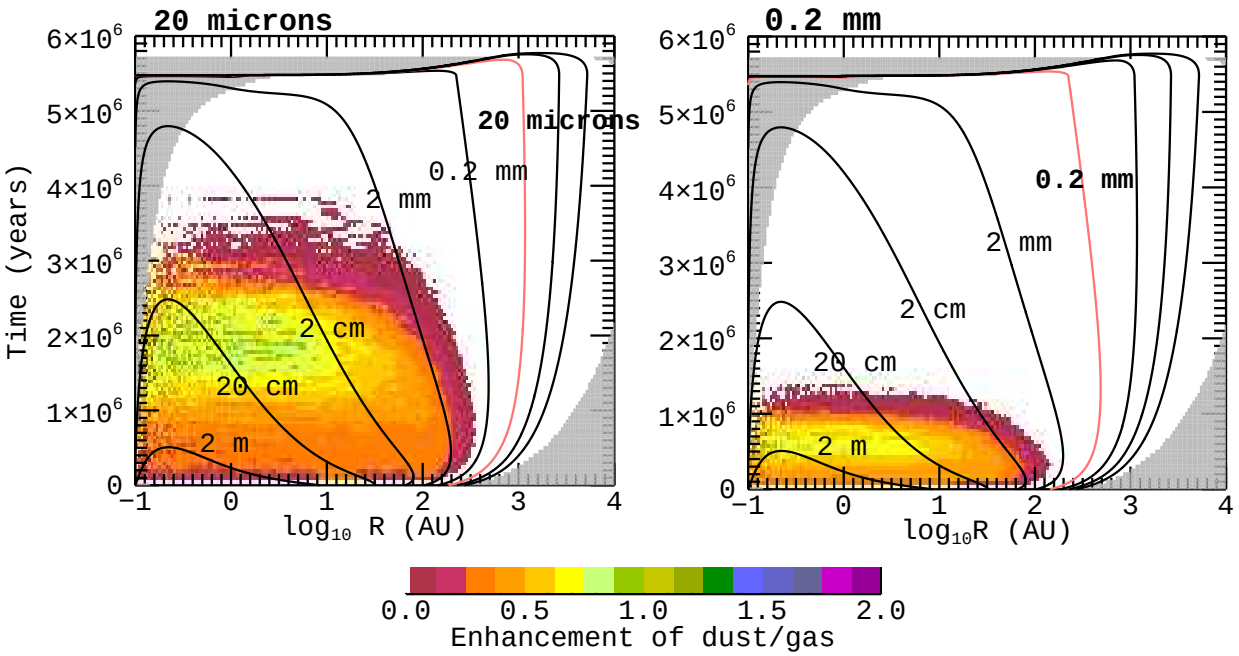

Figure 6.19: $\tau_s = 1$ grain-size contours (0.2 μm–2 m) overlying two maps of dust distribution for two individual grain-size components. Pink contour highlights the contour matching the mapped dust distribution. Component distributions also shown in Figure 6.1 and following the conventions of that figure.

such grain sizes may be well justified. Of course, $\tau_s \sim 1$ requires smaller grain sizes in the outer, more tenuous parts of a disk. In the Epstein-drag regime,

$$\tau_s = \Omega_{\rm K} t_{\rm stop} = \frac{s_d \rho_d \Omega_{\rm K}}{\rho_g v_{\rm therm}}\,, \tag{6.27}$$

where s_d and ρ_d are the dust-grain radius and internal density, ρ_g is the local gas density, and $v_{\rm therm}$ is the thermal velocity of the gas particles. However, $v_{\rm therm} = c_s\sqrt{8/\pi}$, where c_s is the sound speed, and, in a vertically-isothermal disk, $\rho_g = \Sigma_g \exp\left(-z^2/2H_g^2\right)/\sqrt{2\pi}H_g$, where $H_g = c_s/\Omega_{\rm K}$. Therefore, at the midplane of a vertically-isothermal disk, in the Epstein-drag regime,

$$\tau_s = \frac{\pi s_d \rho_d}{2\Sigma_g}\,. \tag{6.28}$$

In Figure 6.19, I plot the grain-size contours matching $\tau_s = 1$ in my evolving, fiducial disk model, overlying the dust-enhancement distributions of both 20 μm and 0.2 mm-sized grains in my fiducial

simulations. From this, one can see that even in the outer disk, grains of all sizes are confined inward of their $\tau_s = 1$ contours by at least one and a half orders-of-magnitude, leaving very few grains within the $\tau_s \gtrsim 10^{-2}$ bounds for participation in the streaming instability. This is because the headwind-drag barrier also operates most strongly near $\tau_s = 1$. This grain-distribution behavior is duplicated with minor variation in the $Sc = 2$ and $Sc = 1/2$ simulations. Grains of a given size are entirely confined within $\tau_s \leq 10^{-1}$, and enhanced final infall of the population occurs when local τ_s contours at the outer edge of the distribution begin to evolve inward within the disk.

As with planetesimal formation via precipitation, simulations suggest that the streaming-instabillity method is also largely confined to certain regions of a disk by the local value of the radial pressure gradient. In *Bai & Stone* (2010b), the authors report simulations of particle clumping via the streaming-instability in which they vary their pressure-gradient term, Π_η, between 0.025, 0.05, and 0.1. They find clumping requires $\tau_s \gtrsim 10^{-2}$ for most particles and super-solar metallicity when $\Pi_\eta = 0.05$, and a monotonic increase in required metallicity for increasing Π_η. *Bai & Stone* (2010b) define $\Pi_\eta \equiv \eta_{\delta\phi} v_{\rm K}/c_s$, where $\eta_{\delta\phi} = \left(v_{\rm K} - v_{\phi,g}\right)/v_{\rm K}$. Therefore,

$$\Pi_\eta = \frac{\left(v_{\rm K} - v_{\phi,g}\right)}{c_s}\,. \tag{6.29}$$

In Figure 6.20 panel-a, I plot Π_η contours in red overlying the $\tau_s = 1$ grain-size contours for the fiducial-disk model. The spatial relationship between the Π_η and τ_s parameter constraints suggests, then, that the streaming-instabillity model mostly confines planetesimal formation from this mechanism to the inner-main regions of the disk, where cm-sized particles are required to allow for marginal-coupling between the solids and the disk gas. This is doubly the case when paired with my global-transport simulations suggesting that the outer disk will tend to be at least somewhat depleted in solids relative to the gas, though again, super-solar metallicities and cm-sized grains, which my simulations are unable to supply simultaneously, are required as well.

The *Bai & Stone* (2010b) simulations are actually run considering a minimum-mass-style Solar Nebula disk, with a steeper Σ_g profile and therefore steeper radial pressure gradient than that of my fiducial disk model. However, observations suggest that some disks have experienced grain-settling and flattening (*Miyake & Nakagawa*, 1995), which will tend to rapidly cool a disk toward larger radii. As discussed briefly in §5.6.2, this effect may produce shallower surface-density profiles and

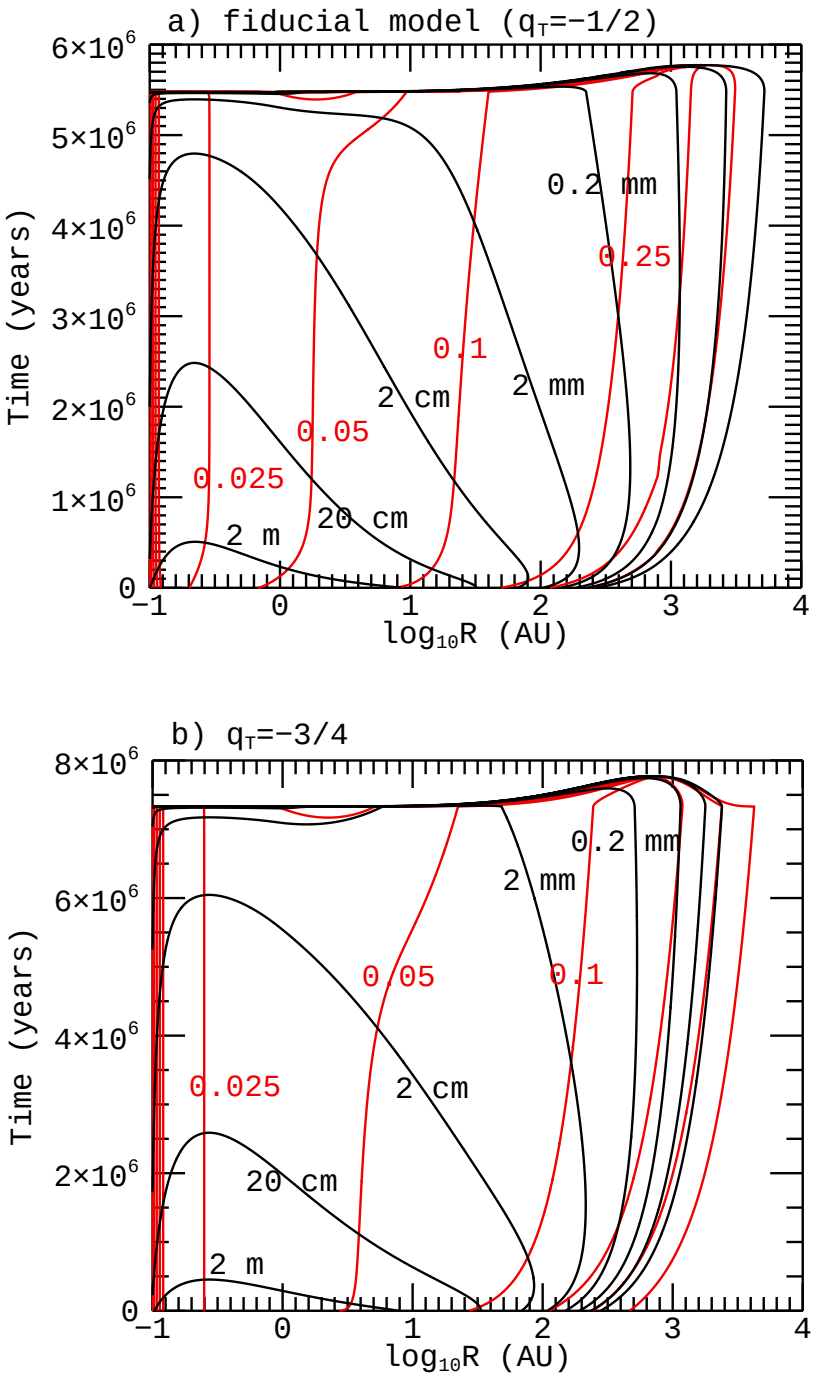

Figure 6.20: Π_η contours **(red)** overlying $\tau_s = 1$ grain-size contours **(black)** for the fiducial-disk model and an evolving-disk model having a steeper temperature gradient and therefore a shallower surface-density profile (see §5.6.2). Π_η contours are for values of 0.025, 0.05, 0.1, 0.25, 0.5, and 1. $\tau_s = 1$ grain-size contours are spaced in decades 0.2 μm–2 m. Note that the second disk is colder and therefore longer lived.

radial-pressure gradients within a disk, and I plot the Π_η and τ_s grain-size contours for such a disk in panel-b of Figure 6.20. From this, one sees that while a steeper temperature gradient and colder outer disk does expand the region of low Π_η more favorable to streaming-instabillity planetesimal formation, it also pushes the $\tau_s = 1$ grain-size contours outward so that large particles are likely still required, even at larger distances, for the streaming-instabillity mechanism to operate. Because headwind drag inspiral is weaker for shallower pressure gradients, my mixing simulations of §5.6.2 suggest that the dust population of a given grain size might not be confined so far inward of it's $\tau_s = 1$ contour in such a disk as in the fiducial-disk model. However, inspiral and loss of large grains is likely to still be problematic, even in a shallow Σ_g-profile disk model.

Observations of disks around other stars suggest that growth of disk solids to at least tens-of-microns size is fairly rapid (signs of grain growth are observed for essentially all disks) (*Kwon et al.*, 2009; *Ricci et al.*, 2010a), and also that disks tend to maintain a small-dust population over a large fraction of their lifetime (*Bouwman et al.*, 2003; *Dominik & Dullemond*, 2008). Furthermore, the fraction of stars observed to have circumstellar debris disks (with scattered-light levels around a thousand times brighter than that of our own zodiacal dust and Kuiper belt) peaks at around 50% for 20 Myr old B and A stars (*Currie, Plavchan, & Kenyon*, 2008). These facts lend credence to the idea that planetesimal formation is a fairly ubiquitous process that can form large bodies early on and over a decent range of disk radii; collisional fragmentation of large bodies orbiting within a disk is one of the most efficient mechanisms for maintaining a small-dust population.

However, my global-dust-transport simulations suggest that aerodynamic transport of dust grains within a smooth, evolving disk model will equally ubiquitously lead to large-scale inspiral and loss of the dust population, directly counter to both observations and current theories of planetesimal formation. It is unlikely that aerodynamic processes of small grains within a tenuous fluid are so poorly understood as to have falsely represented this general trend in behavior for the decades of disk study. Furthermore, the general 1D, fluid-dynamic picture of protoplanetary disks that is most often represented in models appears to be a reasonably good fit between known disk-population properties, such as disk sizes, lifetimes, and accretion rates. Even the mixing simulations I presented in Chapters 4 & 5 are qualitatively consistent with observed disk compositions. Therefore, I propose that a 1D protoplanetary disk model is simply insufficient to represent dust-gas interactions at the global-distribution and planetesimal-building level. Likely,

non-axisymmetric and local structures play an important role in providing locations where dust can concentrate relative to the gas, and it is possible, furthermore, that such structures may be integral to understanding the large-scale distribution and transport of large dust grains.

6.6 Conclusions

In this chapter, I have presented simulations of the global (re)distribution of a protoplanetary-disk dust population that include evolution of the gas-disk surface-density profile, aerodynamic advection and diffusion of the dust-particle ensemble within the gas, and simulated grain-growth constraints confining the appearance of the largest grain sizes to the inner and main regions of the disk. I find that the global distribution of solids within a 1D evolving disk model follows a fairly uniform evolutionary pattern across a range of disk-model parameter space for simulations varying the initial-disk mass, $M_{D,0}$, the initial-disk compactness, R_d, the α-scaling of the disk viscosity, and the relative diffusivity of the particle ensemble, Sc. Specifically,

* Large, mm–cm-sized particles are lost rapidly onto the the parent star (within 0.5 Myr).

* Growth of dust grains up to microns size and larger leads to the depletion of dust relative to the gas toward the outer regions of the disk (beyond $\sim$100 AU).

* And, the dust-to-gas ratio within the main and inner disks remains near solar (near it's initial value) for at least the first 40–60% of the disk lifetime.

In general, grains of a given size are confined to regions of the disk interior to at least $\tau_s \leq 10^{-1}$ and experience accelerated infall as τ_s ($\propto \Sigma_g$) contours near the outer boundary of that dust-population distribution evolve inward.

In *Youdin & Shu* (2002), the authors present calculations of dust-to-gas enhancement factors resulting from radial drift of dust grains within a static disk, finding a steady increase in dust-to-gas ratios at small disk radii with time. Such increases are not seen in the simulations presented in this chapter for two important reasons. **First**, the inclusion of gas-disk accretional evolution adds a bulk inward flow to both the gas and dust within the disk that is absent from the *Youdin & Shu* (2002) calculations. Also, as disk surface-density contours evolve inward, the infall of the dust grains is accelerated beyond the simple accretion+headwind-drag loss rates. **Second**, the

simulations I present include loss of gas and dust past an inner-disk boundary set at $R = 0.1$ AU. The *Youdin & Shu* (2002) calculations extend the disk all the way to $R = 0$. Without loss of dust mass, their calculations must produce dust enhancements at small R.

Currently, local enhancement of the dust-to-gas surface-density ratio above solar metallicity is considered an important component of most active theories of planetesimal formation. Electrostatic and chemical forces appear insufficient to build bodies via sticking of grains above roughly centimeter sizes. However, in order for ensembles of small grains to collapse into large bodies gravitationally, the local dust density must exceed the Roche density, allowing collapsing solids to resist tidal disruption due to stellar gravity. This Roche density is commonly 2–3 orders of magnitude greater than typical midplane densities (*Chiang & Youdin*, 2010). While significant enhancement of the dust density may be achieved through settling of the dust toward the midplane and turbulent-concentration mechanisms such as the streaming instability, these mechanisms have generally been found insufficient to reach Roche density within a disk of Solar metallicity. Therefore, some increase in the dust-to-gas surface-density ratios within the disk is also required.

To consider specific proposed planetesimal-formation scenarios: the results of my simulations suggest that radial drift of particles within an azimuthally-symmetric, evolving disk scenario cannot produce enhancements in the dust-to-gas ratio in the inner disk sufficient to meet requirements for large-scale collapse and planetesimal formation via the *Youdin & Shu* (2002)-precipitation mechanism, particularly not early enough in the disk lifetime to account for the formation of giant-planets via the core-accretion scenario. The precipitation criteria depend on the local disk mass, temperature, and radial pressure gradient, and are most favorable to collapse in disks that are substantially more-massive and colder than a typical Solar Nebula analog. Planetesimal formation via particle clumping and the streaming instability is less dependent on disk mass, but still requires above-Solar local metallicites, as well as a substantial population of mm–cm-sized grains. My simulations suggest that a 1D model of disk evolution and grain transport cannot provide substantial dust enhancements *and* a large-grain population simultaneously, owing to the short lifetime of the later within the disk.

If large-scale radial-drift concentration of solids within a disk is non-viable, it then seems likely that local structure and local concentration of dust grains play an important role in providing the conditions necessary for planetesimal formation. Local disk structures that could prove important

for dust concentration include, e.g., disk-opacity transitions, such as at the snow-line, spiral arms produced within gravitaionally unstable disks, and vortices within the flow of disk gas. Also, some simulations of magnetorotationally unstable disks suggest that MRI turbulence produces local structure sufficiently long lived to concentrate dust particles (*Johansen, Youdin, & Klahr*, 2009).

However, understanding the global dust distribution is important not only for identifying potential sites of enhanced planetesimal formation. The simulations I present are run within 1D disk models assuming azimuthal symmetry and a smooth description of the protoplanetary gas disk. Such models are qualitatively compatible with observational descriptions of global disk structure and evolution, as well as (demonstrated in my mixing simulations of Chapters 4 & 5) with trends between disk compositions and evolutionary parameters. However, as in previous studies of headwind drag and inward grain migration, these simulations are in direct conflict with observations of large grains at large distances in disks around other stars. Therefore, I conclude that a one-dimensional picture of disks and grain-transport is insufficient to represent dust transport and distribution on a global scale, particularly in the regime of marginally-coupled particles. Non-axisymmetric disk structure then also likely plays an important role in the long-distance transport of large dust grains, and should be studied with the radial transport/distribution of grains in mind.

Studies of global dust transport as a function of local structure may prove challenging. Numerically, local strucure is often preferentially captured within small-scale shearing-box-style simulations often poorly compatible with the inclusion of disk evolution and accretional flows (which I have shown are centrally important to understanding long-distance grain transport). However, advances in computing resources and techniques continue to provide ever-richer details concerning disk-flow dynamics and likely will do so on this front as well.

As with the mixing of dust species, future studies of large-scale grain distributions should also include dust transport due to height-dependent grain migration and transport within alternative disk-gas models, such as, e.g., disks that are flattened and colder in their outer regions, and disks experiencing prolonged or episodic infall of material from their parent molecular clouds. However, future disk observations will likely play a key role in improving our understanding of protoplanetary-disk physics. Three areas where further, better observations could prove invaluable include:

1. **Better spatial resolution and more samples of the youngest and forming disks.** Because age-dating evidence suggests that CAIs and iron-core meteorite parent bodies formed around the same — very early — time in Solar Nebula history, the properties of disks as they are forming are likely important for the mixing and distribution of high-temperature material, the earliest growth of solids to larger sizes, and the first-stage opportunities of planetesimal formation. A spatially resolved, clear picture of the gas and dust distribution, as well as the dust size-distribution, in the youngest disks could provide great insight into disk properties relevant to solids processing. Unfortunately, these early times in a disk history are only a small fraction of the disk lifetime, and so such disks are rarer and often observered at greater distances. Also, disks that are first forming are still embedded within their parent molecular cloud and so obscured at many wavelengths (*Eisner et al.*, 2005). However, the Atacama Large Millimeter Array (ALMA) should provide great sensitivity and spatial resolution at wavelengths important for the study protoplanetary disks, and the selected study of trace gas species allows observers to probe some of the densest regions of molecular clouds. Therefore, new and greater observations of the youngest stages of disk formation are hopefully on the horizon.

2. **Stronger constraints on the large-scale radial surface-density structure of the *gas* within a disk.** While headwind-drag (apparently wrongly) predicts the rapid loss of large, mm-sized grains from the outer regions of a disk, that prediction is based on certain assumptions concerning the disk gas distributions at those large distances. Alternative gas distributions providing a much shallower radial pressure gradient in the outer disk would be more likely to retain large grains, and, for example, a scenio of lower disk viscosity leading to slower accretion and mass pile-up at large distances might also be more condusive to the *formation* of such large grains. Therefore, while the dust population provides most of the optical depth within a disk and is therefore easier to probe than disk gas, more examples and better statistics about gas-mass distributions out to large distances would prove most useful. Such information could either confirm the present conundrum of current dust-distribution observations, or else allow us to rethink our understanding of disk structure in ways that are more compatible with those observations.

3. **Information about the turbulent velocities/properties of protoplanetary disk gas.** For decades, the viscosity driving disk evolution has been believed to be derived from turbulent motions within the disk gas (*Shakura & Sunyaev*, 1973). However, the source and nature of that turbulence, particularly within relatively small, cold protoplanetary disks, have remained elusive, and observations have only recently just reached the threshold of possibly detecting turbulence within disks (*M. Hughes et al.*, 2011). At present some of the challenges of observing turbulence include merely separating out turbulent line-widths from signatures of infall of gas onto or outflow from the disk surface. Ideally, though, observations will eventually provide us with not just detection of turbulent motion within disks, but spatial information (radially and vertically within the disk structure) about the varying strength of that turbulence, to compare to current theories of turbulence generation within disks. The nature and strength of disk turbulence is essentially the greatest source of uncertainty in any calculations of disk structure, disk evolution, dust-gas aerodynamic interactions, and dust transport within a disk. Resolving the nature of disk turbulence would vastly strengthen all future calculations of solids processing within protoplanetary disks.

Note that while deep observations of the earliest times of disk formation could prove most valuable for building an understanding of our own Solar system chronology, having a strong understanding of the gas structure and dynamics of any observed disks would prove equally valuable. The apparent ubiquity of debris disks and millimeter grains distributed out to large distances in protoplanetary disks means that there remain problems to solve concerning disk structure and large solids within disks of all sizes and ages.

Bibliography

Alexander, R. D., Clarke, C. J., & Pringle, J. E. 2005, Constraints on the ionizing flux emitted by T Tauri stars, MNRAS, 358, 283–290.

Alexander, R. D., Clarke, C. J., & Pringle, J. E. 2006, Photoevaporation of protoplanetary disks — I. Hydrodynamic models, MNRAS, 369, 216–228.

Alexander, R. D., & Armitage, P. J. 2007, Dust dynamics during protoplanetary disc clearing, MNRAS, 375, 500–512.

Amelin, Y., Krot, A. N., Hutcheon, I. D., & Ulyanov, A. A. 2002, Lead isotomic ages of chondrules and calcium-aluminum-rich inclusions, Science, 297, 1678–1683.

Andrews, S. M., Wilner, D. J., Hughes, A. M., Qi, C., Dullemond, & C. P. 2010, Protoplanetary disk structures in Ophiuchus. II. Extension to fainter sources, ApJ, 723, 1241–1254.

Armitage, P.J. 2010, Astrophysics of Planet Formation, Cambridge University Press, Cambridge.

Bai, X.-N., & Stone, J. M. 2010a, Dynamics of solids in the midplane of protoplanetary disks: Implications for planetesimal formation, ApJ, 722, 1437–1459.

Bai, X.-N., & Stone, J. M. 2010b, The effect of the radial pressure gradient in protoplanetary disks on planetesimal formation, ApJ, 722, L220–L223.

Balbus, S. A., & Hawley, J. F. 1991, A powerful local shear instability in weakly magnetized disks. I. Linear analysis, ApJ, 376, 214–222.

Beckwith, S. V. W., & Sargent, A. I. 1993, Molecular line emission from circumstellar disks, ApJ, 402, 280–291.

Bell, K. R., & Lin, D. N. C. 1994, Using FU Orionis outbursts to constrain self-regulated protostellar disk models, ApJ, 427, 987–1004.

Bell, K. R., Cassen, P. M., Klahr, H. H., & Henning, Th. 1997, The structure and appearance of protostellar accretion disks: Limits on disk flaring, ApJ, 486, 372–387.

Birnstiel, T., Dullemond, C. P., & Brauer, F. 2009, Dust retention in protoplanetary disks, A&A, 503,L5–L8.

Bockelée-Morvan, D., Gautier, D., Hersant, F., Huré, J.-M., & Robert, F. 2002, Turbulent radial mixing in the Solar Nebula as the source of crystalline silicates in comets, A&A, 384, 1107–1118.

Boss, A. P. 2004, Evolution of the Solar Nebula. VI. Mixing and transport of isotopic heterogeneity, ApJ, 616, 1265–1277.

Boss, A. P. 2008, Mixing in the Solar Nebula: Implications for isotopic heterogeneity and large-scale transport of refractory grains, Earth & Planetary Science, 268, 102–109.

Bottke, W. F., Nesvorný, D., Grimm, R. E., Morbidelli, A., & O'Brien, D. P. 2006, Iron meteorites as remnants of planetesimals formed in the terrestrial planet region, Nature, 439, 821–824.

Bouwman, J., de Koter, A., Dominik, C., & Waters, L. B. F. M. 2003, The origin of crystalline silicates in the Herbig Be star HD 100546 and in comet Hale-Bopp, A&A, 401, 577–592.

Brauer, F., Dullemond, C. P., Johansen, A., Henning, Th., Klahr, H., & Natta, A. 2007, Survival of the mm–cm size grain population observed in protoplanetary disks, A&A, 469, 1169–1182.

Brauer, F., Dullemond, C. P., & Henning, Th. 2008, Coagulation, fragmentation and radial motion of solid particles in protoplanetary disks, A&A, 480, 859–877.

Brauer, F., Henning, Th., & Dullemond, C. P. 2008, Planetesimal formation near the snow line in MRI-driven turbulent protoplanetary disks, A&A, 487, L1–L4.

Brownlee, D., et al. (+182 colleagues) 2006, Comet 81P/Wild 2 under a microscope, Science, 314, 1711–1716.

Brownlee, D., Joswiak, D., & Matrajt, G. 2011, Large coarse-grained solid particles in comets — A ubiquitously distributed component in the Solar Nebula? 42nd Lunar and Planetary Sciences Conference, abstract no. 2235.

Cassen, P. 2001, Nebular thermal evolution and the properties of primitive planetary materials, Meteoritics & Planetary Science, 36, 671–700.

Chapman, S., & Cowling, T.G. 1970, *The Mathematical Theory of Non-uniform Gases*, 3rd ed. Cambridge Univ. Press. London.

Chiang, E. I., & Goldreich, P. 1997, Spectral energy distributions of T Tauri stars with passive circumstellar disks, ApJ, 490, 368–376.

Chiang, E., & Youdin, A. N. 2010, Forming planetesimals in solar and extrasolar nebulae, Annu. Rev. Earth Planet. Sci., 38, 493–522.

Ciesla, F. F., & Cuzzi, J. N. 2006, The evolution of the water distribution in a viscous protoplanetary disk, Icarus, 181, 178–204.

Ciesla, F. J. 2007, Outward transport of high-temperature materials around the midplane of the Solar Nebula, Science, 318, 613–615.

Ciesla, F. J. 2009, Two-dimensional transport of solids in viscous protoplanetary disks, Icarus, 200, 655–671.

Ciesla, F. J. 2010, The distributions and ages of refractory objects in the solar nebula, Icarus, 208, 455–467.

Clarke, C. J., & Pringle, J. E. 1988, The diffusions of contaminant through an accretion disc, MNRAS, 235, 365–373.

Clarke, C. J., & Carswell, R. F. 2007, Principles of Astrophysical Fluid Dynamics, Cambridge University Press, Cambridge.

Clarke, C. J., & Lodato, G. 2009, Limits on the location of planetesimal formation in self-gravitating protostellar disks, MNRAS, 398, L6–L10.

Cumming, A., Butler, R. P., Marcy, G. W., Vogt, S. S., Wright, J. J., & Fischer, D. A. 2008, The Keck planet search: Detectability and the minimum mas and orbital period distribution of extrasolar planets, P.A.S.P., 120, 531–554.

Currie, T., Plavchan, P., & Kenyon, S. J. 2008, A *Spitzer* study of debris disks in the young nearby cluster NGC 2232: Icy planets are common around $\sim$1.5–3 $M_\odot$ stars, ApJ, 688, 597-615.

Cuzzi, J. N., Dobrovolskis, A. R., & Champney, J. M. 1993, Particle-gas dynamics in the midplane of a protoplanetary nebula, Icarus, 106, 102–134.

Cuzzi, J. N., Davis, S. S., & Dobrovolskis, A. R. 2003, Blowing in the wind. II. Creation and redistribution of refractory inclusions in a turbulent protoplanetary nebula, Icarus, 166, 385–402.

Cuzzi, J. N., Ciesla, F. J., Pataev, M. I., Krot, A. N., Scott, E. R. D., & Weidenschilling, S. J. 2005, Nebular evolution of thermally processed solids: Reconciling models and meteorites, in Chondrites and the Protoplanetary Disk, A. N. Krot, E. R. D. Scott & B. Reipurth, eds., ASP Conference Series, 341, 732–773.

Cuzzi, J. N., Hogan, R. C., & Shariff, K. 2008, Toward planetesimals: Dense chondrule clumps in the protoplanetary nebula, ApJ, 687, 1432–1447.

Cuzzi, J. N., Hogan, R. C., & Bottke, W. F. 2010, Towards initial mass functions for asteroids and Kuiper Belt Objects, Icarus, 208, 518–538.

Dahm, S. E. 2010, Evidence for evolution among primordial disks in the 5 Myr old Upper Scorpious OB Association, AJ, 140, 1444–1455.

Desch, S. J. 2007, Mass distribution and planet formation in the Solar Nebula, ApJ, 671, 878–893.

Dohnanyi, J. S. 1969, Collisional model of asteroids and their debris, JGR, 74, 2531–2554.

Dominik, C., & Dullemond, C. P. 2008, Coagulation of small grains in disk: The influence of risidual infall and initial small-grain content, A&A, 491, 663–670.

Dullemond, C. P., & Dominik, C. 2004, The effect of dust settling on the appearance of protoplanetary disks, A&A, 421, 1075–1086.

Dullemond, C. P., & Dominik, C. 2005, Dust coagulation in protoplanetary disks: A rapid depletion of small grains, A&A, 434, 971–986.

Dullemond, C. P., Apai, D., & Walch, W. 2006, Crystalline silicates as a probe of disk formation history, ApJ, 640, L67–L70.

Dullemond, D. P., Natta, A., & Testi, L. 2006, Accretion in protoplanetary disks: The imprint of core properties, ApJ, 645, L69-0L72.

Dullemond, C. P., Brauer, F., Henning, Th, & Natta, A. 2008, Dust coagulation and processing in an evolving disk, Physica Scripta, 130, 014015.

Dunham, M. M., Evans, N. J. II, Terebey, S., Dullemond, C. P., & Young, C. H. 2010, Evolutionary signatures in the formation of low-mass protostars. II. Toward reconciling models and observations, ApJ, 710, 470–502.

Eisner, J. A., Hillenbrand, L. A., Carpenter, J. M., & Wolf, S. 2005, Constraining the evolutionary stage of class I protostars: Multiwavelength observations and modeling, ApJ, 635, 396–421.

Enoch, M. L., Evans, N. J. II, Sargent, A. I, & Glenn, J. 2009, Properties of the youngest protostars in Perseus, Serpens, and Ophiuchus, ApJ, 692, 973–997.

Evans, N. J. II, et al. (+17 colleagues) 2009, The *Spitzer* c2d Legacy results: Star-formation rates and efficiencies; Evolution and lifetimes, ApJS, 181, 321–350.

Fedele, D., van den Ancker, M. E., Henning, Th., Jayawardhana, R., & Oliveira, J. M. 2010, Timescale of mass accretion in pre-main-sequence stars, A&A, 510, A72.

Flaig, M., Kley, W., & Kissmann, R. 2010, Vertical structure and turbulent saturation level in fully radiative protoplanetary disk models, M.N.R.A.S., 409, 1297–1306.

Font, A. S., McCarthy, I. G., Johnstone, D., & Ballantyne, D. R. 2004, Photoevaporation of circumstellar disks around young stars, ApJ, 607, 890–903.

Furlan, E., et al. (+11 colleagues) 2006, A survey and analysis of *Spitzer* Infrared Spectrograph spectra of T Tauri stars in Taurus, ApJS, 165, 568–605.

Gail, H.-P. 2001, Radial mixing in protoplanetary accretion disks I. Stationary disc models with annealing and carbon combustion, A&A, 378, 192213.

Gail., H.-P. 2004, Radial mxing in protoplanetary accretion disks IV. Metamorphosis of the silicate dust complex, A&A, 413, 571–591.

Garaud, P. 2007, Growth and migration of solids in evolving protostellar disks. I. Methods and analytical tests, ApJ, 671, 2091–2114.

Grün, E., Morfill, G. E., Terrile, R. J., Johnson, T. V., & Schwehm, G. 1983, The evolution of spokes in Saturn's B ring, Icarus, 54, 227–252.

Gullbring, E., Hartmann, L., Briceño, C., & Calvet, N. 1998, Disk accretion rates for T Tauri stars, ApJ, 492, 323–341.

Haisch, K. E. Jr., Lada, E. A., & Lada, C. J. 2001, Disk frequencies and lifetimes in young clusters, ApJ, 553, L153–L156.

Hanner, M. S., Hackwell, J. A., Russell, R. W., & Lynch, D. K. 1994, Silicate emission feature inthe spectrum of comet Mueller 1993a, Icarus, 112, 490–495.

Hanner, M. S. 2004, Cometary dust: Ancient interstellar dust in the solar system? ASP Conference Series, 309, 285

Harker, D. E., & Desch, S. J. 2002, Annealing of silicate dust by nebular shocks at 10 AU, ApJ, 565, L109–L112.

Harker, D. E., Wooden, D. H., Woodward, C. E., & Lisse, C. M. 2002, Grain properties of comet C/1995 01 (Hale-Bopp), ApJ, 580, 579–597.

Hartmann, L., Calvet, N., Gullbring, E., & D'Alessio, P. 1998, Accretion and evolution of T Tauri disks, ApJ, 495, 385–400.

Hasegawa, Y., & Pudrtiz, R. E. 2010, Radiatively heated, protoplanetary discs with dead zones - I. Dust settling and thermal structure of disks around M stars, M.N.R.A.S., 401, 143–159.

Hollenbach, D., Johnstone, D., Lizano, S. & Shu, F. 1994, Photoevaporation of disks around massive stars and application to ultracompact HII regions, ApJ, 428, 654–669.

Honda, M., et al. (+13 colleagues) 2004, The 10 micron spectra of comet C/2002 V1 (NEAT) and C/2001 RX14 (LINEAR), ApJ, 601, 577–582.

Hueso, R., & Guillot, T. 2005, Evolution of protoplanetary disks: Constraints from DM Tauri and GM Aurigae, A&A, 442, 703–725.

Hughes, A. L. H., Colwell, J. E., & DeWolfe, A. W. 2008, Electrostatic dust transport on Eros: 3-D simulations of pond formation, Icarus, 195, 630–648.

Hughes, A. L. H. & Armitage, P. J. 2010, Particle transport in evolving protoplanetary disks: Implications for results from *Stardust*, ApJ, 719, 1633–1653.

Hughes, A. M., Wilner, D. J., Qi, C., & Hogerheijde, M. R. 2008, Gas and dust emission at the outer edge of protoplanetary disks, ApJ, 678, 1119–1126.

Hughes, A. M., Wilner, D. J., Andrews, S. M., Qi, C., & Hogerheidje, M. R. 2011, Empirical constraints on turbulence in protoplanetary accretion disks, ApJ, 727, 85(17pp).

Isella, A., Carpenter, J. M., & Sargent, A.I. 2009, Structure and evolution of pre-main-sequence circumstellar disks, ApJ, 701, 260–282.

Jacquet, E., Fromang, S., & Gounelle, M. 2011. Radial transport of refractory inclusions and their preservation in the dead zone, A&A, L8.

Johansen, A., Oishi, J. S., Mac Low, M.-M., Klahr, H., Henning, T., & Youdin, A. 2007, Rapid planetesimal formation in turbulent circumstellar disks, Nature, 448, 1022–1025.

Johansen, A., & Youdin, A. 2007, Protoplanetary disk turbulence driven by the streaming instability: Nonlinear saturation and particle concentration, ApJ, 662, 627–641.

Johansen, A., Youdin, A., & Klahr, H. 2009, Zonal flows and long-lived, axisymmetric pressure bumps in magnetorotaional turbulence, ApJ, 697, 1269–1289.

Johansen, A., Youdin, A., & Mac Low, M.-M. 2009, Particle clumping and planetesimal formation depend strongly on metallicity, ApJ, 704, L75–L79.

Jørgensen, J. K., van Dishoeck, E. F., Visser, R., Bourke, T. L., Wilner, D. J., Lommen, D., Hogerheijde, M. R., & Myers, P. C. 2009, PROSAC: A submillimeter array survey of low-mass protostars. II. The mass evolution of envelopes, disks, and stars from the Class 0 through 1 stages, A&A, 507, 861–879.

Joswiak, D. J., Brownlee, D. E., Matrajt, G., Messenger, S. M., & Ito, M. 2010, Stardust track 130 terminal particle: Possible Al-rich chondrule fragment or altered amoeboid olivine aggregate, 41st Lunar and Planetary Sciences Conference, abstract 2119.

Keller, Ch. & Gail, H.-P. 2004, Radial mixing in protoplanetary accretion disks VI. Mixing by large-scale radial flows, A&A, 414, 1177–1185.

Kenyon, S. J. & Hartmann, L. 1987, Spectral energy distributions of T Tauri stars: Disk flaring and limits on accretion, ApJ, 323, 714–733.

Kenyon, S. J., Hartmann, L. W., Strom, K. M., & Strom, S. E. 1990, An *IRAS* survey of the Taurus-Auriga molecular cloud, AJ, 99, 869–887.

Kessler-Silacci, J., et al. (+12 colleagues) 2006, c2d Spitzer IRS spectra of disks around T Tauri stars. I. Silicate emission and grain growth, ApJ, 639, 275–291.

King, A. R., Pringle, J. E., & Livio, M. 2007, Accretion disc viscosity: How big is alpha? MNRAS, 376, 1740–1746.

Kitamura, Y., Momose, M., Yokogawa, S., Kawabe, R., Tamura, M., & Ida, S. 2002, Investigation of the physical properties of protoplanetary disks around T Tauri stars by a 1 arcsecond imaging survey: Evolution and diversity of the disks in their accretion stage, ApJ, 581, 357–380.

Kleine, T., Mezger, K., Palme, H., & Scherer, E. 2005, Tungsten isotopes provide evidence that core formation in some asteroids predates the accretion of chondrite parent bodies, 36th Lunar and Planetary Sciences Conference, abstract 1431.

Krauss, O. & Wurm, G. 2005, Photophoresis and the pile-up of dust in young circumstellar disks, ApJ, 630, 1088–1092.

Kretke, K. A., & Lin, D. N. C. 2010, Structure of magnetorotational instability active protoplanetary disks, ApJ, 721, 1585–1592.

Kwon, W., Looney, L. W., Mundy, L. G., Chiang, H.-F., & Kemball, A. J. 2009, Grain growth and density distribution of the youngest protostellar systems, ApJ, 696, 841–852.

Lee, A. T., Chiang, E., Asay-Davis, X., & Barranco, J. 2010, Forming planetesimals by gravitational instability. I. The role of the Richardson number in triggering the Kelvin-Helmholtz instability, ApJ, 718, 1367–1377.

Lin, D. N. C. & Pringle, J. E. 1990, The formation and initial evolution of protostellar disks, ApJ, 358, 515–524.

Lisse, C. M., et al. (+16 colleagues) 2006, Spitzer spectral observations of the Deep Impact ejecta, Science, 313, 635–640.

Lodders, K. 2003, Solar system abundances and condensation temperatures of the elements, ApJ, 591, 1220–1247.

Luhman, K. L., Allen, P. R., Espaillat, C., Hartmann, L., & Calvet, N. 2010, The disk population of the Taurus star-forming region, ApJS, 186, 111–174.

Manoj, P. 2010, The formation of star and planetary systems: New results from Spitzer, in ASP conference proceedings "Frank N. Bash Symposium 2009: New Horizons in Astronomy", eds. L. Stanford, L. Hao, Y. Mao, J. Green.

Mathis, J. S., Rumpl, W., & Nordsieck, K. H. 1977, The size distribution of interstellar grains, ApJ, 217, 425–433.

Mitchell, C. J., Horányi, M., Havnes, O., & Porco, C. C. 2006, Saturn's spokes: Lost and Found, Science, 311, 1587–1589.

Miyake, K., & Nakagawa, Y. 1995, Dust particle settling in passive disks around T Tauri stars: Models and IRAS observations, ApJ, 441, 361–384.

Molster, F., & Kemper, C. 2005, Crystalline silicates, Space Sci. Rev., 119, 3–28.

Morbidelli, A., Brasser, R., Tsiganis, K., Gomes, R., & Levison, H. F. 2009a, Constructing the secular architecture of the solar system I. The giant planets, A&A, 507, 1041–1052.

Morbidelli, A., Bottke, W. F., Nesvorný, D., & Levison, H. F. 2009b, Asteroids were born big, Icarus, 204, 558–573.

Morfill, G. E., & Völk, H. J. 1984, Transport of dust and vapor and chemical fractionation in the early protosolar cloud, ApJ, 287, 371–395.

Morris, M. A., & Desch, S. J. 2010, The thermal histories of chondrules in solar nebula shocks, ApJ, 722, 1474–1494.

Mousis, O., Petit, J.-M., Wurm, G., Krauss, O., Alibert, Y., & Horner, J. 2007, Photophoresis as a source of hot minerals in comets, A&A, 466, L9–L12.

Nakagawa, Y., Sekiya, M., & Hayashi, C. 1986, Settling and growth of dust particles in a laminar phase of a low-mass solar nebula, Icarus, 67, 375–390.

Nakamoto, T., & Nakagawa, Y. 1994, Formation, early evolution, and gravitational stability of protoplanetary disks, ApJ, 421, 640–650.

Nuth, J. A. III, & Johnson, N. M. 2006, Crystalline silicates in comets: How did they form? Icarus, 180, 243–250.

Öberg, K. I., Qi, C., Fogel, J. K. J., Bergin, E. A., Andrews, S. M., Espaillat, C., van Kempen, T. A., Wilner, D. J., & Pascucci, I. 2010, The disk imaging survey of chemistry with SMA. I. Taurus protoplanetary disk data, ApJ, 720, 480–493.

Okuzumi, S. 2009, Electric charging of dust aggregates and its effect on dust coagulation in protoplanetary disks, ApJ, 698, 1122–1135.

Olofsson, J., et al. (+15 colleagues) 2009, C2D Spitzer-IRS spectra of disks around T Tauri stars IV. Crystalline silicates, A&A, 507, 327–345.

Ormel, C. W., Spaans, M., & Tielens, A. G. G. M. 2007, Dust coagulation in protoplanetary disks: Porosity matters, A&A, 461, 215–232.

Owen, J. E., Ercolano, B., Clarke, C. J., & Alexander, R. D. 2009, Radiation-hydrodynamic models of X-ray and EUV photoevaporating protoplanetary discs, MNRAS, doi:10.1111/j.1365–2966.2009.15771.x.

Pavlyuchenkov, Ya., & Dullemond, C. P. 2007, Dust crystallinity in protoplanetary disks: The effect of diffusion/viscosity ratio, A&A, 471, 833–840.

Press, W. H., Teukolsky, S. A., Vetterling, W. T., & Flannery, B. P. 1992, Numerical Recipes in Fortran 77: Second Edition: The Art of Scientific Computing, available online: http://www.nrbook.com/a/bookfpdf.php, §6.6 and §6.7.

Pringle, J. E. 1981, Accretion discs in astrophysics, ARA&A, 19, 137–162.

Pringle, J. E., Verbunt, F., & Wade, R. A. 1986, Dwarf novae in outburst: Modelling the observations, MNRAS, 221, 169–194.

Pringle, J., & King, A. 2007, Astrophysical Flows, Cambridge University Press, Cambridge.

Prudnikov, A. P., Brychkov, Yu. A., & Marichev, O. I. 1986, Integrals and Series, Volume 2: Special Functions, translated by N.M. Queen (Gordon and Breach Science Publishers: New York).

Raymond, S. N., O'Brien, D. P., Morbidelli, A., & Kaib, N. A. 2009, Building the terrestrial planets: Constrained accretion in the inner Solar System, Icarus, 203, 644–662.

Ricci, L., Testi, L., Natta, A., Neri, R., Cabrit, S., & Herczeg, G. J. 2010a, Dust properties of protoplanetary disks in the Taurus-Auriga star forming region from millimeter wavelengths, A&A, 512, A15.

Ricci, L., Testi, L., Natta, A., & Brooks, K. J. 2010b, Dust grain growth in ρ-Ophiuchi protoplanetary disks, A&A, 521, A66.

Ricci, L., Mann, R. K., Testi, L., Williams, J. P., Isella, A., Robberto, M., Natta, A., & Brooks, K. J. 2011, The (sub-)millimeter SED of protoplanetary disks in the outskirts of the Orion nebula cluster, A&A, 525, A81.

Rice, W. K. M., & Armitage, P. J. 2009, Time-dependent models of the structure and stability of self-gravitating protoplanetary discs, MNRAS, 396, 2228–2236.

Rodmann, J., Henning, Th., Chandler, C. J., Mundy, L.G., & Wilner, D. J. 2006, Large dust particles in disks around T Tauri stars, A&A, 446, 211–221.

Rózyczka, M., Bodenheimer, P., & Bell, K. R. 1994, A numerical study of viscous flows in axisymmetric α-accretion disks, ApJ, 423, 736–747.

Ruden, S. P., & Pollack, J. B. 1991, The dynamical evolution of the protosolar nebula, ApJ, 375, 740–760.

Sargent, B. A., et al. (+11 colleagues) 2009, Dust processing and grain growth in protoplanetary disks in the Taurus-Auriga star-forming region, ApJS, 182, 477–508.

Scott, E. R. D., & Krot, A. N. 2005, Thermal processing of silicate dust in the solar nebula: Clues from primitive chondrite matrices, ApJ, 623, 571–578.

Shakura, N. I., & Sunyaev, R. A. 1973, Black holes in binary systems. Observational appearance, A&A, 24, 337–355.

Shu, F. H., Shang, H., & Lee, T. 1996, Toward and astrophysical theory of chondrules, Science, 271, 1545–1552.

Shu, F. H., Shang, H., Gounelle, M., Glassgold, A. E., & Lee, T. 2001, The origin of chondrules and refractory inclusions in chondritic meteorites, ApJ, 548, 1029–1050.

Sicilia-Aguilar, A., Henning, T., & Hartmann, L. W. 2010, Accretion in evolved and transitional disks in CEP OB2: Looking for the origin of the inner holes, ApJ, 710, 597–612.

Sierchio, J. M., Rieke, G. H., Su, K. Y. L., Plavchan, P., Stauffer, J. R., & Gorlova, N. I. 2010, Debris disks around solar-type stars: Observations of the Pleiades with the *Spitzer Space Telescope*, ApJ, 712, 1421–1432.

Reyes-Ruiz, M. 2007, Evolution of protoplanetary disks driven by the MRI, self-gravity, and hydrodynamic turbulence, M.N.R.A.S., 380, 311–319.

Stepinski, T. F. 1998, The Solar Nebula as a process — An analytic model, Icarus, 132, 100–112.

Stodolna, J., Jacob, D., & Leroux, H. 2010, Mineralogy of Stardust track 80: Evidences for aqueous alteration and igneous process, 41st Lunar and Planetary Sciences Conference, abstract 1657.

Takeuchi, T., & Lin, D. N. C. 2002, Radial flow of dust particles in accretion disks, ApJ, 581, 1344–1355.

Takeuchi, T., & Lin, D.N.C. 2005, Attenuation of millimeter emission from circumstellar disks induced by the rapid dust accretion, ApJ, 623, 482–492.

Testi, L., Natta, A., Shepherd, D. S., & Wilner, D. J. 2003, Large grains in the disk of CQ Tau, A&A, 403, 323–328.

Throop, H. B., & Bally, J. 2005, Can photoevaporation trigger planetesimal formation? ApJ, 623, L149–L152.

Tscharnuter, W. M., Schönke, J., Gail, H.-P., & Lüttjohann, E. 2009, Protostellar collapse: Rotation and disk formation, A&A, 504, 109–113.

Tsukagoshi, T., et al. (+18 colleagues) 2011, Detection of strong millimeter emission from the circumstellar dust disk around V1094 Sco: Cold and massive disk around a T Tauri star in a quiescent accretion phase? ApJ, 726, 45

Turner, N. J., Carballido, A., & Sano, T. 2010, Dust transport in protostellar disks through turbulence and settling, ApJ, 708, 188–201.

Urpin, V. A. 1984, Hydrodynamic flows in accretion disks, Soviet Astronomy, 28, 50.

van Boekel, R., et al. (+22 colleagues) 2004, The building blocks of planets within the 'terrestrial' region of protoplanetary disks, Nature, 432, 479–482.

van Boekel, R., Min, M., Waters, L. B. F. M., de Koter, A., Dominik, C., van den Ancker, M. E., & Bouwman, J. 2005, A 10 μm spectorscopic survey of Herbig Ae star disks: Grain growth and crystallization, A&A, 437, 189–208.

Vinković, D. 2009, Radiation pressure mixing of large dust grains in protoplanetary disks, Nature, 459, 227–229.

Watson, D.M., et al. (+17 colleagues) 2009, Crystalline silicates and dust processign in the protoplanetary disks of the Taurus young cluster, ApJS, 180, 84–101.

Weidenschilling, S. J. 1977a, Aerodynamics of solid bodies in the Solar Nebula, MNRAS, 180, 57–70.

Weidenschilling, S. J. 1977b, The distribution of mass in the planetary system and Solar Nebula, Ap&SS, 51, 153–158.

Weidenschilling, S. J. 1995, Note: Can gravitational instability form planetesimals? Icarus, 116, 433-435.

Weidenschilling, S. J. 2003, Radial drift of particles in the solar nebula: Implications for planetesimal formation, Icarus, 165, 438–442.

Westphal, A. J., Fakra, S. C., Gainsforth, Z., Marcus, M. A., Ogliore, R. C., & Butterworth, A. L. 2009, Mixing fraction of inner solar system material in comet 81P/Wild2, ApJ, 694, 18–28.

Wittenmyer, R. A., Tinney, C. G., O'Toole, S. J., Jones, H. R. A., Butler, R. P., Carter, B. D., & Bailey, J. 2011, On the frequency of Jupiter analogs, ApJ, 727, 102 (16pp).

Wooden, D. H., Woodward, C. E., & Harker, D. E. 2004, Discovery of crystalline silicates in comet C/2001 Q4 (NEAT), ApJ, 612, L77–L80.

Wooden, D. H., Harker, D. E., & Brearley, A. J. 2005, Thermal processing and radial mixing of dust: Evidence from comets and primitive chondrites, ASP Conference Series, 341, 774

Wooden, D., Desch, S., Harker, D., Gail, H.-P., & Keller, L. 2007, in Protostars and Planets V, eds. B. Reipurth, D. Jewitt, & K. Keil (University of Arizona Press: Tuscon) 815–833.

Wooden, D. H. 2008, Cometary refractory grains: Interstellar and nebular sources, Space Sci. Rev., 138, 75–108.

Yasui, C., Kobayashi, N., Tokunaga, A. T., Saito, M., & Tokoku, C. 2009, The lifetime of protoplanetary disks in a low-metallicity environment, ApJ, 705, 54–63.

Youdin, A. N., & Shu, F. H. 2002, Planetesimal formation by gravitational instability, ApJ, 580, 494–505.

Youdin, A. N., & Lithwick, Y. 2007, Particle stirring in turbulent gas disks: Including orbital oscillations, Icarus 192, 588–604.

Zolensky, M. E., et al. (+74 colleagues) 2006, Mineralogy and petrology of comet 91P/Wild 2 nucleus samples, Science, 314, 1735–1739.

Zsom, A., Dullemond, C. P. 2008, A representative particle approach to coagulation and fragmentation of dust aggregates and fluid droplets, A&A, 489, 931–941.

Zsom, A., Ormel, C. W., Güttler, C., Blum, J., & Dullemond, C. P. 2010, The outcome of protoplanetary dust growth: pebbles, boulders, or planetesimals? II. Introducing the bouncing barrier, A&A, 513, A57.

Appendix A

Derivation of Analytical Test Cases for Diffusion

In this appendix, I follow *Clarke & Pringle* (1988) and expand the derivation for a set of analytical test cases for radial diffusion of a contaminant within a gas disk. I demonstrate the fidelity of the random-walk method in my particle-transport model in reproducing these solutions in §3.3.2 of the main thesis. Analytical solutions to the diffusion of a contaminant in a disk may be found for a set of idealized disk scenarios. These scenarios are not always physically meaningful — and so require nonstandard equations with which to obtain them — but they may all be simulated numerically with my code. Therefore, they are useful test cases. Second (§3.3.2), I present numerical simulations of these test cases using my particle-transport model. All solutions and simulations presented below use static-disk–surface-density profiles.

In *Clarke & Pringle* (1988), the authors solve for the time-dependent concentration, C, of a contaminant initiated in a ring at specified radius: $C\left(t=0\right)=C_0\delta\left(R-R_0\right)$, where C is the ratio of the local contaminant mass over the local disk-gas mass, R is the distance from the central star, and R_0 is the initial position of the contaminant. The disk that they consider has a surface-density profile given by $\Sigma_g=\Sigma_0 R^{-a}$, where Σ_0 and a are constants; it is also a steady disk, so that for disk viscosity, $\nu=\nu_0 R^b$ (b and ν_0 constants), $b=a$, and the gas-accretion velocity may be written as $v_R=-3\nu/2R$. For the following derivations, I also consider cases with zero gas velocity and I relax the steady-disk assumption. I use:

$$\begin{aligned}\Sigma_g &= \Sigma_0 R^{-a}\,,\\ \nu &= \nu_0 R^b\,,\end{aligned}$$

$$v_R = v_0 R^{b-1} \quad ; \quad v_0 = 0 \text{ or } -\frac{3\nu_0}{2}\,. \tag{A.1}$$

Assuming azimuthal symmetry and that the gas and contaminant are vertically well-mixed, the diffusion equation in polar coordinates may be written (*Gail*, 2001)

$$\frac{\partial}{\partial t}\left(\Sigma_g C\right) + \frac{1}{R}\frac{\partial}{\partial R}\left(R\Sigma_g C v_R\right) - \frac{1}{R}\frac{\partial}{\partial R}\left[RD_{kg}\Sigma_g\left(\frac{\partial C}{\partial R}\right)\right] = P_k\left(R,t\right)\,, \tag{A.2}$$

where D_{kg} is the coefficient of diffusion of the contaminant within the gas, and P_k corresponds to the rate of production of the contaminant per radial increment within the disk. *Clarke & Pringle* (1988) and the setup of my simulations assume zero production of the contaminant, $P_k\left(R,t\right) = 0$, and that the diffusivity scales with the disk viscosity, $D_{kg} = \zeta\nu$, where ζ is a constant. For my particle-transport simulations using a static disk profile, Equation (A.2) is further constrained by $\partial\Sigma_g/\partial t = 0$, and so v_R refers specifically to the prescribed dust-mean-radial velocity, irrespective of the (nonexistent) gas radial velocity. Equation (A.2) then becomes

$$\Sigma_g\frac{\partial C}{\partial t} + \frac{1}{R}\frac{\partial}{\partial R}\left(R\Sigma_g C v_R\right) - \frac{1}{R}\frac{\partial}{\partial R}\left[R\zeta\nu\Sigma_g\left(\frac{\partial C}{\partial R}\right)\right] = 0\,. \tag{A.3}$$

Note that the standard approach (*Clarke & Pringle*, 1988; *Gail*, 2001) is to assume inwardly-accreting–co-moving disk mass and contaminant (with v_R) and to then employ the equation for mass-conservation,

$$\frac{\partial\Sigma_g}{\partial t} + \frac{1}{R}\frac{\partial}{\partial R}\left(R\Sigma_g v_R\right) = 0.$$

The result is

$$\Sigma_g\frac{\partial C}{\partial t} + \Sigma_g v_R\frac{\partial C}{\partial R} - \frac{1}{R}\frac{\partial}{\partial R}\left[R\zeta\nu\Sigma_g\left(\frac{\partial C}{\partial R}\right)\right] = 0\,.$$

I use Equation (A.3) rather than the above equation in order to match the static-disk conditions used in the simulations of §3.3.2. While my model is capable of evolving the disk surface-density profile so that the usual conservation-of-mass equation would apply, analytically solving for the mass distribution of the contaminant within an evolving disk profile if the disk is nonsteady ($a \neq b$) is not tractable.

Next, I combine Equations (A.1) & (A.3), giving

$$\frac{1}{\nu_0}\frac{\partial C}{\partial t}+\frac{v_0}{\nu_0}R^{b-1}\frac{\partial C}{\partial R}+(b-a)\,\frac{v_0}{\nu_0}R^{b-2}C=R^{a-1}\frac{\partial}{\partial R}\left[\zeta R^{1+b-a}\left(\frac{\partial C}{\partial R}\right)\right]. \tag{A.4}$$

Note that for a steady disk ($a=b$), the third term on the left hand side disappears, producing the same equation as Equation (2.2.2) in *Clarke & Pringle* (1988).

Following *Clarke & Pringle* (1988) I next separate variables by assuming

$$C\left(R,t\right)=R^{p}\,g\left(R\right)\,\exp\left(-\zeta\nu_0\lambda^2 t\right), \tag{A.5}$$

where p is a constant, λ is the separation constant, and the spatial dependence, $R^p\times g\left(R\right)$, follows

$$\begin{aligned} R^2\frac{d^2g}{dR^2} &+ R\frac{dg}{dR}\left(2p+1+b-a-\frac{v_0}{\zeta\nu_0}\right) \\ &+ g\left[p\left(p+b-a-\frac{v_0}{\zeta\nu_0}\right)-(b-a)\,\frac{v_0}{\zeta\nu_0}\right]+g\frac{\lambda^2}{\zeta}R^{2-b}=0\,. \end{aligned} \tag{A.6}$$

This equation looks like it could be a Bessel equation if I choose the correct value for p, but the last term needs to go as R^2. Changing variables using $kx=R^{1/q}$, where k is a constant and $q=2/\left(2-b\right)$, I have

$$\begin{aligned} x^2\frac{d^2g}{dx^2} &+ x\frac{dg}{dx}\frac{q}{2}\left[2\left(2p+1+b-a-\frac{v_0}{\zeta\nu_0}\right)-b\right] \\ &+ gq^2\left[p\left(p+b-a-\frac{v_0}{\zeta\nu_0}\right)+(a-b)\,\frac{v_0}{\zeta\nu_0}\right]+gx^2q^2\frac{\lambda^2}{\zeta k^2}=0\,. \end{aligned} \tag{A.7}$$

Equation (A.7) is not valid for the case of $b=2$, but for all other cases, when $p=\frac{1}{2}\left(a-b+\frac{v_0}{\zeta\nu_0}\right)$, it yields

$$g\left(R\right)=J_\beta\left(\frac{|q|\lambda}{\sqrt{\zeta}}R^{1/q}\right), \tag{A.8}$$

where $J_\beta\left(x\right)$ is the Bessel function of the first kind of order $\beta=\dfrac{|a-b-v_0/\zeta\nu_0|}{|2-b|}$. Therefore,

$$C\left(R,t\right)=\int_{\lambda=0}^{\infty}\exp\left(-\nu_0\lambda^2 t\right)R^pJ_\beta\left(\frac{|q|\lambda}{\sqrt{\zeta}}R^{1/q}\right)A\left(\lambda\right)\lambda d\lambda\,, \tag{A.9}$$

where $A(\lambda)$ is a function used to match the solution to the initial conditions.

Next, I use the initial conditions and insert the delta-function for C at $t = 0$ to write

$$C_0 R^{-p} \delta(R - R_0) = \int_{\lambda=0}^{\infty} J_\beta \left(\frac{|q|\lambda}{\sqrt{\zeta}} R^{1/q} \right) A(\lambda) \lambda d\lambda . \tag{A.10}$$

By using the variable transform $s = |q| R^{1/q} / \sqrt{\zeta}$ and keeping careful track of the signs of the limits on the integral, I can apply a Hankel transform and write

$$\begin{aligned} A(\lambda) &= \int_{s=0}^{\infty} C_0 R^{-p} \delta(R - R_0) J_\beta(s\lambda) \, s \, ds \\ &= \frac{|q| C_0}{\zeta} R_0^{\frac{2}{q}-1-p} J_\beta \left(\frac{|q|\lambda}{\sqrt{\zeta}} R_0^{1/q} \right) . \end{aligned} \tag{A.11}$$

Plugging Equation (A.11) into Equation (A.9) and solving yields:

$$\begin{aligned} C(R,t) &= \frac{|q| C_0 R_0^{1-b}}{2\zeta\nu_0 t} \left(\frac{R}{R_0} \right)^p I_\beta \left(\frac{q^2 R_0^{1/q} R^{1/q}}{2\zeta\nu_0 t} \right) \exp\left[-q^2 \frac{\left(R_0^{2-b} + R^{2-b} \right)}{4\zeta\nu_0 t} \right] , \\ q &= \frac{2}{(2-b)} , \\ p &= \frac{1}{2} \left(a - b + \frac{v_0}{\zeta\nu_0} \right) , \\ \beta &= \frac{|a - b - v_0/\zeta\nu_0|}{|2-b|} . \end{aligned} \tag{A.12}$$

where $I_\beta(x)$ is the modified Bessel function of the first kind of order β. Note, solving the integral in Equation (A.9) requires an identity. I have used the relation listed as Equation (3) in §2.12.39 of *Prudnikov, Brychkov & Marichev* (1986):

$$\int_0^\infty x e^{-px^2} J_\nu(bx) J_\nu(cx) \, dx = \frac{1}{2p} \exp\left[-\frac{\left(b^2 + c^2 \right)}{4p} \right] I_\nu \left(\frac{bc}{2p} \right) .$$

For $a = b$ and $v_0 = -3\nu_0/2$, Equation (A.12) reduces to Equation (3.2.4) in *Clarke & Pringle* (1988). In fact, if I had assumed the usual v_R belonging to the gas with mass conservation, as in *Clarke & Pringle* (1988), instead of using a static disk, I would have obtained the same solution given in Equation (A.12) above, except that the order of the Bessel function would change to $\beta = \frac{|a - b + v_0/\zeta\nu_0|}{|2-b|}$. In this case, I would then also need to know the time-evolution of the

nonsteady disk profile in order to convert Equation (A.12) into a contaminant-mass distribution for $a \neq b$ and nonzero v_R.

The general solution in Equation (A.12) is valid for most combinations of a, b, and v_0. However, it is not valid when $b = 2$, nor in the simplest scenario for diffusion in R: when the mass distribution is uniform in R ($a = 1$), the diffusivity is constant ($b = 0$), and there is zero background velocity ($v_0 = 0$). But, in that simple-diffusion case, the solution is well known:

$$C\left(R,t\right) = \frac{C_0}{\sqrt{4\pi\zeta\nu_0 t}} \exp\left[-\frac{\left(R-R_0\right)^2}{4\zeta\nu_0 t}\right] . \tag{A.13}$$

I do not solve for the general solution when $b = 2$. However, *Clarke & Pringle* (1988) present the solution for the steady-disk case when $a = b = 2$:

$$C\left(R,t\right) = \frac{C_0}{R_0}\left(4\pi\zeta\nu_0 t\right)^{-1/2} \exp\left(-\frac{\left[\ln\left(R/R_0\right) - v_0 t\right]^2}{4\zeta\nu_0 t}\right) . \tag{A.14}$$

Because this is a steady-disk case ($a = b$), the initial diffusion equation used to solve for $C\left(R,t\right)$ in *Clarke & Pringle* (1988) matches the diffusion equation I have used above for my static-disk scenario, Equation (A.4). Note, however, that Equation (A.14) does not match Equation (3.1.3) in *Clarke & Pringle* (1988) because of a typo in that paper, which accidentally presents the solution for twice the background velocity, $v_R \rightarrow 2v_R$. Also, when $a = b = 2$, the natural space to solve the equation is logarithmic space. This happens to be the space used for the width of my model-disk grid cells, which is relavent to the only odd behavior that I find in my particle transport simulations (see §3.3.2).

My particle-transport simulations output the number of particles per radial grid space. Therefore, to compare the solutions provided by Equations (A.12), (A.13), & (A.14) to my simulations, I next need to convert the analytic $C\left(R,t\right)$ function into an expected fractional-mass distribution. The concentration can be expressed as the ratio of the contaminant-to-gas surface densities, $C = \sigma/\Sigma_g$, where σ is the surface density of the contaminant. Because these test cases assume a static-disk–surface-density profile, it is then relatively simple to solve for the fractional mass of the contaminant in a given grid space, m_i, where i denotes the grid space, which I will normalize by

$m_{\rm tot}$, the total mass of the contaminant in the disk at $t = 0$.

$$m_{\rm tot} = 2\pi \int_0^\infty R\Sigma_g C_0\, \delta\left(R - R_0\right) dR = 2\pi R_0 \Sigma_g\left(R_0\right) C_0\,.$$

I write:

$$\left(\frac{m_i}{m_{\rm tot}}\right) = \frac{1}{R_0\Sigma_g\left(R_0\right) C_0} \int_{R=R_{i-1/2}}^{R_{i+1/2}} R\Sigma_g\left(R\right) C\left(R,t\right) dR\,, \tag{A.15}$$

where $R_{i-1/2}$ and $R_{i+1/2}$ are the inner and outer boundaries of the grid space, respectively. Combining Equations (A.12) & (A.15), and using a variable substitution, $s = R^{1/q}$, I can write the general expression for the general-case expected mass distribution as

$$\begin{aligned}
\left(\frac{m_i}{m_{\rm tot}}\right) &= \frac{q|q|R_0^{\gamma_1}}{2\zeta\nu_0 t} \exp\left[-\frac{q^2 R_0^{2-b}}{4\zeta\nu_0 t}\right] \int_{R=R_{i-1/2}}^{R_{i+1/2}} s^{\gamma_2} I_\beta\left(\frac{q^2 s_0 s}{2\zeta\nu_0 t}\right) \exp\left(-\frac{q^2 s^2}{2\zeta\nu_0 t}\right) ds \\
\gamma_1 &= \frac{1}{2}\left(a - b - \frac{v_0}{\zeta\nu_0}\right) \\
\gamma_2 &= \frac{(2 - a + v_0/\zeta\nu_0)}{(2-b)} \\
s_0 &= R_0^{1/q}\,.
\end{aligned} \tag{A.16}$$

For comparison with my simulations, I solve the integral numerically using a Simpson integrator and the Numerical Recipes functions for the modified Bessel functions (*Press et al.*, 1992).

Equation (A.16) represents the expected mass distributions for most cases of a, b, and v_0, but not all. For the simplest diffusion case ($a = 1$, $b = 0$, $v_0 = 0$) with $C\left(R,t\right)$ given in Equation (A.13), the expected mass distribution is given by

$$\left(\frac{m_i}{m_{\rm tot}}\right) = \left(4\pi\zeta\nu_0 t\right)^{-1/2} \int_{R=R_{i=1/2}}^{R_{i+1/2}} \exp\left[-\frac{\left(R - R_0\right)^2}{2\zeta\nu_0 t}\right] dR\,. \tag{A.17}$$

And for the case of $a = b = 2$ given in Equation (A.14) the expected mass distribution in a static disk is given by

$$\left(\frac{m_i}{m_{\rm tot}}\right) = \left(4\pi\zeta\nu_0 t\right)^{-1/2} \int_{R=R_{i-1/2}}^{R_{i+1/2}} \exp\left[-\frac{\left(Y - v_0 t\right)^2}{4\zeta\nu_0 t}\right] dY\,, \tag{A.18}$$

where $Y = \ln\left(R/R_0\right)$, and again, I use a Simpson integrator to solve for the expected $(m_i/m_{\rm tot})$ for these cases.

Appendix B

Notes on Numerical Techniques

To aid in the transparency of my models, in this chapter, I outline some of the numerical techniques used within the code built for this thesis. While the techniques discussed here cannot be classified as new research, they are important tools for implementing the research I have done.

In §B.1, I focus on the numerics of the disk-evolution model, detailing constraints imposed by numerics, numerical conservation of mass and angular momentum, and the fidelity of the numerical model to analytic solutions of the disk-evolution equation. In §B.2, I discuss a range of simple numerical techniques used ubiquitously throughout my code. And in §B.3, I discuss the iterative solvers used to find radial-drift velocities and midplane disk temperatures within my model disks. While iterative solving is simple in concept, it becomes more complex in practice, with each solver tailored to the particular set of equations under consideration.

B.1 Time-Explicit Viscous-Disk Evolution

The material in this section is a supplement to §2.3.2, fully outlining the numeric considerations pertinent to solving the disk-evolution equation including stability, convergence, and conserved quantities, and elucidating choices and constraints for time-step sizes, grid-spacing, and the radial extent of the grid.

B.1.1 Numerical Setup and Fidelity

In setting up the numerical schemes for the disk-evolution code, I have followed Numerical Recipes (*Press et al.*, 1992), which clearly outlines the most straight-foward, stable methods for approaching the evolution of basic PDEs. For a diffusion equation, *Press et al.* (1992) §19.2 provides the single-

level, Forward-Time-Centered-Space (FTCS) scheme, using a finite-difference approximation of the relevant derivatives:

$$\begin{aligned} \frac{\partial u}{\partial t} &= D\frac{\partial^2 u}{\partial x^2}\ , \\ \frac{u_i^{j+1}-u_i^j}{\Delta t} &= D\left[\frac{u_{i+1}^j - 2u_i^j + u_{i-1}^j}{(\Delta x)^2}\right]. \end{aligned}$$

Therefore, for the most compact form of the disk-evolution equation (2.17), one can write:

$$\frac{\Sigma_{g,i}^{j+1}-\Sigma_{g,i}^j}{\Delta t} = \frac{3}{4}\frac{1}{\left(X_i^j\right)^3}\left[\frac{(\nu\Sigma_g X)_{i+x}^j - 2\,(\nu\Sigma_g X)_i^j + (\nu\Sigma_g X)_{i-1}^j}{(\Delta X)^2}\right], \tag{B.1}$$

(assuming constant ΔX grid spacing) where i and j are the spatial and temporal indices, respectively.

If, on the other hand, one wanted to integrate the expanded form of the equation, with the diffusive and advective components separate, one would need a different scheme for the advective component as FTCS is not stable for the advection equation (*Press et al.*, 1992). The simplest approach for advection provided in *Press et al.* (1992) (§19.1) is called upwind differencing, which directly considers the direction of the flow of advection. In this scheme:

$$\begin{aligned} \frac{\partial u}{\partial t} &= -v\frac{\partial u}{\partial x}\ : \\ \frac{u_i^{j+1}-u_i^j}{\Delta t} &= -v_i^j\frac{u_i^j - u_{i-1}^j}{\Delta x}\,, \quad v_i^j > 0 \\ \frac{u_i^{j+1}-u_i^j}{\Delta t} &= -v_i^j\frac{u_{i+1}^j - u_i^j}{\Delta x}\,, \quad v_i^j < 0 \end{aligned}$$

so one could write the advective term in Equation (2.18) as

$$\frac{9}{2R}\frac{\partial}{\partial R}\left(\nu\Sigma_g\right) \rightarrow \frac{9}{2R_i^j}\left[\frac{(\nu\Sigma_g)_{i+1}^j - (\nu\Sigma_g)_i^j}{\Delta R}\right]$$

(assuming constant ΔR grid spacing).

For each of the diffusive- and advective-equation schemes there is a stability criterion (taken

from *Press et al.* (1992)). For the diffusive scheme it is

$$\frac{2D\Delta t}{(\Delta x)^2} \leq 1\,, \tag{B.2}$$

so that the scheme of Equation (B.1) requires

$$\Delta t \,\leq\, (\Delta X)^2 \,\frac{2}{3}\frac{X^2}{\nu} \quad\longrightarrow\quad \Delta t \,\leq\, \frac{2}{3}\,(\Delta X)^2 * \min\left(\frac{X_i^2}{\nu_i}\right)\,. \tag{B.3}$$

The stability criterion for the advective scheme is given by the Courant condition (material may not flow beyond the adjacent grid cells in a given time step):

$$\frac{|v|\Delta t}{\Delta x} \leq 1\,. \tag{B.4}$$

In my disk-evolution model for numerical integration, I use only the most compact form of the disk-evolution equation. The scheme outlined by Equations (B.1) & (B.3), using a constant grid spacing, ΔX, has been used by several authors (e.g., *Hueso & Guillot* (2005); *Alexander & Armitage* (2007)), and I compare it to my preferred scheme below. In my preferred scheme, I do not use constant grid-spacing, but instead space grid points logarithmically in R (and X), as outlined in §2.3.2. Very small grid-cells at small R means that this scheme requires more time-steps and so runs more slowly than the traditional-ΔX scheme, but it also requires fewer grid-spaces to reach convergence and is more conservative (as discussed in §B.1.2). Also, uneven grid-spacing requires a modification to Equations (B.1) & (B.3) in order to be properly applied; they must be expanded to consider the finite-differencing between individual grid cells separately. This gives (Equations (2.24) & (2.25))

$$\frac{\Sigma_{g,i}^{j+1} - \Sigma_{g,i}^{j}}{\Delta t} \;=\; \frac{3}{4}\frac{1}{X_i^3}\frac{1}{\Delta X_i}\left[\frac{(\nu\Sigma_g X)_{i+1}^{j} - (\nu\Sigma_g X)_{i}^{j}}{\Delta X_{i+1/2}} + \frac{(\nu\Sigma_g X)_{i}^{j} - (\nu\Sigma_g X)_{i-1}^{j}}{\Delta X_{i-1/2}}\right]\,, \tag{B.5}$$

$$\Delta t \;\leq\; \frac{2}{3}\min\left(\frac{\Delta X_i \Delta X_{i-1/2} X_i^2}{\nu_i}\right)\,, \tag{B.6}$$

where $\Delta X_i = X_{i+1/2} - X_{i-1/2}$ is the width of grid cell i and $\Delta X_{i+1/2} = X_{i+1} - X_i$ is the distance from grid point i to $i+1$.

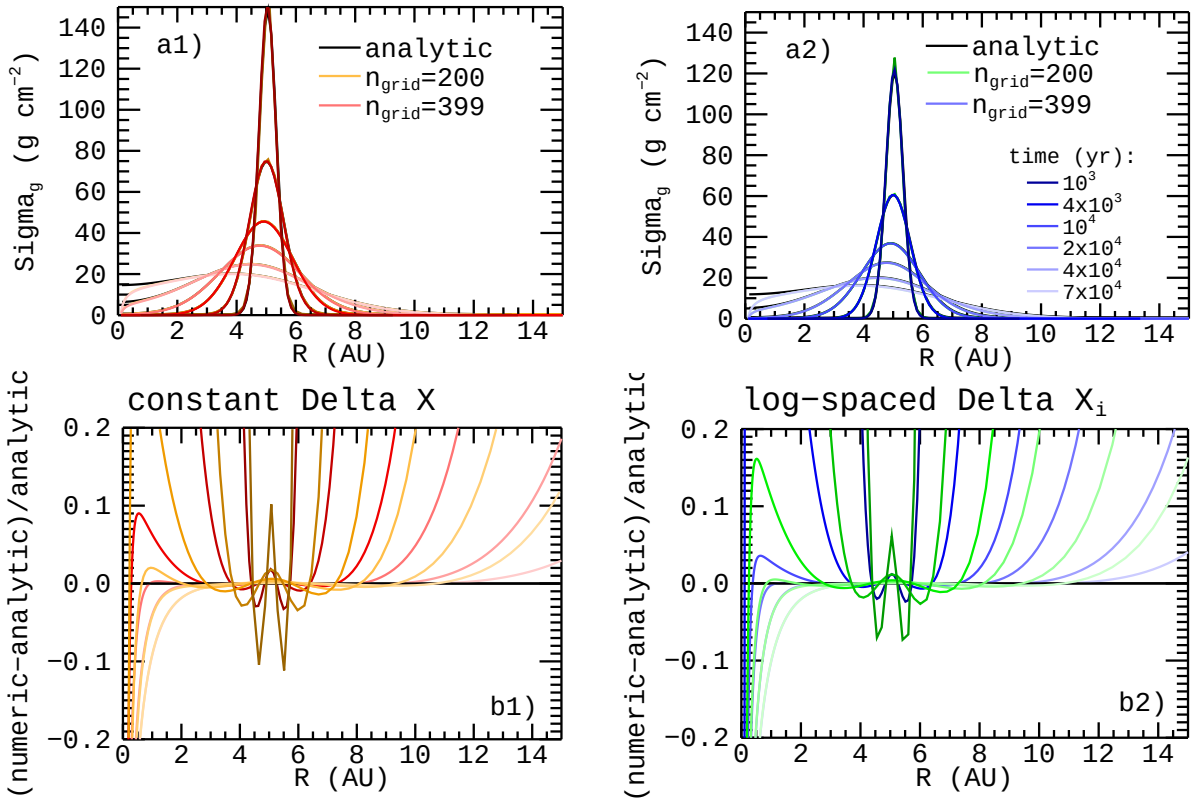

Figure B.1: Comparison between analytic and numerical solutions for disk evolution of an initial delta-function in Σ_g at $R_0 = 5$ AU. Red/Orange simulations run in the constant ΔX numerical scheme, and Blue/Green simulations run in the log-spaced ΔX_i scheme. **Top panels**-a1 and -a2 plot surface-density contours for the analytic solution and the numeric results using two grid resolutions (grid from 0.1–100 AU). **Bottom panels**-b1 and -b2 plot the deviation between the numeric and analytic results. Note that the magnitude of the plotted surface density is dependant on the width of the R_0 grid cell, defining the $t = 0$ disk mass, and that the $n_{\rm grid} = 200$ Σ_g curves are plotted at half-magnitude for ease of comparison with the rest.

In Figure B.1, I plot a comparison of disk evolution for the two numeric schemes outlined above (constant ΔX and log-spacing ΔX_i) versus the analytic solution for the viscous spreading of a ring of disk material (given in §2.3.1). These examples are run at two spatial resolutions of the grid: $n_{\rm grid} = 200$ and $n_{\rm grid} = 399$, extending from 0.1 to 100 AU. While these simulations are not a perfect match for the analytic solution, they are a still a good match, where inspection shows noticeable deviation only at the inner-disk edge at late times. Panels-b1 and -b2 plot the deviation between the numeric and analytic results, and it is clear both that higher spatial resolution does lead to a closer fit with the analytic solution and that the log-grid-spacing scheme has better convergence for a given $n_{\rm grid}$ in the main part of the disk than does the constant ΔX scheme. However, some of

the deviation appears intrinsic to all of the numerical simulations. This intrinsic deviation is due both to a finite inner-grid boundary (causing loss of material that otherwise continues to diffuse in the analytic solution) and to the fact that a discreet grid where Σ_g is constant across the width of a grid cell simply cannot completely replicate the delta-function initial condition.

B.1.2 Conservation of Mass and Angular momentum, and the Grid-Spacing Scheme

In this section, I discuss the link between the choice of grid and grid spacing, and the numerical conservation of mass and angular momentum in an evolving model disk. In the model disk, the surface density is considered constant across the width of a grid cell, and I consider two forms for calculating the mass and (Keplerian) angular momentum of a cell. An approximate formulation:

$$\begin{aligned} M_{1,i} &= 2\pi R_i \Delta R_i \Sigma_{g,i}\,, \\ L_{1,i} &= \sqrt{GM_\star} M_{1,i} R_i^{1/2}\,, \end{aligned} \tag{B.7}$$

and a more precise formulation:

$$\begin{aligned} M_{2,i} &= \pi \left(R_{i+1/2}^2 - R_{i-1/2}^2 \right) \Sigma_{g,i}\,, \\ L_{2,i} &= \sqrt{GM_\star} \frac{4\pi}{5} \left(R_{i+1/2}^{5/2} - R_{i-1/2}^{5/2} \right) \Sigma_{g,i}\,, \end{aligned} \tag{B.8}$$

where $M_{1,i}$ and $M_{2,i}$ are two expressions for the mass contained in grid-cell i, $L_{1,i}$ and $L_{2,i}$ are two expressions for the angular momentum, ΔR_i is the width of grid-cell i, and $R_{i-1/2}$ and $R_{i+1/2}$ are the inner and outer grid-cell boundaries. The angular-momentum expressions also assume Keplerian velocities for the disk, which pressure-support of the gas tells us is not completely accurate. However, the disk-evolution equation was also derived assuming $\Omega_g = \Omega_{\rm K}$, so calculating angular-momentum conservation this way is consistent with investigating numerical fidelity to the base equation.

In order to track mass and angular-momentum conservation in an evolving disk, one must also account for the quantities lost past the inner and outer grid-space boundaries. This can be done easily by creating dummy cells at the inner and outer boundaries, setting the surface-density in these dummy cells equal to the bounding Σ_g used in the code, and tracking the mass and angular

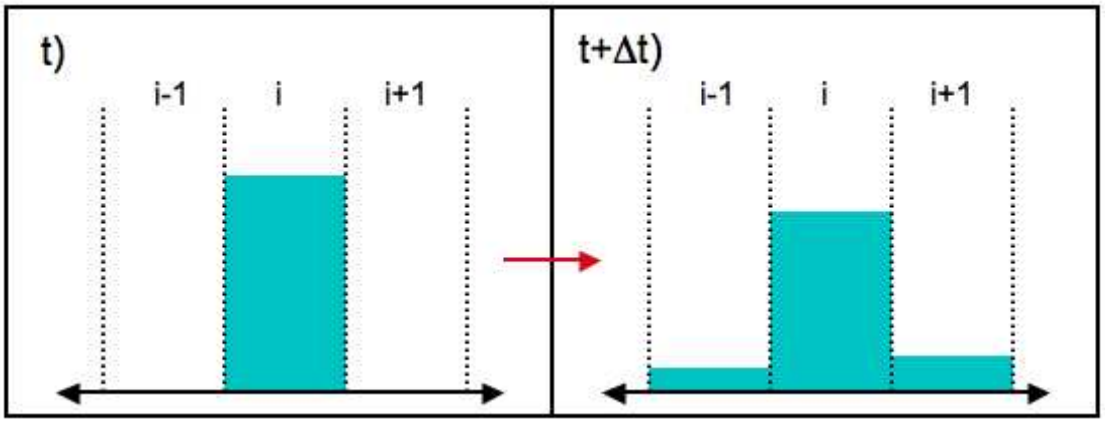

Figure B.2: Diagram of Σ_g evolution using two dummy grid cells.

momentum deposited into them at each time-step.

Finally, dummy cells are also a useful way to calculate a numerical-scheme's potential to deviate from conservation. Consider a grid cell that starts out containing a finite amount of disk mass, while the (dummy) cells to either side have $\Sigma_g = 0$. After one numerical time-step, all three cells will have finite Σ_g, as depicted in Figure B.2, and, if the scheme is conservative, should also have

$$\begin{aligned} M_i^j \equiv M_{i,\mathrm{init}} &= M_{i,\mathrm{fin}} \equiv M_{\mathrm{dummy},i-1}^{j+1} + M_i^{j+1} + M_{\mathrm{dummy},i+1}^{j+1} \,, \\ L_i^j \equiv L_{i,\mathrm{init}} &= L_{i,\mathrm{fin}} \equiv L_{\mathrm{dummy},i-1}^{j+1} + L_i^{j+1} + L_{\mathrm{dummy},i+1}^{j+1} \,. \end{aligned}$$

Therefore, the potential numerical deviation from mass and angular-momentum conservation can be calculated for a grid cell as

$$\begin{aligned} \delta M_i &= M_{i,\mathrm{fin}} - M_{i,\mathrm{init}} \,, \\ \delta L_i &= L_{i,\mathrm{fin}} - L_{i,\mathrm{init}} \,. \end{aligned} \tag{B.9}$$

Performing these calculations with dummy cells for the two disk-evolution grid-spacing schemes, produces for constant ΔX:

$$\begin{aligned} \delta M_{1,i} &= 0 \,, \\ \delta L_{1,i} &= 0 \,, \end{aligned}$$

$$\begin{aligned}
\delta M_{2,i} &= \frac{3\pi}{2}\frac{\Delta t \Delta X^3}{X_i}\frac{\left(3X_i^2-\Delta X^2\right)}{\left(X_i^2-\Delta X^2\right)^2}\nu_i\Sigma_{g,i,0}\,, \\
\delta L_{2,i} &\approx \frac{3\pi}{2}\frac{\Delta t \Delta X^3}{\left(X_i^2-\Delta X^2\right)}\nu_i\Sigma_{g,i,0}\,,
\end{aligned}$$

and for log-spaced ΔX_i:

$$\begin{aligned}
\delta M_{1,i} &= 0\,, \\
\delta L_{1,i} &= 0\,, \\
\delta M_{2,i} &= 0\,, \\
\delta L_{2,i} &= 0\,.
\end{aligned}$$

This method, therefore, predicts that both disk-evolution grid-spacing schemes are conservative to first order, but that only the log-spaced ΔX_i scheme is conservative in the more precise formulation. To verify that this is so, Figure B.3 plots the various mass and angular-momentum quantities and their sum as a function of time for three evolving-disk scenarios using each of the disk-evolution grid-spacing schemes. Of particular interest, are the heavy lines in the figure, which plot a total accounting of all the mass (or angular momentum) in the disk, adding the mass within the disk, the net mass which has been lost inward past the grid, the net mass which has been lost outward past the grid, and substracting and estimated excess deviated mass. This curve is flat for all cases, showingthat this calculation accounts for all of the real or numerically added mass of the systems. Finally, the curves summing the excess-deviated mass (angular momentum) for the constant ΔX scheme, do show this value to be fairly low, and further investigation reveals that this scheme does deviate less from conservation for a higher grid-space resolution. However, a higher grid-space resolution is also needed for the result to reach convergence, as suggested by the difference in disk-evolution produced by the two schemes, particularly when there is significant mass to process in the inner disk.

Finally, consider the fact that Figure B.3 shows a non-negligible amount of mass being lost past the outer-grid boundary (except, of course, where the outer boundary is the mass source). Of course, it is preferable that, in most disk simulations, such loss have only a negligible effect on the overall disk evolution. However, early simulations with $M_{D,0} = 0.05 M_\odot$ disks, $n_{\rm grid} = 500$

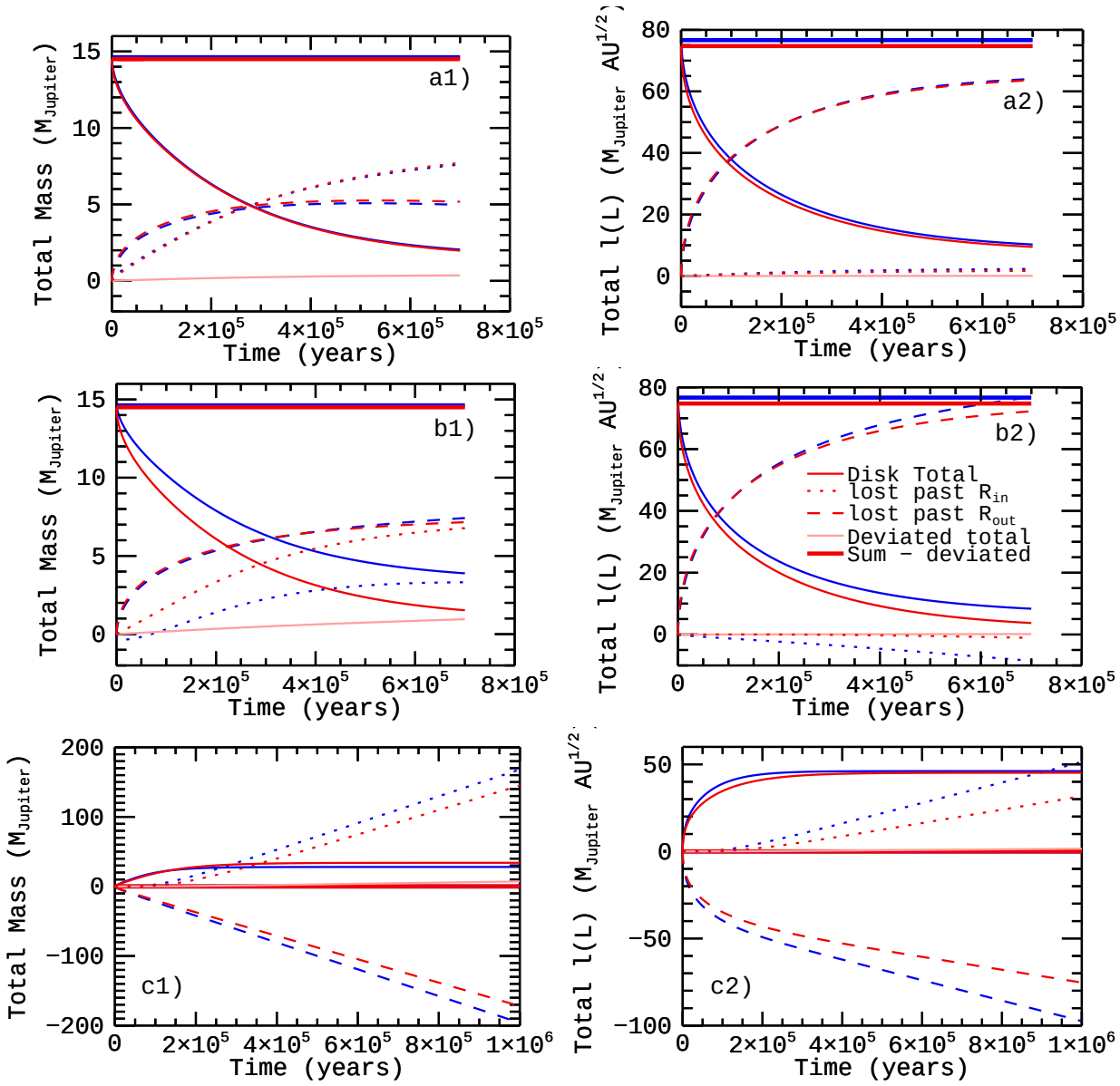

Figure B.3: Plots of the total mass and normalized angular momentum ($l = L/\sqrt{GM_\star}$) in three different evolving-disk scenarios using the constant ΔX **(red curves)** and log-spaced ΔX_i **(blue curves)** numerical schemes. Curves plotted include the total mass (angular momentum) on the disk at a given time, the total lost inward past $R_{\rm in}$, the total lost outward past $R_{\rm out}$, the total excess mass (angular momentum) from deviation (δM or δL) (for the constant ΔX scheme only), and the total+lost-inward+lost-outward−deviated-excess values. **Panels-a1 and -a2** show a disk with constant $\Sigma_g \nu$ (full disk) at $t = 0$ and an outer boundary of $\Sigma_g = 0.1$ g cm^{-2}. **Panels-b1 and -b2** show a full disk with a (silly) inner boundary of $\Sigma_g = 10^5$ g cm^{-2}. And **panels-c1 and -c2** show a scenario where the disk is initial empty and is fed entirely by the $\Sigma_g = 0.1$ g cm^{-2} outer-boundary condition.

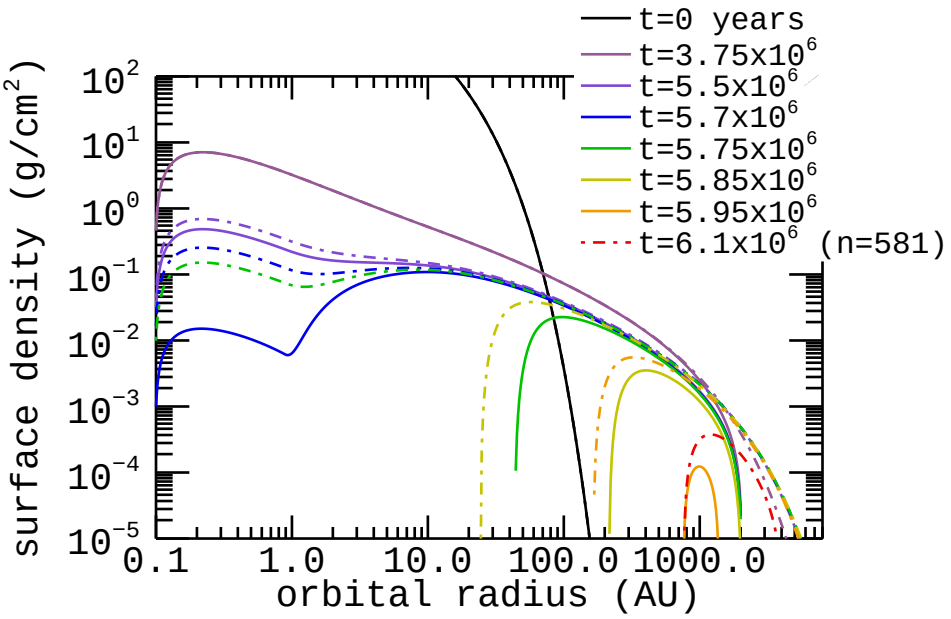

Figure B.4: Comparison of disk evolution between two grid extensions: **Solid lines:** $n_{\rm grid} = 500$, $R_{\rm out} = 2000$ AU; **Dashed lines:** $n_{\rm grid} = 581$, $R_{\rm out} = 9981.4$ AU. $M_{D,0} = 0.05 M_{\odot}$, $R_d = 10$ AU, $\alpha = 10^{-2}$.

and $R = 2000$ AU outer-grid boundaries suggested that the Σ_g profile was being influenced by the location of the outer boundary. Therefore, I ran a comparison simulation with and extra 81 grid points, extending the grid out to $R = 9981.4$ AU, and the results are plotted in Figure B.4. This plot suggests that loss of disk mass past the nearer outer-grid boundary is significant enough to substantially alter the disk evolution near the end of the disk lifetime, causing the disk to thin and dissipate more rapidly than it otherwise would. In light of this result, I have chosen a fiducial grid for the simulations of this thesis that uses $n_{\rm grid} = 600$ and is extended out to $R = 15{,}000$ AU.

B.2 Some Simple Numerical Tools

In this section, I discuss some simple numerical tools that each have multiple applications within the code used for this thesis. These tools are simple enough that there is nothing particular about my use of them, and my purpose for discussing them here is simply to clearly specify the ways they are applied within my code.

B.2.1 Interpolation: Trajectories and Probabilities

Everything used to calculate particle trajectories in my particle-transport model is defined at each discreet grid point of my model-disk grid, and the code outputs the grid-binned particle distribution in order to retain smaller output-file sizes. However, the particles within the simulation exist along the R continuum, and not just at discreet locations. Therefore, it is often necessary to interpolate transport values between two grid points in order to calculate trajectories. This is especially so for the code discussed in §3.2.1 that directly integrates particle trajectories via force-balance. In that code, each of the terms in Equations (3.10) & (3.11) are linearly interpolated between grid points to give values for specific r_d at a given t. However, this direct-integration code is used only to verify the fidelity of my primary transport code. In my primary transport code I use interpolation in two places:

* For $1^{\rm st}$-order (linear) interpolation of particle trajectories according to gridded values of radial dust velocities (§3, Equation (3.1)).

* For $2^{\rm nd}$-order (parabolic) interpolation of the probability that a particle will (diffusively) random-walk inward versus outward for a given time-step, Δt (§3.3.1).

First-order interpolation, to find a local value between two grid points, simply assumes a linear function for that value between points (a and b):

$$y\left(R\right) = y\left(R_a\right) + \left(R - R_a\right)\frac{\left[y\left(R_a\right) - y\left(R_b\right)\right]}{\left(R_a - R_b\right)}\,. \tag{B.10}$$

In order to use interpolation to calculate particle trajectories in my code, I use Equation (B.10) to calculate the local radial-drift velocity, $v_{srd,0}$, and and turbulent-stepping velocity, $v_{\rm turb,0}$ (for the primary particle time-step, Δt) at R_0. If these velocities will carry the particle beyond the next forward grid point, R_i, or $\Delta t > \Delta t_{\rm next} \equiv \left(R_i - R_0\right)/v_{\rm total}$, then I first advance the particle to that grid point following Equation (3.1), then use the local advection velocity at that point, $v_{srd,i}$ to calculate the particle motion for the rest of the time step. To complete the trajectory step this way, I do *not* adjust to $v_{{\rm turb},i}$ at the grid point, because the diffusion-stepping properties are calculated for the whole Δt step at the starting point, R_0. Therefore, for a trajectory step completely within

the bounds of two grid points

$$R_{\rm fin} = R_0 + \Delta t \left(v_{srd,0} + v_{\rm turb,0} \right) ,$$

and for a trajectory-step that crosses grid-point i

$$\begin{aligned} R_i &= R_0 + \Delta t_{\rm next} \left(v_{srd,0} + v_{\rm turb,0} \right) , \\ R_{\rm fin} &= R_i + \left(\Delta t - \Delta t_{\rm next} \right) \left(v_{srd,i} + v_{\rm turb,0} \right) . \end{aligned}$$

I use this simple, first-order interpolation rather than a higher-order scheme because a) lower-order schemes are less computationally expensive, b) a second-order scheme cannot be employed between grid-points with oppositely-directed velocities, and c) as shown in §3.2.3, this first-order scheme reproduces the direct-integrated trajectories to sufficient accuracy.

To calculate the probability of diffusively stepping inward (versus outward) for a given time-step at each grid point, I do use second-order interpolation, this time in Δt. Second-order interpolation assumes a parabolic function, requires three points (a, b, and c), and in general

$$\begin{aligned} y\left(x\right) &= Ax^2 + Bx + C , \\ A &= \frac{\left(y_a - y_b\right) / \left(x_a - x_b\right) - \left(y_b - y_c\right) / \left(x_b - x_c\right)}{\left(x_a - x_c\right)} , \\ B &= \frac{-y_a \left(x_b^2 - x_c^2\right) + y_b \left(x_a^2 - x_c^2\right) - y_c \left(x_a^2 - x_b^2\right)}{\left(x_a - x_b\right) \left(x_b - x_c\right) \left(x_a - x_c\right)} , \\ C &= \frac{y_a x_b x_c \left(x_b - x_c\right) - y_b x_a x_c \left(x_a - x_c\right) + y_c x_a x_b \left(x_a - x_b\right)}{\left(x_a - x_b\right) \left(x_b - x_c\right) \left(x_a - x_c\right)} . \end{aligned} \tag{B.11}$$

For calculating $p_{\rm in}\left(\Delta t\right)$, these equations are somewhat simplified because I calculate $p_{\rm in}$ at each grid point for $\Delta t_{\rm evolv}$ and $\Delta t_{\rm evolv}/2$ (where $\Delta t_{\rm evolv}$ is the global constraining time-step of the disk-evolution model), and I know $p_{\rm in}\left(\Delta t = 0\right) = 1/2$. Then

$$\begin{aligned} p_{\rm in}\left(\Delta t\right) &= A\Delta t^2 + B\Delta t + C , \\ A &= \frac{2p_{\rm in,e} - 4p_{\rm in,he} + 1}{\Delta t_{\rm evolv}^2} , \\ B &= \frac{-p_{\rm in,e} + 4p_{\rm in,he} - 3/2}{\Delta t_{\rm evolv}} , \end{aligned} \tag{B.12}$$

$$C = \frac{1}{2},$$

where $p_{\rm in,e} \equiv p_{\rm in}\left(\Delta t_{\rm evolv}\right)$ and $p_{\rm in,he} \equiv p_{\rm in}\left(\Delta t_{\rm evolv}/2\right)$. This equation is used the find $p_{\rm in}\left(\Delta t\right)$ for the bounding grid points of a particle's starting location, and then linear interpolation is used to find $p_{\rm in}$ for the precise location.

B.2.2 Time Derivatives, Radial Gradients, and q-values

Outside of the disk-evolution equation discussed in §2.3.2 and §B.1, a few other model calculations, particularly equations for the various gas velocities (§2.6), require knowing the gradient of some disk property or properties. In general, for time derivatives, I use a first-order approximation:

$$\left(\frac{\partial y}{\partial t}\right)_j = \frac{y_{j+1} - y_j}{\Delta t}, \tag{B.13}$$

where j is the time-stepping index, and y is the property-of-interest. For spatial derivatives, I generally use a second-order approximation:

$$\left(\frac{\partial y}{\partial R}\right)_i = \frac{1}{2}\left[\frac{(y_{i+1} - y_i)}{\Delta R_{i+1/2}} + \frac{(y_i - y_{i-1})}{\Delta R_{i-1/2}}\right], \tag{B.14}$$

where i is the grid-space index, and $\Delta R_{i+1/2} = R_{i+1} - R_i$. This allows the calculation for the derivative at a given grid point, rather than half-way between two grid points. (Note that the z-derivatives needed for $v_{r,\rm merid}$ (Equations (2.56)–(2.59)) are calculated analytically within the context of a vertically-isothermal disk structure.)

However, many of the spatial derivatives needed to calculate gas velocities come in the form of $\frac{R}{y}\left(\frac{\partial y}{\partial R}\right)$. This is a special case of R-derivatives that has the added numeric pitfall of diverging at grid points where $y \rightarrow 0$. For a simple power-law function in R

$$\begin{aligned} y &= y_0 R^q, \\ q &= \frac{R}{y}\left(\frac{\partial y}{\partial R}\right), \end{aligned}$$

where q is a constant. Therefore, for these special-case derivatives in the gas-velocity calculations, I calculate a separate grid-vector of what I term 'local q-values', that are simply an extension of

the second-order spatial derivative above:

$$q_{y,i} = \frac{R_i}{2y_i}\left[\frac{(y_{i+1}-y_i)}{\Delta R_{i+1/2}} + \frac{(y_i - y_{i-1})}{\Delta R_{i-1/2}}\right], \tag{B.15}$$

and the subroutine for calculating $q_{y,i}$ sets $q_{y,i} = 0$ where $y_i = 0$ to avoid local divergences.

B.2.3 Large Summing Sets

One of the trickiest of the most basic numerical operations is summing, particularly of large sets with component values that range over orders of magnitude. This is simply because of the finite accuracy of even double-precision numbers that cannot record a change to the base value that is too many orders-of-magnitude less than the whole. The places that I have had to be wary of this in my code are in the summing up of mass, both of gas and dust.

The simplest way to correct for errors in summing is to add a loop within the summing that causes the code to first add up subsets of the data and then to add those subsets together:

$$\begin{aligned} M_{\rm tot} &= \sum_{i'=1}^{n/n_{\rm set}} M_{i'}\,, \\ M_{i'} &= \sum_{i=(i'-1)n_{\rm set}+1}^{n_{\rm set}i'} M_i \end{aligned} \tag{B.16}$$

where $M_{\rm tot}$ is the total mass sought, M_i is the mass in, e.g., grid-cell i, n is the total number of cells being summed, and $n_{\rm set}$ is the number of cells in a subset. For a very large set, one might need to use multiple nested loops, but in the code used for this thesis, I generally use a single set, as shown here.

Using a scheme like this is important if I want to calculate the total gas mass of my model disk. My disks are on a grid with $n = n_{\rm grid} = 600$. The inner-most cells are small, due to the logarithmic spacing of grid points, so each contain small amounts of mass. While the outer-most cells are large, the disk surface-density drops off exponentially at the outer edge, so those, too, contain small amounts of mass. Therefore, summing the mass from either direction will lead to the situation of trying to add small-mass values to a large summed total. For this type of summing, I tend to use a subset with $n_{\rm set} = 20$. It is possible that this still does not capture gas added from the very outer edge of the disk at thousands of AU, but such mass *is* negligible for these purposes.

For the dust-mass–allocation scheme used to assign masses to each representative particle in the Chapter 6 global-distribution runs, it is important to use subsets to learn both how much dust mass is currently in a zone-of-interest, and how many particles of each size. For these sets, I use $n_{\rm set} = 200$, because of the large number of particles in the simulation and that could be in given zone (from a few hundred to several thousand). For these, I also sum up the dust mass in each size bin separately, before adding all of that together. For a large range in particle size, there are several orders-of-magnitude difference in the mass allocated between the bins of largest and smallest size, and therefore a wide range in masses assigned to each individual particle.

B.3 Instances of Itterative Solving

There are two important aspects of the disk and particle-transport models that do not have direct, analytic expressions and must be solved for iteratively. These are the the steady-radial-drift velocities of the particles v_{srd}, and the midplane disk temperature in the models using an evolving, energy-balanced temperature profile. Solving for v_{srd} is simpler than for the midplane temperature, because v_{srd} requires only two equations and two unknowns ($v_{r,d}$ and $v_{\phi,d}$), whereas the temperature requires three equations and three unknowns ($T_{\rm mid}$, κ_R, and ν). Both cases also require some trickiness to obtain a full solution set, but in the most general cases encountered in the disk are reasonably well-behaved.

B.3.1 Itteration Strategies and the Early Model for Finding Epstein-drag Velocities

There are two, simple numerical techniques used in my code for iterative solvers. The first is a loop/walk method diagramed in Figuere B.5. This method involves picking a starting-guess solution (x_0), and then alternating back and forth between the equations to be solved (e.g., $y = f(x)$ and $x = g(y)$) until convergence to a solution of sufficient accuracy. However, unless I want only to investigate the direction that this solution carries me in parameter space, my code does not use this method with a pure loop, where

* $y_0 = f(x_0)$
* $x_1 = g(y_0)$

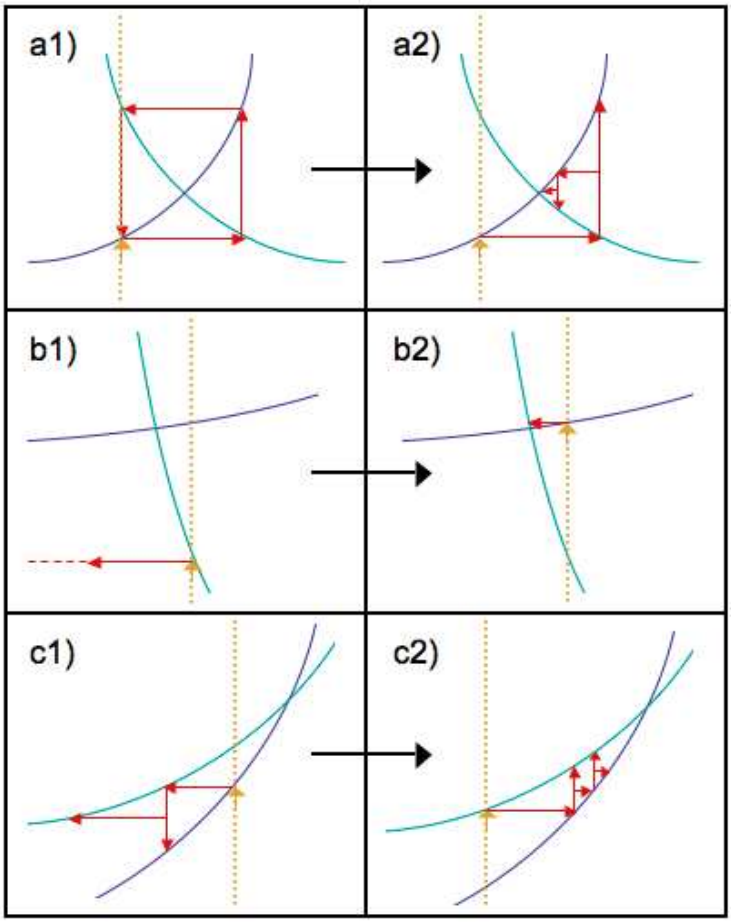

Figure B.5: Diagrams for iterative-solving with a loop/walk method. Blue and teal curves represent two equations to be solved, the orange arrow represents the initial guess, and red arrows represent the motion through parameter space of the solver routine. Direct-looping can lead to non-convergence as shown in panel-a1, and loop/walking in some directions may be non-tractable or lead to divergence, as shown in panels-b1 and -c1.

* $y_1 = f(x_1)$

* $x_2 = g(y_1)$

* etc...

As shown in panel-a1 of Figure B.5, there are cases where a pure loop will not converge, or will be too slow to converge to be numerically useful. Therefore, I modify the loop by only taking a half-step in one of the parameter dimensions, as shown in panel-a2, and prescribed by

* $y_0 = f(x_0)$

* $x_1 = g\left(y_0\right)$

* $y_1 = f\left(x_1\right) \rightarrow y_{1a} = 0.5\left(y_0 + y_1\right)$

* $x_2 = g\left(y_{1a}\right)$

* $y_2 = f\left(x_2\right) \rightarrow y_{2a} = 0.5\left(y_{1a} + y_2\right)$

* etc...

With this method, the solver may converge to a centralized solution much more quickly. However, as shown in panels-b1 and -c1 of Figure B.5, even this half-step method will not work at all if loop/walking causes the solutions to diverge rather than converge. When solving for v_{srd} caused by Epstein drag, this problem can be circumvented by inverting the two equations (to produce $x = f'\left(y\right)$ and $y = g'\left(x\right)$) and loop/walking in the opposite direction, as shown in panels-b2 and -c2, with:

* $y_0 = g'\left(x_0\right)$

* $x_1 = f'\left(y_0\right)$

* etc...

However, panel-c2 also shows the primary drawback of the loop/walk method, which is that it can sometimes be quite slow to converge, with poor constraints on the accuracy of that convergence.

The second iterative-solver method, which is much faster to converge, is the bisection method, diagramed in Figure B.6. This method requires two initial guesses for the solution (x_{0a} and x_{0b}), one on either side of that solution. At each guess, the direction to the other curve and the magnitude of the separation are calculated. As long as the solution lies between the two guesses, the next guess is made half-way between them, the direction and magnitude to the other curve calculated, and the distance halved again. It goes as:

* $y_{0a} = f\left(x_{0a}\right)\ ;\ y_{0b} = f\left(x_{0b}\right)$

* $\Delta x_{0a} = g\left(y_{0a}\right) - x_{0a}\ ;\ \Delta x_{0b} = g\left(y_{0b}\right) = x_{0b}$

* for $\Delta x_{0a}\Delta x_{0b} < 0$:

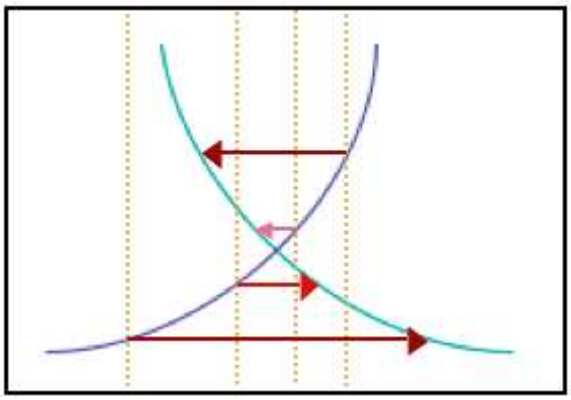

Figure B.6: Diagram for iterative-solving with a bisection method. Blue and teal curves represent the equations to be solved. Dotted lines represent guesses with arrows pointing to the magnitude and direction of separation at each guess. Guesses moving inward from dark to light toward convergence (sufficiently small separation between curves).

    * $x_{1a} = 0.5\,(x_{0a} + x_{0b})$
    * $y_{1a} = f\,(x_{1a})$
    * $\Delta x_{1a} = g\,(y_{1a} - x_{1a})$

* for $\Delta x_{1a}\Delta x_{0a} < 0$:
    * $x_{1b} = x_{0a}\,;\ \Delta x_{1b} = \Delta x_{0a} \rightarrow x_{2a} = 0.5\,(x_{1a} + x_{1b})$
    * etc...

* else for $\Delta x_{1a}\Delta x_{0b} < 0$:
    * $x_{1b} = x_{0b}\,;\ \Delta x_{1b} = \Delta x_{0b} \rightarrow x_{2a} = 0.5\,(x_{1a} + x_{1b})$
    * etc...

This method always converges as fast as possible, and convergence is judged directly by when the separation between the two curves is sufficiently small. It never requires that the equations-to-be-solved are invertible, but it does require knowing ahead of time the general region of parameter space in which the solution exists.

While the loop/walk method is the most computationally expensive of these two methods, as long as $f\,(x)$ and $g\,(y)$ are invertible, it can, however, be applied relatively blindly and still usually produce stable, reliable results. Therefore, the earlier simulations of particle transport (presented

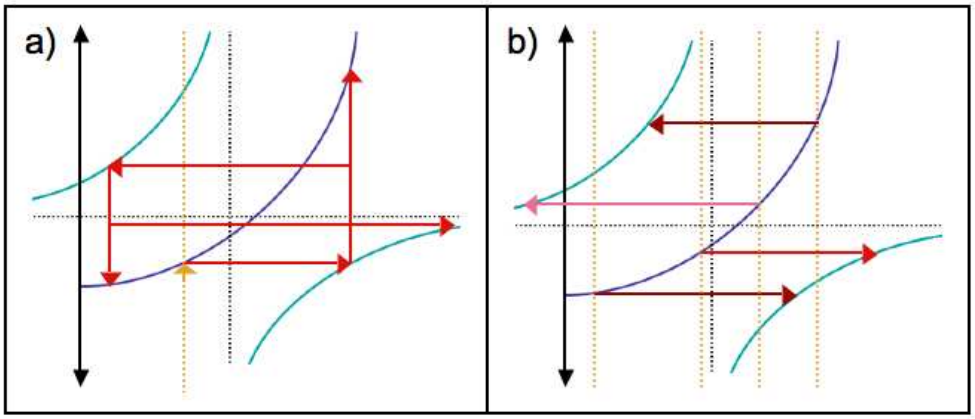

Figure B.7: Diagram of iterative solving by **loop/walk method** (panel-a) and **bisection method** (panel-b) for a case in Epstein-drag v_{srd} when there are no solutions. One of the v_{srd} equations has an asymptote at $v_{\rm K}/2$ with curves open in these directions when $v_{\phi,g} < v_{\rm K}/2$. Black dotted lines denote asymptotes. Left of the black axis line $v_{\phi,d} < 0$, non-viable solution space.

in Chapters 4 & 5) use Epstein-drag v_{srd} values derived from a loop/walk-only iterative solver, with Equation-set (3.24):

$$v_{srd} = v_{r,\rm g} + \frac{3\left(v_{s\phi d}^2 - v_{\rm K}^2\right)}{C_R R \rho_{\rm g} v_{\rm therm}}, \tag{B.17}$$

$$v_{s\phi d} = \left(\frac{C_R R rho_{\rm g} v_{\rm therm}}{3} v_{\phi,\rm g} + \frac{v_{srd} v_{\rm K}}{2}\right) / \left(v_{srd} + \frac{C_R R \rho_{\rm g} v_{\rm therm}}{3}\right), \tag{B.18}$$

and inverse equations:

$$v_{s\phi d} = \sqrt{v_{\rm K}^2 + \frac{C_R R \rho_{\rm g} v_{\rm therm}}{3}\left(v_{srd} - v_{r,\rm g}\right)}, \tag{B.19}$$

$$v_{srd} = -\frac{1}{3} C_R \, R \rho_{\rm g} v_{\rm therm} \frac{\left(v_{s\phi d} - v_{\phi,\rm g}\right)}{\left(v_{s\phi d} - v_{\rm K}/2\right)}. \tag{B.20}$$

Using a loop/walk-only method with these equations is almost always well-behaved. However, because one of the v_{srd} equations is hyperbolic, there is one case, sometimes appearing, for which no steady v_{srd} solution exists. This is diagramed in Figure B.7. Note, that neither the loop/walk method, nor the bisection method can handle this no-solution situation on their own. A better iterative solver does not simply switch to a faster solving method, but instead takes the input equations into account and is carefully designed to search for solutions where they are likely to be found. Such a map for finding the full solution set to the v_{srd} equations is outlined in §B.3.2.

B.3.2 The Mapped Approach to Iteratively Solving for Steady Radial Drift Velocities

Here I present the schematic for finding the full solution set for v_{srd} under the influence of Epstein drag using the equations (B.17)–(B.20) given above and the schematic map (in v_{srd} versus $v_{s\phi d}$ space) shown in Figure B.8. Due to the nature of hyperbolic equations, solutions for v_{srd} are broken into two regimes.

The assymptotes for the hyperbolic exist at

$$v_{s\phi d} = v_{\phi \mathrm{H}} = \frac{v_{\mathrm{K}}}{2} \tag{B.21}$$

$$v_{srd} = v_{r\mathrm{H}} = -v_{\mathrm{drag}}\,, \tag{B.22}$$

where $v_{\mathrm{drag}} = C_R R \rho_g v_{\mathrm{therm}}/3$ and is so-named because it scales the Epstein-drag force and has the units of velocity. While in general $v_{\phi,g} < v_{\mathrm{K}}$, it is almost always greater than $v_{\mathrm{K}}/2$, and therefore solving for v_{srd} usually falls into the simpler of the two regimes. In this $v_{\phi,g} > v_{\mathrm{K}}/2$ regime, there is always a solution (A) intersecting the upper-RH branch of the hyperbolic equation, and sometimes

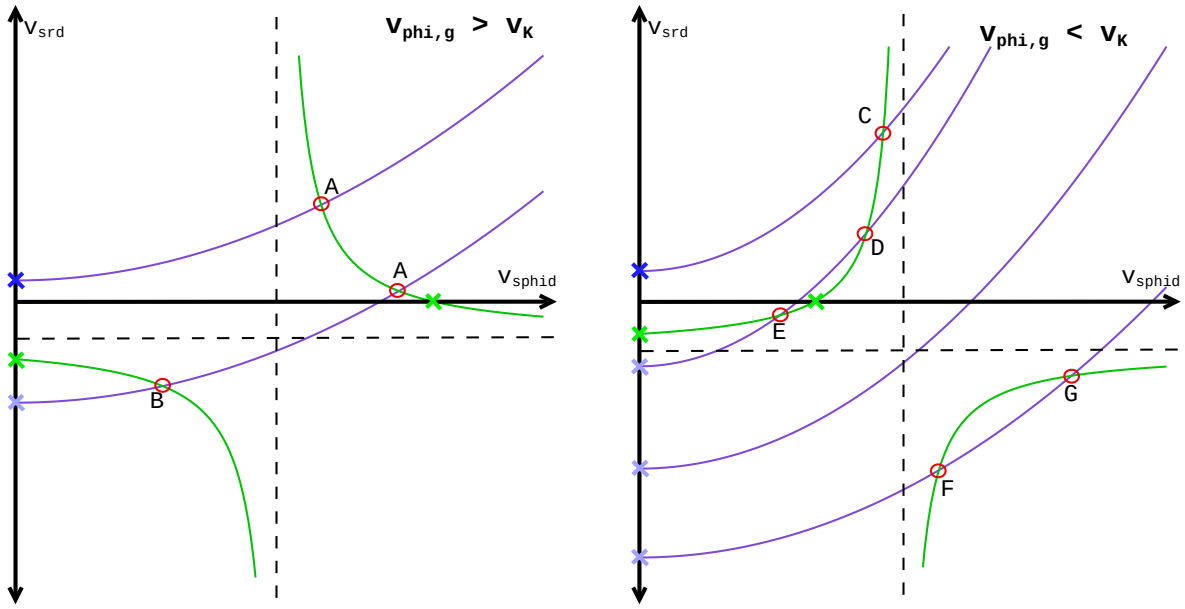

Figure B.8: Schematic for the v_{srd} solutions with Epstein drag (Equations (B.17)–(B.20)). Note, curves have been exaggerated for clarity. Dashed lines mark the assmpytotes of the hyperbolic equation (green curves). Green x's mark where the hyperbolic equation crosses the zero axes ($v_{s\phi d} = v_{\phi,g}$ for $v_{srd} = 0$) and blue x's mark where the parabolic equation (purple curve) intersects the $v_{s\phi d} = 0$ axis.

also a solution (B) for the lower-LH branch as well. The hyperbolic intersects the $v_{s\phi d} = 0$ axis at

$$v_{\rm H0} = -\frac{2 v_{\phi,g} v_{\rm drag}}{v_{\rm K}} \,. \tag{B.23}$$

The parabolic intersects the axis at

$$v_{\rm P0} = v_{r,g} - \frac{v_{\rm K}^2}{v_{\rm drag}} \,. \tag{B.24}$$

Solution (B) exists if $v_{\rm H0} \geq v_{\rm P0}$. Finally, both solutions (A) and (B) can be found with the bisection method, bisecting in v_{srd} — the parameter of most interest. Solution (B) must exist at $v_{\rm P0} \leq v_{srd,(\rm B)} \leq v_{\rm H0}$, and so the bisect bounds are already defined. If solution (B) exists, then one bisect bound for solution (A) should be placed at $v_{srd} = 0$. The other bound must be searched for both toward lower v_{srd} approaching (but not crossing) the hyperbolic assymptote, and toward greater v_{srd}, since it cannot be known before hand in which direction the solution will lie. If, however, solution (B) does not exist, then a bound for (A) can be placed at $v_{\rm P0}$ and the other searched toward larger v_{srd}. In the case that both (B) exists and there are two solutions to chose from, I choose the solution closest to $(v_{r,g}, v_{\phi,g})$, almost always solution (A).

Searching for v_{srd} solutions in the $v_{\phi,g} < v_{\rm K}/2$ regime is rarer (but not negligibly so, as the gas may orbit very slowly just interior to a gap or at the very outer disk edge), and also more complicated, and there may be no solution at all. If in this regime $v_{\rm H0} < v_{\rm P0}$, then there is generally one solution (C) on the upper-LH branch of the hyperbolic that can be found using the same bisect method as for (A) but with the upper-bound already given by where the parabolic crosses the $v_{\rm K}/2$ assmpytote. However, it is conceivable that $v_{\rm H0} < v_{\rm P0}$ harbors three solutions (C1,C2,C3), as depicted in Figure B.9. If three solutions do exist, then the bisect search will locate either (C1) or (C3). Therefore, solution one must search for a possible (C2) using the loop-walk method - starting just above or below the found solution (based on the requested accuracy for convergence), and then loop/walk searching in both directions (which is one reason why the invertible equations for the Epstein-drag case are very nice). (Note that this search will fail incorrectly if two of the solutions are with the error-margine of each other.) Moving toward larger values will not provide (C2) if the loop/walk goes past $v_{s\phi d} = v_{\rm K}/2$. Moving to small values will not provide (C2) if the loop/walk

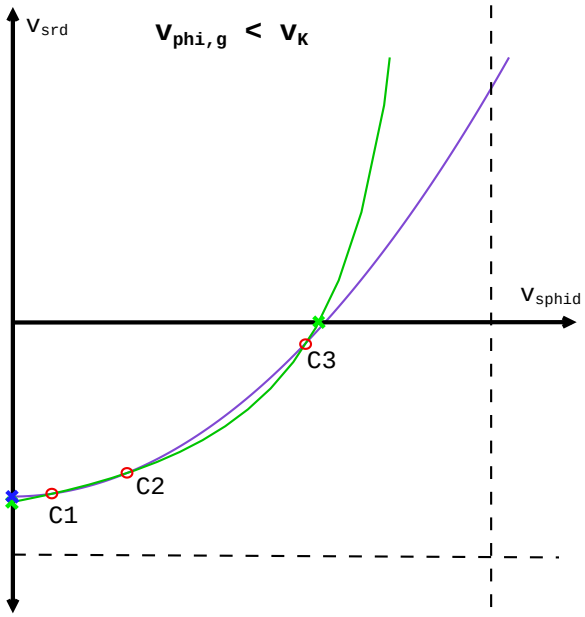

Figure B.9: Map of the solution-space for finding v_{srd} due to Epstein drag when there are three possible solutions (in the $v_{\phi,g} < v_{\rm K}/2$ regime). Same conventions as in Figure B.8.

goes below $v_{srd} = v_{\rm P0}$. Therefore, this search method has clear failure criteria. If, however, (C2) is found, then a third solution must also exist, either between (C2) and v_{P0} or (C2) and where the parabolic crosses $v_{\rm K}/2$. This provides clear bounds for a bisect method. However, numerically, the (C2) bound must be placed at least one error-margine away. If these later two solutions are within an error-margin of each other, then they will have to be treated as a single solution.

Next, in the more difficut $v_{\phi,g} < v_{\rm K}/2$ regime, when $v_{\rm H0} > v_{\rm P0}$, there are either 0 or 2 solutions (either both on the upper-LH branch of the hyperbolic (D and E) or both on the lower-RH branch (F and G)). Fortunately, there are clear criteria for determining whether there are no solutions in this regime, and if that is the case, my code simply sets the radial-drift velocity equal to the assymptote $v_{rH} = -v_{\rm drag}$. The schematic for seeking the first solution in this regime is shown in Figure B.10. The first step is to start at the point where the parabolic crosses the $v_{\rm K}/2$ assymptote and loop/walk toward smaller values. If the walk crosses below $v_{\rm H0}$, then solutions (D) and (E) do not exist. Otherwise, loop/walking will locate solution (D). Solution (E) may then be found with bisection, setting on bound at $v_{\rm H0}$, and searching for the other at $v_{srd} < v_{srd\rm D}$. If solutions (D) and (E) do not exist, next is to loop/walk toward larger values from $v_{\rm P0}$. If the walk crosses

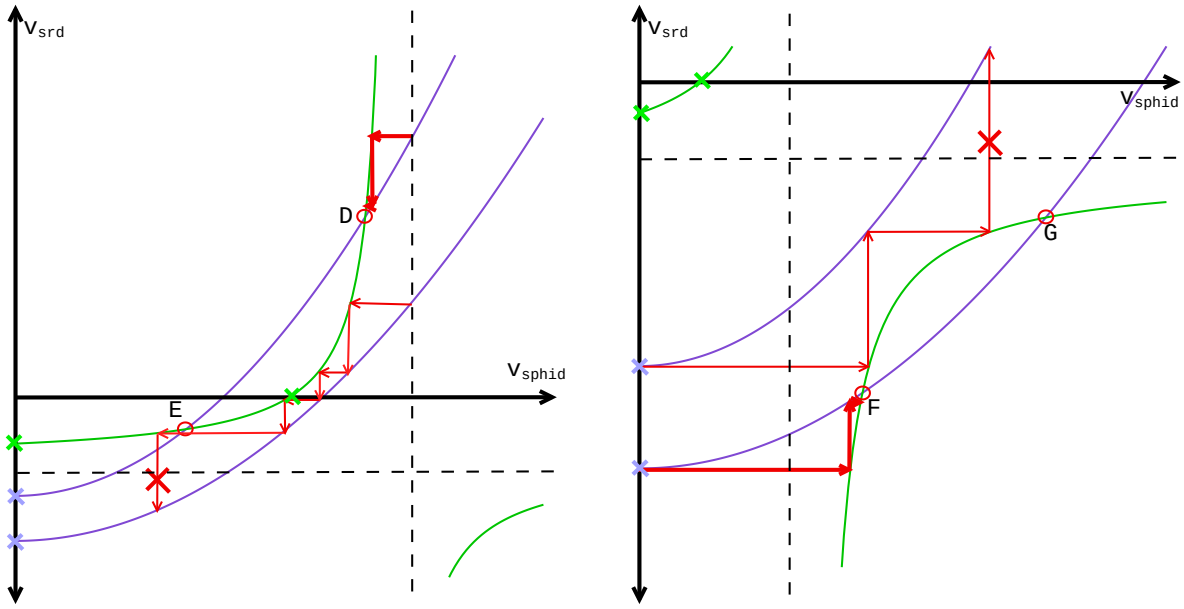

Figure B.10: A map seeking v_{srd} solutions in the case that $v_{\phi,g} < v_{\rm K}/2$ and $v_{\rm H0} > v_{\rm P0}$. Looping forward from two limits will either find the first of two solutions, (D) or (F), or will identify the criteria for zero solutions. Plot uses same conventions as in Figure B.8.

above the assymptote $v_{rH} = -v_{\rm drag}$, then solutions (F) and (G) do not exist (and there are no solutions). Otherwise, the loop/walk will reach solution (F), and solution (G) can be found by bisection. Setting the bisection bounds for (G) are a bit tricky, however, as they must be $> v_{srd\rm F}$ and $< v_{rH}$ and not actually at either.

As complex as these schematics may seem, there are really quite clear paths to reaching all obtainable solutions. Making a map to solve for v_{srd} in the case of Stokes drag would be harder. This is primarily for two reasons. First, because the v_{srd} equations for Stokes drag are made more complex by being spread over three regimes in Re (see §3.2.1), and the boundaries of those regimes depend on one's position in both v_{srd} and $v_{s\phi d}$ parameter space. And second, the Stokes-drag equations cannot be easily inverted, making the direction loop-walking fixed and even some of the axis intersection bounds troublesome to locate. One possible approach would be to solve the equations in each of the thee Re regimes separately, and then sort out which solutions were viable. However, each regime would still have its individual challenges.

B.3.3 To Solve for the Disk Temperature at the Midplane by Balancing Energy Flux

Here, I present my schematic for finding an energy-balanced midplane-temperature solution (see §2.4). Because of the number and complexity of equations involved, my code does not account for finding the full solution set. Instead, I have taken a simplified approach generally appropriate to my protoplanetary-disk models, wherein there are usually only 1 or 3 possible solutions, as depicted in Figure B.11.

The primary equations to itterate to find an energy-balanced midplane temperature are (see §2.4)

$$\begin{aligned}
\sigma_{\rm B} T_{\rm mid}^4 &= \frac{1}{2} R^2 \nu \Sigma_g \left(\frac{\partial \Omega_g}{\partial R} \right)^2 \left(\frac{3}{8} \tau_R + \frac{1}{2\tau_P} \right) + \sigma_{\rm B} \left(T_{\rm irr}^4 + T_{\rm cloud}^4 \right) \, , \\
\kappa_R &= \kappa_i \rho^{a_i} T^{b_i} \, ; \text{ with 8 regimes for } \kappa_i, a_i, \text{and } b_i \, , \\
\nu &= \alpha \frac{1}{\Omega_{\rm K}} \sqrt{\frac{k_{\rm B} T}{\mu m_{\rm H}}} \, ,
\end{aligned}$$

also remembering that

$$\begin{aligned}
\rho_{\rm g,mid} &= \frac{\Sigma_g \Omega_{\rm K}}{\sqrt{2\pi}} \sqrt{\frac{\mu m_{\rm H}}{k_{\rm B} T}} \\
\tau_R &= \kappa_R \Sigma_g \\
\frac{\tau_P}{\tau_R} &\approx 1
\end{aligned} \tag{B.25}$$

This set of equations is not invertible, so, in the case of itteratively loop/walking to find a solution in the space shown in Figure B.11, motion toward the energy-balance (blue) curve must be for a given κ_R (and ν) and is left-right only, while motion toward the Bell-Lin opacity (green) curve must be for a given T and is up-down only.

To begin looking for an energy-balanced temperature solution, I first mark a minimum guessed temperature, $T_{\rm min}$, taken from the energy-balanced curve due to external luminosity only ($\nu = 0$). This then also gives a first guess for ν and κ_R. With this guessed minimum temperature, I next consider the resultant $\kappa_R(T)$ curve and each of the intersection points between the different opacity regimes. For each intersection point, I consider the (left-right) direction to the local energy-balance temperature, T_{EB}, and flag each point for which $T_{\rm min} < T_{\rm point} < T_{EB}$. (The change in the $\kappa_R(T)$

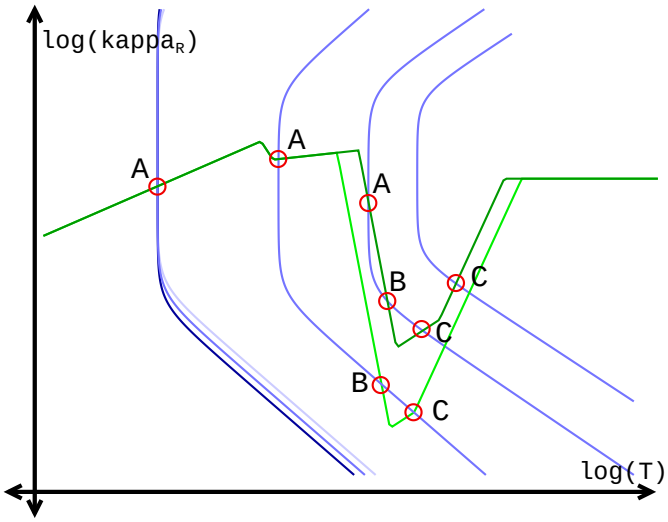

Figure B.11: Schematic for iteratively solving for an energy-balanced midplane disk temperature plotted in κ_R versus T space. However, the solution must actually be found in three parameters, including the disk viscosity, ν. **Green curves** plot the Rossalind-mean opacities κ_R obtained from *Bell & Lin* (1994) for a higher (dark) and lower (light) gas density, $\rho_{g,\mathrm{mid}} \propto T^{-1/2}$. **Blue curves** plot instances of the energy-balance equation (2.44) (for lower (darker) to higher (lighter) disk viscosity, $\nu_\alpha \propto T$).

slope at intersection points means that there is a chance for multiple crossings of the energy-balance and opacity curves under that condition.) In Figure B.11, only the left-most set of blue curves would have no flagged intersection points (so I would need to look for one solution (A) only).

Finally, I first seek a solution to the set using the simple loop/walk method of itteration starting at T_{min}. For each guessed T, I advance both κ_R and ν before seeking the next T. This loop/walk method then produces either solution (A) or (C). If the solution is at T greater than any of the flagged points, then it is solution (C) and I assume this is the only solution (as in the right-most blue curve of Figure B.11). Otherwise it is solution (A) and, if there are flagged points, I next search for solutions (B) and (C).

Solution (C) is at T greater than any of the flagged points, so the greatest flagged T marks one of the bounds for a bisection search. The other bound must be searched for toward larger T. Solution (B) can only be found using bisection, but the only clear bounds are that $T_A < T_B < T_C$. Therefore, the first bound must be guessed between T_A and T_C, and a second bound searched left and right toward those solutions. And (B), of course, cannot be found separately if it is within an accuracy margin of one of the other solutions.

Last, if there are multiple solutions found, my code picks the temperature solution closest to the the previously calcuated temperatre (or $T_{\min}$ if this is the first calculation).

Appendix C

Glossary of Physical Constants and Symbolic Variables

SPECIAL FUNCTIONS

Symbol	Function	Example Use
I_β	Modified Bessel function of the First Kind of order β	Equations (2.21) & (A.12)
J_β	Bessel function of the First Kind of order β	Equation (A.8)
$\delta(x - x_0)$	Dirac-delta function	Equations (2.20), before (A.1)

Table C.1: Table of Special Functions

Symbol	Value	Name	Example Use
AU	$1.4959787066 \times 10^{13}$ cm	astronomical unit	
c	$2.99792458 \times 10^{10}$ cm s^{-1}	speed of light	Equation (3.2)
G	6.6742×10^{-8} cm^3 g^{-1} s^{-2}	the gravitational constant	Equation (2.2)
k_B	$1.3806505x10^{-16}$ ergs K^{-1}	Boltzmann's constant	Equation (2.4)
$L_\odot$	3.846×10^{33} ergs s^{-1}	solar luminosity	
$M_\odot$	1.988×10^{33} g	Solar mass	
$M_{\rm Earth}$	5.9723×10^{27} g	Earth mass	
m_H	$1.67262171 \times 10^{-24}$ g	proton mass	Equation (2.4)
α_B	2.6^{-13} cm^3 s^{-1}	recombination coefficient of atomic Hydrogen	Equation (2.31)
$\sigma_{13.6eV}$	6.3×10^{-18} cm^2	absorbing cross-section for EUV ionizing radiation	after Equation (2.32)
$\sigma_{\rm B}$	5.6704×10^{-5} ergs s^{-1} cm^{-2} K^{-4}	Stefan-Boltzman constant	Equation (2.38)
σ_{H_2}	2.4×10^{-15} cm^2	collisional cross-section of molecular Hydrogen	
π	3.1415926....	pi	

Table C.2: Table of Physicals Constants

Symbol	Common Units	Description	Example Use
a	–	(negative) power-law constant for power-law disk surface density	Equation (A.1)
A	s^{-1}	local rate of shearing in the disk	Equation (2.15)
$A(\lambda)$	***	initial-condition fitting function for contaminant-diffusion distribution	Equation (A.9)
a_i	–	power-law for ρ_g in the *Bell & Lin* (1994) opacity parameterization	Equation (2.47)
a_{ph}	–	fitting constant for EUV photoevaporation	Equation (2.33)
A_{ph}	–	fitting constant for EUV photoevaporation	Equation (2.31)
b	–	power-law constant for power-law disk viscosity	Equation (A.1)
b_i	–	power-law for T in the *Bell & Lin* (1994) opacity parameterization	Equation (2.47)
B_{ph}	–	fitting constant for EUV photoevaporation	Equation (2.30)

Table C.3: Table of Symbolic Variables

Symbol	Common Units	Description	Example Use
b_{q_T}	–	power-law for time-scaling for q_T in the TPR fit to disk temperature	Equation (2.50), Table 2.1
$b_{T_{AU}}$	–	power-law for time-scaling for T_{AU} in the TPR fit to disk temperature	Equation (2.50), Table 2.1
b_x	–	power-law of time-scaling of T_{AU} or q_T for TPR fit to disk temperature	Equations (2.50) & (2.51)
C	–	concentration (local contaminant-to-gas mass ratio) of diffusing contaminant	Equation (A.2)
C_0	***	scaling constant for $t = 0$ contaminant concentration	before Equation (A.1) & (A.10)
$C_{1,ph}$	–	fitting constant for EUV photoevaporation	Equation (2.31)
$C_{2,ph}$	–	fitting constant for EUV photoevaporation	Equation (2.35)
C_D	–	coefficient of Stokes drag	Equation (3.14)
C_N	–	the normalized concentration of a contaminant in a region (the outer disk in this thesis)	Equation (4.2)
C_R	cm^2 g^{-1}	surface-area-to-mass ratio of a dust particle	Equation (3.10)
$C_{R,\mathrm{maxv}}$	cm^2 g^{-1}	C_R that gives fastest inward drift from headwind drag	Equation (3.23)
$C_{R,\mathrm{steady}}$	cm^2 g^{-1}	C_R that balances drag for a stable orbit	Equation (3.22)

Table C.3 continued: Symbolic Variables

Symbol	Common Units	Description	Example Use
c_s	km s^{-1}	local sound speed	Equation (2.4)
$c_{s,\mathrm{ionz}}$	km s^{-1}	sound speed of ionized gas	Equation (2.29)
D_g	cm^2 s^{-1}	diffusivity of the gas	Equation (3.30)
D_{kg}	cm^2 s^{-1}	diffusivity of a contaminant	Equation (A.2)
D_p	cm^2 s-1	diffusivity of the particle ensemble	Equation (3.29)
$D_{p,\mathrm{CDC1993}}$	cm^2 s^{-1}	particle-ensemble diffusivity according to *Cuzzi, Dobrovolskis, & Champney* (1993)	Equation (3.34)
$D_{p,\mathrm{YL2007}}$	cm^2 s^{-1}	particle-ensemble diffusivity according to *Youdin & Lithwick* (2007)	Equation (3.33)
D_{ph}	–	fitting constant for EUV photoevaporation	Equation (2.30)
E	–	local enhancement factor of the dust-to-gas ratio	Equation (6.5)
E_{precip}	–	enhancement required for collapse/precipitation	Equation (6.19)
E'_{precip}	–	enhancement required for precipitation using Ri'_c	Equation (6.25)
E_{Q_p}	–	enhancement required for direct collapse of particle layer	Equation (6.21)
E'_{Q_p}	–	enhancement required for direct collapse of particle layer	Equation (6.26)
dF_ν	g s^{-2}	viscous force per unit length	Equation (2.15)
F_{cloud}	ergs s^{-1} cm^{-2}	energy-flux of molecular-cloud illumination	Equations (2.37) & (2.40)

Table C.3 continued: Symbolic Variables

Symbol	Common Units	Description	Example Use
$F_{\rm cool}$	ergs s^{-1} cm^{-2}	energy-flux of disk cooling	Equations (2.37) & (2.38)
F_D	g cm s^{-2}	force of gas drag	below Equation (3.8)
$F_{D,r}$	g cm s^{-2}	radial component of the gas-drag force	Equation (3.7)
$F_{D,\phi}$	g cm s^{-2}	azimuthal component of the gas-drag force	Equation (3.8)
f_{ph}	–	smoothing function for the direct-photoevaporation wind	Equations (2.33) & (2.34)
$F_{\rm ph}$	g cm s^{-2}	force of photophoresis	Equation (3.3)
$F_{\rm rad}$	g cm s^{-2}	force of radiation pressure	Equation (3.2)
$F_{\rm star}$	ergs s^{-1} cm^{-2}	energy-flux of stellar illumination	Equations (2.37) & (2.39)
$F_{\rm visc}$	ergs s^{-1} cm^{-2}	energy-flux of disk viscous heating	Equations (2.37) & (2.42)
$g\,(R)$	***	R-dependence of variable-separated $C\,(R,t)$	Equation (A.5)
G_ν	g cm^2 s^{-2}	local viscous torque	Equations (2.14) & (2.15)
$h\,(\psi)$	–	gravitational scaling for critical particle layer	Equation (6.20)
H_0		scaling constant for power-law disk scale-height	Equation (2.10)
H_g	AU	local disk-gas scale-height	Equations (2.3) & (2.4)
H_p	AU	particle scale-height in the disk	Equation (3.4)
$H_{p,c}$	cm	height of critical particle layer	Equation (6.20)

Table C.3 continued: Symbolic Variables

Symbol	Common Units	Description	Example Use
i	–	index variable of disk-model grid cells	Equation (2.23)
i'	–	index variable contracted grid-space: one i' corresponds to several i	Equation (6.10)
I	ergs s^{-1} cm^{-2}	intensity of incident light	Equation (3.2)
j	–	index variable for disk-evolution time steps	Equation (2.24)
J_1	–	assymetry parameter for calculating photophoresis	Equation (3.3)
k	***	change-of-variables constant	Equation (A.7)
$K_{\rm diff}$	g cm^{-2} $s^{-1/2}$	scaling constant for the diffuse-photoevaporation wind	Equations (2.30) & (2.31)
$K_{\rm dir}$	g $cm^{-1/2}$ $s^{-1/2}$	scaling constant for direct-wind photoevaporation	Equations (2.33) & (2.35)
$k_{\rm th}$	ergs s^{-1} cm^{-1} K^{-1}	thermal conductivity of a grain	Equation (3.3)
$l\,(L)$	g $cm^{1/2}$	normalized angular-momentum measure	Figure (B.3)
$L_\star$	$L_\odot$	stellar luminosity	Equation (2.39)
$L_{1,i}$	g cm^2 s^{-1}	less-precise angular-momentum calculation in grid-cell i	Equation (B.7)
$L_{2,i}$	g cm^2 s^{-1}	more-precise angular-momentum calculation in grid-cell i	Equation (B.8)
m	g	mass of a (growing) dust grain	Equation (3.35)

Table C.3 continued: Symbolic Variables

Symbol	Common Units	Description	Example Use
m_1, m_2	g	masses of two colliding/coagulaing dust grains	before Equation (3.35)
$M_{1,i}$	g	less-precise mass calculation in grid-cell i	Equation (B.7)
$M_{2,i}$	g	more-precise mass calculation in grid-cell i	Equation (B.8)
$M_\star$	$M_\odot$	mass of the central star	Equation (2.2)
$\dot{M}$	$M_\odot$ yr^{-1}	local accretion rate	Equation (2.19)
$\dot{M}_0$	$M_\odot$ yr^{-1}	initial disk accretion rate	Equation (2.1)
m_d	g	mass of a dust particle	Equation (3.7)
$M_{D,0}$	$M_\odot$	initial disk mass	Equation (6.4)
$M_{\rm dummy}$	g	mass viscously transfered into a dummy grid-cell with no mass initially in it	before Equation (B.9)
M_g	g	disk-gas mass	Equation (3.32)
$M_{g,i}$	g	gas mass in grid-cell i	Equation (6.10)
$m_{\rm GE}$	g	gas-equivalent mass of a dust particle	after Equation (6.5)
$M_{\rm GE}$	g	(source-) gas-equivalent mass of dust particles	Equation (6.5)
$M_{{\rm GE},i}$	g	gas-equivalent mass of dust particles in grid-cell i	Equation (6.10)
m_i	g	contaminant mass in grid-cell i	Equation (A.15)
$m_{\rm tot}$	g	total mass of diffusing contaminant	Equation (A.15)

Table C.3 continued: Symbolic Variables

Symbol	Common Units	Description	Example Use
n	cm^{-3}	gas particle number density	after Equation (2.2)
n_{grid}	–	number of disk-model radial grid cells	Equation (2.23)
n_p	$\#\ \mathrm{cm}^{-3}$	number density of particles	Equation (6.6)
P	$\mathrm{g\ cm}^{-1}\ \mathrm{s}^{-2}$	local gas pressure	Equation (2.2)
p	–	power-law–index variable change for diffusion-of-a-contaminant solution	Equation (A.5)
p_{in}	–	probability of a particle diffusively stepping radially inward	Equation (3.32)
P_k	$\mathrm{g\ cm}^{-2}\ \mathrm{s}^{-1}$	production rate of a contaminant	Equation (A.2)
p_{out}	–	probability of a particle diffusively stepping radially outward	Equation (3.32)
q	–	change-of-variables power-law constant	Equation (A.7)
q_H	–	disk scale-height power-law constant in R	Equation (2.10)
Q_p	–	Q-collapse criterion of particle layer	Equation (6.20)
q_s	–	grain-size distribution power-law index	Equation (6.6)
q_T	–	disk temperature power-law constant in R	Equation (2.10)
$q_{T,0}$	–	q_T at $t = 0$	Equation (2.50), Table 2.1
$q_{T,\infty}$	–	q_T at $t = \infty$	Equation (2.50), Table 2.1

Table C.3 continued: Symbolic Variables

Symbol	Common Units	Description	Example Use
q_ν	–	disk viscosity power-law scaling in R	Equation (2.10)
q_Σ	–	local power-law constant for the disk surface density	Equation (2.54)
R	AU	radial distance from the central star	Equation (2.1)
R_0	AU	initial radial position of a diffusing quantity	Equation 2.20
r_d	cm	dust radial distance from the star	Equation (3.1)
R_d	AU	initial-disk exponential fall-off radius	Equation (2.1)
Re	–	Reynold's number	Equation (3.12)
$R_{\rm edge}$	AU	outer edge of photoevaporative gap	Equation (2.32)
$R_{\rm fin}$	cm	radial position of a particle at the end of a time-step	§3.3.2
R_g	AU	radius where an ionized (hot) gas is gravitationally unbound from the star	Equation (2.29)
$R_{\rm gap}$	AU	location where EUV photoevaporative gap opens	before Equation (2.32)
Ri	–	Richardson number	before Equation (6.15)
Ri_c	–	critical Richardson number	Equation (6.15)
Ri'_c	–	critical Richardson number scaled to E following *Lee et al.* (2010)	Equation (6.24)
R_i	AU or cm	radial position of grid-cell i	Equation (2.23)

Table C.3 continued: Symbolic Variables

Symbol	Common Units	Description	Example Use
$R_{i+1/2}$	cm	radial-position of the outer-boundary of grid-cell i	Equation (B.8)
$R_{\rm in}$	AU	(steady) inner edge of gas disk	Equation (2.1)
$R_{\rm max}$	AU	outer-most disk-grid-cell position	Equation (2.23)
$R_{\rm min}$	AU	inner-most disk-grid-cell position	Equation (2.23)
$R_{\rm out}$	AU	$\sim$ outer observable edge of a gas disk	§2.5
$R_{\rm start}$	cm	radial position of a particle at the beginning of a time-step	§3.3.2
$R_{\rm thin}$	AU	inner edge of photevaporative gap	Equation (2.32)
s	***	spatial change-of-variables for contaminant-diffusion distribution	Equation (A.11)
s_0	***	s for R_0 for contaminant-diffusion distribution	Equation (A.16)
$s\left(\psi\right)$	–	gravitational scaling for collapse criterion	Equation (6.15)
$s_{b\rm max}$	cm	maximum grain radius of a given grain-size bin	Equation (6.8)
$s_{b\rm min}$	cm	minimum grain radius of a given grain-size bin	Equation (6.8)
Sc	–	the Schmidt number: ratio of disk viscosity to the gas diffusivity	before Equation (3.33)
s_d	cm	radius of a dust particle	Equation (3.2)

Table C.3 continued: Symbolic Variables

Symbol	Common Units	Description	Example Use
s_{d1}, s_{d2}	cm	radii of two colliding/coagulating dust grains	Equation (3.36)
$s_{\max}$	cm	maximum grain-radius for the dust-size distribution	Equation (6.7)
$s_{\min}$	cm	minimum grain-radius for the dust-size distribution	Equation (6.7)
St	–	the Stokes number: ratio of the gas-drag stopping to the eddy turn-over times	Equation (3.34)
t	years	time	Equation (2.1)
t_0	yr	time (relative to $t = 0$ of the disk evolution) that particles are initiated in the transport simulations	§5.3
$t_{\rm eddy}$	s	time-scale for one eddy turnover	before Equation (3.33)
$t_{\rm orbit}$	s	orbital period	before Equation (3.23)
$t_{\rm stop}$	s	gas-drag stopping time of a particle	Equations (3.4) & (3.5)
$t_{T_{AU}}$	years	time-scaling for T_{AU} in the TPR fit to disk temperature	Equation (2.50), Table 2.1
t_{q_T}	years	time-scaling for q_T in the TPR fit to disk temperature	Equation (2.50), Table 2.1
t_x	years	time-scaling for T_{AU} or q_T in the evolving-power-law fit of disk temperature	Equations (2.50) & (2.52)
T	K	local disk temperature	Equation (2.4)
T_0	***	scaling constant for power-law disk temperature	Equation (2.10)

Table C.3 continued: Symbolic Variables

Symbol	Common Units	Description	Example Use
T_{AU}	K	disk temperature at 1 AU	Equation (2.49)
$T_{AU,0}$	K	T_{AU} at $t = 0$	Equation (2.50), Table 2.1
$T_{AU,\infty}$	K	T_{AU} at $t = \infty$	Equation (2.50), Table 2.1
$T_{\rm bound}$	K	boundary temperature between opacity regimes in the *Bell & Lin* (1994) parameterization	after Equation (2.47)
$T_{\rm cloud}$	K	temperature of the (molecular cloud) disk environment	Equation (2.40)
T_e	K	effective radiative temperature of the disk	Equation (2.38)
$T_{\rm irr}$	K	effective temperature from stellar irradiation	Equation (2.39)
$T_{\rm mid}$	K	midplane disk temperature	Equation (2.44)
v	cm s^{-1}	background contaminant radial velocity	§3.3.2
v_0	***	scaling-constant for power-law radial velocity	Equation (A.1)
$v_{\rm K}$	cm s^{-1}	Keplerian velocity	Equation (3.5)
v_R	cm s^{-1}	1D disk-model or contaminant radial velocity	Equations (2.13) & (A.1)
$v_{r,\rm acc}$	cm s^{-1}	$v_{r,g}$ in the accretion-flow case	Equation (2.55)
$v_{r,d}$	cm s^{-1}	radial dust velocity	Equation (3.5)
$v_{r,\rm drag}$	cm s^{-1}	dust radial velocity induced by gas drag	Equation (3.28)
$v_{r,\rm drift}$	cm s^{-1}	dust radial-drift velocity from headwind drag	Equation (3.25)

Table C.3 continued: Symbolic Variables

Symbol	Common Units	Description	Example Use
$v_{r,g}$	cm s^{-1}	radial gas velocity	Equation (2.56)
$v_{r,\mathrm{merid}}$	cm s^{-1}	$v_{r,g}$ in the midplane-flow case	Equation (2.57)
v_{settle}	cm s^{-1}	settling (toward the midplane) velocity of a dust particle in a gas disk	Equation (3.37)
v_{srd}	cm s^{-1}	dust steady mean-radial velocity	Equations (3.1) & (3.24)
$v_{s\phi d}$	cm s^{-1}	steady azimuthal dust velocity	Equation (3.24)
v_{therm}	cm s^{-1}	thermal velocity of the gas particles	Equation (3.10)
v_{turb}	cm s^{-1}	dust turbulent random-walk velocity	Equations (3.1) & (3.29)
$v_{z,g}$	cm s^{-1}	vertical (midplane normal) gas velocity	Equations (2.56) & (2.58)
$v_{\phi,d}$	cm s^{-1}	azimuthal (orbital) dust velocity	Equation (3.5)
$v_{\phi,g}$	cm s^{-1}	azimuthal (orbital) velocity of the disk gas	after Equation (2.54)
x	***	spatial change-of-variables for contaminant diffusion	Equation (A.7)
x_0	K or –	T_{AU} or q_T at $t = 0$	Equation (2.50)
x_∞	K or –	T_{AU} or q_T at $t = \infty$	Equation (2.50)
X	$\mathrm{cm}^{1/2}$	spatial variable used in the disk-evolution equation	Equation (2.17)
X_i	$\sqrt{\mathrm{AU}}$ or $\sqrt{\mathrm{cm}}$	X-spatial position of grid-cell i	Equation (2.23)

Table C.3 continued: Symbolic Variables

Symbol	Common Units	Description	Example Use
Y	***	spatial change-of-variables for contaminant-distribution solution	Equation (A.18)
z	cm	height above the disk mid-plane	Equation (2.2)
Z	–	disk metallicity (dust-to-gas surface-density ratio)	Equation (3.38)
$Z_\odot$	–	solar/initial dust-to-gas ratio (metallicity)	Equation (6.13)
Z_0	–	ratio of all-condensibles-to-gas (base metallicity)	Equation (6.13)
$Z_{\rm rel}$	–	relative fraction of all condensibles solid at a given disk temperature	Equation (6.13)
α	–	alpha-scaling for disk viscosity	Equation (2.8)
α_c	–	power-law constant used in solution for analytic diffusion	Equation (2.21)
β	–	order of the modified Bessel function solution to diffusive evolution	Equation (2.21)
χ_{ph}	–	scaling constant for $\Phi_{\rm dir}$	Equation (2.36)
χ_R	–	radial position scaled by R_g	Equation (2.30)
δL_i	g cm^2 s^{-1}	extra angular-momentum created (or destroyed) in one numeric viscous-evolution time-step from grid-cell i	Equation (B.9)

Table C.3 continued: Symbolic Variables

Symbol	Common Units	Description	Example Use
δM_i	g	extra mass created (or destroyed) in one numeric viscous-evolution time-step from grid-cell i	Equation (B.9)
$\Delta R_{\rm advect}$	cm	displacement of particle due to gas-drag advection	§3.3.2
ΔR_i	cm	width of grid-cell i	Equation (B.7)
ΔR_{rms}	cm	root-mean-square of particle diffusive translation	Equation (3.31)
$\Delta R_{\rm turb}$	cm	displacement of particle due to diffusive random-walk stepping	§3.3.2
Δt	years or s	size of various time-steps	Equations (2.24) & (2.25)
$\Delta t_{\rm evolv}$	years or s	time-step of disk-model viscous evolution	after Equation (3.32)
Δv	cm s^{-1}	collisional velocity for dust-grain coagulation	Equation (3.35)
Δv_B	cm s^{-1}	collisional velocity for dust coagulation via Brownian motion	Equation (3.39)
ΔX_i	$\sqrt{\rm cm}$	width in X of grid-cell i	Equation (2.24)
$\Delta X_{i+1/2}$	$\sqrt{\rm cm}$	distance in X between grid-cells i and $i+1$	Equation (2.24)
ϵ	–	radiative efficiency of the disk gas	Equation (2.38)
ϵ_ρ	–	local-dust-to-gas volume-density ratio	Equation (3.27)

Table C.3 continued: Symbolic Variables

Symbol	Common Units	Description	Example Use
$\epsilon_{\rho,0}$	–	dust-to-gas density ratio at the midplane	Equation (6.22)
ϕ	–	incidence angle between disk surface and stellar illumination	Equation (2.39)
Φ	photons s^{-1}	EUV ionization flux	Equation (2.32)
$\Phi_{\rm diff}$	photons s^{-1}	ionization flux for diffuse-wind photoevaporation	Equation (2.30)
$\Phi_{\rm dir}$	photons s^{-1}	EUV ionization flux for direct-wind photoevaporation	Equations (2.33) & (2.36)
γ_1	–	power-law constant in contaminant-distribution solution	Equation (A.16)
γ_2	–	power-law constant in contaminant-distribution solution	Equation (A.16)
η	g cm^{-1} s^{-1}	kinematic viscosity of the gas	Equation (3.13)
$\eta_{\delta\phi}$	–	normalized difference between Keplerian and gas orbital velocities	Equation (3.27)
κ_i	cm^2 g^{-1}	local opacity scaling in the *Bell & Lin* (1994) parameterization	Equation (2.47)
κ_R	cm^2 g^{-1}	Rossalind mean opacity	Equation (2.45)
λ	–	separation constant for separation of variables	Equation (A.5)
λ_{mf}	cm	mean-free path of a gas particle	below Equation (3.20)

Table C.3 continued: Symbolic Variables

Symbol	Common Units	Description	Example Use
μ	–	average gas-particle mass	Equation (2.4)
μ_{ionz}	–	m_H-scaled mass of an ionized gas particle	Equation (2.31)
ν	$\text{cm}^2\ \text{s}^{-1}$	local disk viscosity	Equations (2.1) & (2.8)
ν_0	***	scaling constant for power-law viscosity	Equation (A.1)
Ω_g	s^{-1}	local gas orbital/azimuthal velocity	Equation (2.14)
Ω_{K}	s^{-1}	Keplerian azimuthal angular velocity	Equation (2.54)
$\Omega_{\text{K,mid}}$	s^{-1}	local Keplerian velocity at the midplane	Equation (2.4)
Π_η	–	radial-pressure-gradient parameter	Equation (6.29)
ρ_d	g cm^{-3}	dust-particle internal density	Equation (3.25)
ρ_g	g cm^{-3}	local disk gas density	Equations (2.2) & (2.3)
$\rho_{g,\text{mid}}$	g cm^{-3}	midplane gas density	Equations (2.3) & (2.6)
ρ_p	g cm^{-3}	local dust-particle volume density	Equation (6.7)
ρ_{p,s_d}	g cm^{-3}	volume density of particles in a given s_d size bin	Equation (6.8)
σ	g cm^{-2}	surface density of diffusing contaminant	before Equation (A.15)
Σ_0	***	scaling constant for power-law disk surface-density	Equation (A.1)

Table C.3 continued: Symbolic Variables

Symbol	Common Units	Description	Example Use
σ_c	cm^2	collisional cross-section for dust-grain coagulation	Equations (3.35) & (3.36)
σ_{cross}	cm^2	collisional cross-section of a gas particle	below Equation (3.11)
$\dot{\Sigma}_{\mathrm{diffuse}}$	g cm^{-2} s^{-1}	loss rate of Σ_g due to diffuse-wind EUV photoevaporation	Equation (2.30)
$\dot{\Sigma}_{\mathrm{direct}}$	g cm^{-2} s^{-1}	loss rate of Σ_g due to direct-wind EUV photoevaporation	Equation (2.33)
Σ_g	g cm^{-2}	local disk-gas surface density	Equation (2.1)
$\Sigma_{g,0}$	***	initial scaling for a delta-function in surface density	Equation (2.20)
Σ_i^j	g cm^{-2}	disk surface density in grid-cell i at time-step j	Equation (2.28)
Σ_p	g cm^{-2}	surface density of dust solids	Equation (6.12)
$\Sigma_{p,c}$	g cm^{-3}	critical particle surface density for collapse/precipitation	Equation (6.15)
Σ_{visc}	g cm^{-2}	the disk surface-density that results from viscous evolution	Equation (2.28)
$\dot{\Sigma}_{\mathrm{wind}}$	g cm^{-2} s^{-1}	loss-rate of disk surface density due to photoevaporation	Equation (2.27)
τ_e	–	the normalized eddy time	before Equation (3.33)
τ_P	–	Plank optical depth	Equation (2.44)
τ_R	–	Rossalind mean optical depth	Equations (2.44) & (2.45)
τ_s	–	normalized gas-drag stopping time	Equation (3.27)
ψ	–	gravitational scaling constant	Equation (6.17)

Table C.3 continued: Symbolic Variables

Symbol	Common Units	Description	Example Use
ζ	–	scale-constant between gas diffusivity and disk viscosity	after Equation (A.2)
$\zeta_{\Delta t}$	–	scaling of disk-evolution timesteps relative to the stability criterion	Equation (2.26)

Table C.3 continued: Symbolic Variables

Units marked as:

– These variables are unitless.

*** These variables have units that may change depending on the parameters of their equations, or units that are important only within their given equations.